Experimentally supported computational method for the optimal design selection of 3D printed fracture healing implant geometries

Eric Lehder, MSc

Thesis submitted to the University of Nottingham for the degree of Doctor of Philosophy

April 2022

Contents

List of Figures

List of tables

Abstract

The development of AM technologies has brought about very promising opportunities in the field of tissue regeneration, especially due to the design freedom they enable. However, the tools and procedures needed to enable medical designers to make use of these revolutionary technologies still need to be developed. In particular, design tools to make implants with optimal geometries for tissue regeneration and procedures to manufacture and test such implants need to be developed to enable the adoption of these technologies by medical designers and biologists designing implants. This thesis aims to address this need.

In order to best use the design freedom that AM brings; it is necessary to define the optimal geometries for specific applications. A novel tool that enables the design of optimal scaffold geometries and could be easily adopted by medical designers was developed here by proposing an intuitive design selection framework that graphically allows the user to gain an understanding of how design variables affect the chosen response variables. The novel framework is flexible, enabling the incorporation of any number of necessary computational models. Triply periodic minimal surface (TPMS) equations were used to simplify the design variables needed to generate an optimal porous scaffold geometry. The potential of this framework was demonstrated by using it to find the optimal TPMS type and volume fraction for a fracture fixation scaffold.

Experiments were carried out to demonstrate that TCDMDA biocompatible scaffolds of appropriate pore size could be manufactured via projection micro stereolithography. The experiments successfully demonstrate for the first time that TCDMDA scaffolds can be manufactured via PµSLA by using a suitable combination of UV intensity and layer time. It was also demonstrated for the first time that hMSCs adhere to the surface of TCDMDA samples manufactured via PµSLA. To further enhance the cell adhesion, an oxygen plasma treatment was carried out. For the second part of this study it was found that the media could not penetrate the scaffold pores sufficiently, invalidating the results. The presented results highlighting a permeability challenge with TCDMDA scaffolds manufactured via PµSLA are nevertheless expected to contribute to future studies in this area.

Experiments were also carried out to demonstrate the biocompatibility of scaffolds manufactured via stereolithography using Dental LT resin (Formlabs, UK). Successful adhesion of hMSCs to the surface of these scaffolds was shown in Chapter 4. Another novel finding of this thesis was that the Dental LT scaffolds manufactured via SLA were able to successfully enable cell growth, cell differentiation and mineralization in the presence of osteogenic media and BMP-2.

The final part of the thesis focused on expanding the developed design selection framework to include not only a scaffold for fracture healing, but also a matching fracture fixation plate. Fracture fixation plates have been studied for centuries, but there is little research investigating the combination of a fracture fixation plate and a scaffold. The rise of AM has inspired the development of auxetic geometries, which have been applied to fracture fixation plates before and shown to reduce stress shielding. Moreover, stiffness grading has also proved very promising in improving fracture healing. In this thesis these two promising concepts are combined for the first time demonstrating reduced stress shielding compared to a conventional fixation plate geometry. Moreover, the thesis presents a novel computational design selection framework to find optimal scaffold and fracture plate geometries which lead to an improved healing outcome. The framework may be easily adopted by medical designers.

Publication and Conference

Acknowledgements

Dedication

Apart from supporting me in the technical aspects of the PhD, Laura Ruiz and Ian Maskery have been incredibly supportive at a personal and motivational level, which was especially important to me during the COVID-19 pandemic.

I would also like to acknowledge and thank key individuals for their vital personal support throughout this journey: my mother Lucia Botero and my girlfriend Nerea Bejar.

Covid-19 Impact statement

Due to the Covid-19 pandemic I could not carry out much of the experimental work as planned from March 2020 up to April 2021 and had to therefore extend the computational work instead.

Abbreviations

DfAM   Design for AM

SLA   Stereolithography

μSLA   Micro-Stereolithography

PμSLA   Projection Micro-Stereolithography

SEM   Scanning Electron Microscope

SLM   Selective Laser Melting

SLS   Selective Laser Sintering

UK   United Kingdom

USA   United States of America

XCT   X-Ray Computed Tomography

3D   Three Dimensional

2D   Two Dimensional

AM   Additive Manufacturing

3DP   3D Printing

CAD   Computer Aided Design

IFS   Inter-Fragmentary Strain

IFM   Inter-Fragmentary Movement

TRITC   Tetramethyl rhodamine

hMSC   human Mesenchymal Stromal cells

FE   Finite Element

FEM   FE Method

TPMS   Triply Periodic Minimal Surface

Glossary

TCDMDA   Tricyclo[5.2.1.02,6]decanedimethanol diacrylate.

BMP-2   Bone morphogenetic protein 2.

Autograft   Tissue transplanted from one location to another in the same individual.

Allograft   Tissue transplanted from one individual to another.

Accuracy   The closeness of a value to the true value or to a reference standard.

Isosurface   A 3D surface representing points of a constant value within a given volume.

Orthogonal   Involving 90 degree angles.

Skeleton   The supporting framework of points describing a given shape.

Polymerization   Forming polymer chains by reacting monomer molecules.

Symbols and units

Formulas

σ	Stress	t	Thickness
π	Pi	ρ	Volume fraction
A	Area	L	Length
D	Diameter	F	Force
E	Young's Modulus	k	Curvature
B	Width	N	Newtons

Unit Prefixes (base ten magnitude)

n	nano (10^{-9})	k	kilo (10^3)
μ	micro (10^{-6})	M	mega (10^6)
m	milli (10^{-3})	G	Giga (10^9)
c	centi (10^{-2})		

Units of Measure (Unit Type)

N	Newtons (Force)	L	Litres (Volume)
W	Watts (Power)	m/s	Metres per second (Velocity)
m	Metres (Length)	rpm	Revolutions per Minute (Rotational Speed)
s	Seconds (Time)	px	Pixels (Digital Length)
cm^2	Square Centimetres (Area)	°	Degrees (Angle)
cm^3	Cubic Centimetres (Volume)	°C	Degrees Celcius (Temperature)

Chapter 1: Introduction and Motivation

1.1 General Introduction

The development of AM technologies has brought about very promising opportunities in the field of tissue regeneration, especially due to the design freedom they enable. However, the tools and procedures needed to enable medical designers to make use of these revolutionary technologies still need to be developed. In particular, design tools to make implants with optimal geometries for tissue regeneration and procedures to manufacture and test such implants need to be developed to enable the adoption of these technologies by medical designers and biologists designing implants. This thesis aims to address this need.

Overall, this thesis addresses the identified need for a design selection tool that allows medical designers and biologists to design optimal implants for AM in an intuitive manner. Moreover, the work done sets out useful structure-property relationships. Thus, this work paves the way for enabling workers within the medical sector to exploit the revolutionary AM technologies that are being developed in order to make optimal tissue healing implants.

1.2 Bone regeneration scaffolds

Tissue regeneration scaffolds find many applications in healthcare, these applications can be categorized based on the target tissue type to be regenerated. In this thesis the focus is on bone tissue scaffolds, where they are used to aid and support the healing of a defect or fracture. Although bone, like most tissues in the body, is capable of self-healing, when there is a bone defect of 2 cm or larger a bone cannot heal itself [2]. In this situation bone grafted from elsewhere is often used to fill the defect, allowing bone cells from the graft in combination with cells from the host tissue, to heal the defect. There are many complications with such an approach, which gives rise to the need for bone regeneration scaffolds. These scaffolds work in much the same way as grafted bone, but they must be supplied with cells, which are taken as immature cells from the patient's bone marrow and allowed to differentiate into bone cells when attached to the scaffold. There has been much research into what the ideal materials and geometries for such a bone scaffold are. In this thesis the focus is mostly on the geometry and how AM can be used to enable optimal scaffold designs.

1.3 Fracture fixation plates

When a bone fractures, regardless of whether it is expected to heal spontaneously or requires a supporting graft/scaffold, a fracture fixation device is needed to support the fracture while the healing process occurs. The most common fracture fixation devices are external fixation plates, intramedullary nails and internal fixation plates. The most promising of these three are internal fracture fixation plates given that they offer the necessary stability in all degrees of motion. Such plates have encountered many challenges since they were first introduced, such as screw pullout, too high or too low interfragmentary motion, and material mismatch. The concept of locked compression plates solved several of these challenges although they still suffered significantly from what has been described as stress shielding. The main approach to reduce stress shielding is reducing the effective stiffness of an internal fixation plate locally. This is an important challenge, and with the emergence of AM there is a promising opportunity to minimize the stress shielding caused by internal fixators. This thesis explores that opportunity and combines the use of auxetic materials with that of stiffness grading to propose a novel internal fixation plate design strategy.

1.4 Additive Manufacturing

AM is a relatively modern term, although techniques that now fall within the field of AM have been around for a long time, previously being used as prototyping rather than final part construction

methods, and hence, known as Rapid Prototyping (RP). AM can be summarized as a technology that enables the creation of a physical part from digital data, via a layer-by-layer manufacturing process. While other manufacturing technologies require time-consuming planning of the manufacturing process depending on the part or assembly geometry, AM largely minimises the amount of planning required. Unlike other manufacturing techniques such as gas foaming, AM also doesn't require consideration of different types of tooling or steps. More importantly for the work discussed in this thesis, AM offers a unique design freedom due to its layer-by-layer approach, making it possible to realise designs that were previously limited by manufacturing capabilities.

1.5 Design of lattices for AM

Designing for AM is significantly different than designing for manufacturing techniques such as gas foaming, mostly due to the design freedom that AM brings with it. This thesis is mostly concerned with the use of porous geometries known as lattices. "A lattice structure is an architecture formed by an array of spatial periodic unit cells with edges and faces" [3]. Applications for lattices include: light weight structures with relatively high effective stiffness and strength, heat exchangers taking advantage of the large surface area, energy absorption as these lattices can handle large deformations without breaking, and the most relevant application for this thesis is making use of both the large surface area as well as the high effective stiffness of lattices to enable the creation of optimal tissue engineering scaffolds.

Lattices have previously been manufactured with conventional manufacturing techniques such as investment casting, deformation foaming and metal wire approaches [4]. All these processes involve many steps, are limited in the geometries that can be realized and the accuracy of the geometry is low. AM on the other hand enables complex lattice geometries to be manufactured in an effortless manner while providing the possibility to control the geometry to a high degree of accuracy [5]. The design of lattice structures involves the unit cell design as well as the design of the pattern, both of which were be discussed in the Literature Review chapter of this thesis.

1.6 Significance and novelty of this research

Scaffolds based on triply periodic minimal surfaces (TPMS) are attractive for bone tissue engineering because their porosities are easily tuneable to match functional requirements [6], they have been shown to yield a scaffold structural stiffness close to that of bone [7], and because they possess high surface-to-volume ratio, thus enabling more cell attachment compared to other geometries [6]. Various studies have examined the effect of TPMS type on scaffold properties such as porosity, pore size, stiffness and curvature [[8][6]] but structure-property relationships relating to cell growth in TPMS scaffolds have not been developed to date. This study provides such structure-property relationships for several of these scaffolds as well as a novel optimisation method for bone scaffold design.

In the area of modelling the performance of scaffolds, many models and optimisation procedures have been developed, but few consider the adoption of such technologies by medical designers and biologists designing implants [9]. Moreover, although the novel curvature dependent cell growth model has been implemented recently, this was only done with simple lattice geometries and without consideration for key physic fields. This curvature dependent cell growth model is helpful because it allows for modelling the effect of scaffold geometry on the predicted quantity of cell growth over time. The proposed design optimisation method makes use of a curvature dependent cell growth model to optimise the TPMS geometry of scaffolds, while also considering the stiffness of the scaffold as well as the adequate infiltration of arteries and transport of nutrients. It also uses an intuitive approach that can be easily adopted by medical designers and biologists designing scaffolds.

The advantages of projection micro-stereolithography to make scaffolds with high resolution and adequate size have previously been demonstrated in many studies, but never before for the specific biocompatible TCDMDA formulation used here. Furthermore, previous studies have not investigated the use of TCDMDA scaffolds manufactured via projection micro-stereolithography for cell culture applications, as is done in this study. The experiments discussed in this thesis also investigate for the first time the combined benefits of TPMS geometries with BMP-2 growth factors, demonstrating their effect on cell proliferation, cell differentiation and cell mineralisation. What is new here is not an exploration of BMP-2 growth factors, only the exploration of how combining TPMS geometry scaffolds with BMP-2 growth factors compares to having TPMS scaffolds with no BMP-2 growth factors.

Very few studies deal with both a tissue regeneration scaffold and a fracture fixation plate, they usually focus on one or the other. However, it is essential to consider their combined performance which is done in this study using a novel Finite Element optimisation approach which is also graphically intuitive, thus again narrowing the gap between biomedical engineering research and practical application. Finite Element optimisation here refers to a design framework that makes use of a novel Finite Element model in order to arrive at an optimal design. What is novel about the framework is the use of an easily adoptable graphical approach that enables a designer or medical practitioner to quickly and clearly follow the process from the available design space up to the optimal solution that satisfies all constraints. The current study also represents the first time that the promising concept of graded material properties and recent advances in auxetic materials are combined to develop a methodology which may be used to yield an optimal additively manufactured fracture fixation plate.

1.7 Thesis Overview

1.7.1 Hypotheses

The first hypothesis of this thesis was that a computational framework could lead to the selection of an optimal implant geometry for fracture healing applications, while still allowing a medical designer to get a clear picture of the explored solution space. This hypothesis was explored by developing a novel graphical design framework, and using it in combination with suitable computational models to select an optimal tissue growth scaffold geometry. By using limits, constraints and an objective function, as is done in optimisation routines, the framework leads to an optimal solution relative to the defined problem. Moreover, the graphical approach demonstrated how a medical designer may easily get a clear picture of the solutions explored and the process carried out to reach an optimum.

The second hypothesis was that stereolithography technology offers the ability to 3D print scaffolds with small enough pore sizes as well as relevant outer dimensions. This hypothesis was explored firstly by analysing how the resolution affects theoretical layers of scaffolds 3D printed via either stereolithography (SLA) or micro-stereolithography (PμSLA). Next, scaffolds were 3D printed using both of these technologies and microscopy images were used to demonstrate how the scaffolds manufactured via PμSLA had both well-defined pores as well as relevant outer dimensions for tissue healing applications.

Another hypothesis of this thesis was that Tricyclo[5.2.1.02,6]decanedimethanol diacrylate (TCDMDA), which had been successfully shown to yield biocompatible scaffolds via inkjet based 3D printing [10], could be used to 3D Print biocompatible scaffolds via PμSLA. This hypothesis was explored firstly by preparing the material formulation as described in chapter 4, followed by finding the combination of UV irradiation intensity level and exposure time that leads to a layer height closest to that desired. Having demonstrated that samples of this material could be printed using PμSLA, the next step was to show that the samples were biocompatible, which was done using a cell attachment test as described in section 4.2.2.1.

The next hypothesis was that TPMS scaffolds lead to higher osteogenic cell growth than when using a flat geometry of the same outer dimensions. Moreover it was hypothesized, based on the results from chapter 3, that the Lidinoid TPMS scaffold type would lead to higher cell growth than the Gyroid TPMS scaffold type. These hypotheses were explored by carrying out a cell growth experiment over a period of seven days with three time points. As described in section 4.2.2.3, a presto blue working solution was used to quantify and compare the cell activity, and toluidine assay was used to visualize and compare the cells attached to the scaffolds.

The following hypothesis was that scaffolds manufactured via stereolithography using Dental LT (FormLabs, UK) were able to yield scaffolds that are biocompatible, that allow for cell growth, that allow for cell differentiation, and that enable cell mineralisation. Moreover it was hypothesized that when using TPMS gyroid geometry, the scaffold would lead to enhanced cell growth, cell differentiation and cell mineralisation. BMP-2 was expected to enhance these as well based on the literature. To explore this hypothesis an experiment was carried as described in section 4.2.3, where the biocompatibility, cell growth, cell mineralisation of scaffolds made with FormLabs dental resin is measured and compared.

For the final results chapter of this thesis, chapter 5, the first hypothesis is that an extension of the design framework presented in chapter 3 can be used to find an optimal combination of a fracture fixation plate design and a critical fracture scaffold design, while again allowing a medical designer to clearly understand and visualise the design selection process. This hypothesis was explored via the design framework extension to include a second design variable, the selection of suitable limits, constraints and an objective function, the development of a Finite Element Method and a novel graphical representation of the results within the constrained solution space. For more details please see section 5.2.

The next hypothesis that chapter 5 dealt with was that a stiffness graded auxetic fracture fixation plate leads to a lower amount of stress shielding than a conventional solid homogeneous fracture fixation plate. This hypothesis was explored both via the use of a computational model as well as an experimental demonstration. For more details please see section 5.3.9.

1.8 Aim, Objectives, Methodology and Structure

1.8.1 Aim

The overall aim of this project was the development of a novel experimentally supported design framework for the selection of optimal implant geometries for fracture healing applications. The design framework has a special focus on the ease of adoption by medical designers. Furthermore, the project aims to provide useful structure-property relationships for medical designers.

1.8.2 Objectives

1. Establish a suitable model implementation to predict the effect of geometry on the performance of a tissue regeneration TPMS scaffold.
2. Include the tissue scale to consider the effect of geometry on the mechanical performance of the scaffold.
3. Develop a generic geometry optimisation routine for tissue regeneration scaffolds.
4. Demonstrate that the selected bone regeneration scaffold geometries can be manufactured via Additive Manufacturing.
5. Verify the potential of the scaffold geometry optimisation results by use of cell growth experiments.
6. Consider the combined performance of a scaffold and a fracture fixation plate.

7. Utilise an optimisation method that yields optimal scaffold and plate geometries.
8. Verify the potential of the plate geometry optimisation technique experimentally.

1.8.3 Methodology

The overall methodology used throughout this thesis is shown in Figure 1-1. The specific methods used are discussed in each relevant chapter. Initially, the focus was on objectives 1,2 and 3; as illustrated in the first four boxes of Figure 1-1. Chapter 3 presents the results of these stages. Next, as described in the following two boxes of Figure 1-1, the focus was on objectives 4 and 5, and the results of this element of the work are presented in chapter 4. The final results chapter, chapter 5, addresses objectives 6, 7 and 8. The six boxes on the right of Figure 1-1 describe the steps carried out in that analysis.
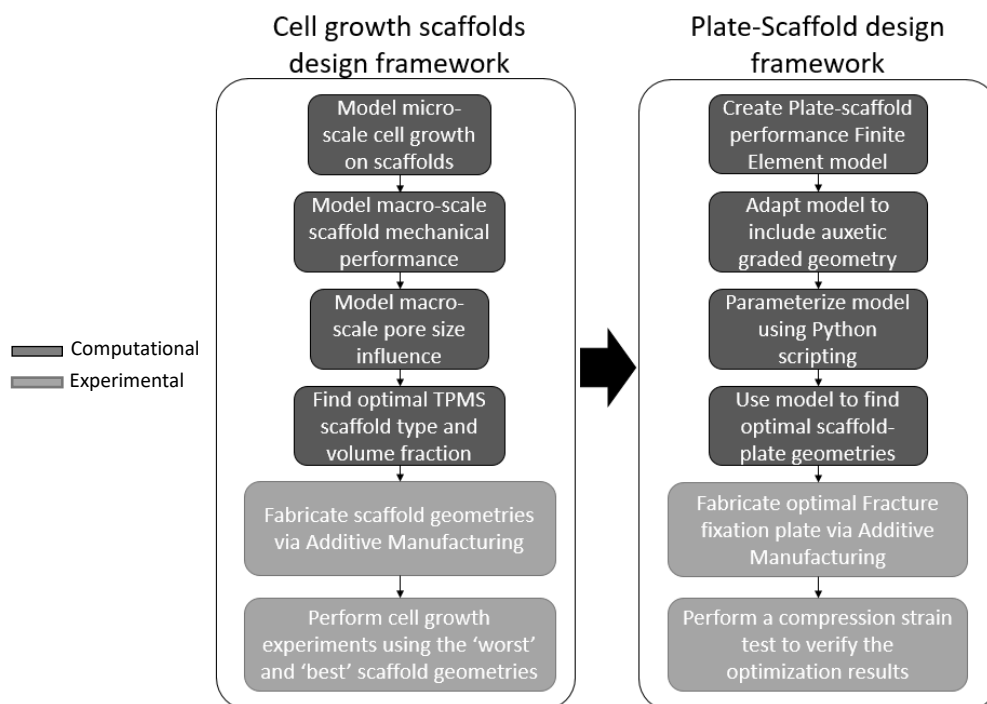
Figure 1-1: Methodology used throughout this research study to develop a strategy for intuitively optimising fracture fixation implants. Dark grey for computational tasks and light grey for experimental tasks. "'Worst' scaffold geometry" in the figure refers to the scaffold geometry that led to the lowest predicted volume of cells growing on the scaffold after 21 days.

1.8.4 Structure

Chapter 1: An overview of the areas of research this thesis is concerned with: Tissue regeneration scaffolds, Fracture fixation plates, AM and Design of lattices for AM.

Chapter 2: A literature review of the research about key topics of this thesis:

- Performance measures for cell growth scaffolds.
- Computational modelling of scaffolds performance (multi-physics and multi-scale).
- Effect of geometry on tissue regeneration, with a focus on TPMS geometries.
- AM of scaffolds.
- Performance measures for fracture fixation.
- Modelling fracture fixation.
- Plates with Auxetic geometry or stiffness grading.

Chapter 3: Developing and implementing a computational strategy to analyse and optimise the performance of cell growth scaffolds.

Chapter 4: Additive manufacture of the scaffolds introduced in chapter 4, as well as results of cell culture experiments carried out.

Chapter 5: Design selection strategy that considers the scaffold from chapter 4 in a realistic fracture fixation assembly together with the fractured bone and a stiffness graded fixation plate. The strategy allows for tuning the fracture fixation performance by adjusting parameters of the plate and the scaffold simultaneously.

Chapter 6: A discussion of the main results, focusing on how they relate to the aim, objectives and literature review set out above.

Chapter 7: A conclusion of the work and recommendations for future work.

References.

Appendices.

Chapter 2: Literature Review

2.1 Introduction

This thesis focuses on developing a strategy to optimize the geometry of a fracture fixation plate and a scaffold. To do this, computational modeling techniques, AM, and cell culture have been used. Before explaining how such technologies were used to achieve the objectives laid out, a thorough review of the literature relating to the relevant concepts is presented in this chapter.

The review begins with a section describing the need for tissue regeneration scaffolds, followed by a section on the modeling of tissue regeneration on scaffolds. In the latter a systematic review of articles that attempted to model tissue regeneration on scaffolds has been carried out, including articles previously reviewed up to 2016 [11]. This was followed by describing the literature referring to the effect of geometry on tissue regeneration.

Both conventional and AM techniques used for making scaffolds are discussed next. Conventional manufacturing techniques involve Gas foaming, Phase separation, Electrospinning, Solvent casting, Particulate leaching and Decellularization. All these techniques are explained together with their key limitations. The AM techniques reviewed are Material extrusion, Bioprinting, Stereolithography (SLA) and Projection micro-stereolithography (PμSLA).

Next, the modeling of fracture fixation plates is discussed. This section begins with a review of the need for Finite Element modeling. General findings of this review were described in the next part of this section, where a statistical analysis of various parameters under investigation was carried out. In a similar fashion, the decisions taken within the research studies in terms of how to create the finite element models of fracture fixation plates were also statistically described.

The section that follows presents the research that has been conducted to model a fracture fixation plate and a scaffold simultaneously. Lastly, stiffness graded and auxetic fracture fixation plate studies were reviewed.

2.2 Scaffolds for bone regeneration

Currently the standard procedure to aid in the healing of bone defects or fractures is the use of bone allograft, bone graft from another patient, or autograft; bone graft from the patient with the bone defect/fracture. The latter leads to the best results because the graft is highly compatible with the surrounding bone given that it comes from the patient her/himself. More specifically, they offer no immunological rejection and provide the best osteoconductive, osteo-inductive and osteogenic properties [12]. Osteoconductive being the ability to support the attachment and migration of osteoblast and osteo-progenitor cells, osteo-induction is the potential for primitive cells to differentiate into bone forming cells and osteogenesis is the potential for new bone formation [12]. However, there are several drawbacks of these processes: limited material availability, longer operation time as bone needs to be both removed and implanted, increased blood loss and pain, as well as other potential complications at the donor site [13].

Alternatives to natural bone grafts are engineered synthetic bone grafts. Synthetic graft materials such as Calcium phosphate (CaP), tricalcium phosphate (TCP) and hydroxyapatite possess mechanical properties like those of the organic part of bone. However, for cells to migrate, attach, proliferate and differentiate, an adequate porous structure is necessary [14]. Manufacturing techniques such as gas foaming cannot accurately control the porous architecture of a scaffold and are limited to one single material. AM on the other hand, allows for accurate control of the porous geometry to be used and with certain techniques it is also possible to construct multi-material scaffolds [14]. Being able to

control the geometry more accurately allows for complex porous scaffold geometries such as TPMS to be explored, which may enhance the outcome of tissue regeneration due to increased surface area or curvature-dependent mechanisms. Multi-material capabilities are beneficial because they allow for the creation of scaffolds that lead to regeneration of multiple tissue types. An example would be a multi-material bone scaffold that allows for blood formation along the central region radially and for bone formation at the outer region radially.

The ideal scaffolds are those with the best osteo-regeneration properties as well as being able to keep mechanical properties at an acceptable level throughout the entire regeneration process. osteo-regeneration involves the three biological properties described above: osteo-conduction, osteo-induction and osteogenesis [14]. The osteoconductive capacity of a scaffold can be measured by quantifying the attachment of cells to the scaffold as well as the amount of migration of these cells throughout the scaffold [14]. The higher the osteo-conductivity of a scaffold the better since it will lead to a higher efficiency of the process. A measure of the osteo-inductive capacity of a scaffold is the amount and rate of differentiation of primitive cells into osteoblasts [14]. Rate of differentiation here refers to the speed at which immature cells turn into bone-forming cells. This should also be as efficient as possible. Lastly, the osteogenic capacity can be measured by quantifying the amount of new bone formation in the scaffold. This should result in as high an average bone formation rate as possible.

The mechanical function of a scaffold can be measured by determining its axial stiffness, which should ideally be high enough to support any loads without breaking, and low enough not to inhibit bone formation [15]. It should be noted that every patient and every fracture/defect is different and thus the ideal performance parameters for a scaffold are specific to the given patient and fracture.

The input parameters of a scaffold can be divided into the solid material, the fluid material and the geometry. The solid material may consist of several parameters if it is heterogeneous, such a varying Young's modulus or poisons ratio, in which case one could describe the scaffold as multi-material. The fluid materials are the cells and the growth factors. The most used growth factors for bone regeneration are bone morphogenetic proteins (BMP-2) because of their superior osteo-inductive properties. More specifically they induce osteoblastic differentiation from Mesenchymal Stromal cells [13]. BMP-7 is another commonly used growth factor in tissue engineering, it can directly promote the formation of blood (angiogenesis) [13], which is also a crucial (but often ignored in tissue engineering studies) component of bone.

The geometry may consist of any number of parameters depending on how it is defined. The lower the number of parameters used to define the geometry the easier it will be for them to be optimised. However, a low number of parameters also means less of the solution space is explored, which is a limitation of the proposed design framework. A large surface area is desired in order for as many cells as possible to attach and thus form tissue. Triply periodic minimal surface (TPMS) lattice structures offer very high ratios of surface area to volume and can be easily defined with just the pore size and the volume fraction [6], making them ideal geometries for tissue engineering.

2.3 Modeling tissue regeneration on scaffolds

The work done until 2016 on computational modelling of how cell-scaffold interactions affect the tissue formation has been thoroughly reviewed [11]. These articles as well as articles from 2016 on have been reviewed here using the following keyword criteria: "modelling" AND ("bone regeneration scaffold" OR "tissue regeneration scaffold"). There are multiple physic fields as well as multiple scales involved in the tissue regeneration process. The main physic fields involved are solid mechanics, fluid mechanics and biochemistry. The most important scales are the tissue-scale (macro-scale), the pore-

scale (micro-scale) and the cell-scale (nano-scale). The review concluded amongst other things that the inclusion of the multiple physic fields as well as length scales involved is crucial to develop an accurate model. The review article also concludes that multi-scale models are important especially because it should be ensured that the scaffold has a sufficient mechanical integrity to bear loads while at the same time allowing for optimal cell development conditions [11].

2.3.1 Multi-physics modeling

As can be seen in Appendix F, most of the reviewed computational modelling studies have focused on using either just solid mechanics or solid mechanics combined with fluid mechanics. Very few studies make use of biochemistry to model the tissue generation process and only one study considered all physic fields. Solid mechanics is used to investigate the influence of geometry parameters, which are the parameters that can benefit most from the advances in AM [16]. However, less intuitively, material parameters could also benefit greatly from AM, given that through AM techniques it is possible to use multiple materials in a single part [17]. Moreover, it is possible to attach growth factors to a scaffold in selective regions through the use of certain AM technologies such as inkjet [18]. These techniques can be useful when a different type of cell differentiation is desired in different regions of the scaffold. Understanding the effects of parameters from all physic fields is important even if those parameters are not under investigation, given that they still affect the accuracy of the results. For a complete list of the papers that were reviewed please refer to Appendix G.

2.3.2 Multi-scale modeling

As can be seen in Appendix F, the reviewed studies have mostly focused on analysing effects either at the cell-scale or at the tissue and pore scales. Few studies looked at either all scales (2/31) or at the cell-scale combined with any other scale (0/31). The tissue scale is mostly important for considering macroscopic properties such as stiffness or compliance [11]. It could be argued that the pore scale (micro-scale) is the most important when looking at geometry variations, given that the pore geometry will influence the cell development processes most [19]. Processes at the cell-scale (nano-scale) have actually been thoroughly investigated, this review only includes some studies on that field, for a review of studies focusing on the cell-scale processes see [20]. In the latter various significant conclusions were stated: "Cell traction generally increases as distance from the cell centre increases"[20], "Cell traction exhibits a biphasic dependence on substrate stiffness: It increases as the stiffness of a soft substrate increases (corresponding to a constant deformation or strain), and then levels off to a constant value on a stiff substrate"[20] and "Mechanosensing events take place at the single-molecule level with the aid of mechanical forces induced by myosin motors in stress fibres"[20].

2.4 Effect of geometry on tissue regeneration

2.4.1 Micro-scale geometry

The cell proliferation, differentiation and tissue deposition that is observed on scaffolds is a result of the interactions between cells as well as their independent reactions to external signals. Both of these aspects are needed to understand why cells react the way they do to changes in scaffold curvature. It should be noted that curvature here refers to curvature radi larger than the size of a cell, not to sub-cellular curvature. For a review of the work done on sub-cellular curvature see the work of Chen et al. [21]. Two key findings are essential to understand the effects of how curvature affects a group of cells and a single cell: a) the rate of bone tissue regeneration increases with increasing concave curvature and b) no regeneration is observed on planar or convex structures.

The work of The department of Biomaterials in the Max Planck Institute of Colloids and Interfaces [22] [23] [24] has been essential towards understanding the effect of geometry on tissue growth. In 2008 their pioneering work [22] proved the above mentioned observations and suggested that the

dependence of tissue growth on geometrical features is due to mechanical forces that develop at the surface of the scaffold. For example, higher curvature results in higher stress concentration and thus higher levels of tissue regeneration stimulus. That tissue grows on concave surfaces but not in convex ones was explained by the "presence of contractile tensile stresses produced by cells near the tissue surface" [24]. These surface stresses could prevent tissue from growing on convex surfaces. However, after a delay period tissue will begin to grow even on flat and convex regions as tissue layers from other regions approach the flat or convex regions. Cell alignment has also been shown to have a great impact in the tissue regeneration and lower curvature can lead to stronger cell alignment [25]. See Figure 2-2 for an illustration of the cord model, which is explained below and illustrates some of the described behaviour.

The effect of curvature on cell growth was further explained in the results of the work of Bidan et al. in a series of papers [26][27][28] where they demonstrated that concave curvature enhances tissue growth on scaffolds while there is very little tissue growth on convex and flat surfaces [27]. The in-vitro studies that they conducted show actin stress fibres, staining with TRITC-Phalloidin, nuclei, stained with TO-PRO3 and collagen fibres captured using phase contrast microscopy [26]. A simple model was also developed to explain the results [28]. Figure 2-1 and Figure 2-2 illustrate how the model works, the idea is that as cells adhere to concave surfaces, they expand as shown. However, it is not the reaction of single cell what explains the higher amounts of tissue growth according to the model, but rather the organization of groups of cells that all expand and form adhesion points only at the edges as shown [28]. As illustrated, cells on convex surfaces are expected not to expand due to the surface tension. This simple model was shown to agree well with the experimental results.
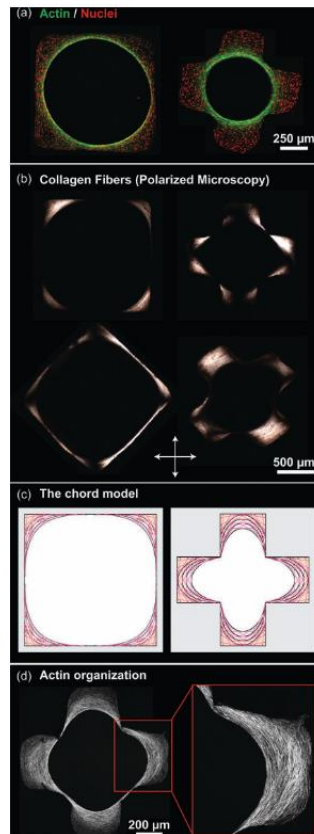
Figure 2-1: Figure taken from [28]. "a) Whatever the geometry of the pore, cells are homogeneously distributed in the tissue (nuclei in red) but actin concentration is much higher at the interface which tends to be circular. b) Polarized microscopy reveals collagen fibres having the same orientation as the cells, i.e., parallel to the tissue–medium interface. c) The geometrical construction that considers tissue as an assembly of tensile elements representing contractile cells [15] applies to convex and non-convex geometries. d) Tissue stained for actin fibres reveals stretched cells organized along the interface as predicted by the chord model." [28].
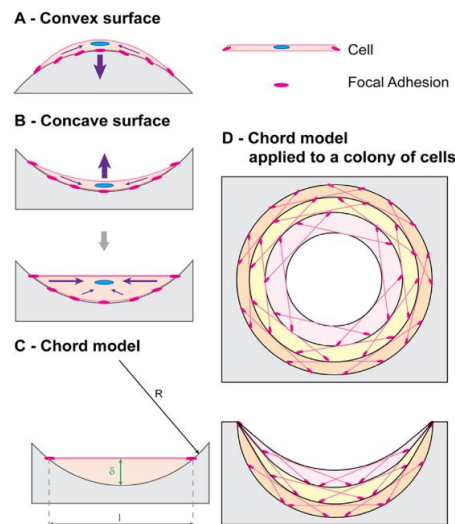
Figure 2-2: Image taken from [26]. "A chord model to describe tissue growth. After adhering on a substrate (pink dots), a cell contracts its cytoskeleton (purple arrows) to reach a stable tensile state. A - On a convex surface, the cell remains bent and exerts pressure on the substrate. B - On a concave surface, cell contraction stretches the membrane and results in a local flattening of the surface. C - A chord representing a static stretched cell defines an element of tissue, which thickness d is proportional to the local curvature of the surface. D - A collection of stretched cells sitting on a concave surface can be seen as an assembly of segments. Each cell locally generates a zero curvature and defines an element contributing to the local thickness of tissue produced. With this new interface being defined, another collection of cells can settle and

According to Zadpoor [19], the pore size and porosity influence tissue regeneration through three different mechanisms. The fluid flow velocity and mass transport within the scaffold are dependent on the pore size and porosity. The higher fluid velocity that comes with a larger pore size means that the cells have less time for attaching to the surface of the scaffold. However, larger pore sizes enhance the transport of oxygen, nutrients and waste through diffusion [29]. Lastly, a higher porosity decreases the mechanical properties of a porous scaffold and given that cell differentiation and proliferation is dependent upon the stress magnitudes experienced by the cells, a change in mechanical properties could lead to a change in the rate and type of cell differentiation [30].

2.4.2 Nano-scale geometry

Such models are useful for predicting tissue growth and thus can serve as the basis for a scaffold optimisation tool such as the one developed here. It is not however, a thorough explanation of why cells produce more tissue on concave surfaces of higher curvature, nor does it bring me any closer to understand how curvature might cause human Mesenchymal Stromal cells (hMSCs) to eventually produce bone, cartilage, tendon or muscle. For that, it is necessary to dive deeper into the effects that curvature has on a single cell. This is what Werner et al. [31] did, they analysed the migration and osteogenic differentiation of hMSCs on concave and convex surfaces of varying radi (62.5-187.5 µm) within a cell culture chip [31]. See Figure 2-3.
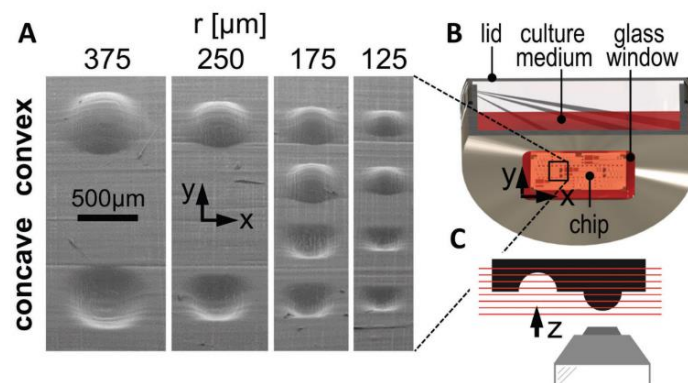
Figure 2-3: cell culture chip to measure effects of curvature, figure taken from [31]. "Setup used to investigate curvature-dependent cell behaviour. A) Scanning electron microscopy image of the cell culture chip showing flat, convex, and concave spherical surfaces. B) Experimental microscope setup for time lapse and immunohistochemistry imaging. The chip was placed on the glass window of a custom-made culture dish with the structures facing downward. C) 3D image stacks were recorded using an inverted confocal/ multiphoton microscope." [31].

On the one hand they found, in agreement with the previously discussed studies, that single hMSCs on concave surfaces would end up adhered to the surface only at the edges as shown in Figure 2-4, while on convex surfaces the cells remained attached throughout most of their surface [31]. This explains why the migration speeds were found to be higher for cells on concave surfaces, the cells detach more easily and thus migrate more.

a)

b)
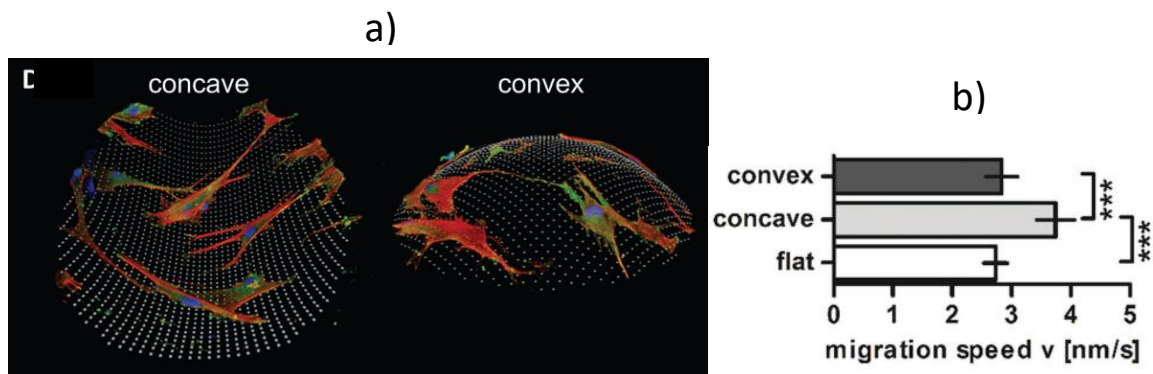
*Figure 2-4: a) Concave vs Convex surfaces (3D), image taken from [31]. "3D reconstruction of immunohistological stained cells (F-actin in red, FAs in green, and nuclei in blue) on a concave and convex surface. Cells on concave surfaces showed an upward stretched cell morphology where a substantial part of the cell body is not attached to the surface. Cells on convex surfaces were fully attached to the surface." [31]. b) cell migration speed for convex, concave and flat geometries, image taken from [31]. "Quantification of hMSC migration speed on flat, concave and convex surfaces over 24 h shown as mean ± 95% confidence interval. ***P < 0.001." [31].*

On the other hand there was a more interesting finding: convex surfaces were found to induce more osteogenic differentiation as shown by the figure below (osteocalcin in green, nuclei in blue and F-actin in red) of surfaces with a radius of 175 µm.
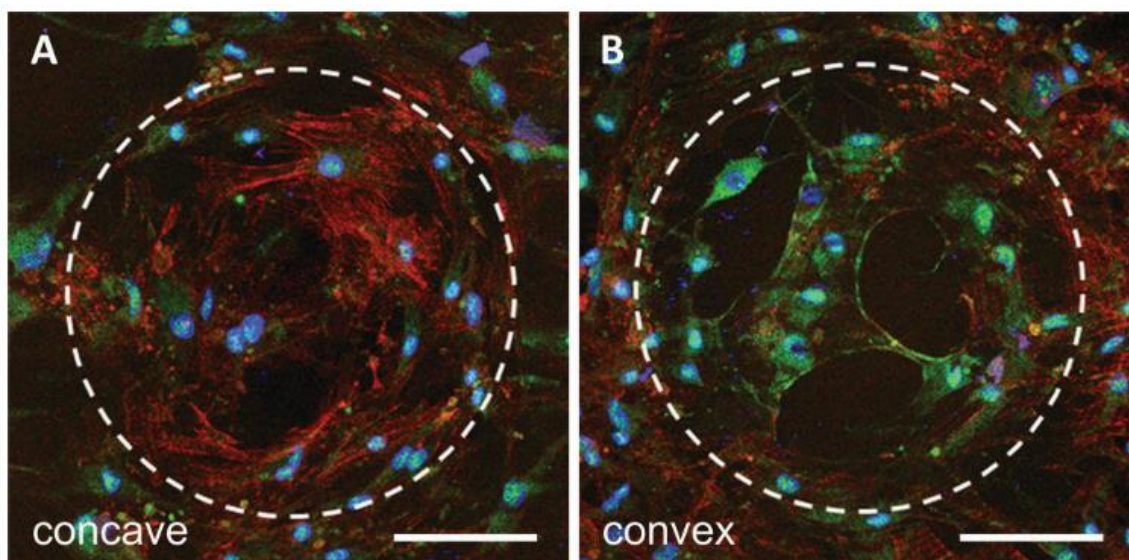
Figure 2-5: Concave vs Convex surfaces (2D), image taken from [31]. "Representative immunohistochemical images of osteocalcin in hMSCs on A) a concave and B) a convex spherical surface (κ = 1/175 µm−1) after 10 d in osteogenic medium (osteocalcin in green, nuclei in blue, and F-actin in red). Scale bar 100 µm. Dashed lines highlight the contour of the spherical surface." [31].

Moreover, they suggested an explanation for why there was a higher amount of osteogenic differentiation on convex surfaces [31]. The explanation relates to the deformation of the nucleus as well as the Lamin-A levels. As shown in the figure below (green for lamin-A, red for F-actin and blue for nuclei), F-actin bundles, which represent the cytoskeleton of the cell, cross over and indent into the nucleus of the cell on convex surfaces creating grooves in the nuclear membrane. The nucleus morphology shown corroborates this as well [31]. Lamins are proteins inside the nuclear membrane that have an important influence on the elastic modulus and viscosity of the nucleus. They have been reported to be involved in protecting the chromosomes of the nucleus against external forces exerted

through the cytoskeleton. Thus, why the higher levels of Lamin-A shown below are further proof that the nucleus of cells attached to convex surfaces is deformed and indented much more than in the flat or concave surfaces [31].
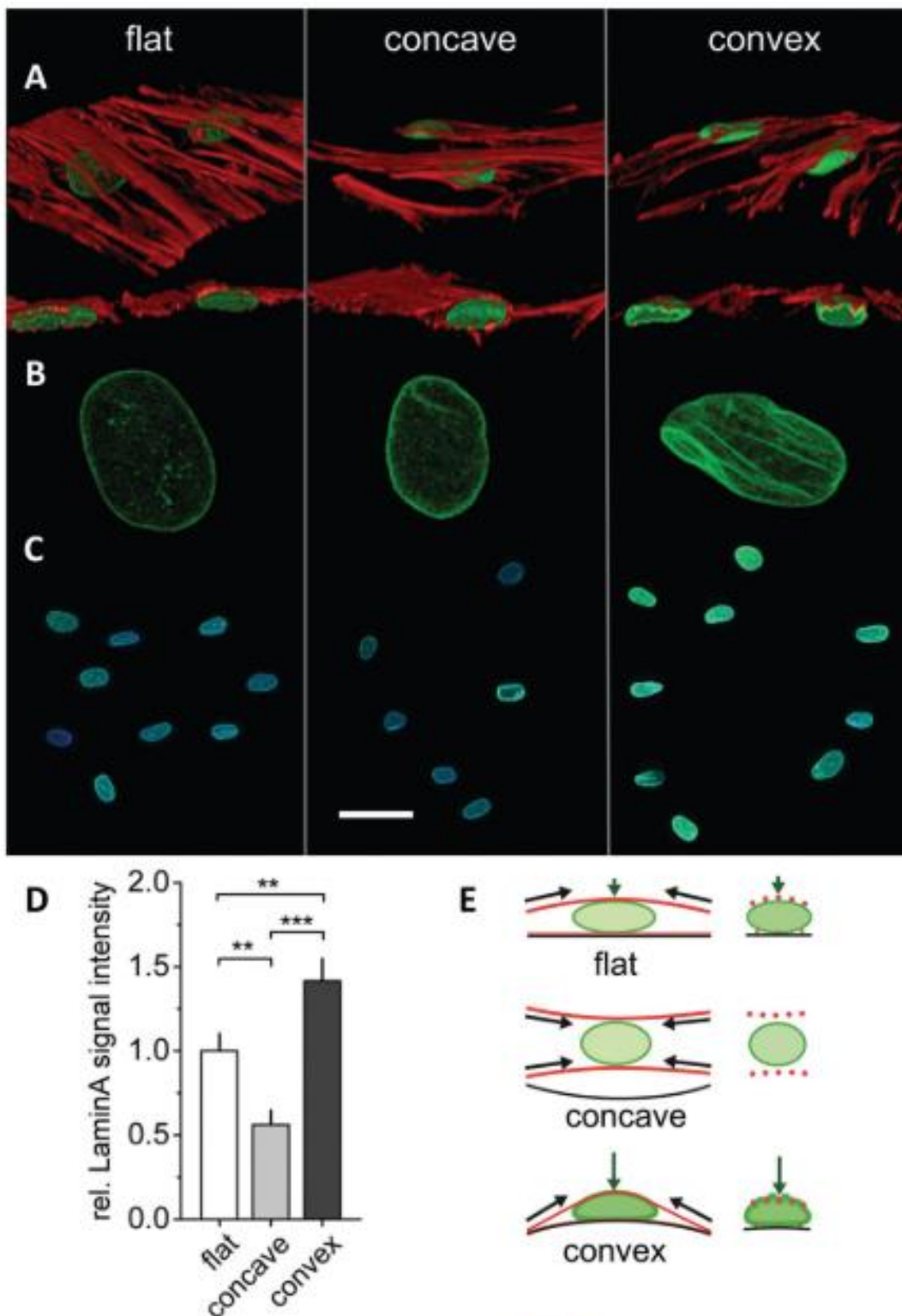
Figure 2-6: Concave vs Convex vs flat surfaces, image taken from [31]. Scale bar in (C) equals to 50 µm. "a–c) Representative immunohistochemical images of lamin-A (green), F-actin (red), and nuclei (blue) in hMSCs on concave and convex spherical surfaces (κ = 1/175 µm−1) and a flat surface after 10 d culture in expansion medium. d) quantification of lamin-A signal intensity shown as mean ± 95% confidence interval. **P < 0.01, ***P < 0.001. e) Schematic representation of the cytoskeletal forces acting on the nucleus (F-actin in red, lamin-A in green)." [31].

2.4.3 Intrinsic and extrinsic effects on cell behaviour

The effects of geometry do not explain why an hMSC differentiates into an osteoblast rather than a chondrocyte, myoblast or a fibroblast. As shown below, Steward et al. [32] divided the influences on MSC cell differentiation lineage into intrinsic and extrinsic mechanical cues. The former consists of substrate stiffness and cell shape, while the intrinsic mechanical ques are fluid flow, pressure, compression and tension [32]. There have been a number of studies that show how MSCs adapt to the substrate stiffness, differentiating into osteoblasts on the stiffest materials and into fibroblast in the softest materials [[33] [34] [35]].
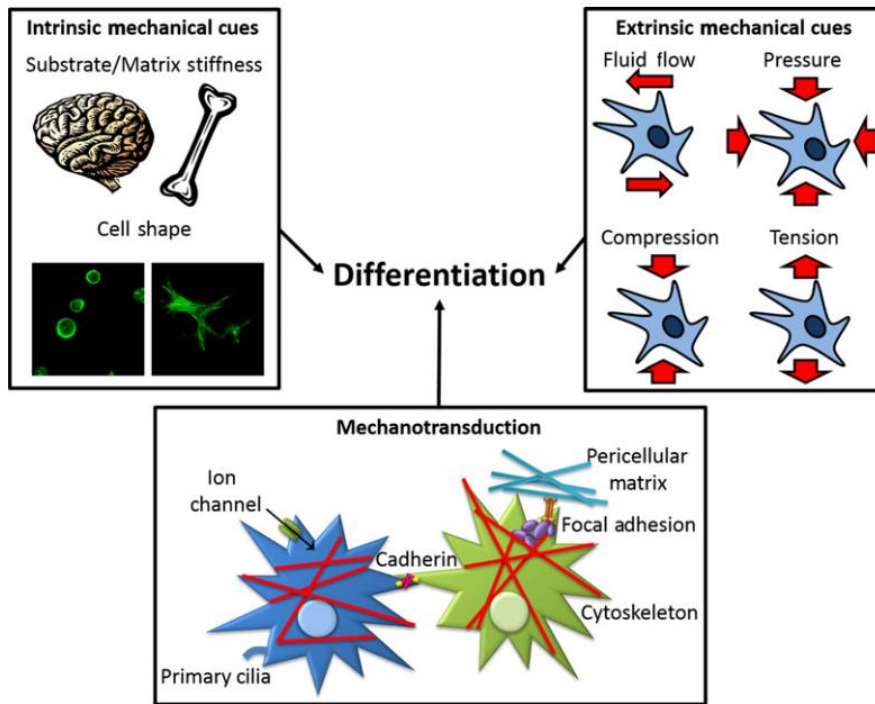
Figure 2-7: : Image taken from [32]. "…intrinsic and extrinsic mechanical cues that regulate the differentiation of MSCs and the specific cellular components hypothesized to be involved in MSCs mechanotransduction." [32].
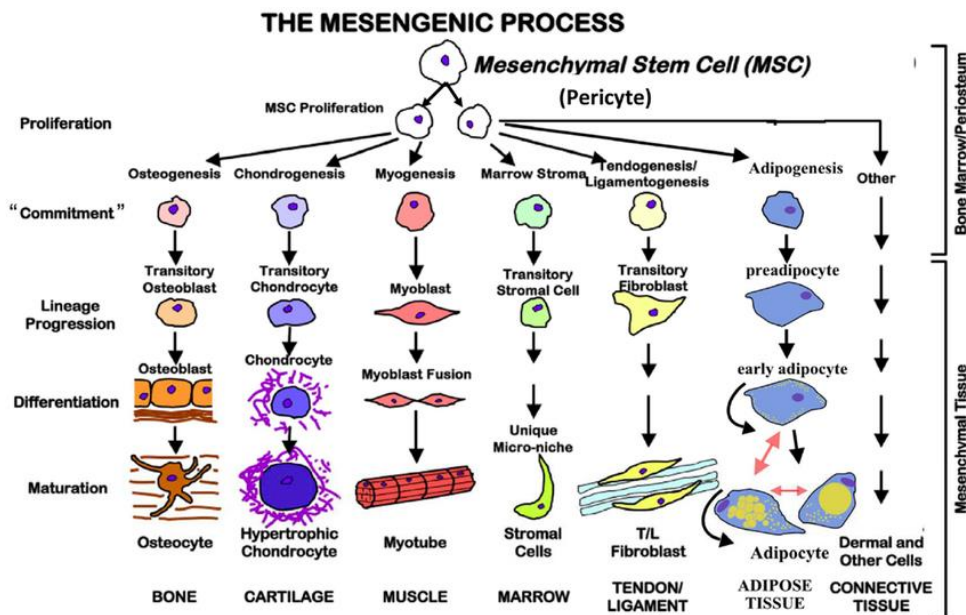
Figure 2-8: Mesenchymal Stromal Cell lineage, image taken from [36].

It has been shown that the binding of integrin to the membrane of the MSCs is necessary for osteogenic differentiation to occur on stiff substrates [33]. It has been further demonstrated that with increasing stiffness the number of integrins bound to the matrix forms a bell curve distribution, with the peak of integrin binding corresponding to the optimal stiffness for osteogenic differentiation [33]. Figure 2-9 illustrates this.
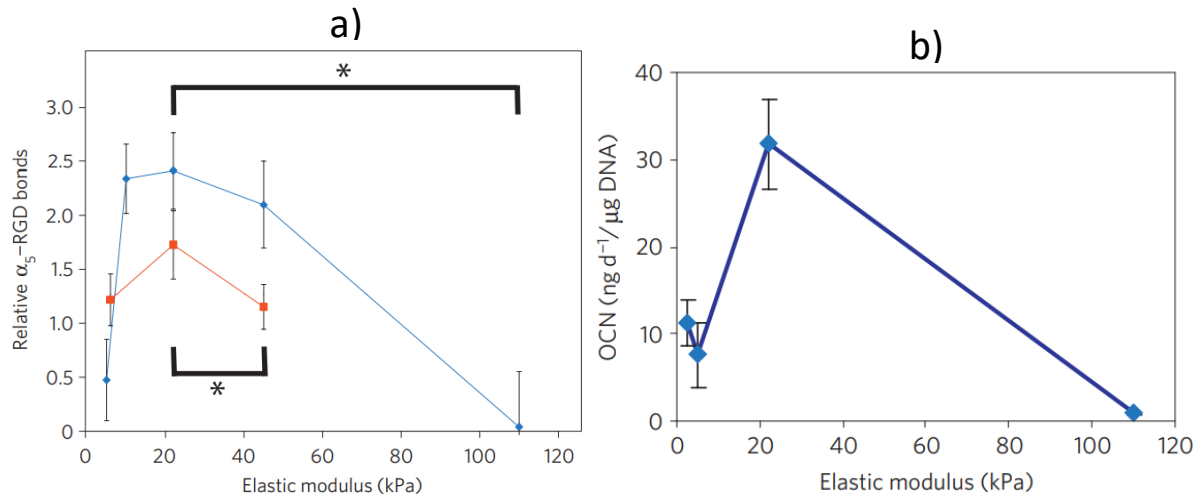
Figure 2-9: a) Image taken from [33]. "α5-integrin–RGD bond formation in matrices with varying stiffness presenting either 37 µM (red square) or 754 µM (blue diamond) RGD–biotin (∗p<0.01, t-test). α5-integrin binding to matrices presenting 754 µM RGE–biotin was negligible. Error bars represent standard errors for the mean (n=4–5)." [33]. b) Image taken from [33]. "Normalized osteocalcin (OCN) secretion by hMSCs after 3 weeks of 3D matrix culture." [33].

Moreover, it was found that in small scaffold islands MSCs became round and differentiated into adipocytes (fat cells) while in large scaffold islands the cells spread out and differentiated into osteoblasts [34]. Thus, a spread-out morphology of MSCs is linked to osteogenic differentiation. The same study also showed that RhoA GTPase activity, a key regulator of contractility, was higher for spread-out cell morphology and thus promoted an osteogenic phenotype [34].

Overall for intrinsic effects, it is understood that integrin binding allows MSCs to feel the stiffness of its surrounding matrix and the cytoskeleton tension then adapts to that stiffness. "These changes in cytoskeletal tension lead to changes in a myriad of cell signalling cascades that control cell behaviour"[32]. The degradability of hydrogels has also been found to affect lineage, with higher degradability enhancing osteogenic differentiation [35].

Fluid flow in perfusion systems appears to enhance osteogenic differentiation of MSCs in 3D constructs [35]. "Perfusion flow not only induces mechanical stress across the cell but also increases nutrient and gas transfer through the gel" [32]. Hydrostatic pressure has not been found to have a significant effect in osteogenic gene expression. It was however found to decrease calcification of MSCs in agarose culture [32]. Compression has been shown to affect other MSC lines but not the osteogenic one. Tension strain on the other hand has been shown to enhance osteogenic differentiation as well as calcium deposition [32]. It was further shown that it is low tensile strains that favour osteogenic differentiation while high tensile strains favour myogenesis [32]. Cyclic tension was shown to induce the expression of proinflammatory cytokines which are inhibitors of bone resorption thus helping to maintain bone formation [32].

2.4.4 Models relating geometry to tissue growth

The theories about how geometry affects cell growth can be helpful by using them to predict tissue regeneration performance and thus find optimal geometries. There are two types of models that can

be used here [19]. One type is where some tissue regeneration output variable is directly linked to a geometrical input parameter such as curvature. A recent example of such a model is the work of Guyot et al. [37] where the relationship between surface curvature and the rate of tissue growth, derived by Rumpler et al. [23], was combined with the level set method in order to predict the tissue growth of an initial layer of cells attached to the surface of a scaffold. The accuracy of such a model is of course dependent on the accuracy of the phenomenological model used for relating the geometrical features to growth dynamics.

The mentioned study was validated and computational results agreed well with experiments. Live-dead Images of the cell seeded scaffolds after 7 and 14 days served as validation by allowing for values of 'projected tissue area' to be computed. The 'projected tissue area' measured from the images was then compared to the predicted tissue area from the computational model, in order to carry out the validation. The method provided a rough comparison between experimental and computational results, however, a better representation of the tissue growth could be achieved by using a CT scan of the scaffold. Moreover, It was hypothesized that taking measurements at more points in time would allow for a better comparison and thus also for a more reliable assessment of the accuracy of this model to predict tissue growth on cell seeded scaffolds. The approach is nevertheless one that has been found to be a reliable technique [38].

The work was later expanded to include other parameters such as fluid flow[39] and oxygen content. However, the study does not consider various length scales, which as stated earlier in section 2.3.2, is crucial for a realistic analysis of the scaffold performance. In that section it is also discussed how the most important performance measures could be said to be the mechanical performance of the scaffold and its capacity to enhance tissue growth after cell seeding. Given that the mechanical performance is a measure of how the scaffold performs relative to the rest of the tissue this suggests a need for the tissue scale to be considered. Moreover, to assess the tissue growth on the scaffold the pore scale is necessary. Thus, a model should at least take into account these two length scales.

The other type of computational models are where the tissue regeneration performance output variable is linked to geometrical features through more fundamental parameters such as the stress or strain transfer between cells and the scaffold. There are many such models, which are particularly useful for predicting what type of cell differentiation will take place [40][41]. These methods, however, can be more computationally expensive. Nevertheless, it is important to predict what type of cell differentiation will occur and so combining these models with the previously described type would be beneficial.

2.4.5   TPMS scaffold geometries

Minimal surfaces are surfaces that locally minimise their surface energy, which is the same as saying they have a mean curvature of zero [42][6]. These geometries are very attractive for tissue engineering applications, not only because they resemble the porous geometry of trabecular bone, which was also observed to have a mean curvature close to zero [24]; but because they maximize the surface area to volume ratio of a scaffold, thus allowing for higher cell attachment as compared to other geometries [6]. Various studies have looked at the effect of different TPMS parameters on a scaffold's performance [18] [19] [44] but they have not done this combining time-dependency as well as multiple scales. Time dependency is important because at different stages of the cell development process the curvature profile of a scaffold will change as well as its porosity and pore size. Therefore, an analysis that only considers the initial scaffold before tissue growth is not thorough enough. Considering multiple scales is important as mentioned because there are performance parameters that can only be measured at different length scales.

As Zadpoor et al. [19] emphasise, there are also no experimental or computational studies which investigate the effect of gradients of geometrical features on cell seeded scaffolds thoroughly. Such gradients could be useful because there are different requirements at different stages of tissue regeneration and at different regions of the scaffold. However, the main gap in the literature that this report focuses on is the lack of a thorough analysis of whether TPMS scaffolds are in fact beneficial for tissue regeneration, which cell type is best, and finally what is a suitable way to determine optimal geometry parameters for a TPMS scaffold. "optimal geometry parameters" is used here referring to geometry parameters that allow the scaffold to satisfy specified constraints and minimise a specified objective function.

Lattices have previously been manufactured with conventional manufacturing techniques such as investment casting, deformation foaming and metal wire approaches [4]. Investment casting is a complicated process involving many steps, and the quality of the resulting part is not very good [45]. Moreover, it does not offer as much design freedom as AM techniques. Deformation foaming does not allow for accurate control of the lattice geometry [46] and therefore doesn't allow for the material properties to be carefully adjusted to improve performance. Wire approaches require many steps and are limited to geometries that can be made with braiding techniques [4]. AM on the other hand enables complex lattice geometries to be manufactured in an effortless manner while providing the possibility to control the geometry to a high degree of accuracy [5].

The design of lattice structures involves the unit cell design as well as the design of the pattern [3]. Regarding the unit cell design, it can be designed in one of three ways. The first way is to use primitives to which Boolean operations are applied [3]. Such a geometry is therefore dependent on the geometry of its primitives. The second way is using topology optimisation, where the geometry is optimised to minimize some objective such as weight while satisfying constraints (typically stiffness) [47]. The third and most relevant here as it is the technique used in this thesis, is the use of implicit equations to represent the surface of a unit cell [3].

$$
\begin{aligned}
F(x, y, z) &= \cos(2\pi x) + \cos(2\pi y) + \cos(2\pi z) \\
&+ a\big(\cos(2\pi x)\cos(2\pi y) \\
&+ \cos(2\pi y)\cos(2\pi z) \\
&+ \cos(2\pi z)\cos(2\pi x)\big) + b = 0
\end{aligned}
$$
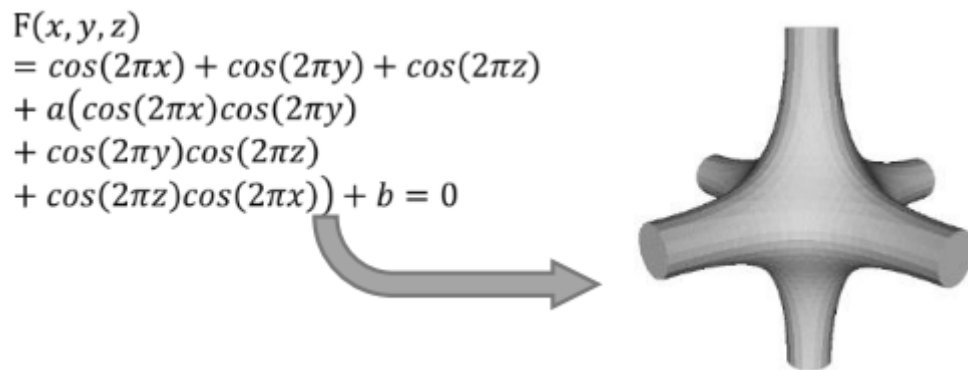
Figure 2-10: Implicit surface-based method to design lattices. Image taken from [3].

When it comes to pattern design, or the organization of unit cells in space, there are also three ways to achieve this [3]. The first is to translate the unit cell in different directions, the second would be to use a curve or surface to which the unit cells conform, and the third would be to use topology optimisation but this time with the unit cells effectively becoming the elements of the model. When unit cells are designed via a mathematical equation, as is the case in this thesis work, this process is simplified because the range of the function can be adapted to allow for the unit cells to be mathematically patterned [3].

The mechanical properties of a lattice structure are partly dependent on the geometry. The main geometry factor influencing the mechanical performance for a given unit cell type is the relative

density or volume fraction [3]. Mathematical relationships for much of the effect that implicit surface geometries have on the mechanical performance of a part have been derived by Gibson-Ashby's model [48]. It is worth noting that the Gibson-Ashby model is more general than this. In this thesis such relationships are used as part of the design framework for tissue regeneration lattice scaffolds.

2.5 Conventional manufacturing of scaffolds

The main manufacturing techniques that have been used for the manufacturing of tissue regeneration scaffolds so far aside from AM are: Gas foaming, Phase separation, Electrospinning, Solvent casting and particulate leaching, and Decellularization [49]. These techniques can all create scaffolds that satisfy some of the criteria for their performance, however, none provides as much design freedom as AM techniques, which is very important for controlling the pore architecture and porosity accurately and precisely. Nevertheless, they are still used as they offer some advantages over AM in its current state. A scaffold should generally satisfy the following requirements: biocompatibility, biodegradable at a suitable rate, high porosity, high interconnectivity and sufficient mechanical performance.

2.5.1 Gas foaming

In this process, the use of solvents is avoided. Firstly, the polymer is compressed at high temperature and moulded into a solid disc. Then the solid polymer is exposed to high pressure gas for several days [50]. During the latter, as the pressure is reduced, the gas infiltration into the polymer creates pores with sizes up to 500µm [51]. This process often results in scaffolds with porosity greater than 90% but there is not much control over pore size and pore interconnectivity is usually low.

2.5.2 Phase separation

Thermally induced phase separation (TIPS) works as a polymer-solvent solution is rapidly heated if the solution has a lower critical temperature or rapidly cooled if the solution has an upper critical temperature. The gas becomes so unstable that it causes the solution to separate into polymer-rich and solvent-rich regions thus creating a porous scaffold [52]. These scaffolds can achieve porosities of up to 97% but the use of organic solvents is necessary. Moreover, the pores are usually too small for tissue engineering.

2.5.3 Electrospinning

With this technique, a porous structure is created as a polymer solution is drawn out of a thin syringe using a strong electrical potential [53]. The geometry can be controlled by adapting process parameters such as the electrical potential, the distance to the substrate and the diameter of the syringe. Scaffolds manufactured in this way tend to have low mechanical strength and it is difficult to control pore shape [53]. Harsh solvents are often used to dissolve the polymer.

2.5.4 Solvent casting and particulate leaching

In this method a polymer is first dissolved in an organic solvent. This is followed by adding particles with specified dimensions to the solution. The solution is cast in a three-dimensional mould to produce a scaffold. A composite material consisting of both the polymer and the particles is then created as the solvent evaporates. By dissolving the particles, the porous structure made of only the polymer, the final porous structure is finished [54]. Unlike other manufacturing techniques, such as gas foaming, this process leads to high interconnectivity between pores as well as a high porosity. Moreover, cell adhesion and viability have been reported to be good with many materials [54]. Given that relatively hard materials can be used, this process is often used to make bone regeneration scaffolds [51]. The problem with this technique is the same found in all conventional manufacturing techniques, the lack of control over the pore shape and interconnectivity.

2.5.5 Decellularization

In this technique biological cells and proteins are removed from an allogenic or xenogeneic scaffold. These cell-removal techniques include freeze-thawing, the perfusion of enzymes such as trypsin and nucleases into the tissue and the use of detergents and saline solutions [55]. Some of the proteins often remain after decellularization and cause an immune response. Another drawback is that with this technique the ECM is usually altered. Other problems are the unavailability of tissue and the pain involved in extracting tissue from a donor. Nevertheless this remains a promising technique with much ongoing research [55].

2.6 AM

AM is a relatively modern term, although techniques that now fall within the field of AM have been around for a long time, previously being known as Rapid Prototyping (RP) [56]. RP was more commonly thought of as a technique to quickly visualize designs by creating a part from which other parts would be derived, until eventually engineers move onto manufacturing the final design with another manufacturing technique [57]. RP or now AM, can be summarized into a technology that allows for the creation of a physical prototype from digital data, via a layer-by-layer manufacturing process. Other terms that have commonly been used to describe what is now AM are Direct Digital Manufacturing [58], Solid Freeform Fabrication [56] and 3D Printing (3DP) [56].

Nowadays, the term "Rapid Prototyping" has become less popular since advancements in the technology have meant that finished products can now be realised, not only prototypes [59]. Moreover, they all fabricate parts in a layer-by-layer fashion which isn't captured by such a definition. This has given rise to the popularity of the term "Additive Manufacturing" [16]. While other manufacturing technologies require time-consuming planning of the manufacturing process depending on the part or assembly geometry, AM largely minimises the amount of planning required [56]. Unlike other manufacturing techniques such as milling and lathing, AM also doesn't require consideration of different types of tooling or steps [59].

As mentioned previously, AM relies on a layer-by-layer manufacturing approach, although this is the key to its geometry flexibility, it is also where some of its key limitations arise from [59]. Not all materials can be used in such a fashion, the thickness limits the resolution that can be achieved, and bonding issues between layers can result in poor mechanical properties [58]. Another drawback of AM is time, especially when using very small layer thickness, where the time taken to print a part can be unaffordable for a given application [56]. Finally the cost of equipment and materials is a major drawback as well, although this is expected to improve in the coming years [60].

AM techniques can generally be divided into powder based, liquid based and filament based [56]. Fused Deposition Modelling (FDM) is the main filament based technology used and it is the most common AM method, due to its affordable cost and relative simplicity [59]. When it comes to liquid based technologies, the most widely known is stereolithography (SLA) [61] but there are also other techniques such as liquid binding three dimensional printing (3DP) [59] as well as technologies derived from SLA such as two-photon polymerization (TPP) and projection micro stereolithography (PμSLA) [59]. The existing powder bed technologies are selective laser sintering (SLS) and selective laser melting (SLM) [56]. In this thesis, the main AM technologies that have been used for manufacturing are SLA, PμSLA and SLS, so these are discussed in more detail below.

2.6.1 Stereolithography (SLA)

This was the first commercial AM process ever used, developed by Charles (Chuck) Hull in the 1980s [56]. The technique works as a photopolymer vat is scanned with UV light (or visible light, electron beam, gamma rays and x-rays) layer by layer to fabricate solid objects [59]. The photopolymer vat is

usually a monomer solution which is UV-active such that it can instantly convert to polymer chains once radicalisation occurs. This polymerisation process occurs only at the desired regions defined by the digital geometry file, such that a pattern for each respective layer is created [61]. The beam of light or electrons is steered in X and Y directions using galvanometric mirrors [61]. The platform can then be lowered or raised to allow the subsequent layer of resin to be polymerised [61]. Once the printing has been completed, all the monomer solution that has not been polymerized is removed [61]. Post-processes such as UV-curing may be used to improve mechanical properties as desired. Moreover, cleaning of the part to ensure no resin is left is crucial to ensure appropriate quality of the print [61].

SLA is a fast AM technology, it is relatively affordable, and can produce parts with good resolution as well as excellent surface finish [61]. The resolution of an SLA printer is in the range of 100 μm in X, Y and Z directions, where the resolution in Z depends on the layer height, while the X and Y resolution values depend on diameter of the light beam used. The resolution can be lowered but this comes with large reductions in time of print. The use of mask projection to irradiate one layer at a time (projection SLA) has allowed for high resolution with reasonable print time [61].

2.6.2 micro-stereolithography (μSLA)

The vertical resolution of SLA or PμSLA is only dependent on the photopolymerization reaction [61]. In order to make thinner layers, the light beam used must focus as close to the surface as possible rather than penetrating far into the monomer resin [61]. During the photopolymerization reaction, monomers and oligomers come together to form polymers. This is possible due to a unit volume of the resin absorbing photons of suitable energy level, and this generates radicals or cations which results in the chain reaction being propagated [61].

There are various ways to decrease the layer thickness. One way is to reduce the irradiation time, such that it is just enough to start the polymerization process [61]. Another way is to ensure the resin used is strongly absorbing of the irradiation wavelengths, such that the light is fully absorbed and thus not able to penetrate far. The first method has major disadvantages such as producing poor mechanical properties and more importantly it is very difficult to control layer height accurately with this method. With the second method, there is no need to control the irradiation conditions and it is thus the preferred approach for μSLA machines [61].

In order to make such an absorbent photosensitive resin, a photoinitiator or photosensitizer can be used. The photoinitiator or photosensitizer must be optimised to match the irradiation wavelength as closely as possible [61]. Moreover, the proportion of this compound that is found in the resin must be high enough. Another way to produce a suitable resin is by using a neutral photoabsorber. These are chemicals that absorb the irradiation wavelength but do not use this energy for photopolymerization reactions, thus in effect also limiting the chain reaction [61]. A major problem with this is that it reduces the reactivity of the resin so in the regions where polymerization is expected, it will be difficult to ensure the desired properties. Since neutral absorbers were first used by Zissi et al. [61], they have been widely used to adjust the cure depth of μSLA resins.

Ultimately, for the beam not to penetrate too deep into the resin, the irradiation and absorption wavelengths must be as close to each other as possible [61]. The optimal situation for a μSLA resin is when it has enough reactivity as well as enough absorptivity. This will then not allow the light to penetrate deep, ensuring a small layer height, while at the same time due to the resin's high reactivity, the polymerization will occur as desired where the light does penetrate [61]. This can be ensured by optimising the amount of photoinitiator and photoabsorber used.

When it comes to the resolution of µSLA in the X and Y directions, the photoinitiator and photoabsorber are no longer the key parameters that require tuning [61]. One simple way to increase this lateral resolution is to change the laser that is used, which can increase the resolution from about 250 µm to 100 µm [61]. Another method is to adapt the optics of the system for the respective resin such that the light could be more precisely focused leading to a smaller spot size. Moving away from scanning methods towards projection µSLA (PµSLA), where an entire layer is projected at once, also reduces the lateral resolution by reducing the number of moving parts and a larger depth of focus can be achieved [61]. A final way to improve the resolution up to sub-µm levels was to ensure the layers of resin are solidified within the resin rather than at its surface. This was made possible by using either two-photon polymerization or exploiting nonlinearities of the photopolymerization process [61].

2.6.3   Projection micro-stereolithography (PµSLA)

An obvious advantage of PµSLA over scanning µSLA is the speed, given that each layer is built at once [61]. PµSLA begins as the geometry file is sliced into layers containing black and white pixels, bitmap files. After this, the light beam is projected onto the surface of the resin using a dynamic mask. Such dynamic masks are those found also in video projection applications, such as liquid crystal displays (LCDs), digital micro mirroring devices (DMDs) and liquid crystal on silicon (LCOS). PµSLA was first demonstrated by Bertsch et al. in 1995 using an LCD. This first machine used an argon-ion laser emitting light at a wavelength of 515 nm, which was very close to the resin absorption peak. It was also capable of redistributing the irradiance of the beam from a gaussian to a flat-top profile [61].

Since then, systems using DMDs and LCOS have also been made [61]. LCOS can be used with UV light which is advantageous to extend the range of materials that can be used. An important advancement of the technology came about with the introduction of the "step and repeat" method, where the platform is displaced along the lateral directions such that one layer is built by several projections, allowing for much larger parts to be built [61]. This is of particular importance for manufacturing tissue engineering scaffolds of appropriate sizes as is the case in this thesis work.
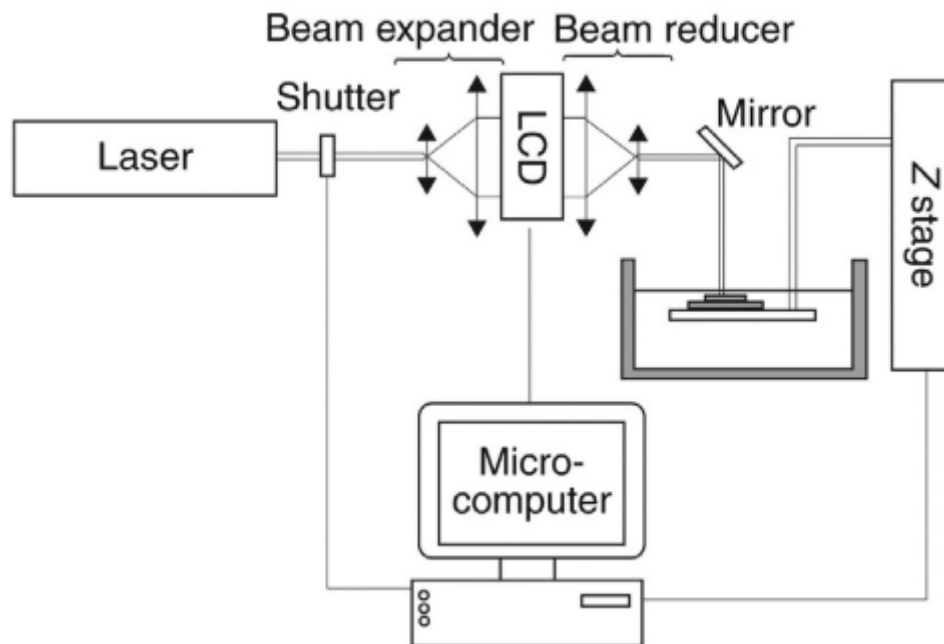
Figure 2-11: Diagram of the first Projection Micro stereolithography Machine. Image taken from [61].

2.6.4 Selective Laser Sintering:

In Selective Laser Sintering (SLS), a laser beam is again used but this time for scanning successive layers of powdered materials rather than resins [59]. As with all AM techniques, the process starts by creating a geometry digital CAD file, which is then processed by slicing software generating automatically a pattern for each layer [56]. The key difference between various powder based AM technologies is in the binding mechanism of the layers [62].

This binding can be either in a solid state, where the binding occurs below the melting temperature, or in a liquid state, where at least part of the material reaches its melting temperature and turns liquid [62]. Within the liquid state techniques there are also two possibilities, the powder is either entirely melted or only an additive of the powder is melted to allow for binding. The first of these options, solid-state sintering, is the most commonly used for polymers [62].

The factors that most significantly influence the quality of parts in SLS are the laser energy density, the layer thickness, the bed temperature and the hatch distance. The laser energy density that should be used depends on the melting point of the material and can be tuned by using the laser power and scan speed [62]. Using a lower scan speed ensures there is more time for the powder to interact with the laser beam, resulting in denser parts, however it is often impractical to have low scan speeds as the print time would then be too long. Using a higher laser power also results in more dense parts since more of the powder will turn to liquid phase allowing it to infiltrate the voids between particles [62].

Another way to improve the density of the parts is by optimising the bed temperature [62], a study by Tan et al [62] showed that a bed temperature of 140°C was optimal in combination with a laser energy of 12 W. Layer thickness has been shown to have the most significant impact in the porosity of the fabricated parts. This is because thicker powder layers allow less fusion between the particles, effectively creating more pores and less densification. Overall, it is now understood that a lower layer thickness produces denser parts and improves bonding between layers [62]. A lower hatch distance will produce a denser part, as can be intuitively deduced by thinking of the linear path the beam goes through and considering the overlapping of subsequent lines. If the spot size is greater than the hatching distance there will be some overlap, the more the overlap, the denser the part [62].
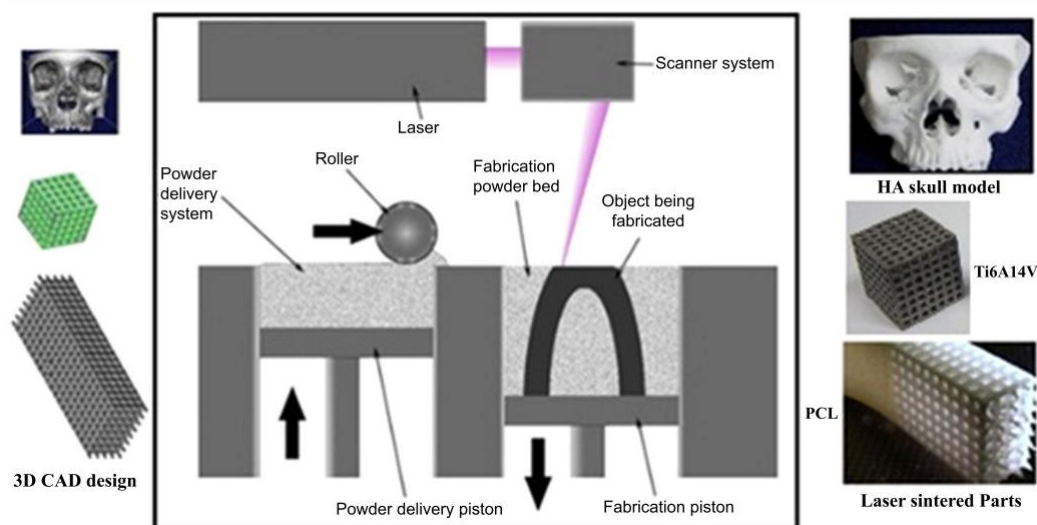
Figure 2-12: Selective Laser Sintering process, image taken from [62].

2.7   AM of scaffolds

2.7.1   Material extrusion

This technique works as a filament is extruded, usually at a high temperature, and then deposited onto a substrate (which may or may not be heated) through a nozzle to make a part layer by layer [55]. Advantages of this technique include that the machines and materials can be quite inexpensive and that there is a wide range of materials that can be used. Cells and growth factors cannot be printed simultaneously with the material because of the necessary high temperatures. The main problem with material extrusion is that it is difficult to create complex porous structures without with smooth surfaces due to the need for support material.

2.7.2   Bioprinting

Bio printing refers to printing both the scaffold material and the biological cells simultaneously [63]. Growth factors may also be printed simultaneously with these two. This can be done through extrusion, inkjet or laser assisted techniques.

2.7.2.1   Extrusion bioprinting:

Unlike material extrusion, in this process the filament and cells are not heated to high temperatures, instead, a plunger, screw or pneumatic system is used to push them out of a small syringe [64]. This is a very popular technique as it is inexpensive, and many types of cells can be printed with a wide range of viscosities and densities. However, the major drawback is that when velocities are high and the nozzle is too small, the cells experience significant shear forces which can lead to them dying or their membranes being destroyed. This is a major issue because a small nozzle is needed in order to obtain high resolution.

2.7.2.2   Inkjet bioprinting:

This process uses an ink rather than filament and the inkjet head usually resembles those of 2D printers. Small drops of the ink mixed with cells and growth factors are deposited onto a substrate layer by layer to create the porous scaffold [63]. Cell viability is usually higher with this process than with extrusion techniques and the resolution is also higher. A drawback of this technique is that the cell densities that can be achieved are much lower than with other printing methods. Moreover, the range of viscosities that can be used for the inks is quite low, thus limiting the materials that can be used.

2.7.2.3   Laser assisted bio printing (LAB):

In this technique, the Laser Induced Forward Transfer (LIFT) process is used, where a thin layer of cell containing material from a donor is first placed over a build plate, followed by ejecting small droplets of it using a pulsed laser beam [63]. With this technique droplet sizes of less than 50μm can be achieved as well as very high densities. An important disadvantage of this printing method is the need for a donor substrate.

2.7.3   Stereolithography (SLA) and micro-stereolithography (μSLA)

As more thoroughly described in the Introduction chapter, this technique works via controlled layer-by-layer polymerisation of a monomer resin either scanning one point at a time or projecting one region at a time. Although SLA is limited by a relatively large layer height of about 100 μm [61], significant advancements in the field have brought about μSLA and two-photon SLA, both of which significantly reduce the layer height [65]. The invention of μSLA was made possible by optimising the interaction between the irradiation wavelength and the resin absorption of this wavelength. This in turn was achieved via the use of photoinitiators and photoabsorbers [66], which allow for the

irradiation to be absorbed only at the desired locations without propagating deep into the resin, thus achieving a layer height as low as 5 μm [65].

2.7.4   Projection micro-stereolithography

Projection stereolithography is where instead of scanning every point on the resin layer, an entire area is projected at once [61]. This was made possible by the use of dynamic masks such as those found in video projection applications [61]. Interestingly, projection stereolithography also serves to enhance the resolution because it involves less movements of the parts thus making it easier to control localised polymerisation [65]. Combining such a projection mechanism with the use of photoinitiators and photoabsorbers gives rise to projection micro-stereolithography (PμSLA), a game changing technology that allows for parts to be made at high resolution as well as higher speeds [67]. Although the size of the area that can be projected currently isn't large enough to make full scale fracture healing scaffolds, by moving the projection mechanism and thus projecting several areas per layer, full scale scaffolds can be fabricated.

2.8   Fracture fixation plates

When a bone fractures, a hematoma occurs which undergoes tissue differentiation in a series of stages. First comes inflammation, then the formation of a callus at the periosteal and endosteal surfaces of the cortical bone at a distance from the fracture, which then grows towards the fracture gap with increasing diameter through endochondral and intramembranous ossification, as shown in the figure below. Such bone healing is often referred to as 'secondary healing'. This callus stabilizes the fracture to a level at which the final bridging of the gap can occur through bone remodelling (often referred to as 'direct' or 'primary' bone healing). This is characterized by bone formation without the need for any intermediate callus, instead, bone remodelling (osteoclast cells resorb bone while osteoblast cells form new bone in a constant cycle) occurs directly [68][69].
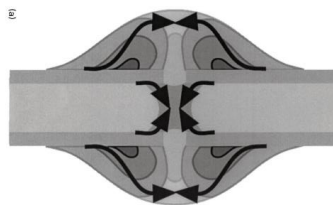
Figure 2-13: Figure taken from [70] showing the process of fracture healing.

If the bone is left to heal on its own, it can be intuitively deduced that the large natural loads imposed by a patient's body will cause high levels of interfragmentary movement (IFM). As explained above, and further demonstrated by another study of Lutz Claes [71], if the structure is not stable enough, direct bone healing will not take place. Thus, some form of fixation is needed to ensure the bone heals appropriately. The most common forms are external fixation, plate fixation and intramedullary nails [72].

A fracture fixation plate is a plate that fixes the two broken bone ends together by being attached to them. The most common form of attachment are screws as shown below.
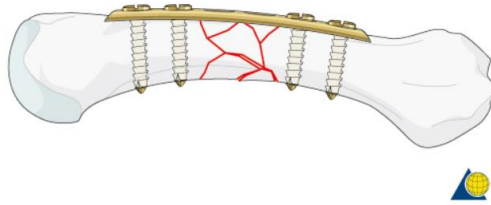
Figure 2-14:Fracture fixation plate attached to a bone with a comminuted fracture. Image taken from [73].

It has been found that both the direction and magnitude of the stiffness offered by the fixation device are related to the stimulated healing. Small and moderate dynamic axial loading has been demonstrated to enhance healing both through Finite Element Modelling and through interface experiments [74][75][72]. Translational shear movement however, has been shown to result in delayed as well as incomplete fracture healing [70]. The advantages of axial motion over shear motion are made much more obvious in the study conducted by Malte Steiner et al. [72] where the two interfragmentary motion directions are thoroughly compared.

External as well as plate fixation cause mostly an IFM in the axial compressive direction due to a relatively low bending stiffness . Intramedullary nails on the other hand, cause large shear IFM as a consequence of the relative movement between the nail and the bone fragments [76][77]. Considering also the previous statements, it can be deduced that intramedullary nailing is not generally the preferred fixation method.

Figure 2-15: Intramedullary nail. Image taken from [78].

External fixation is the only fixation technique that allows a person to modify stability intraoperatively and post operatively [77]. However, the stability it can provide is limited by the large necessary gap between the plate and the bone. Hence, a larger stability can be achieved using internal plate fixation devices. Lastly, external fixation appears to be much more uncomfortable and less aesthetically pleasing for a patient than internal plate fixation.

Figure 2-16: Image of external fixation device. Taken from [78].

Unfortunately, the stability offered by conventional internal fixation plates in the axial direction is usually too low. Even though it was stated that a relatively low axial stiffness combined with a high shear stiffness would be ideal [72], if the axial stiffness is too low, the bone wont heal well either. Thus, the target is to be able to control the axial stiffness accurately such that it is not too low and not too high. Moreover, bone resorption underneath rigid plates was detected [79] and is now very well

accepted as a fact thanks to further experiments such as that carried out by A.J. Tonino et al. [80]. This phenomenon is often referred to as 'stress shielding' because the bone effectively feels less stress due to it being 'shielded' by the rigid plate ([81],[82]). The cause for this lack of stress experienced by the bone is however not only due to a difference in Young's modulus between the parts, as is shown in the results section of this thesis.

Many innovative designs have been created to solve the above problems. For tackling the 'stress shielding' problem, the use of titanium, whose modulus of elasticity is half as large as that of stainless steel, has been very beneficial [83]. On the other hand, controlling the stability of the fracture fixation plate to achieve the desired healing type at the fracture gap has proven to be more difficult. A suitable solution to increase the level of stability offered by fracture fixation plates was developed: Locked Compression Plates (LCP).

Much like external fixation devices, these plates allow for a gap between the bone and the plate by forcing the screws to be locked inside the plate. In this manner, the construct becomes more resistant to shear because a locking screw resists shear along its entire length [84]. A very simplified study about the concept of locking plates [84] shows this quite nicely by loading a piece of wood axially both with the conventional method as well as with the LCP system. See Figure 2-17.
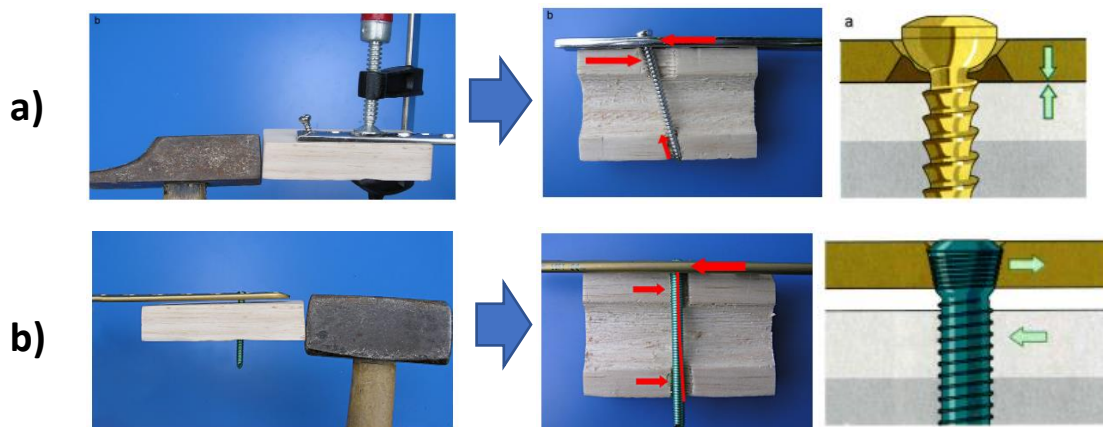
Figure 2-17: a) Conventional fracture fixation plate vs b) Locked Compression Plate (LCP). Images taken from [84]. Notice than in b directions do not match as they should, these are directly copied from the referenced article.

Several concepts have been developed in order to solve this 'stress shielding' problem. Titanium plates have reduced stress shielding somewhat due to their lower modulus of elasticity [83], but this is still not sufficient given that the modulus of elasticity of titanium is about seven times higher than that of cortical bone [85]. Continuing to lower the modulus of elasticity of the whole plate would in fact reduce the 'stress-shielding' further, but it would also cause the IFM at the fracture gap to increase. This would in turn cause the fracture not to heal. The challenge is to minimise the 'stress-shielding' while still providing enough stability at the fracture site.

A promising solution to this dilemma is the use of plates with graded stiffness. The stiffness may be varied by varying either the Young's modulus or the geometry (which affects the Inertia) along the length of the plate. The bending stiffness is defined as the product of the Young's modulus and the Inertia [72], and since the inertia of the construct is dependent on the cross sectional area, changing the geometry of the plate along its length changes the stiffness at that location. An approach that modifies the thickness was recently investigated through the use of a Finite Element model [86]. The concept was a plate with a thickness that decreased gradually from the middle towards the longitudinal ends. This solution did in fact minimize both the stress-shielding and the axial IFM,

however, it is expected that in the regions of low thickness the connection between the screw and the plate will not be very effective.

The concept of a stiffness graded plate was investigated in a 2D Finite Element analysis both longitudinally as well as transversely [87]. In the longitudinal case the Young's modulus of the fracture fixation plate was 200 GPa at the middle and was gradually decreased towards the ends down to 20 GPa. The same was done in the transverse direction. The study successfully proved that a stiffness graded plate will reduce the 'stress-shielding' both in the case of transverse grading as well as axially grading. Whether the stability of the construct would be sufficient was however not so clear. Moreover, it has been shown that when analysing local stress patterns, 3D Finite Element studies should be carried out rather than 2D [88]. Another study attempted this experimentally via AM but was not successful due to issues at the interface between different materials, caused by unmelted niobium (Nb) particles [89].

Another exciting concept that has recently been investigated is the use of plates with an Auxetic lattice structure [90]. Auxetic structures are especially interesting lattice structures because they provide a negative Poisson's ratio (NPR) which means that they expand under tension and contract under compression [91]. This property has been shown to be beneficial for several biomedical applications [92]. For use in fracture plates there was first a study that investigated the use of a completely auxetic plate made of polyurethane [93] and showed that auxetic fracture plates lead to more contact points thus reducing the contact pressure. Recently a study was conducted which proved that by having an auxetic geometry on a section of the plate, not only can the stress shielding be reduced but the plate will remain strong enough to avoid failure [90]. The latter study used a Finite Element model as well as experimental results.

2.9   Modeling fracture fixation plates

2.9.1   The need for Finite Element modeling

A fracture Fixation plate is a device that fixes broken ends of a bone together by means of a plate as well as something to attach the plate to the bone ends (usually screws) [94]. The image below illustrates a typical fracture fixation plate for the Humerus. Intuitively, a fracture fixation plate must allow the bone of a patient to perform given daily functions quickly after implantation. However, it must also allow for the bone to heal optimally. Thus, the design of Fracture fixation plates should address both of these matters [94].

Figure 2-18: Fracture fixation plate for the Humerus. Image taken from [94].

More specifically, the design parameters of the plate as well as the attachment form (e.g. screws) must allow for optimal healing as well as a good mechanical performance at any given healing stage. Moreover, the bones of patients are all different, so the parameters must be the right ones for any given bone. The main obstacle in the design of a Fracture Fixation plate is finding the optimal values for these parameters [83].

The performance of a fracture fixation plate can be measured either experimentally or computationally. In the case of a computational simulation this almost always involves a Finite Element Model [95]. There are several reasons why one would choose a Finite Element Model over an experimental test. Firstly, a most accurate experimental test would require that the trial plate is implanted on a patient, which puts his/her health at risk. Secondly and perhaps most importantly, the number of possible combinations of implant parameters is enormous, as is the cost and time that would need to be invested if one attempted to optimize an implant via experiments. Using Finite Element Analyses, it is much less expensive and time consuming to test an implant design. Lastly, a Finite Element study yields results that cannot be acquired experimentally such as local stress values within a material.

Finite element models of fracture fixation implants are made for various purposes. Sometimes they are used to analyze the influence that certain design or material parameters have in a given output variable (e.g. the effect of implant thickness on maximum Von Mises Stress), as done by one of the studies reviewed here [96]. Other times they are used to better understand the performance of an existing implant, since a Finite Element Analysis yields results that are not accessible through experimental testing, such as local stress tensors [83]. For either case, the method of analysis is usually either a comparison between various implants, or a full optimization which is in a way a comparison of many implants, but with a feedback loop that does the comparing for me and allows for a smart search through the space of possible combinations in order to arrive at an optimal implant.

The goal of a study about Finite Element modelling of fracture fixation plates might vary somewhat, but there are two main objectives that fit to most studies: 1. Analysis of the stability of the construct. This defines the healing mechanism and the rate of healing of the bone, so this is often used to compare implants or for optimization purposes. 2. On the other hand, other studies focus on preventing the failure of the construct, thus, they use some output variable to measure the probability of failure of the construct, either for implant comparison or for optimization purposes. A concise yet highly informative review of the developments of Fracture Fixation plates was done by L. Claes [83]. In it he emphasizes the importance of the two performance parameters mentioned above.

2.9.2   Selection of articles in systematic review

Here a systematic literature review was conducted using PubMed. The search heading was: 'Finite Element Models' AND 'Fracture Fixation' AND 'Plate'. PubMed searches for these terms in the title, abstract or keywords and returns all the studies that meet the criteria. Initially only duplicates and studies in a language other than English, Spanish or German were excluded. The initial database was conducted in October 2020. Furthermore, the abstracts of the papers that met the above criteria were manually screened to include only studies where the results of the Finite Element analysis were validated through an experiment. A chart with the inclusion and exclusion criteria is shown below. All the 21 papers left after all inclusion and exclusion stages were thoroughly read.

2.9.3   General findings of systematic review

In this section, some general statistics can be found regarding the selected studies. This review was done in order to get an idea of how the Finite Element Modeling for this study could be carried out. Below is a table of the data that was analyzed in this section. For an overview of the 21 reviewed papers please see appendix G. As can be seen in Figure 2-19, most of the articles were from 2010 to 2018. Moreover, most of the articles deal with the Femur, followed by the Radius. Overall, it is clear that many types of long bones were analyzed. Furthermore, it can be seen that most papers deal with a comparison of implants rather than an optimization.

Most papers used the whole bone and implant construct, but there are a few that chose to use only a certain region. The reason for using a certain region of the construct only is usually that the implant only influences a part of the bone. However, other times this is done because a symmetric model is used. For instance, in the case of the paper by B. R. Simon et al. [88], which deals with a comparison of one, two and three dimensional Finite Element Models, a quarter model is used because two planes of symmetry are assumed [88].
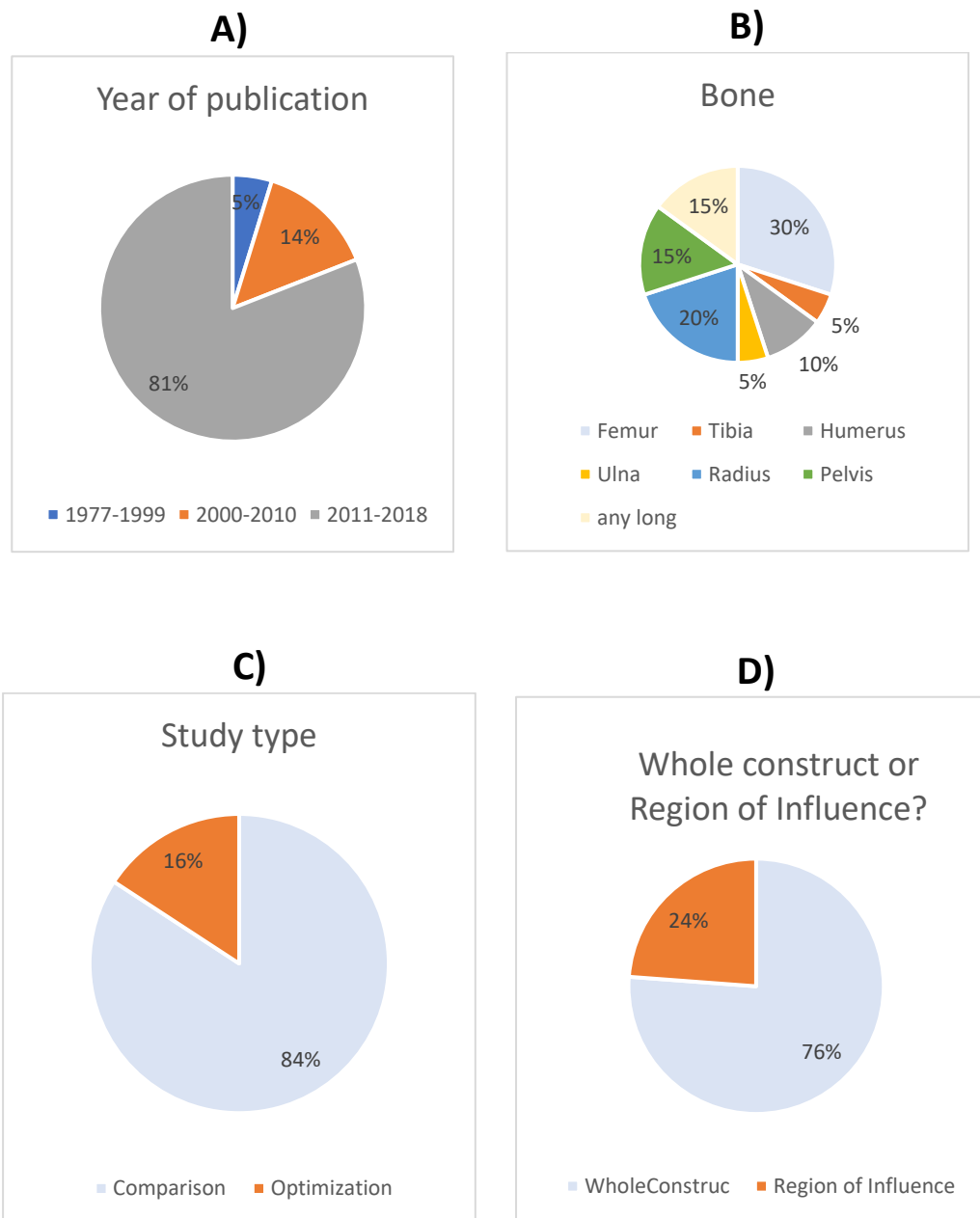
Figure 2-19: A) Percentage of articles for a given year range. Percentages are out of the total of 18 papers. 'Any long' refers to studies that do not specify what type of bone the study is for, simply state that it is a long bone. B) Percentage of articles that dealt with a given bone. C) Percentage of studies that carried out an Optimization or a Comparison. D) Percentage of articles that used the whole construct vs percentage of studies that used only a certain region of influence of the construct. Moreover, this data is shown in percentage here, but to see the number of papers please refer to the above table.

It can be observed from the box plot below that the mean accuracy of the validation of Finite Element models considered, was around 90%. Moreover, most of the calculated validation accuracies (half of

them) were between around 88 and 94%. There was an outlier that measured an accuracy as low as 75%. From the second graph it is clear that the variable that was most used for this validation was the stiffness, followed by the strain.

a)

b)
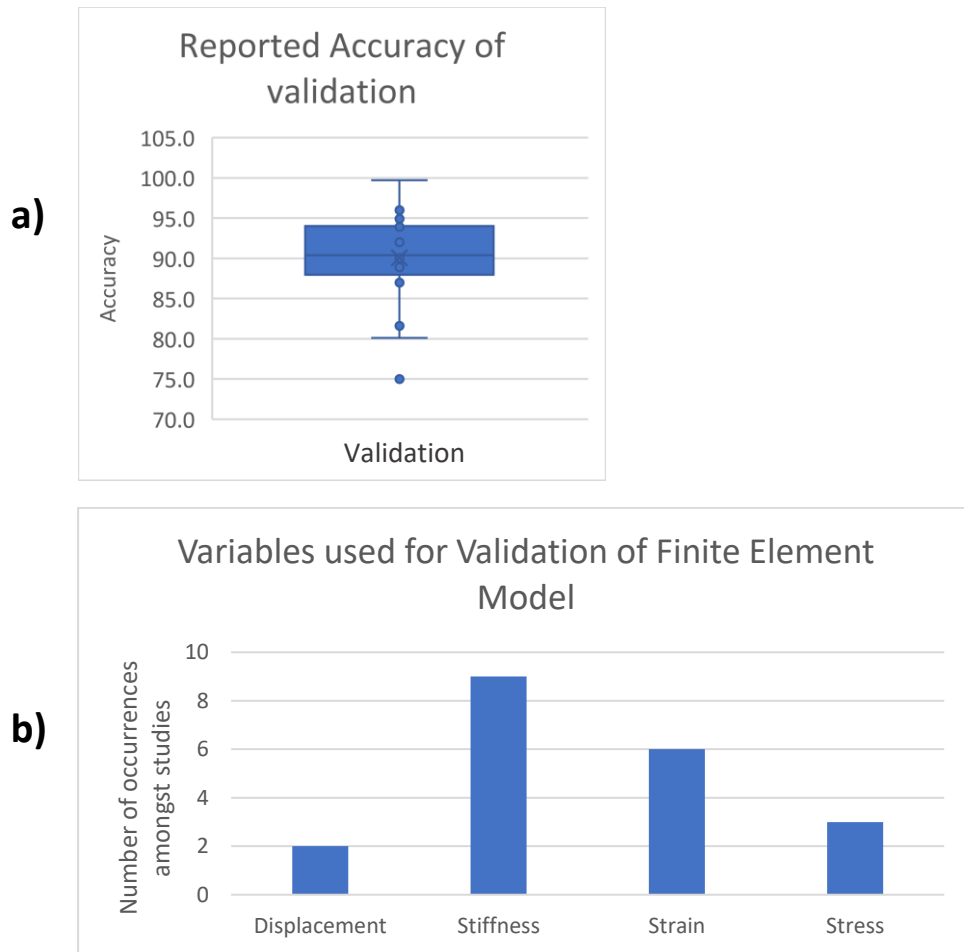
Figure 2-20: a) Box plot of reported accuracy of validation. The x represents the mean of the data. b) Variables used for validation.

The type of bone used for the experimental validation test was recorded below. Most studies validated their Finite Element study using a cadaver bone, but a about 1/5 used a simple tube.
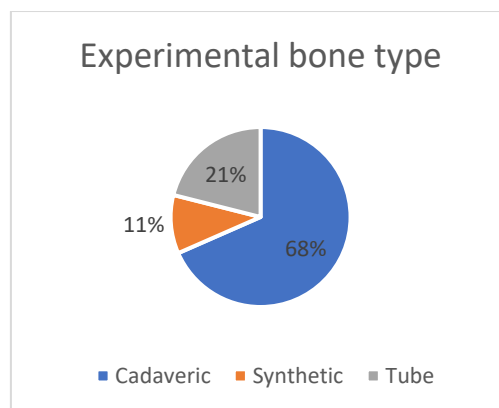
Figure 2-21: Type of bone used for experimental validation.

The three reviewed articles that stated to have performed optimisations were: "On optimization of a composite bone plate using the selective stress shielding approach" [97], "Computer-Aided

Engineering Approach for Parametric Investigation of Locked Plating Systems Design" [96] and "Optimisation of composite bone plates for ulnar transverse fractures" [98]. None of these papers used an optimisation approach, instead, the problem was solved in a simplified way.

The first [97], aimed at finding the right combination of laminate orientation amongst 14 different plies of material. They used a series of constraints to neglect most of the possible combinations, then they used a threshold value of plate stiffness to neglect more combinations and finally they grouped the combinations that were left into plate stiffness intervals and selected one combination from each interval, leaving only 13 feasible combinations which were the only ones treated with the Finite Element Method [97]. The combination with the lowest axial stiffness and highest bending stiffness was chosen as the optimum.

The second study [96], used an even simpler approach. They aimed at finding the optimal combination of plate material, plate thickness, use of screw inserts and use of an oblique screw. They used only nine of the possible combinations, given by the L_9 Taguchi orthogonal array. They compared the factor of safety (Yield strength of plate / Maximum Von Mises Stress) of each level for a given category and chose that with the highest value [96]. Then they ran a final Finite Element Analysis using that final combination. A total of 10 simulations. The third study used a similar approach to that of the first in order to optimise the width/thickness ratio of the plate [98].

2.9.4 Process modelling findings of systematic review

There are five main steps involved in making a Finite Element Model of a Fracture Fixation implant [95]: 1. Geometry: Obtaining the geometry for the bone and implant, 2. Materials definition for both the bone and the implant, 3. Boundary conditions and Loading, 4. Contact constraints, 5. Meshing of the parts: choosing what type of elements and how many finite number of elements to discretize the parts into.

Regarding the geometry of the bone, most studies (76%) used the geometry of a real bone by taking a CT scan of it and converting it into a CAD model. The plate was also mostly generated directly from a CT scan or acquired directly from a manufacturer (48%), but in some cases it was modelled with some simplifications (24%). Other times, the plate was oversimplified to an extruded rectangle (28%).

The screws were most often modelled as perfect cylinders (71%), which is regarded here as 'very simplified'. Very seldomLy, were the screws scanned or the geometry was obtained from the manufacturer (10%). Lastly, in some cases they were modelled with some simplifications but not as perfect cylinders (19%). An example of such simplifications is modelling the screw as having a thread that is not helical but rather making it a patterned revolve of an extruded triangle.
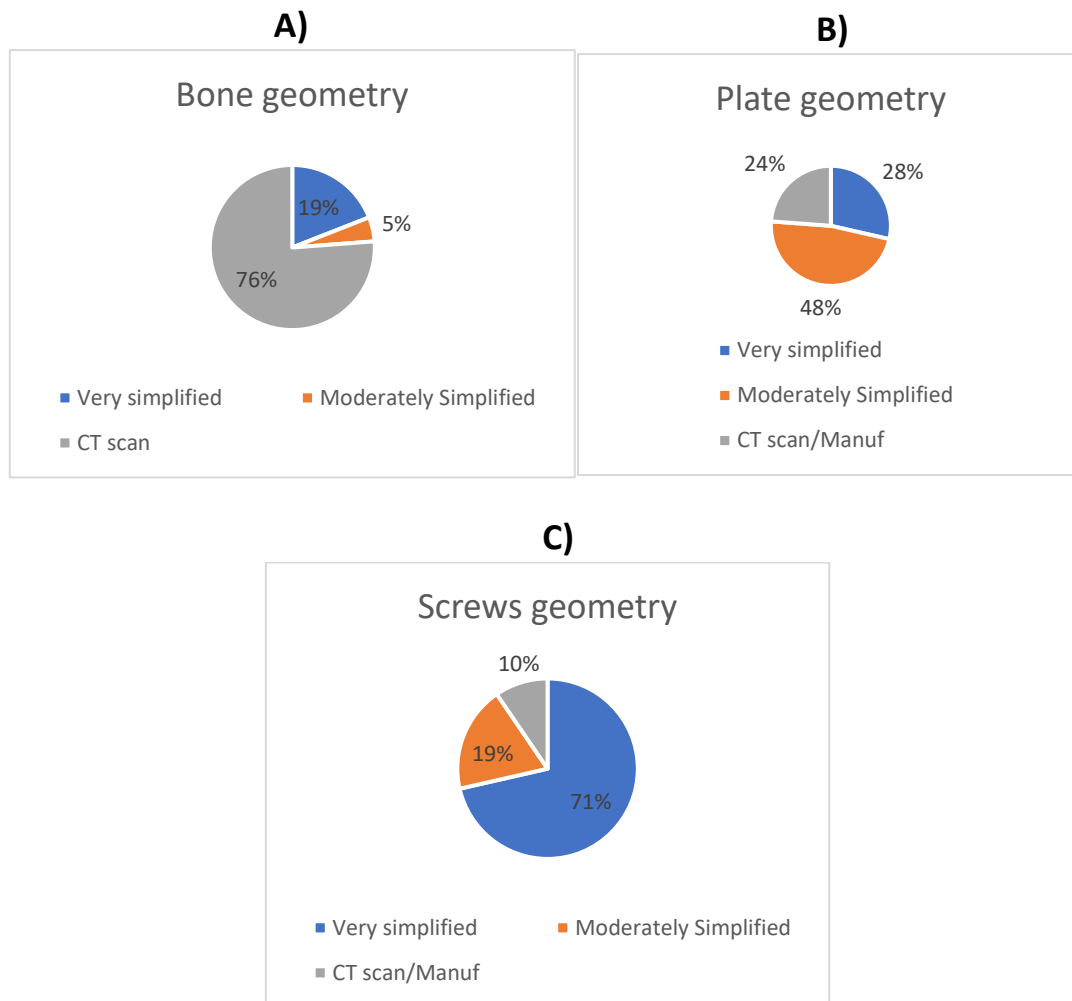
Figure 2-22: Percentage of articles that used very simplified, moderately simplified or accurate geometry. A) For the bone geometry, very simplified refers to a tubular bone and moderately simplified refers to a bone that has more parameters than just diameter, cortical thickness and length, but not as many as a real bone. B) For the plate, very simplified refers to a plate that has only thickness length and width as parameters and moderately simplified is a plate that has more than those but not as many as a real plate. C) The same is the case for the screws. Manuf. Refers to cases where the geometry is directly acquired from the manufacturer. Percentages are out of the total number of studies that answered the specific field, see table above for more details.

As can be seen in Figure 2-23, out of the 21 papers reviewed, all of them modelled the bone as linearly elastic. Regarding the isotropy, all but three studies (14%) assumed full isotropy. Out of those which did not assume full isotropy, two assumed transverse isotropy and one assumed orthotropy (the most realistic anisotropy for a bone). Orthotropy implies that the material properties are different in all of the construct's three orthogonal directions, while transverse isotropy assumed that the properties are the same in two out of these three directions. Intuitively, and more clearly explained using a stiffness matrix, transverse isotropy implies that three young's moduli, three poisons ratios and three shear moduli values are required (9 parameters in total), whilst for transverse isotropy only two young's moduli, two shear moduli and one poisons ratio are required (5 parameters in total).

The studies that used transverse Isotropy did not specify what values they used for the parameters, but the article that used orthotropy [99] did specify that it used the Mean Intercept Length (MIL)

method in order to define these parameters. An article was written about the implementation of this technique [100]. There are different ways to measure the Mean Intercept Length which gives an idea of the direction-dependent density of the material. One is by using an image such as that shown below. The MIL is inversely proportional to the number of intercepts between different 'phases' (interpreted as tone gradients in the picture) in a set of evenly spaced parallel lines. In this manner, a Young's modulus can be calculated for every single direction [100].
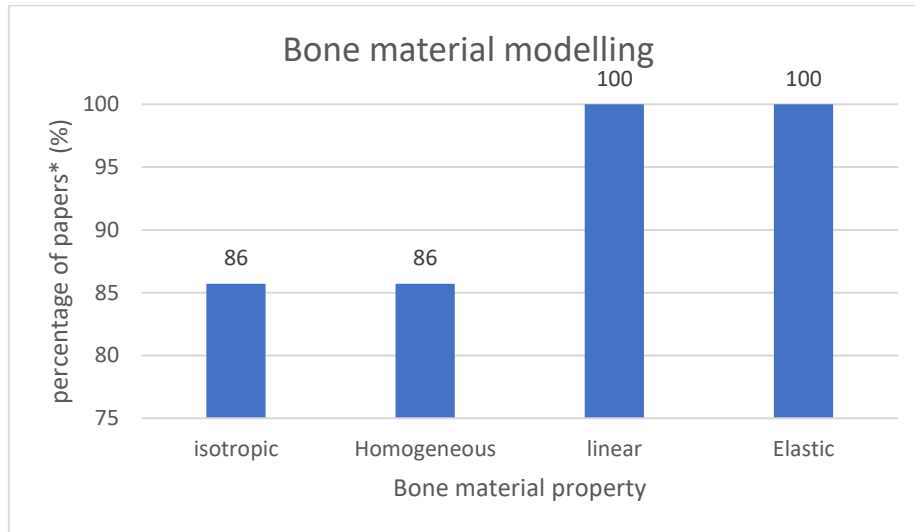
Figure 2-23: Percentage of papers where either of the 4 material modelling simplifications for the bone was used. To work out the percentage of papers that were modelled more accurately for each category simply subtract the percentage above from the total of 100. The only category with more than two subcategories was the isotropy, further details of which are graphically presented below.

*The percentage is calculated using the total as the number of articles that gave information about the given modelling assumption.

Lastly, there were 3 studies that modelled the bone as inhomogeneous, all others modelled it as homogeneous. The three studies used density measures throughout the cortical bone in order to obtain Young's modulus values. The relationships these studies used are denoted by the equations below. Studies A [101] and C [102] used the relationship reported by Gragomir-Daescu et al. [103]. Study B used the relationship reported by Cowin, C [104].

Study A [101]: $E = 14664 + \rho^{1.49}$

Study B [96]: $E = 19327 + \rho^{1.63}$

Study C [102]: $E = 14664 + \rho^{1.49}$

Where ρ is the local density in g/cm^3 and E is the Young's modulus in MPa. To put it into perspective, a density of 300 kg/m^3 would result in a Young's modulus of about 19.6 GPa with studies A and C, while it would mean a modulus of elasticity of about 30.2 GPa with the relationship used in study B.

All studies gave details of the loading they used, and out of all the studies, only 24% used a complex, accurate representation of the reaction forces present (this yields a value for all the 6 possible loads (Mx,My,Mz,Fx,Fy,Fz). For the directions definition, z is the axial direction, y is the radial direction towards the implant and x is the radial direction towards the side of the bone. Most studies (62%) assumed a two-dimensional loading scenario, meaning that either just an axial load (Fz) was applied, both an axial load and a radial load towards the implant, or also a moment around the third direction x.

It can be seen below that for the contact between the screw and the plate, all studies but four used a tie. Regarding the contact between the bone and the screw, 70% of the studies used a tie, and for the bone-to-plate contact only 25% used a tie. Additional facts that are not graphically reported are that one study neglected the contact between the bone and the plate, and one study did not give any contact details.
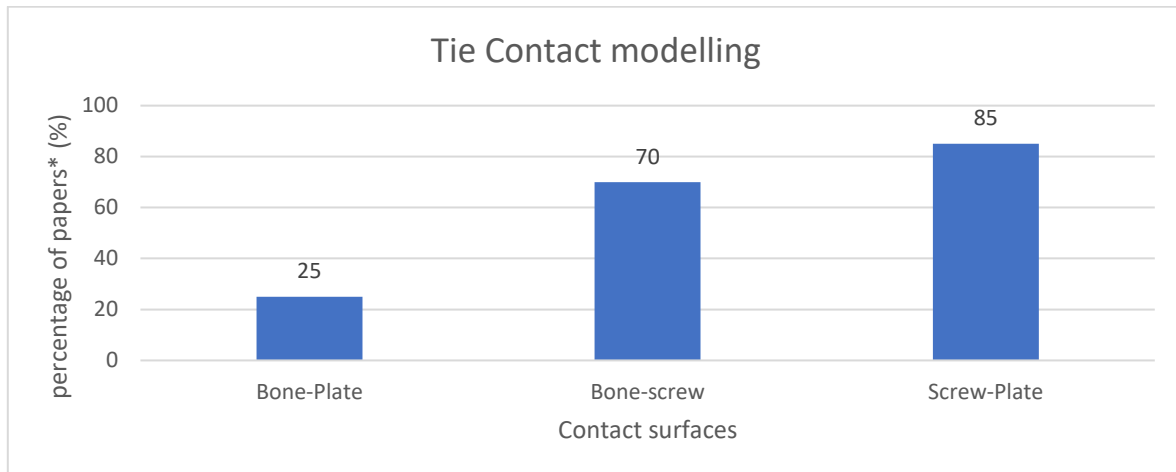
Figure 2-24: Percentage of papers that used a Tie for any one of the contact definitions. Since only two categories were defined: Tied or not Tied, no further details are presented. To work out the percentage of papers that used more accurate contact modelling, simply subtract the percentage above from 100.

Only 17/21 studies reported the final mesh size used. Moreover, only 15/21 reported the variable/s used for the mesh convergence study. This means that in 6/21 reviewed studies, it was simply stated that a mesh convergence study was carried out, without specifying the variable used for convergence. Below is a chart showing the range of mesh sizes most commonly used. It can be observed that most of the studies used a total mesh size range of more than 100,000 elements. The response variable most often used for the mesh convergence study appears to be the stiffness of the construct, followed by the strain in the bone. Here, "response variable" refers to a result parameter that is used to ensure convergence is reached.
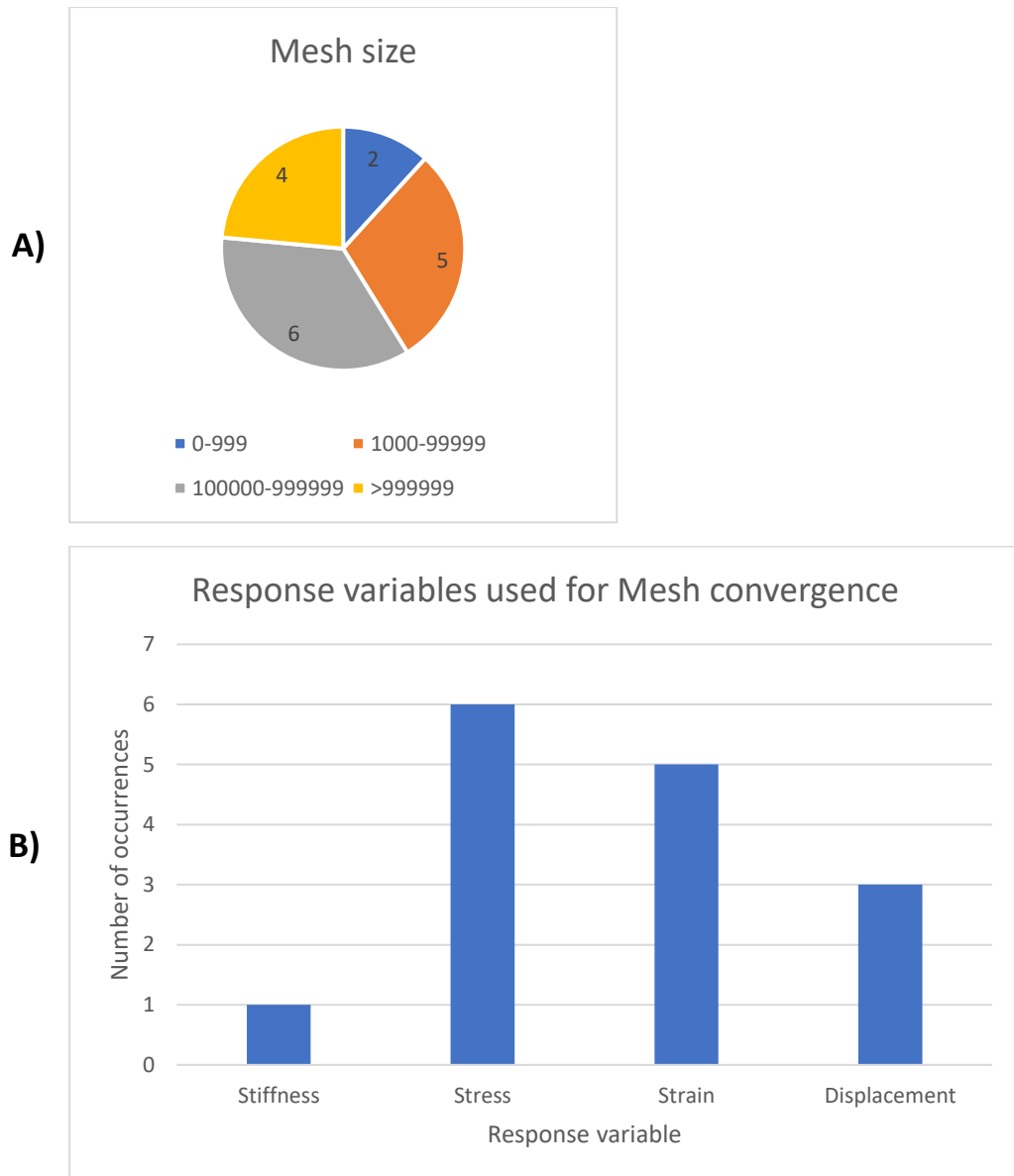
Figure 2-25: A) Percentage of papers that used a given range of total number of elements for the mesh. B) Number of occurrences of a given variable for the mesh convergence study.

2.9.5 Input and output variables from systematic literature review

Most studies performed a comparison between implants by means of one or more output variables. Output variables were used to measure either stability of the construct or risk of failure. Figure 2-26 shows some statistics about which studies measured stability and which measured risk of failure, and which measured both.
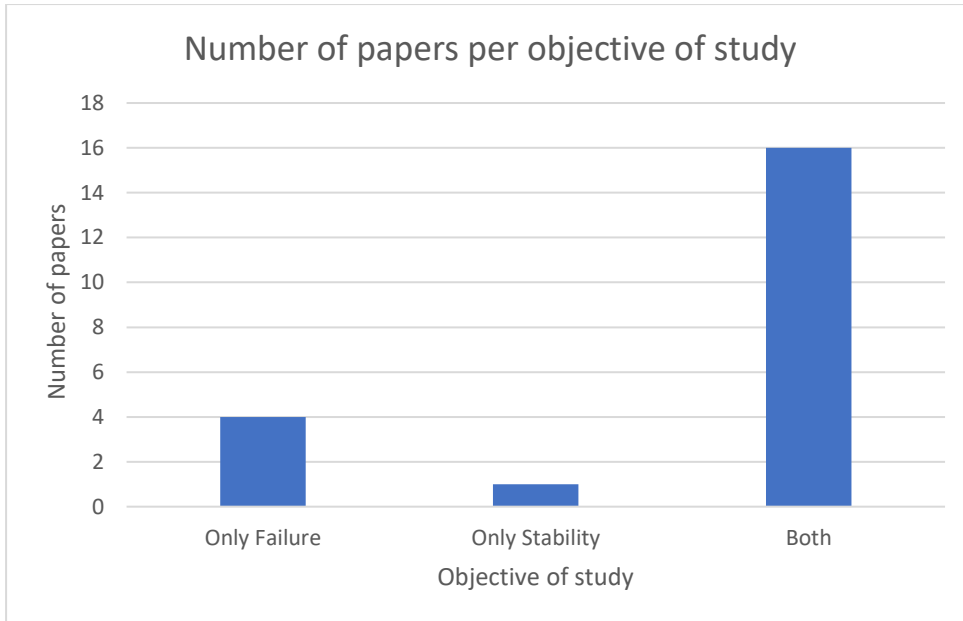
Figure 2-26: Number of articles that dealt with any one objective or with both.

As can be seen in Figure 2-27, the response variable that was most used to measure stability was the Interfragmentary Motion (IFM) while the response variable most used to measure risk of failure was the Von Mises Stress. It is not reported here but for the risk of failure the articles usually measure this by comparing the maximum Von Mises Stress to the Yield limit of the material. For the stability, a threshold was defined by some studies, but no clear trend was found.
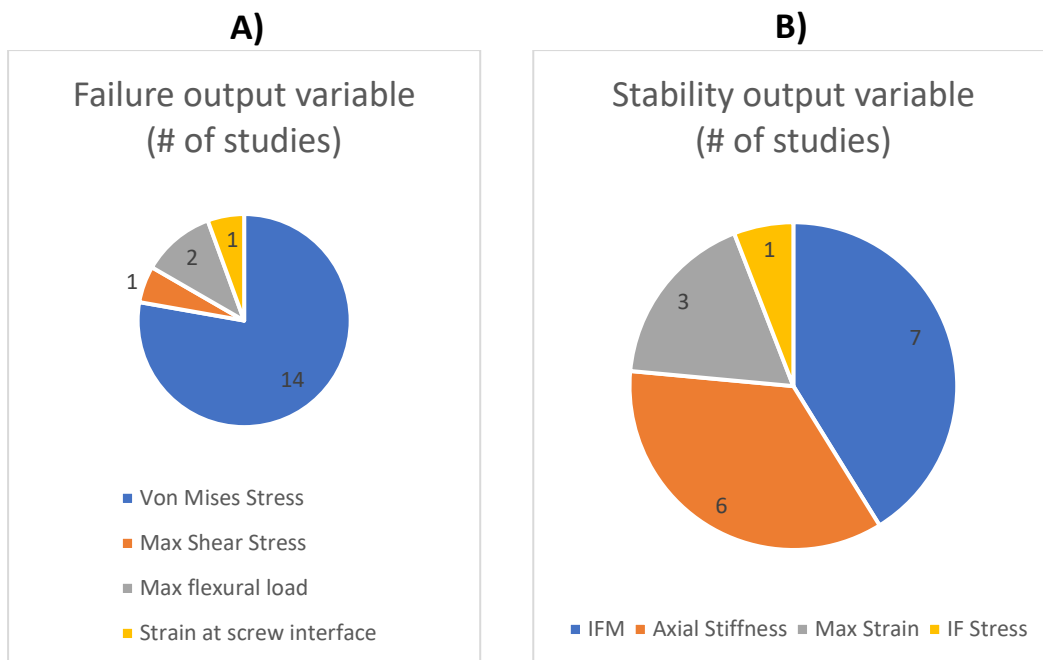
Figure 2-27: A) Number of papers within those that dealt with a 'risk of failure' study, which used any one of the given output variables to analyse the risk of failure. B) Number of papers within those that dealt with a 'stability' study, which used any one of the given output variables to analyse the stability.

Regarding the parameters that were analysed, it can be seen in Figure 2-28 that the most investigated were those of the plate, followed by those of the fracture gap. Moreover, from Figure 2-28, it can be observed that the Gap geometry is the most studied parameter amongst these studies, and that the Screw Diameter is the least studied. Lastly it should be noted that the material of the screws was not included and that is because no study investigated its effect in the implant performance.

a)

b)
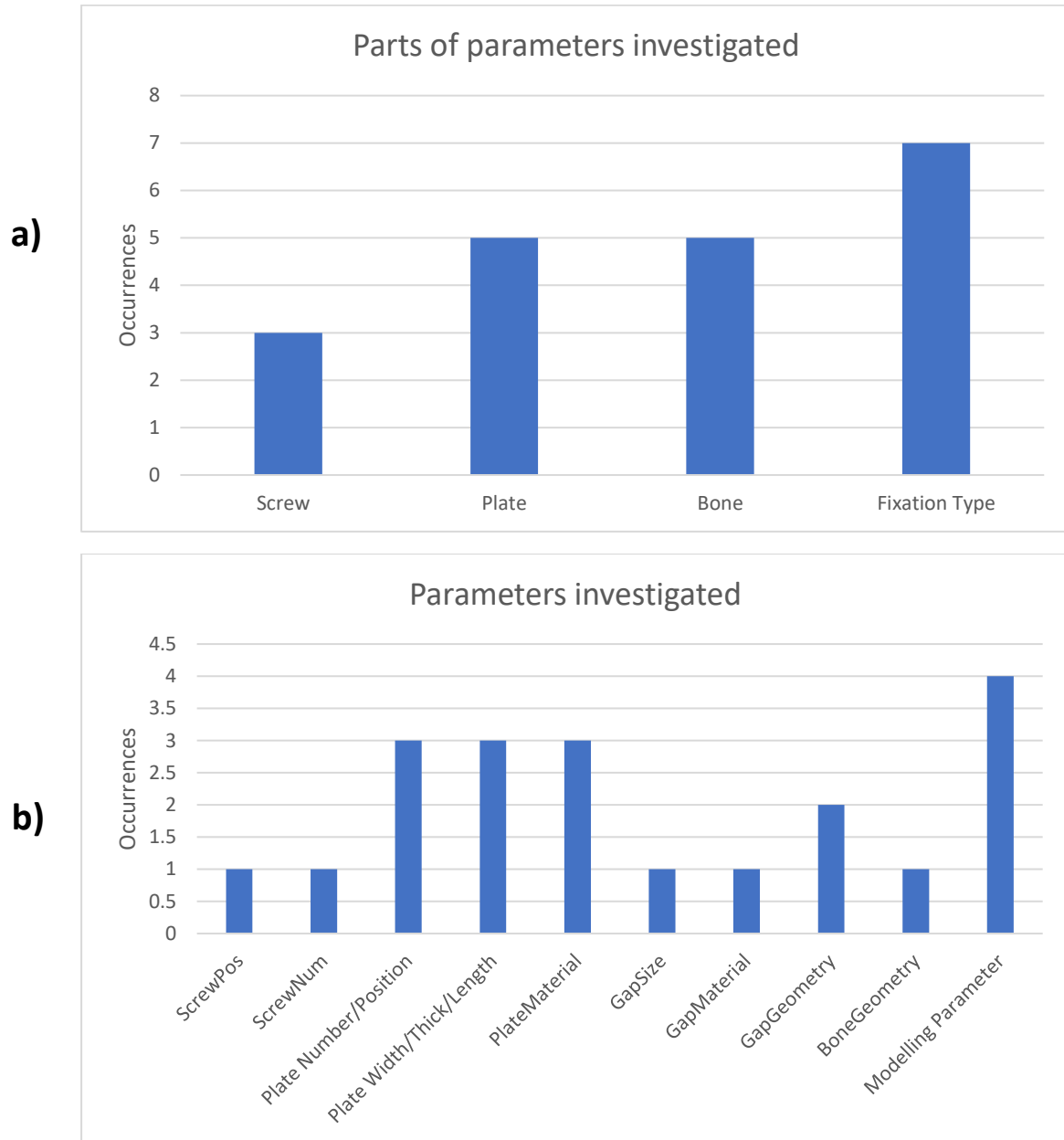
Figure 2-28: Parameters that were analysed. a) these are the parts whose parameters were analysed per study. b) These are the specific parameters that were studied. Modelling parameters refers to parameters such as the material isotropy that was assumed or the dimensions that were used in the study or the loading type.

Both the stability and the risk of failure of the Fracture Fixation construct are crucial for an analysis of the performance of the Fracture Fixation device.

Risk of Fracture:

The variable most used to measure the risk of failure of the construct was the maximum von mises stress. This is reasonable given that the Von Mises Stress takes into account all normal stresses and shear stresses as shown by the equation below [94].

$$\sigma_v = \sqrt{\frac{1}{2}[(\sigma_{11} - \sigma_{22})^2 + (\sigma_{22} - \sigma_{33})^2 + 6(\sigma_{12}{}^2 + \sigma_{23}{}^2 + \sigma_{31}{}^2)]}$$

Where, σ_{11} is the normal stress along the x axis, σ_{22} is the normal stress along the y axis, σ_{33} is the normal stress along the z axis. σ_{12}, σ_{23} and σ_{31} are shear stresses.

Stability:

For the stability, a less clear trend was seen. Although many of the papers (7/21) used the Inter-Fragmentary Motion (IFM) at the fracture gap to measure the stability of the construct, almost just as many (6/21) used the Axial stiffness of the construct as a measure of stability. Studies calculated this axial stiffness differently, one of the formulas used (for the axial stiffness of the plate) is presented below [97].

$$EA = b/A_{11}{}^*$$

Where E is the Young's modulus of the plate material, b is the width of the plate, A is a 6 x 6 extensional stiffness matrix, and $A_{11}{}^*$ is the 1st element of the matrix defined by [A]$^{-1}$.

Parameters investigated:

It can be clearly seen from the relevant results that the fixation type was the most investigated parameter. This refers to whether the fracture is fixed with an Intramedullary Nail, one plate, two plates, just a screw, wires, or any other type of fixation. For the fracture plate, the most investigated parameters were the plate number/position, plate material and plate width/thickness/length. The least investigated parameters appear to be those for the screws. Moreover, it is not graphically reported but only two of the studies investigated composite material properties for the plate.

Thus, it is recommended to do more Finite Element studies to analyse the screws and for composite fracture fixation plates. Furthermore, it was observed during the screening of the abstracts that there are few non-validated articles that investigate the potential advantages of functionally graded implants. With the emergence of 3D printing these can become a reality and may solve some of the key problems of fracture fixation, such as the much discussed 'stress-shielding' phenomenon. Validated Finite Element studies should be carried out the investigate the potential of these implants.

2.10 Modelling plate and scaffold

Only two studies were found which modelled both a plate and a scaffold simultaneously. One of these focused on a multimaterial analysis of the scaffold [105]. They used a composite bone plate in combination with scaffolds of a simple strut-based geometry as shown in Figure 2-29 [105]. A critical size fracture of 30 mm was used. Using a mechano-regulation theory with deviatoric strain, the healing performance of the construct was computed for varying scaffold and plate materials [105]. Although the study proposes an interesting combination of plate and scaffold materials to improve the performance of such an assembly, the procedure is not carried out in a clear systematic way that can easily be adopted by medical designers. The geometry of the implants is not particularly interesting compared to other geometries being investigated such as TPMS or auxetic. Moreover, there was no experimental study to verify or support the results.
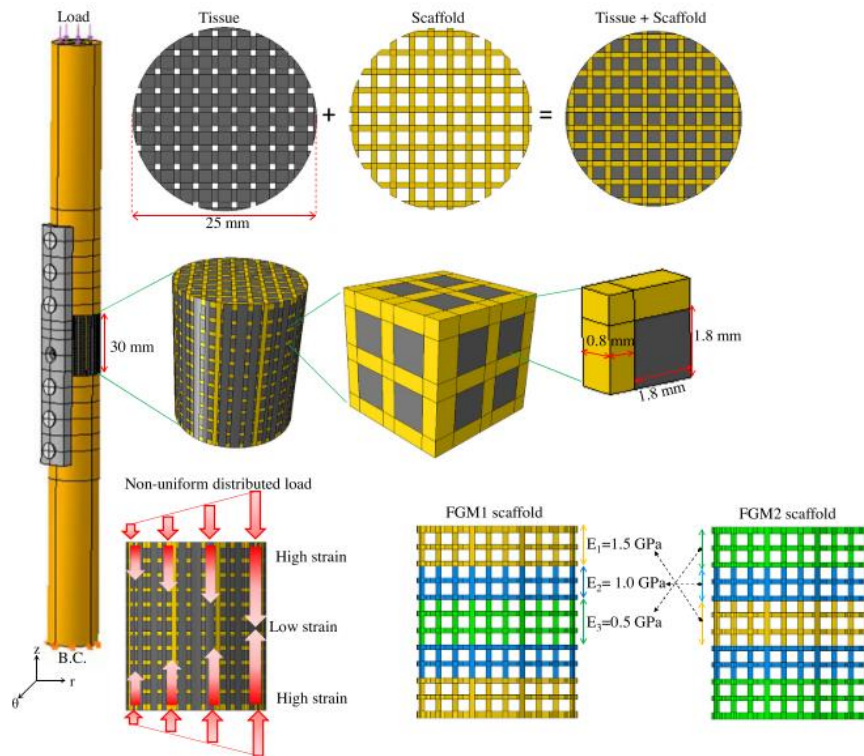
Figure 2-29: Geometry and materials of a reviewed plate-bone-scaffold model. Image from [105]

The other study where a plate and a scaffold were modelled simultaneously was that of Pobloth et al. [106]. In it, honeycomb-like scaffolds were used in combination with either a common locking compression plate or a rigid plate. The fracture gap was of 4 cm and the scaffold stiffness was altered by modifying the strut thickness as can be seen in Figure 2-31. The different scaffold combinations were tested *in-vivo* using sheep bone. Although the study brilliantly shows the potential benefits of computationally optimising fracture healing implants, the investigated combinations of design variables is limited to four, leaving much room for improvement. Similar to the previous study, it does not propose an intuitive yet thorough approach to tune the performance of the implants construct. The plate design was limited to traditional designs. That the model is supported by *in-vivo* experiments makes it reliable and hence much of the modelling done in this thesis for a fracture fixation construct is based on this work.
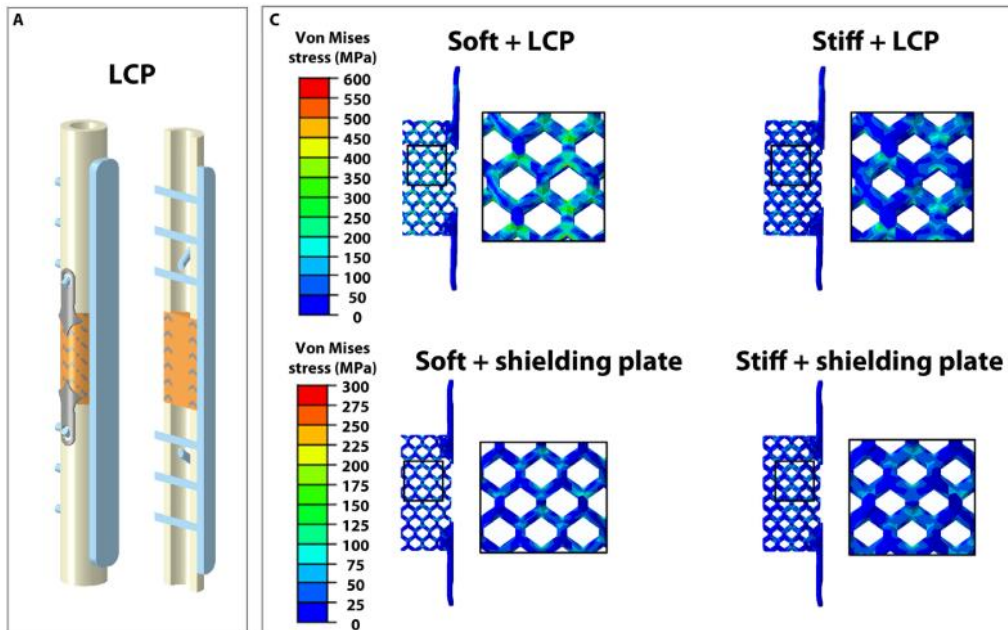
Figure 2-30: Image taken from [106]. "Finite element model and calculations. (A) Three-dimensional (3D) finite element (FE) model of the 4-cm tibia defect in sheep stabilized with a locking compres- sion plate (LCP) and augmented with a Ti-mesh scaffold. … (C) Honeycomb scaffolds formed by titanium struts of the same length (7 mm) but different diameters (1.2 and 1.6 mm). Scaffolds consist of a cylinder (2 cm in diameter and 4 cm in length) and a hole that follows the medullary canal (1 cm in diameter). Top: Von Mises stresses in soft and stiff scaffolds stabilized with an LCP. Bottom: Von Mises stresses in soft and stiff scaffolds stabilized with a custom-made shielding plate." [106].
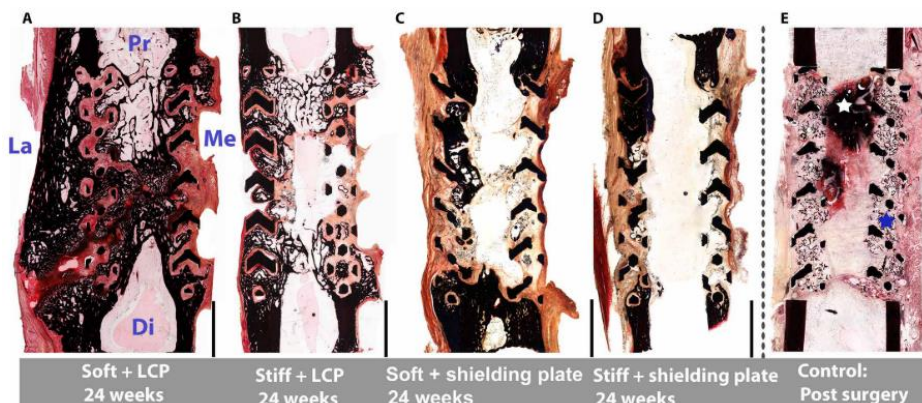
Figure 2-31: Image taken from [106]. "Histomorphological evaluation of the segmental defect healing. (A to D) Safranin Orange/von Kossa–stained thin section of a representative tibia sample in the mid-sagittal plane from each group; additional images are given in fig. S4. Scale bars, 10 mm. La, lateral; Me, medial; Pr, proximal; Di, distal, contralateral to the plate. (E) Sample harvested within the first weeks after surgery used as a control. The augmentation of the honeycombs with autologous cancellous bone graft (ABG) (remnants stained in black; marked with a blue star) and a prominent osteotomy hematoma in the central hole of the scaffold (white star) are still visible." [106].

2.11 Stiffness graded and Auxetic fracture fixation plates

An unconventional fracture fixation plate concept that has shown much promise is that of stiffness grading. It was found that the stiffness may be varied by use of either the material modulus of elasticity or the thickness (which affects the moment of Inertia of the construct). The material modulus of elasticity here refers to the young's modulus of a section of the plate and the thickness refers to the thickness of a section as well. An approach that modifies the thickness was recently investigated through the use of a Finite Element model [86]. The concept was a plate with a thickness that decreased gradually from the middle towards the longitudinal ends. This solution did in fact minimize

both the stress-shielding and the axial IFS, however, it is expected that in the regions of low thickness the connection between the screw and the plate will not be very effective.

The concept of a stiffness graded plate via altering the material was investigated in a 2D Finite Element analysis both longitudinally as well as transversely [87]. In the longitudinal case the Young's modulus of the fracture fixation plate was 200 GPa at the middle and was gradually decreased towards the ends down to 20 GPa. The same was done in the transverse direction. The study successfully proved that a stiffness graded plate will reduce the 'stress-shielding' both in the case of transverse grading as well as axial grading. Whether the stability of the construct would be sufficient was however not so clear. Moreover, it has been shown that when analysing local stress patterns, 3D Finite Element studies should be carried out rather than 2D [107]. It is explained in the article that one- and two-dimensional models can only be qualitative, they do not provide accurate values of screw stresses or contact pressures [107]. Another study attempted this experimentally via AM but was not successful due to adhesion issues at the interface between different materials relating to unmelted particles [89].
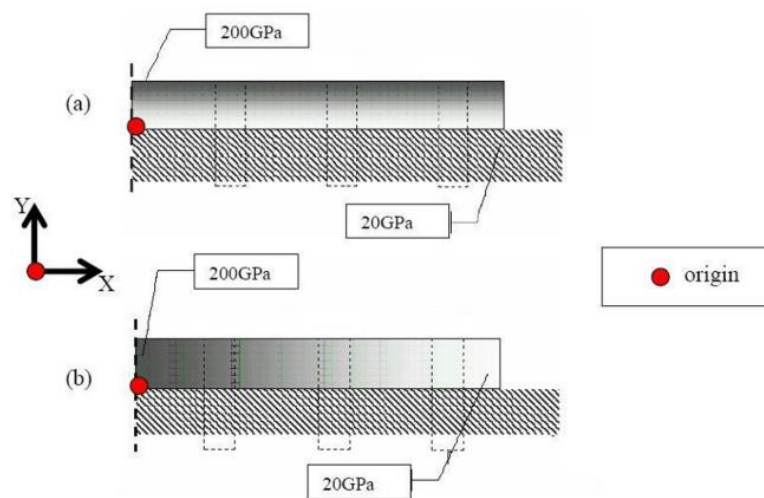
Figure 2-32: Stiffness grading both axially and transversely. Image from [87]. a) shows a plate with stiffness grading applied along the thickness, while b) shows a plate with stiffness grading applied along the length.
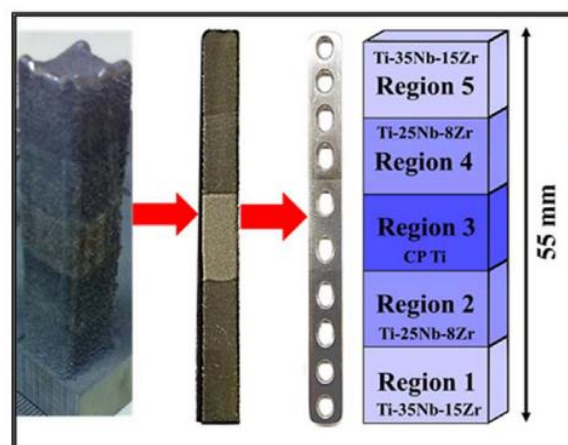
Figure 2-33: Stiffness graded 3D printed plate. Image from [89]. "(a) Actual component produced by LENS™ in the as-deposited state (b) sectioned component on which the characterization was done (c) final component being shown as the representative bone plate (d) dimensions of the printed part with the expected composition profile along its length." [89].

Another exciting concept that has recently been investigated is the use of plates with an auxetic lattice structure [90]. Auxetic structures are especially interesting lattice structures because they provide a

negative Poisson's ratio (NPR) which means that in the plane perpendicular to the loading they expand under tension and contract under compression [91]. This property has been shown to be beneficial for several biomedical applications [92]. For use in fracture plates there was first a study that investigated the use of a completely auxetic plate made of polyurethane [93] and showed that auxetic fracture plates lead to more contact points thus reducing the contact pressure. Recently a study was conducted which proved that by having an auxetic geometry on a section of the plate, not only can the stress shielding be reduced but the plate will remain strong enough to avoid failure [90]. The latter study used a Finite Element model as well as experimental results. The idea of combining such an auxetic geometry with the stiffness grading concept has never been explored before and is one of the gaps this thesis focuses on.
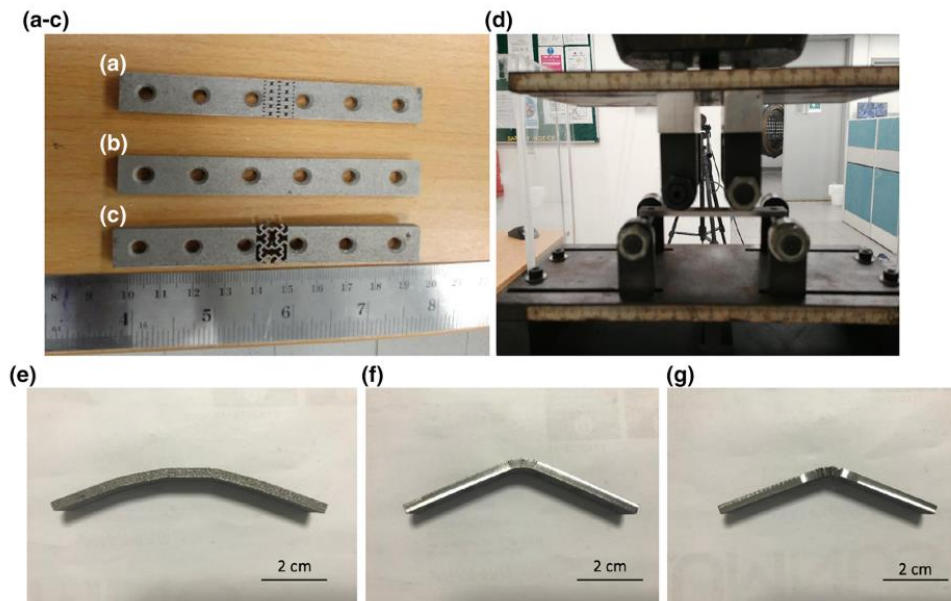
*Figure 2-34: Plate with section utilising auxetic geometry. Image from [90]. "3D-printed bone plates **a** with re-entrant honeycomb auxetic structure at the center, **b** control (without any auxetic structure), **c** with missing rib auxetic structure at the center, **d** 4 point bending test setup used for testing of bone plates, bending contour of **e** control (without any auxetic structure), **f** bone plate with re-entrant honeycomb aux- etic structure at the center, and **g** bone plate with missing rib auxetic structure at the center." [90].*

2.12 Summary

The review of the literature regarding the modeling of tissue regeneration scaffolds concluded that there are many articles focusing on any one of the length scales relating to tissue regeneration, or to any one of the physic fields; but very few explore the inclusion of multiple length scales and multiple physic fields. Multiple length scales are important because an understanding of macro-scale properties, such as effective scaffold stiffness, is just as important as an understanding of micro-scale properties such as local cell growth.

The review of literature relating to the effect of geometry on tissue regeneration yielded key findings for the work done in this thesis. It was found that through in-vitro experiments, a theory to relate micro-scale cell and tissue growth to the curvature of a scaffold has been developed. Research on the effect of geometry on tissue growth at the nano-scale showed how a single cell is stretched when subjected to different types of geometry. An investigation of the intrinsic and extrinsic effects on cell behavior explains the mechanisms through which cell differentiation is affected by intrinsic and extrinsic parameters. Regarding the models that have so far related geometry to tissue growth, it was found that although there are studies where the relationship of cell growth to scaffold curvature has been exploited, no studies were found which use such a model and combine it with macro-scale

stiffness models to propose a scaffold optimisation strategy which could easily be adopted by medical designers. An analysis of the literature about TPMS scaffolds leads to an explanation of how there are no studies proposing a method to select an optimal TPMS unit cell for tissue growth scaffolds.

The review of literature regarding conventional and AM showed that there is a clear advantage to be exploited in the AM of tissue regeneration scaffolds. AM provides a design freedom that no other manufacturing technique can match, moreover, it offers the possibility to control the parameters of promising lattice geometries with a high degree of accuracy. Stereolithography is limited by the relatively large layer height but the invention of projection micro-stereolithography now allows for polymer scaffolds to be manufactured with a layer height of 5 μm while at the same time making it possible for these scaffolds to be of an appropriate size to fill a fracture gap.

From the review of papers concerned with modeling the performance of fracture fixation plates several things can be concluded. Firstly, it is clear that finite element modeling is recognized as a powerful tool to predict the performance of fracture fixation. The high accuracy of validation found by most studies further demonstrates this. It was also evident that most studies do not focus on optimisation of designs but rather on comparisons between different designs. This is relevant for this thesis as it highlights the need for an intuitive optimisation methodology that researchers designing implants would find easy and practical to use as an additional design tool. Several of the modeling decisions discussed here have been used to ensure FE models were built in a suitable manner. The von mises stress for instance was used in this thesis as a measure of risk of failure of the fracture fixation parts, as was most done in the articles reviewed.

The two articles found in the literature that investigated the use of a fracture fixation plate and a scaffold simultaneously, provided interesting insights used in this thesis. The first of these presented results of the IFM for different conditions, which were useful for comparison to the results presented here. Moreover, the plate design parameters of this study were inspired partly by their work. The second article verified their results using in-vivo experiments with sheep, therefore, most of the modeling parameters of this study are based on this article. Furthermore, their work set out a clear range of Inter-fragmentary strain values that would result in appropriate healing, which was a key constraint during the analysis carried out here.

Stiffness grading has been proven to provide beneficial healing conditions for fracture fixation constructs, both via the use of thickness grading as well as material grading. Multi-material printing as a means to achieve such stiffness grading does not appear to work well at the moment. Auxetic fracture fixation plates have recently been proposed and offer much promise to reduce stress shielding due to their negative Poisson's ratio. Via the use of AM, this thesis combines stiffness grading and auxetic geometry to propose a novel fracture fixation plate together with an optimisation routine to optimise the design.

Chapter 3: Design selection framework of bone growth scaffolds

3.1 Introduction

Various studies have examined the effect of TPMS type on scaffold properties such as porosity, pore size, stiffness and curvature [[6], [44]] but structure-property relationships relating to cell growth in TPMS scaffolds have not been developed to date. This chapter provides such structure-property relationships for several of these scaffolds as well as a new optimisation method for bone scaffold design. TPMS scaffolds have been used here especially because the geometry can be easily tuned with two design parameters, and also because they offer a high surface area-to-volume ratio as explained in section 2.4.5.

The in-vitro study of Rumpler et al. [23] yielded two important results concerning the growth of pre-osteoblast cells on the surface of scaffolds: a) the rates of bone tissue and cell growth increased with increasing concave curvature, and b) very little bone tissue and cell growth was observed on planar and convex surfaces, until the local environment became concave due to cell growth from other areas. Bidan et al. [27] presented a model in which the dependence of cell and tissue growth on geometrical features was due to mechanical forces at the surface of the scaffold. This same model was used by Gamsjäger et al. [108] and they say that pre-osteoblast cells grow faster on concave surfaces because of, "the presence of contractile tensile stresses produced by cells near the tissue surface" [24]. The predictions from the model by Bidan et al. [27] agreed well with results from 2D scaffolds, including those of Rumpler et al. [[23], [24]].

In the model presented by Guyot et al. [37] the relationship between surface curvature and the rate of pre-osteoblast growth (derived for tissue growth in 2D scaffolds [8]) was combined with the level set method to accurately predict cell growth in 3D porous scaffolds [37]. Guyot et al. [37] tested for pre-osteoblast cells in their study, and thus, since the work here is based partly on their model, this thesis refers only to cell growth rather than tissue growth throughout this chapter.

The requirements for a bone regeneration scaffold can be divided into osteoconductive, osteo-inductive and osteogenic [12]. As explained in section 2.2, osteoconductive here refers to the migration and proliferation of pre-osteoblast cells on the scaffold, osteo-inductive to the potential for these cells to differentiate into bone forming cells and osteogenic refers to the potential for new bone formation. Importantly, these properties include the ability to recruit necessary signalling molecules, without which this process could lead to scar tissue formation rather than bone. For more details of these topics please see sections 2.2 and 4.1. In the work presented here the focus was solely on cell proliferation and it was assumed that there is no cell migration. Therefore, the term 'cell growth' refers only to cell proliferation, which is modelled as a volume of cells growing on the scaffold. It is assumed that at the start there is a homogeneous layer of cells throughout the entire surface of the scaffold, which proliferate to form subsequent layers of cells in the way described in section 3.2.5. Cell growth is important because for bone tissue to populate the fracture, it must first be populated by cells that undergo maturation and mineralisation. The necessary conditions for cells to survive and proliferate away from the scaffold surface, such as the formation of a suitable extracellular matrix, are assumed to take place. Vascularisation is considered here in the determination of an appropriate pore size which ensures that cells have access to oxygen and nutrients by being close enough to capillaries, as explained in section 3.2.3.

In this chapter the level set model introduced by Guyot et al [37] was used in combination with mechanical performance and pore size analysis to predict and optimise the performance of TPMS bone scaffolds for femoral fractures. The process consisted of a volume fraction optimisation where the property to be maximised was the average growth rate of pre-osteoblast cells. The optimisation

constraints were based on the axial stiffness and the pore size of the scaffolds (which must be sufficient to allow oxygen and nutrient delivery via capillaries). The aim of the study was to develop a methodology to select the optimal lattice type and volume fraction for a bone scaffold. Such a method is needed to ensure a chosen scaffold design will provide the fastest cell growth rate. The proposed design method provides a distinct advantage over previous methods in that it allows for a very clear graphical representation of the constrained solution space. The motivation stems from the big gap between biomedical engineering research and the actual implementation of that work for practical applications, which often comes from researchers not taking into consideration the adoption of the technology by biologists designing implants or medical designers [9]. Moreover, the proposed stiffness and pore size models have not been used for this purpose before, so this work represents an advancement in the use of computational design and analysis methods for biomedical implants.

The chapter begins with the results of the pore size and stiffness analysis of the scaffolds introduced in section 3.2.3, which serves as an initial filtering process to discard unsuitable scaffold geometries. Next follows a section with the results of the cell growth model showing both the cell growth as a function of time as well as the average cell growth rate as a function of the volume fraction and scaffold lattice type. Lastly there is a summary of the chapter.

3.2 Materials and Methods

3.2.1 Scaffold design selection framework

General optimisation problems are defined by an objective function, design variables and constraints, and are usually solved with iterative algorithms subject to some convergence criterion. The geometry of a TPMS scaffold of fixed size is determined by two design variables (assuming that the two triply periodic minimal surfaces used to define the volume are both at the same distance from the level-set = 0); the TPMS type and the volume fraction, and in this case the interest is in maximising a single objective function, the pre-osteoblast cell growth rate. The objective function to be maximised was the pre-osteoblast cell growth rate, subject to pore size and stiffness constraints. The optimisation method therefore benefits from ease of graphical representation, which is a strong motivator for its use, as it allows for the clear correlation between lattice design variables and performance (i.e., stiffness and cell growth). This is crucial if the optimisation method is to be translated into implementable design rules for designers of bone growth scaffolds, where the ability to 'tune' the performance of a scaffold, for example, its stiffness, allows for the creation of patient- and fracture-specific designs to provide minimal stress-shielding. The optimisation method is illustrated in Figure 3-1. The method is denoted as 'multi-scale' because the cell growth is computed for a single pore (the pore scale or micro-scale), while the axial stiffness is computed for the entire scaffold (the scaffold scale or macro-scale). "Optimisation" is used here in some places because the method effectively ensures that optimal design parameters are found within a defined solution space, satisfying specified constraints and minimising an objective function. However, it should be noted that following the conventional use of the term, an optimisation is not actually carried out in this work because there is no iterative algorithm. A more accurate term is "design selection framework".

First, an arbitrary scaffold unit cell size of 1 mm was selected. The unit cell size could have been a third variable to be optimised, but it was fixed here to develop an easily implementable optimisation method for TPMS type and volume fraction. These have been shown, unlike scaffold size, to have a significant effect on both scaffold stiffness and cell growth rate [[109][110]]. This allowed for the selection of suitable volume fraction limits. After this, the TPMS scaffold geometry was generated using the method of Maskery et al. [111], as described in section 3.2.2. This was followed by applying

pore size and stiffness constraints as described in sections 3.2.3 and 3.2.4, respectively. Applying these constraints provides the viable volume fraction 'window' for each TPMS scaffold type. The final step was simply to find which volume fraction corresponds to the maximum pre-osteoblast cell growth rate for each scaffold type. This was carried out using the level set cell growth model described in section 3.2.5.
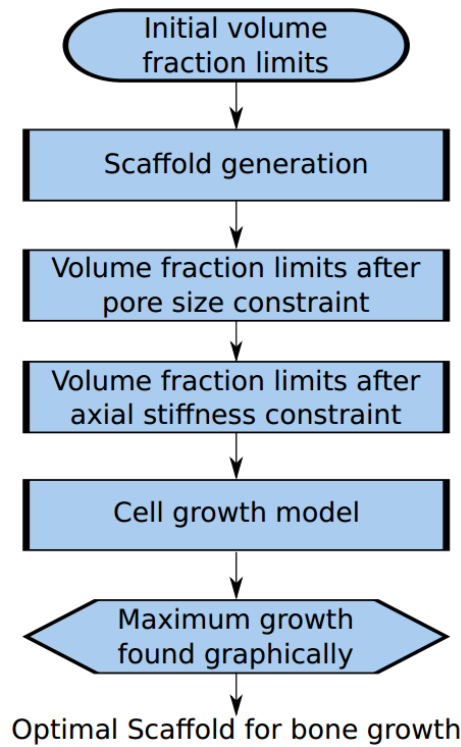
Figure 3-1: Schematic of the graphical multi-scale design selection strategy.

3.2.2   Scaffold generation

The scaffold types used for this study are based on triply periodic minimal surfaces (TPMS). Six available TPMS scaffold types were examined: Primitive, Gyroid, Split P, Diamond, Lidinoid and Neovius. The Gyroid, Diamond, Primitive and Neovius are among the most commonly studied TPMS types [110], while the other types were chosen due to their large surface area-to-volume ratios and high mean gaussian curvature [44], both of which promote rapid cell growth [110]. The surface equations used to generate these scaffold types share the terms presented in equations 3.1a and 3.1b [111]. k_i are the TPMS periodicities;

$$k_i = 2\pi n_i, \tag{3.1a}$$

where i = x, y, z and n_i are the numbers of cell repetitions in each direction in the resulting scaffolds. The next common terms are shorthand notations for sine and cosine expressions:

$$S_i = \sin\left(k_i \frac{i}{L_i}\right), \tag{3.1b}$$

$$S_{2i} = \sin\left(2k_i \frac{i}{L_i}\right), \tag{3.1c}$$

$$C_i = \cos\left(k_i \frac{i}{L_i}\right), \tag{3.1d}$$

$$C_{2i} = \cos\left(2k_i \frac{i}{L_i}\right), \tag{3.1e}$$

where L_i are the absolute sizes of the scaffold in the three orthogonal directions. The axes of the scaffold are aligned to X,Y and Z in the global reference system. The U=0 isosurface is then found from:

$$U_{primitive} = \left(C_x + C_y + C_z\right)^2 - t^2, \tag{3.2a}$$

$$U_{gyroid} = \left(S_x C_y + S_y C_z + S_z C_x\right)^2 - t^2, \tag{3.2b}$$

$$U_{split\,P} = \Big(1.1\left(S_{2x}C_y S_z + S_{2y}C_z S_x + S_{2z}C_x S_y\right) - \tag{3.2c}$$

$$0.2\left(C_{2x}C_{2y} + C_{2y}C_{2z} + C_{2z}C_{2x}\right) -$$

$$0.4\left(C_{2x} + C_{2y} + C_{2z}\right)\Big)^2 - t^2,$$

$$U_{diamond} = \left(C_x C_y C_z + S_x S_y C_z + S_x C_y S_z + C_x S_y S_z\right)^2 - t^2, \tag{3.2d}$$

$$U_{lidinoid} = \Big(\left(S_{2x}C_y S_z + S2_y C_z S_x + S_{2z}C_x S_y\right) - \left(C_{2x}C_{2y} + \right.$$

$$\left. C_{2y}C_{2z} + C_{2z}C_{2x}\right)\Big)^2 - t^2, \tag{3.2e}$$

$$U_{neovius} = \left(3\left(C_x + C_y + C_z\right) + 4C_x C_y C_z\right)^2 - t^2, \tag{3.2h}$$

where t is a parameter used to control the volume fraction of the resulting scaffold [111]. The U=0 isosurface is then treated as a boundary between solid and void domains of the scaffold. This was followed by a voxelisation of the solid region to apply the cell growth model. These voxels were later translated into hexahedral elements for Finite Element assessment of the modulus of the scaffold under compressive loading. The modulus prediction is necessary because as described in more detail in section 3.2.4, the healing outcome is significantly affected by the effective scaffold modulus. Figure 3-2 shows the eight TPMS lattice types used. For a thorough understanding of the scaffold generation process see the work of Maskery et al. [19,20].
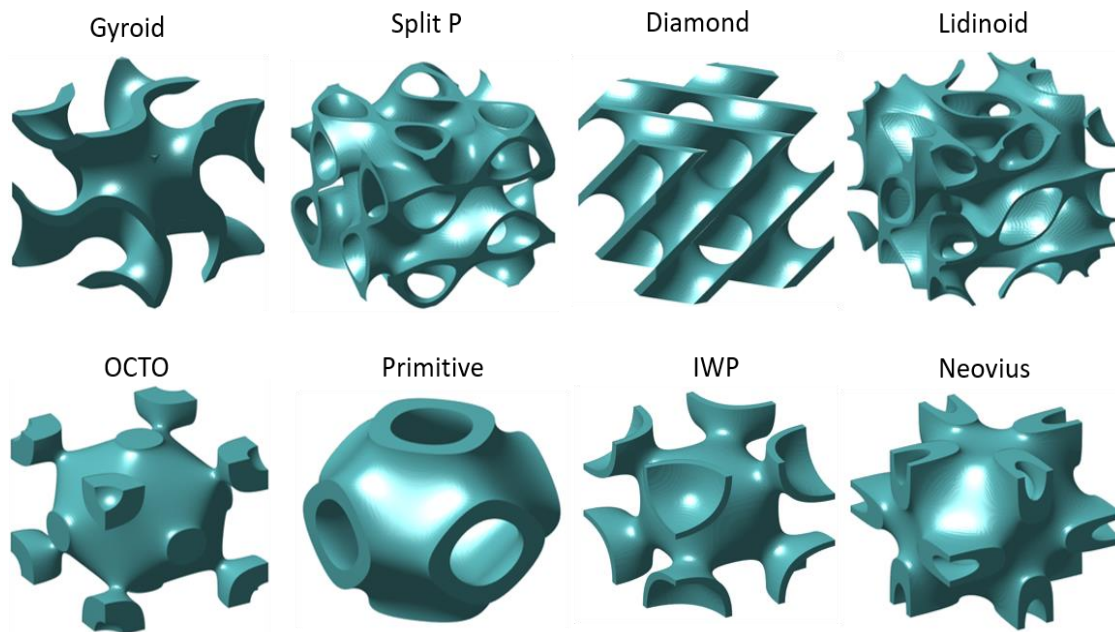
Figure 3-2: The eight triply periodic minimal surface (TPMS) geometries used in this study. All at 0.2 volume fraction and 100 voxels in every dimension.

3.2.3   Pore size constraint

It was previously found that 100 μm is the minimum pore size diameter that allows for capillary infiltration into the scaffold in vivo [21,22]. This is due to the diameter of capillaries that must populate the scaffold to provide oxygen and nutrients for cell survival [115]. Additionally, several studies have shown that the diffusion limit of oxygen and nutrients is 200 μm [116], so it follows that cell growth on scaffold surfaces may be inhibited if they are separated by 200 μm from a pore. Therefore, scaffold pores should not have a diameter larger than 400 μm so that the scaffold may become fully populated with cells. Thus, the maximum and minimum allowed pore diameters were defined to be 400 μm and 100 μm, respectively. It should be noted that these pore size limits are different for scaffolds where the cells are encapsulated within solid scaffold walls, as opposed to residing at the surface [117].

The minimum and maximum pore sizes of TPMS scaffolds were found by first determining the medial axis skeleton of the void domain with a method adapted from that of Kerscnitzki et al. [118] to measure the position of minerals within a porous network [118]. For each scaffold type this was done using a voxel representation of a 3×3×3 unit cell scaffold, which is sufficient to ensure that the largest and smallest void volumes are included in the analysis. An illustration of the medial axis skeleton is shown in Figure 3-3(a). A distance function [119] was then computed for every part of the medial skeleton and every voxel in the solid scaffold domain, giving the minimum and maximum sizes of virtual spheres that could sit inside the scaffold's empty space (see the examples in Figure 3-3(b)). The diameters of these spheres were taken to represent the minimum and maximum pore size for each scaffold.
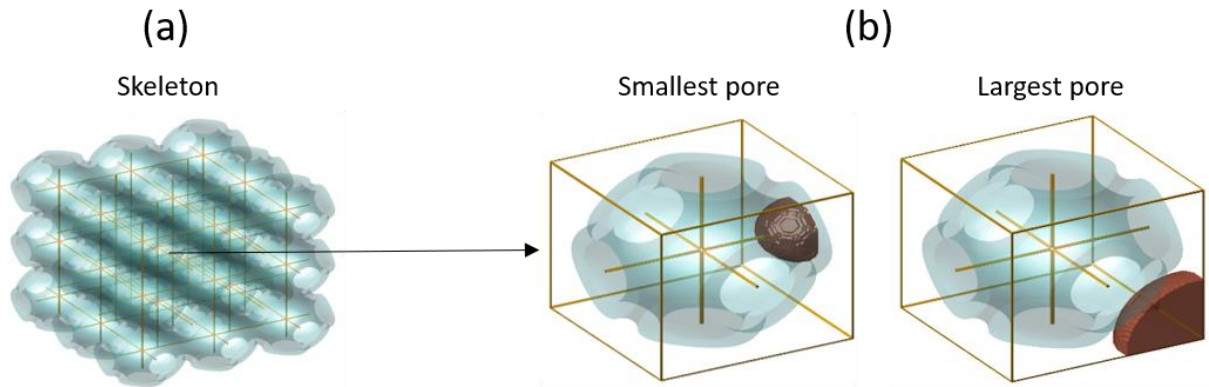
Figure 3-3: Computation of smallest and largest pores in the scaffolds. (a) The medial skeleton is computed using a 3×3×3 cell TPMS scaffold. (b) The minimum and maximum pores are calculated using a distance function.

3.2.4 Axial stiffness constraints

An optimal bone scaffold should possess sufficient stiffness to avoid refracture under loading. For the femur, the critical loading is axial along the length of the bone [120]. The fracture fixation plate (shown in Figure 3-4) may be designed to provide sufficient stiffness, but stiff plates lead to bone resorption under the plate through stress shielding [69]. However, the scaffold cannot be too stiff either because the bone interfragmentary movement (IFM) [69], which refers to the movement between the fractured bone fragments in the axial direction, must be above a minimum value. This is necessary for the bone cells to experience sufficient strain for bone formation. It follows that there is a minimum allowable scaffold stiffness as well as a maximum. A suitable range of axial stiffness for a bone fracture of 30 mm was defined by Steiner et al. to be between 1000 and 2700 N/mm [72].
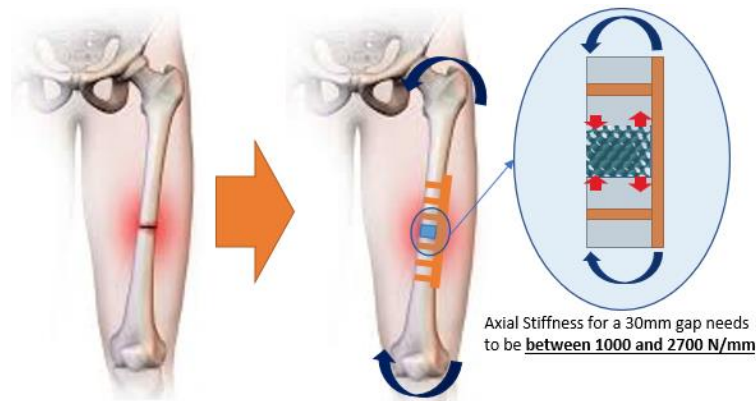
Figure 3-4: On the right is a fractured femur implanted with both a fixation plate (orange) and scaffold (light blue). Moments and loads are shown by arrows. Axial stiffness for a 30 mm gap needs to be between 1000 and 2700 N/mm [72]. The image on the left shows the original artwork from [121].

For a cylindrical scaffold of diameter D and height L, the axial stiffness k_{scaff}, can be expressed as

$$k_{\text{scaff}} = E^* E \frac{\pi D^2}{4L},$$
(3.3)

where E* is a dimensionless factor known as the relative modulus and E is the elastic modulus of the scaffold material. The material was assigned the modulus of additively manufactured Nylon, 1.8 Gpa. Nylon was selected as a model material because it has similar mechanical properties to trabecular bone [122] which has been shown to be beneficial as it allows the scaffold to act as a woven-bone surrogate for lamellar bone [123]. Nylon has been previously used to create additively manufactured non-degradable scaffolds for bone regeneration and showed higher bone ingrowth compared with the standard material, titanium, in a sheep femur bone defect [123].

General scaling laws relating E^* to the scaffold volume fraction, ρ^*, were obtained using the same finite element (FE) approach as Maskery et al. [111]. Compressive loading was applied to the top surfaces of FE scaffold models, and the reaction force and displacement were used to calculate the modulus. This was done for each scaffold type in this study (i.e., those originating from equation 3.4) and for a range of volume fractions from 0.2 to 0.9. The resulting moduli were fit with laws of the same form as those in the work of Maskery et al. [111]:

$$E^*(\rho^*) = C_1 \rho^{*n} + E_0^* \quad , \tag{3.4}$$

where the parameters C_1, n and E_0 differ for each scaffold type. The determined parameters for several scaffold types are given in Table 1. These were selected from the full range of scaffold types due to their particular relevance to the scaffold optimisation method in section 3.2.1. The parameters in Table 1, along with values for D and L, were used to predict k_{scaff} for each scaffold type. *D* was given the value 30 mm, the diameter of the femur, and *L* was 30 mm, the length of the critical bone fracture.

Table 1: Gibson-Ashby scaling parameters

Cell type	C_1	n	E_0^*
Split P	1.33	2.04	-0.078
Gyroid	1.33	2.68	-0.002
Diamond	1.26	2.74	0.039
Lidinoid	1.38	2.59	-0.050

3.2.5 Cell growth model

A computational model for pre-osteoblast cell proliferation was developed based on the work of Guyot et al. [37]. Cell proliferation is represented here as an advancing surface which grows from the original solid scaffold into the void domain. Guyot et al's [37] work included validation of the cell growth model with experimental observation [37] and was found to be representative of cell growth in a cell-seeded bone regeneration scaffold. The model implemented here is particularly convenient because, by using the level set method, it can be applied to any 3D geometry, not just TPMS scaffolds. In this study, a central difference method was used, while Guyot et al. [37] used a finite element method, hence a validation study is presented in the results showing that the two implementations yield similar results. The same time step as in the study by Guyot et al. [37], 10^{-4}, was used.

For each scaffold, a 3D distance function, φ, is calculated through a defined series of time steps, t. The $\varphi = 0$ isosurface describes an interface which advances from the original solid scaffold into the available empty space (the pores), as given in the following equation:

$$\frac{\partial \varphi}{\partial t} + \boldsymbol{u} \cdot \nabla \varphi = 0 \tag{3.5}$$

The rate of advance of the $\varphi = 0$ interface is the advection velocity, $\boldsymbol{u}$;

$$\boldsymbol{u} = \begin{cases} -k\boldsymbol{n} & if\ k > 0 \\ 0 & if\ k \le 0 \end{cases} \tag{3.6}$$

which is proportional to the local curvature, k;

$$k = \nabla \cdot \boldsymbol{n} \tag{3.7}$$

In turn, k is calculated at each time step and is proportional to the normal of the interface denoted by n;

$$\boldsymbol{n} = \frac{\nabla \varphi}{|\nabla \varphi|} \tag{3.8}$$

The cumulative cell growth at any time is given by the difference in volume between the $\varphi = 0$ interface at that time, and the original scaffold. An illustration of this model applied in a simple 2D case is shown in Figure 3-5; the local curvature due to the corner of the original scaffold drives rapid cell growth.
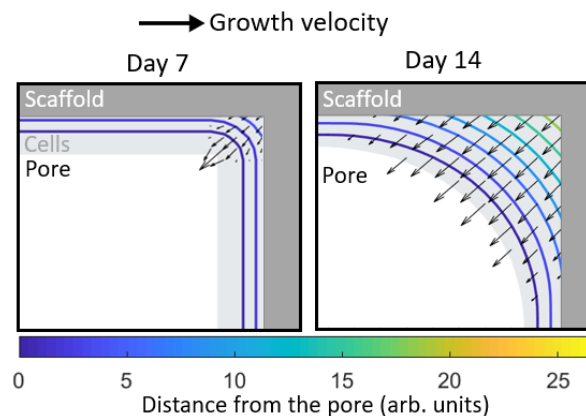
Figure 3-5: The principle of the cell growth model. On the left (day 7) is a thin layer of cells (grey) attached to the scaffold with contours showing the distance from the pore. Arrows show the growth velocity with both magnitude (length of arrow) and direction. On the right (day 14) the cells have proliferated to form a roughly circular pore.

A convergence analysis was performed to determine the number of elements required for accurate cell growth modelling. The cell growth rate was calculated for scaffolds discretised into increasing numbers of voxels, from 125,000 up to 15.625 million. As shown in Figure 3-6, the total number of elements was deemed appropriate when the absolute change in cell growth rate between successive discretisation values was lower than 1%. The 1% cut-off point was at half a million elements per unit cell as shown in Figure 3-6. Scaffolds with one million elements satisfied this criterion and were therefore used for cell growth modelling throughout this study.
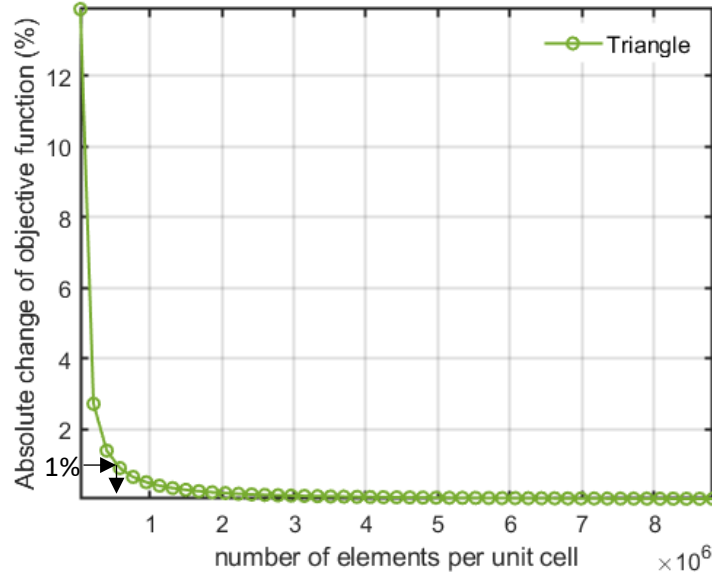
Figure 3-6: Mesh convergence for the triangular geometry. The objective function was the average growth rate and the y-axis on the plot represents the absolute change of this objective function in percentage. The x-axis shows the number of elements per scaffold unit cell. At half a million elements per unit cell the threshold was reached.

3.3   Pore diameter and stiffness constraints results

As discussed in section 3.2.3, an optimal bone scaffold must satisfy pore size constraints determined by the delivery of oxygen and nutrients to the growing cells. Figure 3-7 (a) shows that while the Lidinoid, Split P, Diamond and Gyroid scaffold types have a maximum pore size below the limit of 400 µm for some of the volume fraction range, the Primitive and Neovius scaffold types do not satisfy this constraint and were therefore discarded from the study. The smallest pore size constraint in Figure 3-7 (b), which ensures that scaffold pores are large enough to allow arteries to fit through them, eliminates some of the volume fraction range for the Gyroid, Split P, Diamond and Lidinoid types.
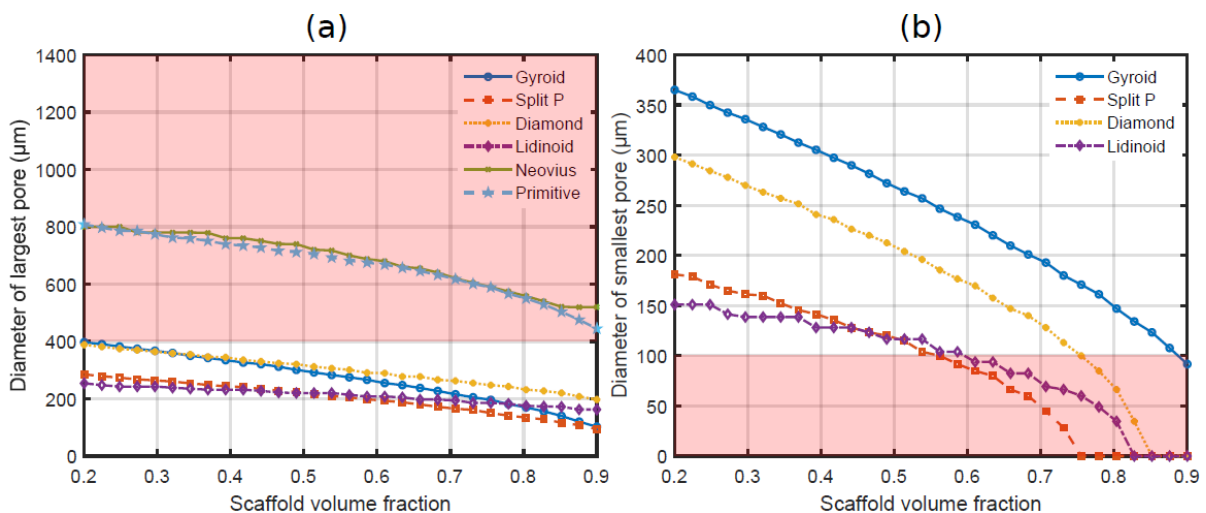
Figure 3-7: (a) the diameter of the largest pore for all scaffold types. (b) the diameter of the smallest pore of the five scaffold types that satisfied the maximum pore size constraint. The red shaded areas represent the constrained space. All scaffolds have only one unit cell and dimensions of 1 × 1 × 1 mm.

Based on the pore size analysis, the volume fraction limits for remaining scaffold types were updated and Figure 3-8 illustrates the application of these limits to the stiffness data from Finite Element models. For a description of how this was implemented please see section 3.2.4.
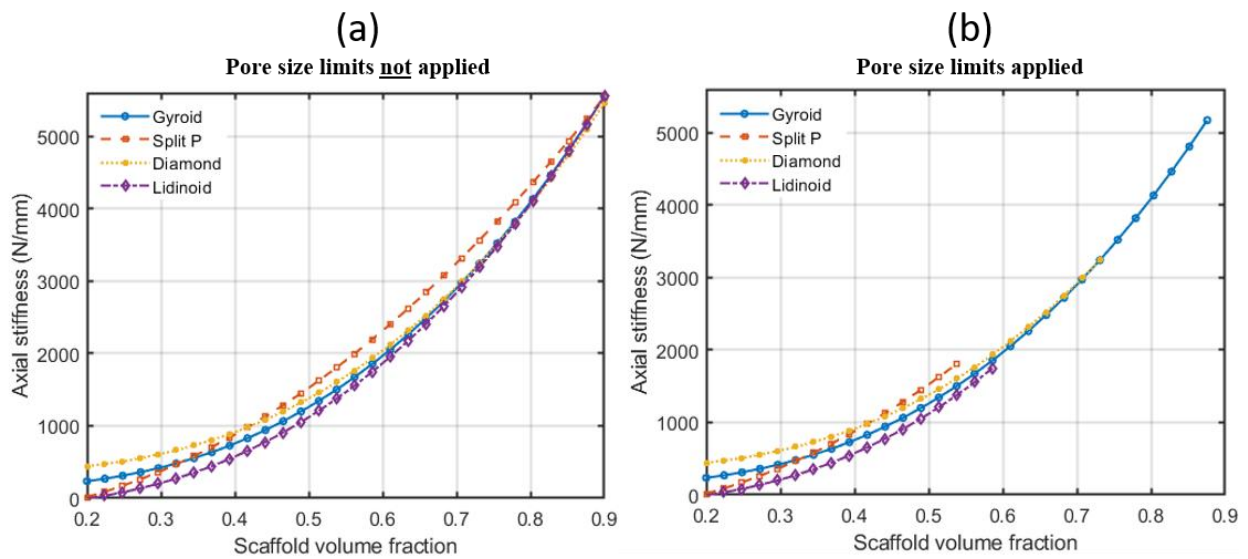
Figure 3-8: Applying pore limits to stiffness data.

In the next optimisation step, any scaffold design that did not provide an axial stiffness between 1000 and 2700 N/mm was discarded. As described in the methodology, these constraints ensure appropriate healing, as they will lead to suitable mechano-sensing conditions for bone healing [72]. Figure 3-9 shows the process of applying the stiffness constraints while Table 2 provides the final minimum and maximum limits for the allowed volume fraction taking both allowable cell pore size and stiffness ranges into account.

Table 2: Final volume fraction limits after applying axial stiffness constraints.

	Minimum volume fraction	Maximum volume fraction
Gyroid	0.47	0.66
Split P	0.44	0.54
Diamond	0.44	0.66
Lidinoid	0.49	0.59
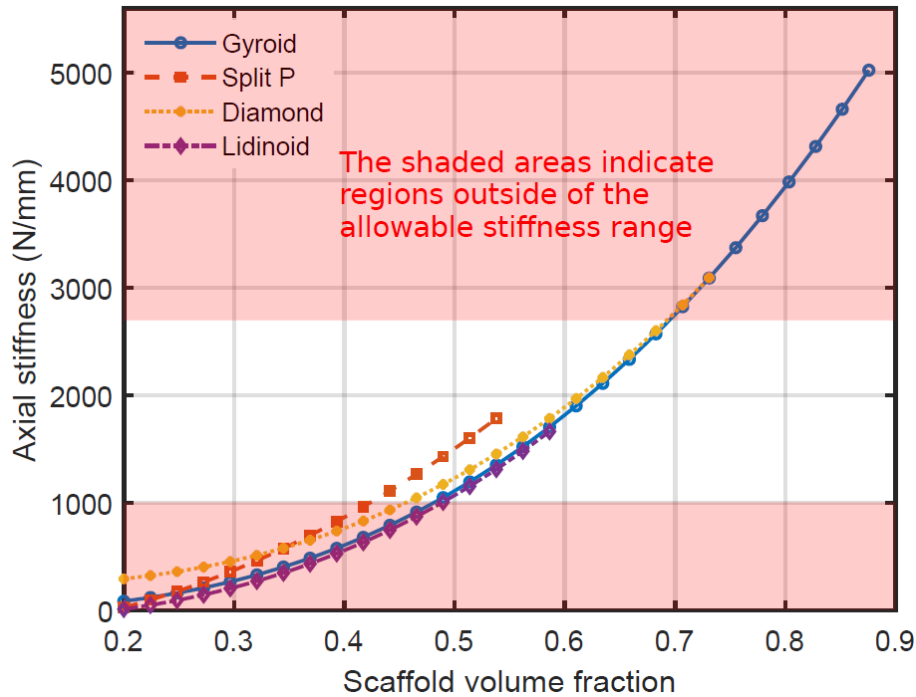
Figure 3-9: Axial stiffness with constrained space shown with red shading.

3.4   Cell growth

Figure 3-10a, b, c show the cell growth predicted by the level set model detailed in section 3.2.5 over a period of 21 days. The level set model was implemented by defining a distance function with the $\varphi = 0$ isosurface at the interface between the growing volume of cells and the available empty space. This distance function grows into the pores simulating the growth of cells, in accordance with the curvature dependent laws detailed in section 3.2.5. Just three plots, for volume fractions of 0.2, 0.9 and 0.49, are shown here, but cell growth was calculated for the full range of volume fractions from 0.2 to 0.9.

The Lidinoid type yields the highest cell growth for the entire volume fraction range, but the Split P type yielded a very similar growth curve at a volume fraction of 0.49 and 0.9. The average growth rate for each scaffold was calculated by dividing the volume of cells by the time taken for the cells to entirely fill the space of the scaffold which was initially empty; i.e. the time at which the curves in Figure 3-10a, b, c plateaued. A visualization of the cell growth throughout the surface of the scaffold is presented in Figure 3-11.
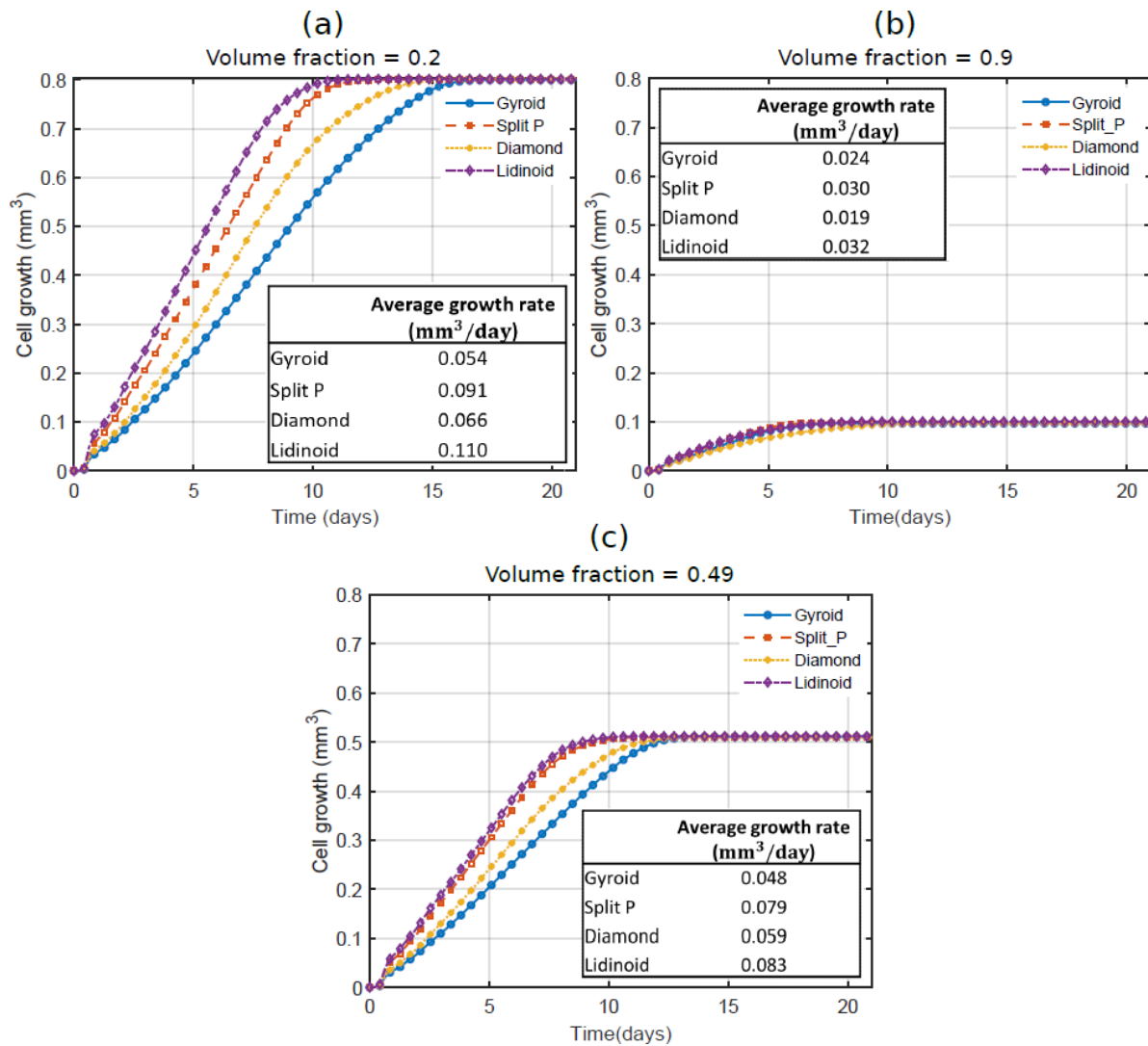
Figure 3-10: Cell growth after 21 days for scaffold volume fractions of 0.2, in (a), and 0.7, in (b).
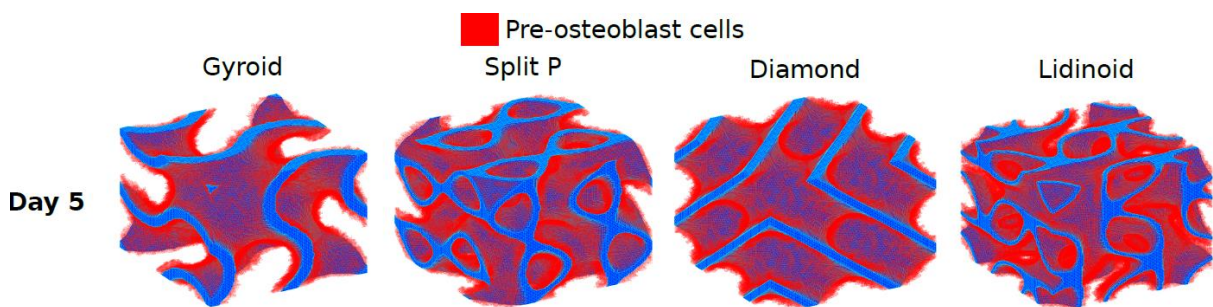
Figure 3-11: Pre-osteoblast cells growth after 5 days on scaffold types, all at 0.2 volume fraction.

For each volume fraction, the average growth rate was determined to compute the curves shown in Figure 3-12. At all volume fractions the Lidinoid scaffold type provides the greatest average growth rate. In Figure 3-12 it can be observed that after removing the volume fractions that did not satisfy the stiffness and pore size constraints, the maximum average cell growth rate of both the Split P and Lidnoid scaffold types is very similar. Table 3 shows that the highest cell growth rate is predicted to be

0.0872 mm^3/day for the Lidinoid type. That was achieved with an optimal volume fraction of 0.49. However, the maximum growth rate for the Split P type was only 6% lower.
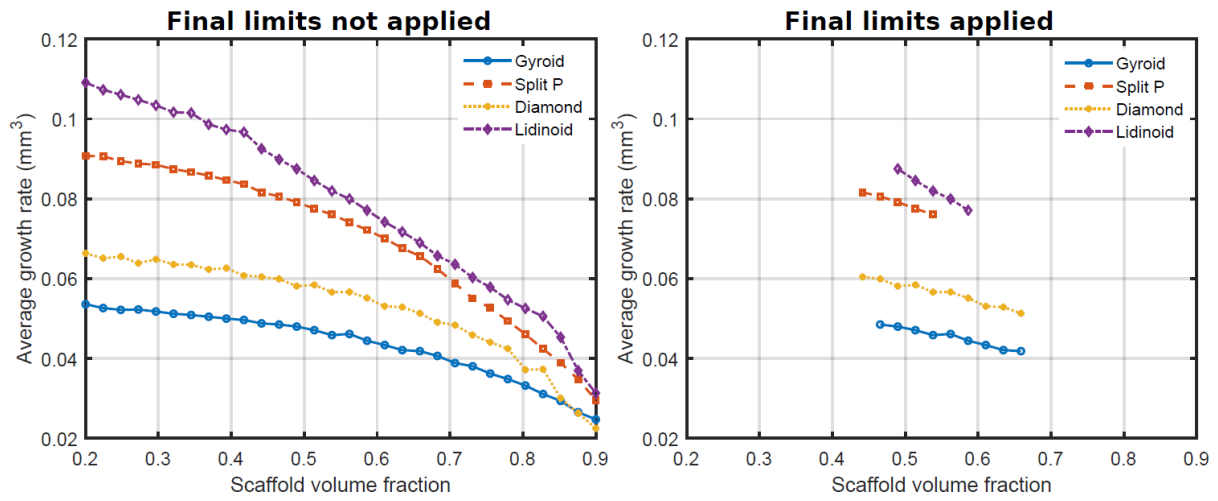
Figure 3-12: Average pre-osteoblast cell growth of each of the TPMS scaffold types after 21 culture days.

Table 3: Final volume fraction limits after applying axial stiffness constraints.

	Maximum cell growth rate (mm^3/day)	Optimal volume fraction
Gyroid	0.048	0.47
Split P	0.082	0.44
Diamond	0.060	0.44
Lidinoid	0.087	0.49
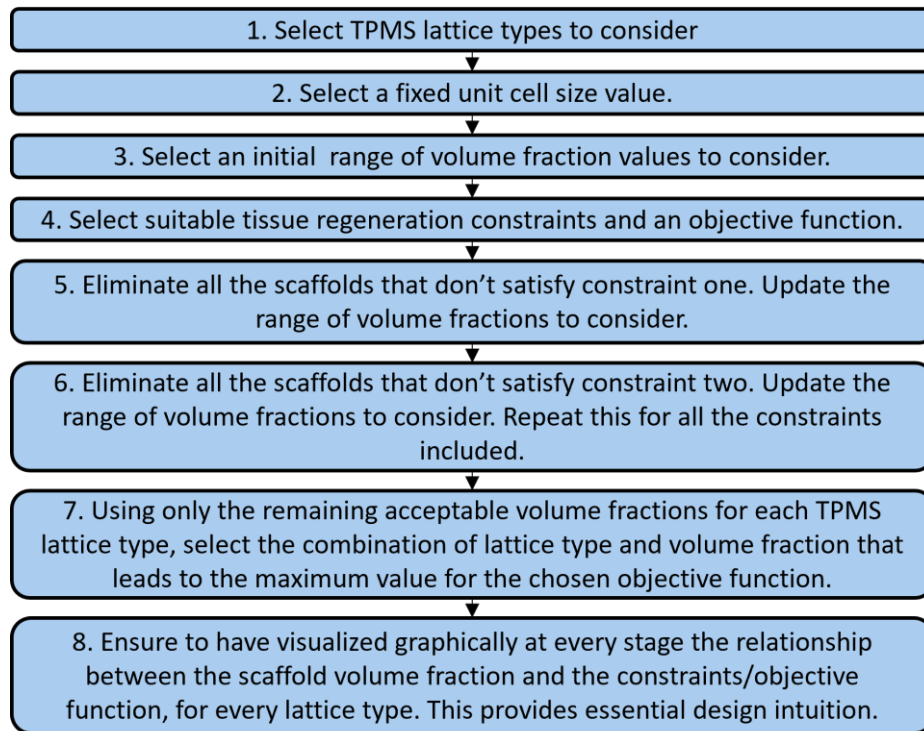
Figure 3-13: Decision making workflow showing the design inclusion/elimination steps throughout the proposed framework.

3.5   Summary

For a discussion of the results see chapter 6, the text below simply summarizes the content presented in this chapter.

The first part of this chapter introduces a method to relate the geometry of a TPMS scaffold to its cell growth performance. The latter focused on maximising the average rate at which osteoblast cells are expected to grow once attached to the scaffold. However, the stiffness and the pore size of the scaffolds were also considered by including them as constraints to be satisfied. Each of these three performance metrics required a computational model. These models were from previously published literature and then adjusted them to be applied to chosen TPMS geometries. To make it easily adopted by medical designers, only two design variables were used: the TPMS unit cell type and the volume fraction. This provides the user not only with the optimal geometry but also with a clear correlation of how the performance measures are affected by the design variables.

This chapter also included the results of the geometry optimisation of TPMS scaffolds for enhanced osteoblast cell growth. Having chosen the TPMS unit cell type and the volume fraction as the design variables to be optimised, the first step here consisted of applying the pore diameter and stiffness constraints to the solution space, thus providing a reduced set of possible solutions which satisfy the constraints. Next, the growth of cells on the scaffolds was simulated for a period of 21 days using a previously validated level-set model. A validation for the specific geometry used here by comparison to this previously published paper was also carried out. After this, the average cell growth rate was computed for every TPMS unit cell type and volume fraction under analysis, such that a correlation graph could be made showing how the average cell growth rate in a scaffold changes with the volume fraction, for different TPMS unit cell types. Lastly, the volume fraction and unit cell type yielding the maximum cell growth rate were identified. These parameters can be used to design scaffolds for AM

and the next chapter shows how this was done using stereolithography as well as projection micro-stereolithography.

The novelty of the work presented here consists of several aspects: (1) the development of a framework to enable medical practitioners and biologists designing implants to design a TPMS scaffold that satisfies desired constraints and maximises a chosen objective function. Unlike existing frameworks that also lead to an optimal design ('optimal' relative to the defined requirements and available solutions), the one presented here allows for a clear graphical visualisation of the considered solution space, helping the designer to develop essential design intuition; (2) the Finite Difference implementation of the cell growth model, (3) the graphical representation of the relationship between TPMS volume fraction and max/min pore size, and between TPMS volume fraction and average cell growth rate have been presented here for the first time and may be useful design tools on their own. (4) the method adaptation used to define the minimum and maximum pore size of a TPMS scaffold has not been presented before and may be useful for designers to quickly assess the pore size range for any given scaffold geometry.

Chapter 4: Additive Manufacturing and cell culture experiments of TPMS scaffolds for osteogenic tissue formation.

4.1 Introduction

The results from chapter 3 showed that triply periodic minimal surface (TPMS) scaffolds are expected to enhance cell growth when compared to other geometries. Moreover, it was found that the Lidinoid scaffold type yields higher cell growth rate than the other TPMS scaffold types. Although the model has already been validated against experimental results by Guyot et al[37], in this chapter the aim is to support the modelling results with experimental results specifically on TPMS scaffolds. TPMS scaffold types are promising not just due to their high surface-to-volume ratio but also due to their high total concave curvature-to volume ratio as shown in Figure 4-1. This shows that the highest amount of total concave curvature is provided by the Lidinoid scaffold type.

a)
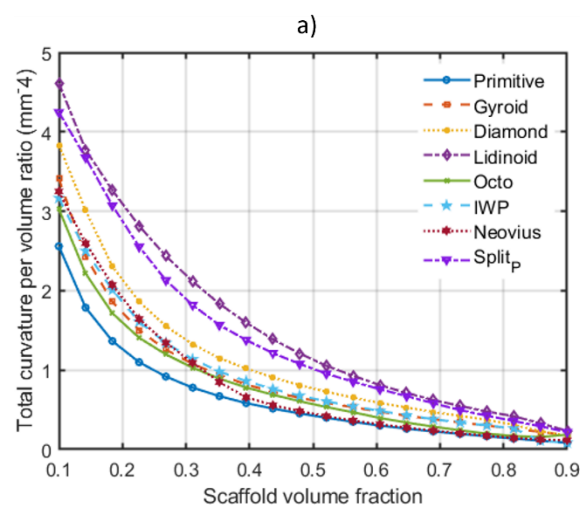
Figure 4-1: Total concave curvature of various TPMS scaffolds.

Additive Manufacturing is revolutionising the way scaffolds are fabricated, most significantly because it allows for matching specific geometry requirements, both internally and externally [124]. This design freedom is important to be able to match the specific outer geometry of patient bones [125], but perhaps more importantly it allows the creation of scaffolds with sub millimetre pore sizes, which has been shown to be critical for appropriate cell growth [115]. To print scaffolds with such small pore sizes, either Micro-stereolithography (μSLA) [61] or Two-photon polymerisation [61] must be used. Although two-photon polymerisation can achieve higher resolution than μSLA, it is currently very time consuming to manufacture large enough scaffolds with this technique.

Projection μSLA (PμSLA) consists of the photopolymerization of a resin, similar to Stereolithography (SLA) or Two-photon stereolithography, however, PμSLA can achieve higher speeds as it is triggered by area projection rather than point-light-source illumination [65]. By adjusting the magnification of the projection lens this allows PμSLA to achieve much higher resolution than SLA and much higher printing speeds than Two-photon micro-stereolithography. As shown in Figure 4-2, for this printing technique, an acrylate group, a photoinitiator and a photoabsorber are required. The photoinitiator is used as it gets excited at a certain wavelength, for the BMF this is around 405 nm, there are then two unstable electrons. The carbon-to-carbon double bond in the acrylate group (in TCDMDA) cleaves and forms a bond with the photo-initiator, causing the formation of a polymer chain. The photoabsorber blocks polymerisation around the object one is printing so that the very reactive diacrylate does not cause additional polymerisation where it is not intended. The photoabsorber is a reducing agent so it

donates a hydrogen atom to the unstable photoinitiator, killing the reaction between the diacrylate and the photoinitiator [61].
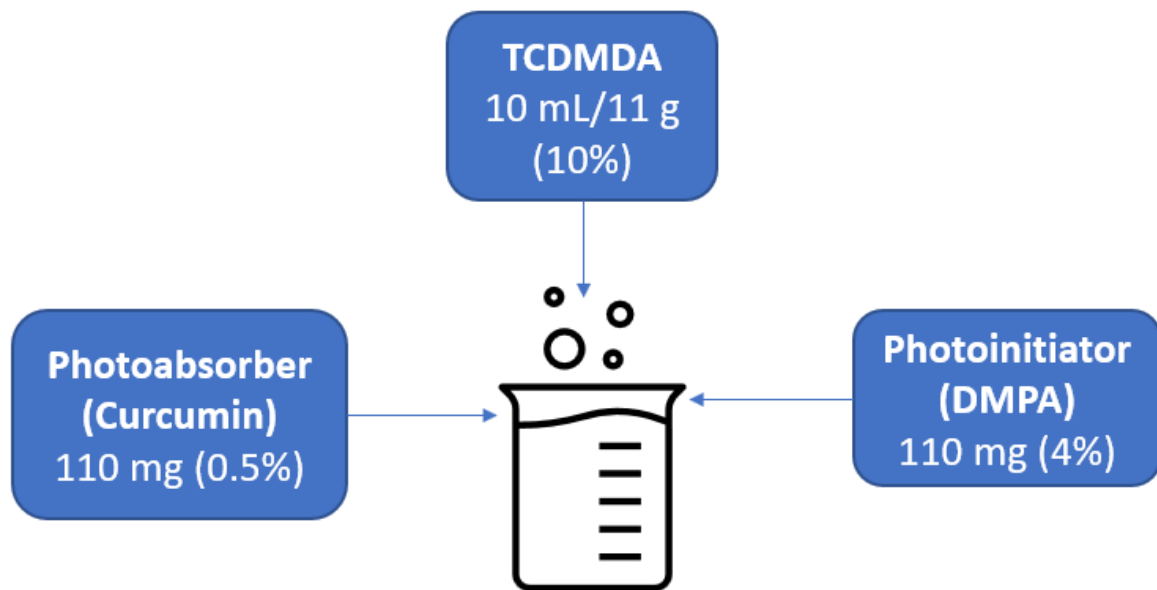
Figure 4-2: Image illustrating the components of the resin used for printing with the BMF micro-stereolithography printer.

Some of the most promising scaffold geometries for bone healing scaffolds are TPMS scaffolds [[126],[110]], which can only be realised via AM due to their complex internal geometry [127]. Some articles attempt to relate the mechanical properties of such scaffolds to their tissue regeneration capabilities [6], but very few have actually investigated their tissue regeneration capabilities directly [[128],[129]]. One of these studies investigated how human Caucasian osteosarcoma cells grow on TPMS gyroid scaffolds manufactured via SLM with 316 stainless steel [128]. They found that cells grow faster on the gyroid scaffolds with a pore size of about 1300 µm than on other gyroid scaffolds with larger pores or a blank control [128]. They did not however, compare this to other TPMS scaffold types neither did they investigate the effect on human Mesenchymal Stromal cells (hMSCs).

hMSCs are multipotent cells that can differentiate into different types of tissue, amongst them bone. This process is called osteogenic differentiation. hMSCs can be isolated from donors with relatively little need for invasive techniques since they can be found in the bone marrow [130]. The osteogenic differentiation of MSCs can be divided into four steps: (i) the commitment step produces lineage-specific progenitor cells; (ii) the proliferative phase of osteoprogenitors, in which genes associated with the cell cycle and histone signals are expressed; (iii) the phase of ECM secretion and morphological changes of immature osteoblasts; (iv) osteoid mineralization initiated by mature osteoblasts, which become terminally differentiated osteocytes [131]. It has been found that osteogenic media enhances both the proliferation and differentiation of hMSCs and pre-osteoblasts [130]. Bone morphogenetic protein-2 (BMP2) has shown very promising results in clinical trials [132], there has been some debate about whether these growth factors enhance only the differentiation or also the proliferation of hMSCs, but a recent study showed that BMP2 does in fact enhance both of these since not only did they observe high proliferation but also the gene expression of RUNX2, COLI, ALP, OC, COLI and ALP, which are associated with osteogenic differentiation [133].

It has been demonstrated that combining the benefits of geometry, substrate type, osteogenic media and BMP-2 may greatly enhance osteoprogenitor hMSCs proliferation, differentiation and mineralisation, more so than when using any one of these parameters in isolation [134]. The material

plays a key role in guiding the differentiation pathway of hMSCs [[40],[135]], but also in the amount of differentiation and proliferation that is seen [136]. Perhaps less intuitive, the geometry of the scaffolds has also been shown to play a key role in the differentiation pathway [137] as well as amount of differentiation and proliferation of hMSCs and pre-osteoblasts [[31],[23]]. Although the combination of scaffold geometry with osteogenic media and BMP-2 has been proposed to greatly enhance regeneration potential [134], this has not been addressed when using the promising geometry of TPMS scaffolds.

The objectives of this chapter were: (1) to investigate if stereolithography is a suitable technique to manufacture scaffolds with TPMS geometries with the desired design variables, and test the hypothesis that micro-stereolithography allows for printing scaffolds with the required pore size as well as being capable of producing them at relevant outer dimensions, (2) to compare the modelling results from chapter 3 with experimental work (3) to study whether combining the promising geometry of TPMS scaffolds with osteogenic media and BMP-2 would lead to even better results in terms of cell growth and differentiation than recently presented with other scaffold geometries [134].

4.2   Materials and Methods

4.2.1   AM of scaffolds

4.2.1.1   Scaffolds design

Based on the pore size constraints described in section 3.2.3, five different Triply Periodic Minimum Surface (TPMS) structures were selected for printing (Lidinoid, Diamond, Gyroid and Primitive). The Lidinoid, Diamond and Gyroid scaffold types satisfy the constraints, the Primitive type does not but was used here during the manufacturing experiments for comparison to literature. The Primitive type was also printed at smaller pore sizes (smallest pore) of 300 μm and 50 μm to assess the printing resolution capabilities of this technology.
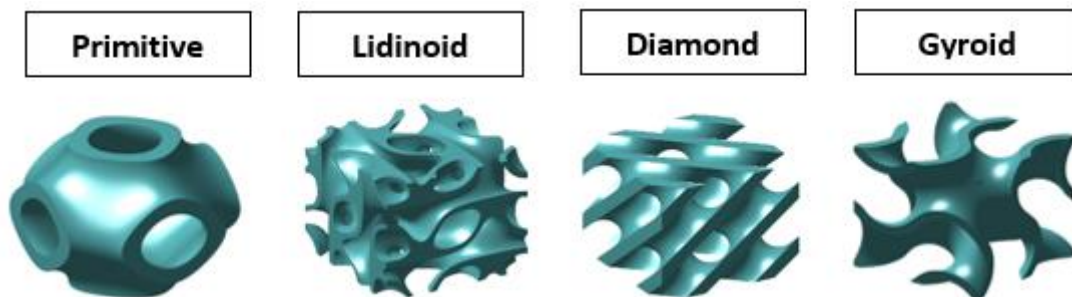
Figure 4-3: Computational designs of the initial geometries for printing. Each of these represents only one single unit cell of the lattice geometries.

4.2.1.2   Projection micro-stereolithography

Projection micro-stereolithography (PμSLA) is an AM method that uses light-induced photopolymerization of a liquid resin to create small-size 3D components by superimposition of a large number of thin polymers [61]. This printing method was selected because it can achieve a resolution as low as 2 µm. The PμSLA printer used here was that from Boston Micro Fabrication (BMF) [138]. The image below illustrates the process followed in this project for printing the scaffold with this printer. A binary file of each layer of the scaffold is first imported into the software from BMF, followed by calibration of the printer. The scaffolds are then UV cured onto a metallic substrate layer by layer and stored for post-processing.
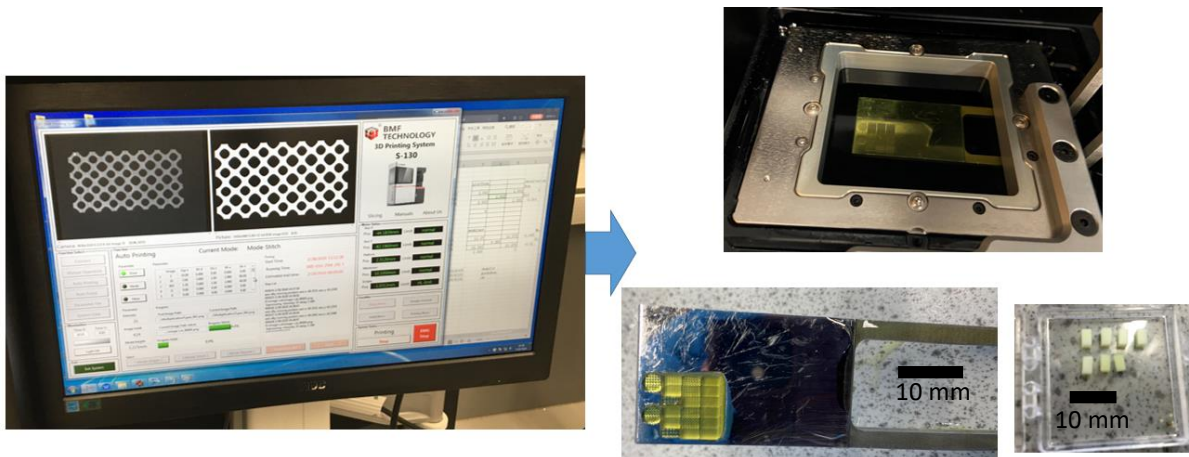
Figure 4-4: Process of printing scaffolds with the BMF μSLA printer. The left image shows the software, the top right image shows the film and on the bottom right are the printing plate showing also the scaffolds that were printed. Scale bar equals 10 mm.

A custom-made Graphical User Interface (GUI) was developed to create the printing files. This software was required because of the high-resolution files needed. Regular software to make similar printing image files would slice a 3D structure, meaning that the 3D structure must first be generated, stored and then sliced to create many high-resolution images. This requires a high amount of computational power, so instead the approach used in the software which was developed using MATLAB was to never store 3D structures of the lattices but rather generate each slice at the same time as the image for printing is being generated and then discard it from memory. The software also allows for the arrangement of various structures in the same build as shown in Figure 4-5.
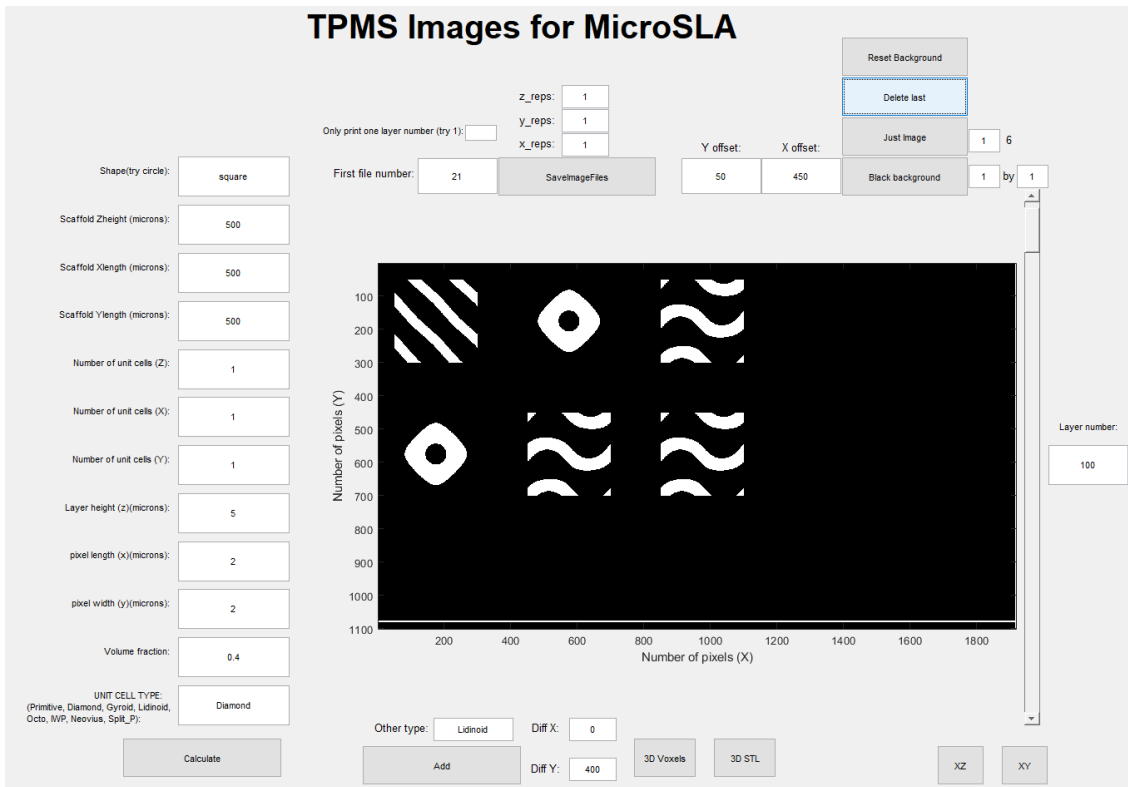
Figure 4-5: Graphical User Interface (GUI) developed to avoid the need for high computational power.

4.2.1.2.1 Photoreactive Resin material provided by BMF Nano Material Technology:

The material used was a Photoreactive Resin (Boston Micro Fabrication, USA). This material is a mixture of methacrylic and acrylic acid esters as well as a photoinitiator. For printing with this material, the minimum layer thickness achievable was used (5 µm). The x-y resolution that it can achieve is 2 μm.

4.2.1.2.2 TCDMDA material:

Tricyclo[5.2.1.02,6]decanedimethanol diacrylate (TCDMDA) has been shown to yield biocompatible scaffolds when combined with 0.5 wt % 2,2-Dimethoxy-2-phenylacetophenone (DMPA) photoinitiator, via Inkjet based 3D printing [10]. Scaffolds were therefore printed with this material to ensure biocompatibility.

The process of preparing the resin consisted of first mixing the components, then stirring them for 24 hours inside a flask covered with aluminium foil to prevent unwanted photopolymerization. The stirring was done with a magnetic stirrer at 500 rpm and 45°C. Image capturing was carried out both with an Optical Microscope and a Scanning Electron Microscope (SEM) [10]. For the SEM analysis, the parts were first coated with gold to increase conductivity.

4.2.1.2.3 Printer parameters ad-hoc optimisation:

The most important printer parameters for ensuring an appropriate layer height are the intensity and the exposure time [65]. The intensity refers to the level of UV radiation used for excitation of the resin to cause polymerisation. The structure used to optimise these parameters is shown in Figure 4-6. The 'stairs' in this structure consist of single layers printed at varying exposure time. The intent was to measure the curing depth at varying exposure time and intensity values. The parameter combinations that were tried are shown in Table 4. The curing depth was measured on the microscope image by using the digital ruler on the microscope program.

Table 4: Combinations of UV intensity and exposure time

Intensity level	Exposure time (s)
60	1
60	2
60	4
60	6
60	8
70	1
70	2
70	4
70	6
70	8
80	1
80	2
80	4
80	6
80	8
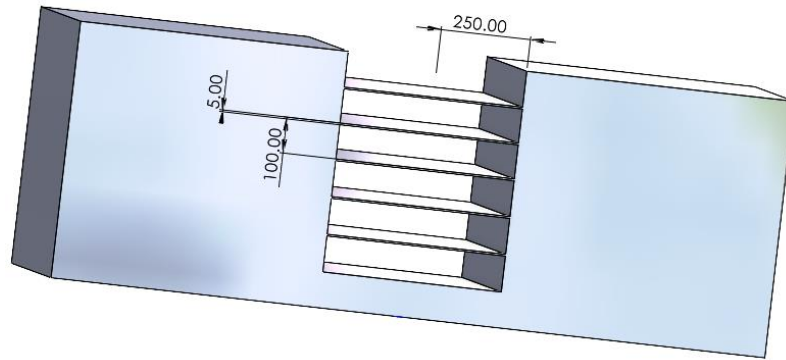
Figure 4-6: Calibration structure for ad-hoc optimisation of the intensity and exposure time. All dimensions in μm.

4.2.1.3   Stereolithography

The Form 2 SLA 3D printer from FormLabs [139] was used to print scaffolds with TPMS geometry. The material selected for this work was the Dental LT Clear (FormLabs). This resin was selected because it is a biocompatible material according to the manufacturer specifications [140]. Once the scaffolds were printed, they were placed inside the Form Wash (FormLabs) to remove any uncured resin, followed by placing them inside the Form Cure (FormLabs), where the parts were post cured to increase their strength [141], which is important here to ensure they won't break when performing cell culture experiments on them so the intended architecture is retained.

Four scaffolds with TPMS geometries were designed using an in-house software tool [111]. The volume fraction chosen was 40% and the size was 5 x 5 x 5 mm^3. The geometry chosen was the TPMS type Gyroid, which has been recommended in previous studies [[142], [143]]. For an explanation of why TPMS geometries were chosen see section 4.1 or for a more thorough explanation of the theory behind TPMS equations see Maskery et al. [111][112].

4.2.2   Cell culture experiments on micro-SLA scaffolds: Cell proliferation and differentiation

4.2.2.1   Cell attachment test

Cells used were Mesenchymal Stromal Cells (hMSCs) at a density of 5000-6000 cells per cm^2. Human immortalized mesenchymal stromal cells (hMSCs) were generated in-house by lentiviral transfection of E6/E7 and hTERT genes as previously described ([144],[145],[146]). The cells were between passage 10 and 15. The cells were stained with Toluidine blue (Sigma-Aldrich, UK) which allows for visualisation of DNA material. When using the TCDMDA material, three samples were evaluated with a plasma treatment and three samples without plasma treatment as it was expected that plasma treatment would enhance cell attachment. It has been suggested that the reason oxygen plasma treatment enhances cell adhesion is because it increases nano-topographical surface roughness and wettability of the scaffold surface [147].

4.2.2.2   Plasma treatment

"Plasma activation is a surface modification procedure, which is widely used to hydrophilize material surfaces industrially. The effect is known to be attributed to the composition of polar functional groups (i.e., OH, COOH, NH2, SO2) on the materials and modification of nanotopography by etching and sputtering." [147].

The samples were activated using oxygen plasma (pi = 0.3 mbar, 100 W, 10 min). They were immediately transferred into dry (4 Å MS) toluene (500 mL) (Sigma-Aldrich, UK) under argon. 3-(Trimethoxysilyl) propyl methacrylate (10 mL) (Sigma-Aldrich, UK) was then added to the solution, and the reaction mixture heated to 50°C for 24 h. The samples were then cooled to room temperature and

washed by sonication with 2 x 100 mL fresh toluene. The slides were then dried under vacuum in a silicone-free vacuum oven (50°C) for 24 h.

4.2.2.3   Cell growth on scaffolds

The cell growth experiment was divided into the groups shown in Figure 4-7, a positive control, a negative control, and the scaffolds under analysis. The positive control consisted of a sample with the same overall dimensions as the scaffolds, 2 × 2 × 0.5 mm. Normalisation of the results to the surface area was performed. The negative control consisted of Gyroid scaffolds which were not seeded with cells. The final fluorescence values were computed relative to the fluorescence of the negative control scaffolds. The scaffolds used for comparison were the Lidinoid type and Gyroid type.

Days 1, 4 and 7 were used to assess the cell growth, such that the total number of scaffolds was 36. The cell quantification process consisted of first preparing the presto blue working solution by mixing presto blue (Thermo Fisher Scientific, UK) with standard media (90% media, 10% presto blue), then adding this to the scaffolds and incubating (37°C and 5% CO2) for 1 hour. Presto blue turns increasingly fluorescent pink in the presence of viable cells, correlating with metabolic activity and therefore indicating cell viability and number. Afterwards the working solution was transferred to a 96 well plate and a plate reader was used to measure the amount of fluorescence. The well plate reader provides a table of values which was post-processed to compute the net fluorescence coming from the cells. The wavelength used to measure presto blue was 590 nm.

To visualize the cells inside the scaffolds, the toluidine assay was once again used. For this, the cells were fixed using 3.7% paraformaldehyde for 2 h at 4 deg C. This was followed by washing the samples with PBS and staining them with toluidine blue for 2 h. Images were recorded before and after sectioning, using a microscope.

Error! Reference source not found.
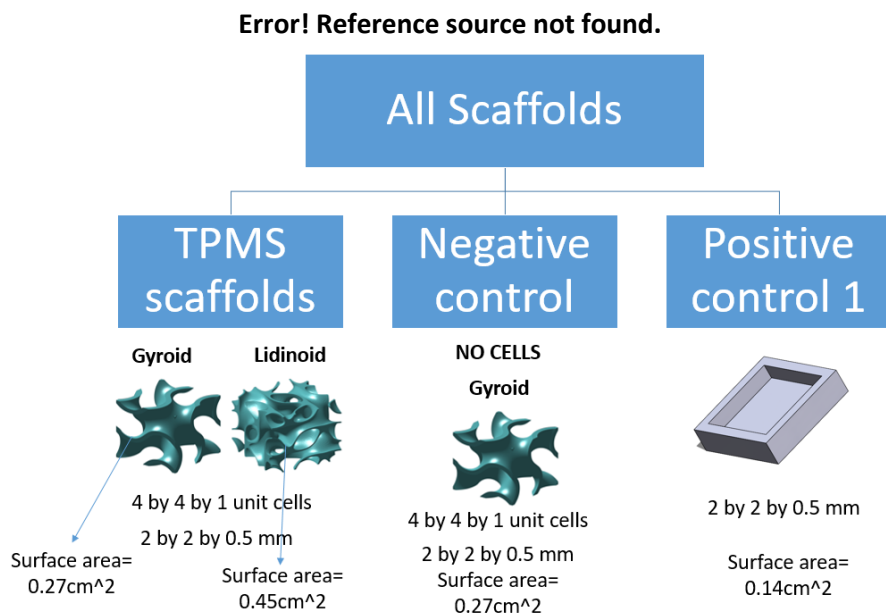
Figure 4-7: The different groups of scaffolds used for the cell growth experiments.

1) Calculate amount of cells and media needed

2) Add media and cells to scaffolds

INCUBATOR

3) Remove media and add presto blue, leave for one hour for colour change.

… wrap in aluminium to stop changes due to light

6) Repeat 3)-5)process for all time points

5) Output translates to fluorescence in each well

4) Use plate reader

7) Post-process results to calculate cell growth in the different groups and compare

Figure 4-8: Illustration of the procedure carried out to measure the cell density via Presto blue luminescence.

4.2.2.4   Permeability test

A permeability test was carried out on the scaffolds by first weighting the scaffold using a scale, then injecting 10 μL of water using a pipette and measuring how much water managed to penetrate the pores. The pipette was used pressing it against the surface of the scaffold, and the amount of water on each scaffold was measured by weighting the scaffold post water injection and comparing that weight to the initial weight. Furthermore, a percentage of the water on the scaffold was deducted as it was assumed to be sitting at the walls of the scaffolds due to surface tension.

Assuming that the film thickness of water is constant all over the surface of the scaffold, the percentage of water attached to the outer surfaces of the scaffold would be equal to the percentage of surface area of the outer surfaces of the scaffold. To compute the surface area of the outer walls, the scaffold outer pixel slices were summed up to find the total outer surface area. For the gyroid scaffold, the total outer surface area is 0.045 cm^2, which is 17% of the scaffold surface area. For the Lidinoid, the outer surface area was also 0.045 cm^2, but the percentage this represents from the total scaffold surface is only 10%.
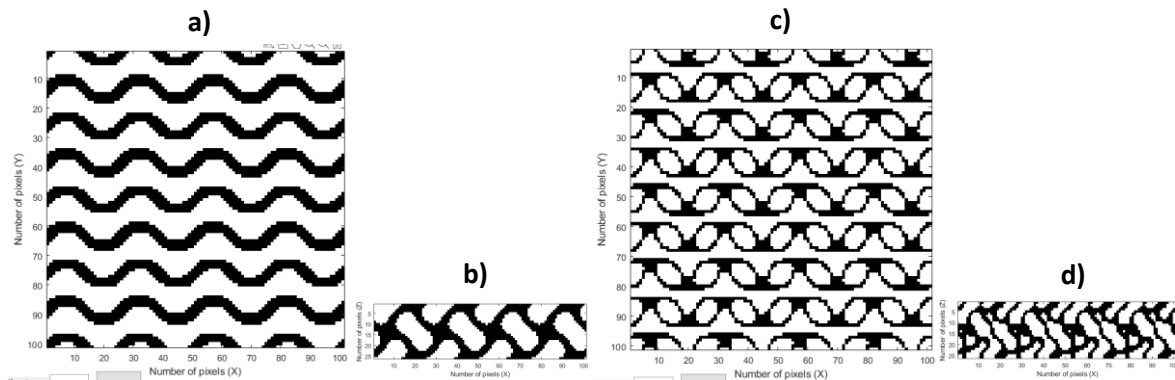
Figure 4-9: Water film thickness assumption. a) pixelated image of top surface of gyroid scaffold, b) pixelated image of side surface of gyroid scaffold, c) pixelated image of top surface of lidinoid scaffold, b) pixelated image of side surface of lidinoid scaffold.

4.2.3 Cell culture experiments on SLA scaffolds: Cell proliferation, differentiation, and mineralization within scaffolds

4.2.3.1 Preparing standard media

The contents of the mesenchymal stromal cell basal medium (MSCGM) (Sigma-Aldrich, UK) were first added to the 440 mL Mesenchymal cell growth supplements bottle (MSCBM) (Sigma-Aldrich, UK). Then 50 mL of serum (Sigma-Aldrich, UK) were added to a 100 mL beaker. This was followed by adding 10 mL of L-Glutamine (Sigma-Aldrich, UK) and 500 μL of GA-1000 (Sigma-Aldrich, UK) to the 100 mL beaker. Using a syringe with filter, everything from that 100 mL beaker was aspirated into the MSCBM bottle.

4.2.3.2 Preparing osteogenic and BMP-2 media

Secondly, the osteogenic media was prepared. This involved the mixing of human Mesenchymal Stromal Cell (hMSC) differentiation basal medium bottle (Sigma-Aldrich, UK) with dexamethasone (Sigma-Aldrich, UK), L-glutamine (Sigma-Aldrich, UK), ascorbate (Sigma-Aldrich, UK), penicillin/streptomycin (Sigma-Aldrich, UK), MCGS (Sigma-Aldrich, UK) and β-glycerophosphate (Sigma-Aldrich, UK). The osteogenic media was stored in a dark fridge at 2-8°C. Another flask was prepared with osteogenic media plus BMP-2. BMP-2 are the most used growth factors for bone regeneration because of their superior osteo-inductive properties. They induce osteoblastic differentiation from Mesenchymal Stromal cells [13], so it is included in the media to enhance cell differentiation.

4.2.3.3 Preparing cells

Human Mesenchymal Stromal cells (hMSC) were initially stored at -196°C. Human immortalized mesenchymal stromal cells (hMSCs) were generated in-house by lentiviral transfection of E6/E7 and hTERT genes as previously described ([144],[145],[146]). The cells were between passage 10 and 15. The cryovial with the cells was placed in a 37°C water bath until the last bit of ice melted. 1 mL of cells were then added to 5 mL of temperature-equilibrated medium followed by centrifuging the vial at 500 x g for 5 minutes at room temperature. The cells were seeded at a seeding density of 5000-6000 cells per cm^2 with 0.2-0.4 mL of medium per cm^2.

4.2.3.4 Scaffolds preparation

36 printed scaffolds were sterilised with 70% industrial methylated spirit (IPA) (Sigma-Aldrich, UK) for 1h, dried for 1h and soaked in serum for 5 days to allow protein adsorption to improve cell attachment.

4.2.3.5   Preliminary cell attachment test with Toluidine blue

After this, to test for cell attachment, 5 μL of cells (15-25 cells per μL) were added on top of three of the scaffolds to cover for 2hrs. Then the wells were filled with media and left for 3 days in the incubator in order to culture the cells with optimal humidity, temperature, as well as levels of CO2 and oxygen. Next, the cells were fixed using paraformaldehyde (Sigma-Aldrich, UK) and stained them using Toluidine blue (Sigma-Aldrich, UK) to be able to see the cells. The staining process consisted of adding 1 mL of Toluidine blue at a concentration of 0.05% for 15 min at first, then adding PBS and removing it several times until there was almost no blue visible. Toluidine blue selectively stains acidic tissue components such as DNA and RNA [148]. The wavelength used to measure toluidine blue was 621 nm.

4.2.3.6   Preparing well plates with scaffolds and controls

The 36 scaffolds were placed inside a well-plate. Then 10 mL of osteogenic media was used to resuspend a pellet of cells (15000-25000 cells per mL). 10 µL of this media with cells was added to each well and the scaffolds were then left in the incubator for 1 hr for cells to attach. At this point, osteogenic media plus 10 ng/mL of BMP-2, osteogenic media alone and standard media were added to 12 wells each respectively. The image below shows why 36 wells were needed, namely there are two time points (day 7 and day 14), three scaffolds are needed for differentiation and three for fixing cells onto scaffolds and visualizing the scaffolds. Controls were prepared for the standard media, the osteogenic media and the osteogenic media with BMP-2.

4.2.3.7   Quanti-iT PicoGreen for DNA quantification

The number of cells at any one time point was first calculated by dividing the total observed DNA weight by the weight of DNA in one cell, which is about 6 pg [149]. Next, 30 µL of triton x-100 (Sigma-Aldrich, UK) [150] was used to permeabilise the cells (allows things to get in and out of the cells more easily) after dissolving it in 10 mL antibody dilution buffer (Sigma-Aldrich, UK). This was followed by a sonication to break the cell membrane using sound waves [151] and the remaining liquid contained all the DNA. The final step was to add Quanti PicoGreen (Sigma-Aldrich, UK) allowing for quantification of the amount of DNA and therefore the number of cells. This quantification process consisted of measuring the fluorescence by placing a 96-well plate inside a plate reader. The wavelength used to measure Quani-iT PicoGreen was 520 nm.

4.2.3.8   Alkaline Phosphatase for ALP secretion (cell differentiation)

In order to measure cell differentiation, the same solution that remained after the sonication process was mixed with Alkaline Phosphatase (Sigma-Aldrich, UK) which allowed for the quantification of ALP in units per mg of DNA. This solution contained para-nitrophenol phosphate (pNPP), the substrate for the ALP enzyme. As ALP is a phosphatase, it removes the phosphate from pNPP making pNP. Since pnPP is colourless and pNP is yellow, it was possible to measure the activity of the ALP enzyme by observing how quickly the solution turned yellow. Higher ALP activity is indicative of a higher osteogenic differentiation rate. The wavelength used to measure ALP was 405 nm.

4.2.3.9   Alizarin red S for cell mineralisation

The cells were treated with 2% alizarin red S solution (pH 4.5) (Sigma-Aldrich, UK) for 10 min and washed several times with distilled water to remove any remaining stain after fixing. Alizarin red stains for calcium mineral. Optical microscope images were taken for visualisation. The wavelength used to measure Alizarin red was 540 nm.

4.3 Results

4.3.1 Micro-stereolithography

4.3.1.1 BMF standard material

As described in the methods chapter, scaffolds were manufactured with PμSLA using previously tuned parameters at a chosen resolution of 5 μm in the z-direction and 2 μm in x-y. Initially, the standard resin provided by the machine manufacturers was used, a resin described as a mixture of methacrylic and acrylic acid esters as well as photoinitiators [19]. In order to demonstrate how accurate the geometry of these scaffolds printed with μSLA is even at a pore size (largest) of 300 μm or 150 μm, microscope images of these scaffolds were taken and are shown in Figure 4-10,

Figure 4-11 and Figure 4-12.

It can be noted that this manufacturing technique allows for a relatively high resolution while at the same time making it possible to print structures of several mm. When comparing to other AM techniques, two-photon polymerization is a technique which allows for sub 100 nm resolution [152], however, it is very challenging and time consuming to make structures of 1 mm or larger with this technique. Moreover, while SLA could easily produce larger scaffolds, the resolution of the pores could never be as good as that shown here. Hence why μSLA is an optimal technique to produce tissue regeneration scaffolds. The major drawback would be time, it took about five hours to manufacture each of these scaffolds. However, projection μSLA allows for many scaffolds to be printed at once.
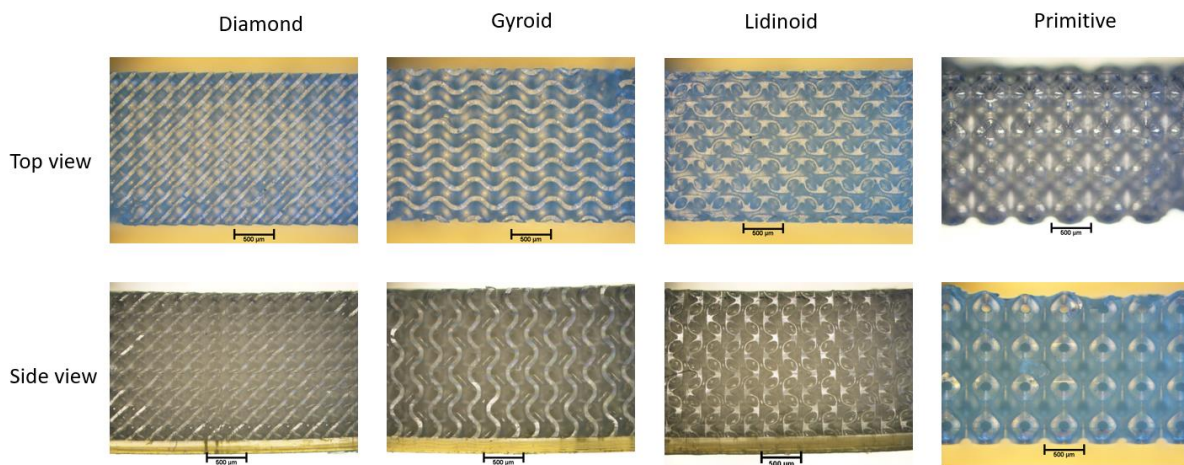
Figure 4-10: Scaffolds of 2 x 3.5 x 2 mm with unit cells of 500µm. Hence there are 4 unit cells along the y and z directions, and 7 unit cells along the x direction. Scale bars are all 500 µm.
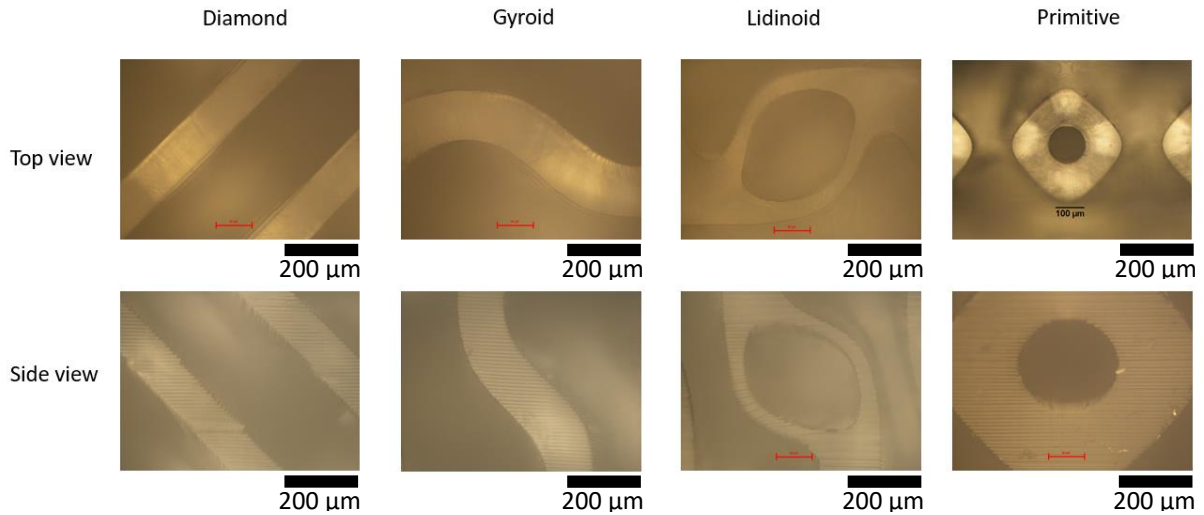
Figure 4-11: High magnification images of the same scaffolds shown in the previous figure. Scale bars are 200 µm.
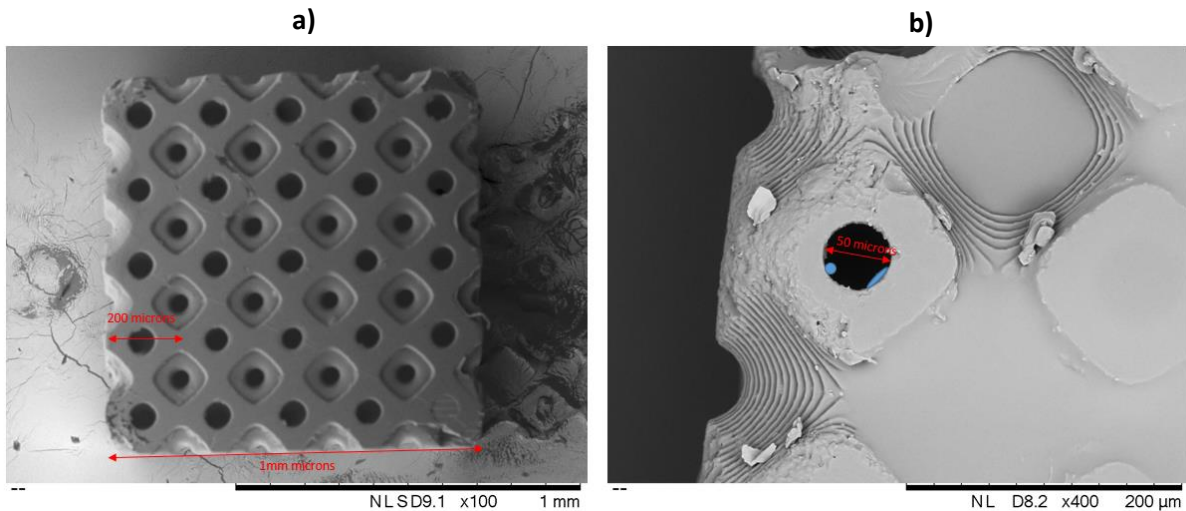
Figure 4-12: Scanning Electron Microscopy (SEM) images of a 1mm x 1mm x 1mm scaffold with 5 unit cells of 200 µm in each direction. It can be noted on the right that the smallest pore diameter is now 50 µm, half the allowed size for a pore. This image shows that even though µSLA can still capture the geometry relatively well at these length scales, it is also clear that the surface is not as smooth anymore. Scale bar for a) is 1 mm and for b) it is 200 µm.

4.3.1.2   TCDMDA material

Tricyclo[5.2.1.02,6]decanedimethanol diacrylate (TCDMDA) has been shown to yield biocompatible scaffolds when combined with 0.5wt% 2,2-Dimethoxy-2-phenylacetophenone (DMPA) photoinitiator [10]. Scaffolds were therefore printed with this material to ensure biocompatibility. The scaffolds shown in this section are the same scaffolds that were used for the cell culture experiments, these had a scaffold unit cell size of 1 mm and a volume fraction of 40% as recommended by the modelling results in chapter 3. The Scanning Electron Microscopy (SEM) images below are presented to show that while the surfaces are of course not continuous due to this being a layer-based manufacturing approach, the small layer height ensures that the surfaces are relatively smooth. Initially the standard BMF printer material was used to get an idea of how the scaffold geometry would look, but having found the material not to be biocompatible, TCDMDA was used for the actual cell growth experiments.
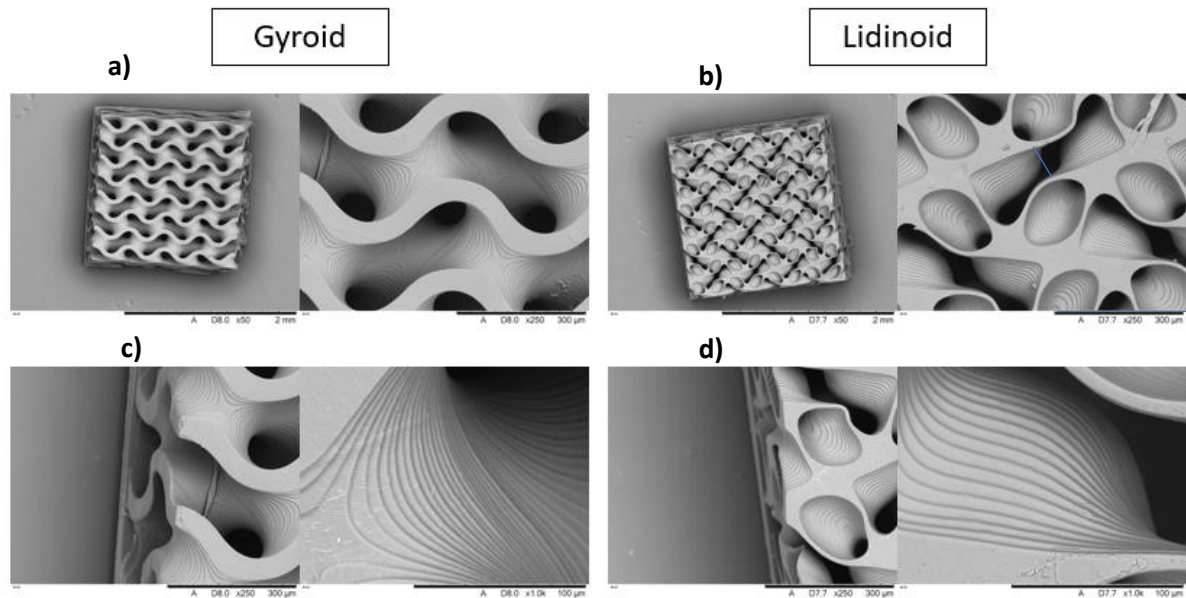
Figure 4-13: SEM images of the printed Gyroid and Lidinoid structures. From left to right respectively, scale bar for figures a), b), c) and d) are (2 mm and 300 μm), (2 mm and 300 μm), (300 μm and 500 μm), and (300 μm and 500 μm) respectively.

4.3.1.3 *Printer parameters ad-hoc optimisation*

In order to ensure a reasonable accuracy of the layer height, the intensity and exposure time parameters were optimised as shown in Table 5. The goal was to have the curing depth as close to 10 μm as possible while keeping the exposure time as low as possible. Therefore, it was decided to use an intensity level of 80 and an exposure time of 5 seconds.

Table 5: Results of the printer parameters ad-hoc optimisation

Intensity level	Exposure time (s)	Cure depth (μm)
60	1	didn't print
60	2	didn't print
60	4	didn't print
60	6	didn't print
60	8	10.52
70	1	didn't print
70	2	didn't print
70	4	didn't print
70	6	8.43
70	8	15.51
80	1	didn't print
80	2	5.64
80	4	9.68
80	6	10.48
80	8	17.8
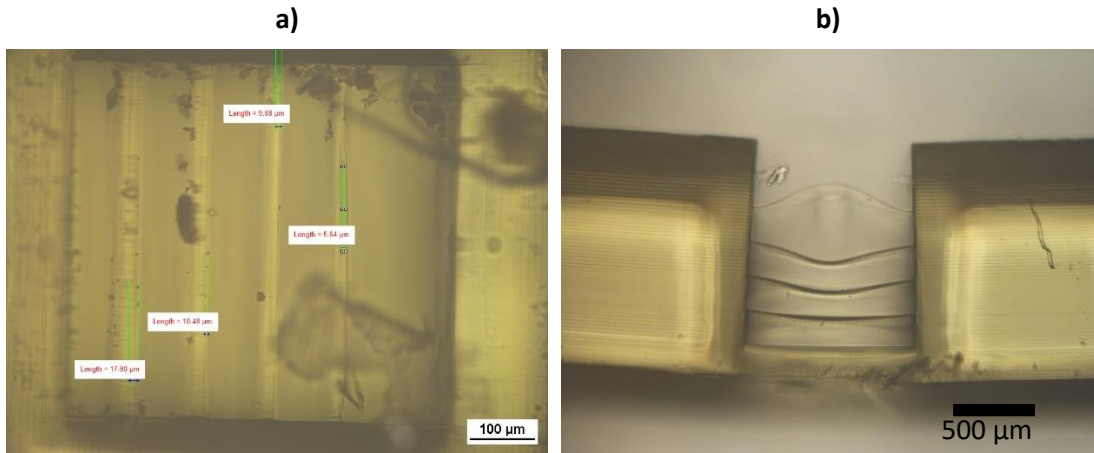
Figure 4-14: a) Image showing how the curing depth was measured as well as the curing depth values for the sample of intensity level 80. Scale bar is 100 μm. b) Image showing the sample from the side. Scale bar is 500 μm. Please note that this image was taken after having mistakenly moved it which caused the deformation seen.

4.3.2 Stereolithography

The scaffolds that were printed with SLA are shown in Figure 4-15. The material used was Dental LT (FormLabs, UK). The images show that there are small dents in several places because of the support material necessary given the printing direction of the Form 2 printer from FormLabs [139]. Figure 4-16 shows a pixelated comparison between the resolution that can be achieved with μSLA and that which can be achieved with SLA.
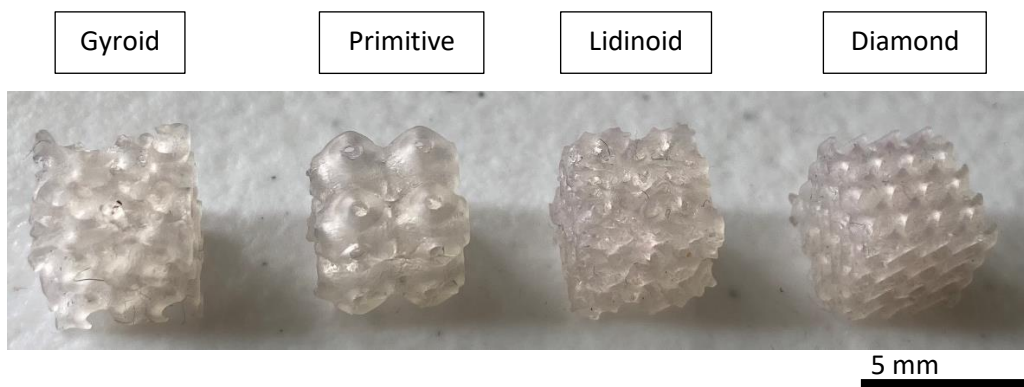
Figure 4-15: Scaffolds of Gyroid, Primitive, Lidinoid and Diamond lattice types printed with stereolithography (SLA). Scale bar is 5 mm.

500 micron scaffolds

μSLA (5,2,2)　　　　SLA (100,25,25)

Side: z　　　　z

x

Top: y　　　　y
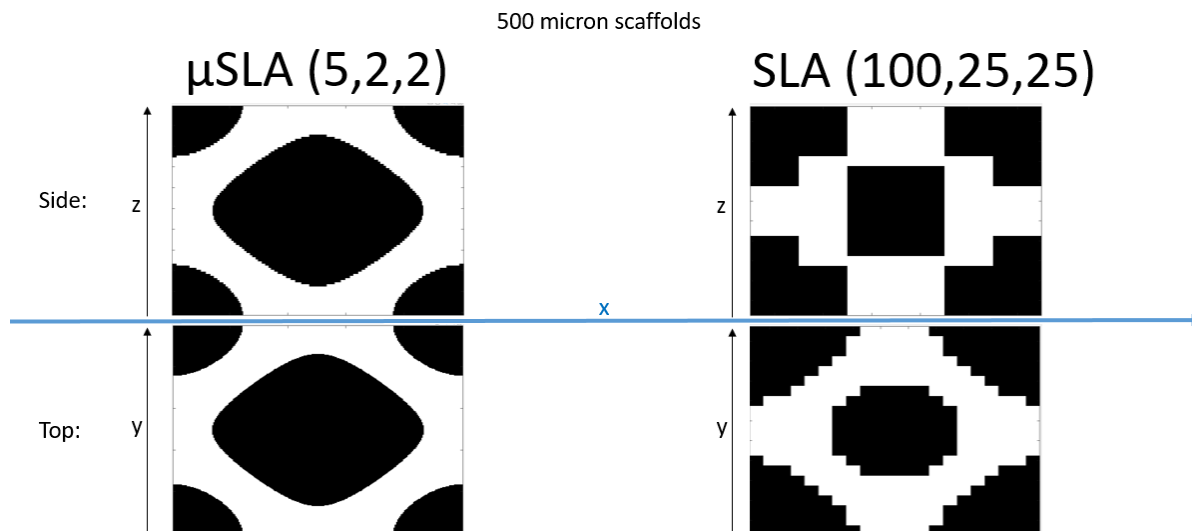
Figure 4-16: Resolution comparison between μSLA and SLA for 500μm scaffolds. It can be seen clearly that whilst with μSLA there are enough layers to define the surface smoothly, with SLA that is not the case.

4.3.3 Cell culture experiments on micro-SLA scaffolds: Cell proliferation and differentiation

For these experiments, the Gyroid and Lidinoid scaffolds were chosen. The Lidinoid was chosen because it was predicted in chapter 4 to yield the highest cell growth rate out of the candidate TPMS scaffolds, and the Gyroid was selected for continuity and comparison with the literature given that it has been studied much in previous works [[6], [142]].

4.3.3.1 Cell attachment:

In order to ensure that the Mesenchymal Stromal cells are able to adhere to the surface of the material, cell adhesion tests were done with the TCDMDA material. The test consisted of seeding the cells onto flat samples and visualizing them under a microscope. For more details on these experiments please refer to section 4.2.2.1. As can be seen below, a lot more hMSCs attached to the samples which were plasma treated. Cells also did attach to the samples with no plasma treatment, but in lesser amounts. Having seen this promising result, Plasma treatment was used.

No Plasma　　　　With Plasma

200 μm　　　　200 μm
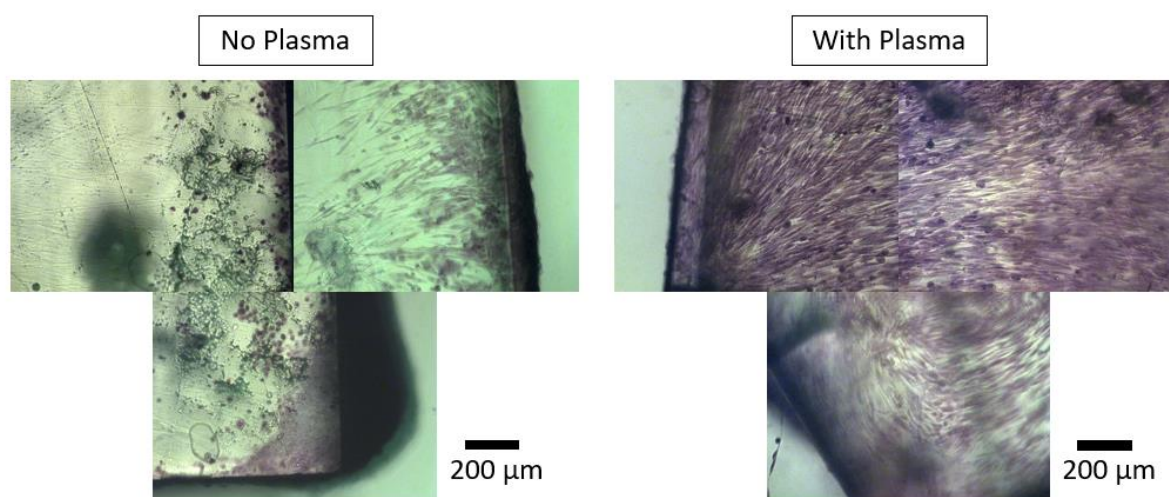
Figure 4-17: Microscope images of cells cultured on TCDMDA scaffolds with and without plasma treatment. The scaffolds were manufactured via Micro-SLA. Magnification 20x. Error bars are 200 μm.

4.3.3.2   Cell growth:

As can be observed in Figure 4-18, the gyroid scaffold type and the square type yielded higher cell growth than the Lidinoid type. The hypothesis based on chapter 3 was that the Lidinoid leads to a larger amount of cell growth. This was shown using the cell growth model results presented in section 3.4, where for a range of volume fractions from 0.2 to 0.9 and a unit cell size of 1 mm, the Lidinoid lattice type consistently showed a higher average predicted cell growth rate. This could likely be due to the higher amount of total concave curvature of the Lidinoid scaffolds, as shown in figure Figure 4-1. However, the issue was that the media and cells could not get through to the inside of the scaffolds because when the experiment was being carried out, the liquids were observed not to permeate the scaffolds. To corroborate this, a permeability test was carried out as shown in the following section.
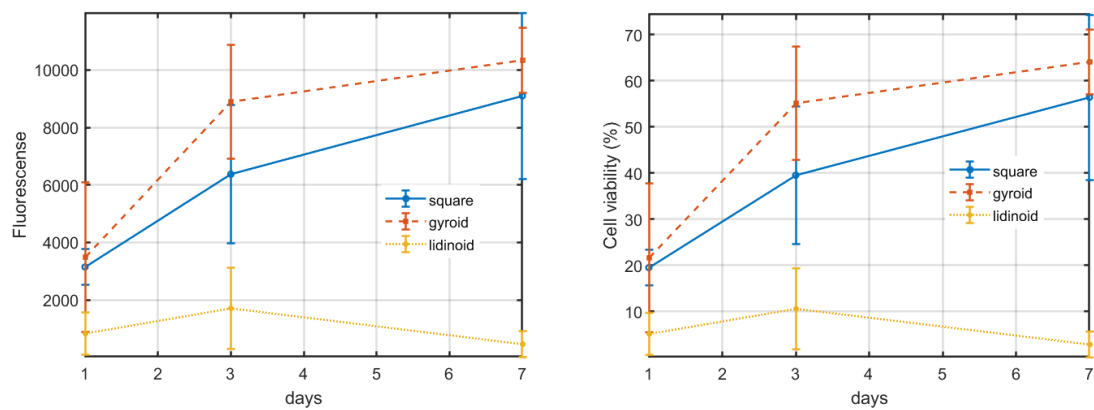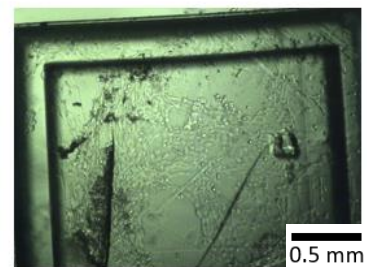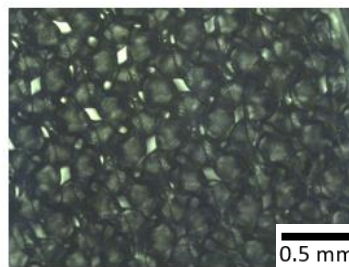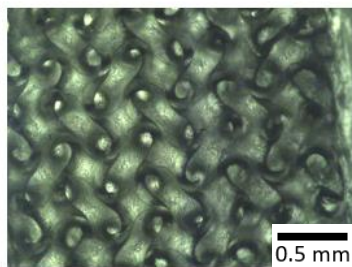
Figure 4-18: (Top left) Fluorescence results in a.u. at days 1,3 and 7 for the positive control as well as the gyroid and Lidinoid scaffolds, normalized to the surface area, (Top right) cell viability results acquired by assuming 100% is the average fluorescence seen from the tissue culture plastic, 16131; and scaffolds at day 1 from the different groups viewed under the microscope (Bottom). n=3 for each scaffold type and time point and the error bars represent the standard deviation.

It can be observed from Figure 4-19 that when looking at the surface only, before segmentation, both in the case of the Gyroid and the Lidinoid cell type, the surface is thoroughly populated with cells by day 7.

	Lidinoid scaffold type	Gyroid scaffold type
Day 7	0.5 mm	0.5 mm
Day 3	0.5 mm	0.5 mm
Day 1	0.5 mm	0.5 mm
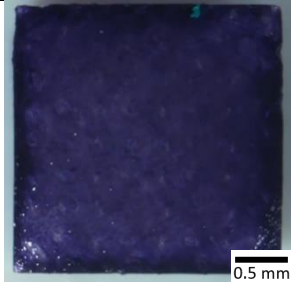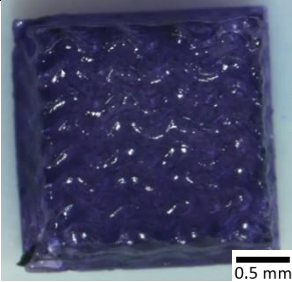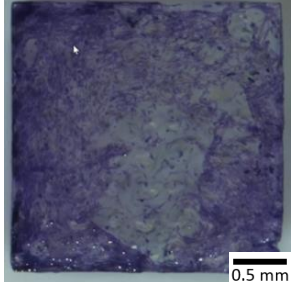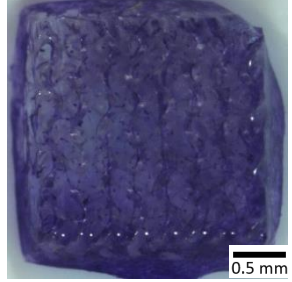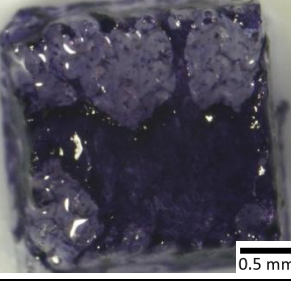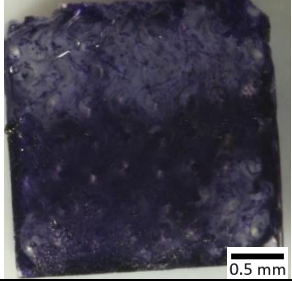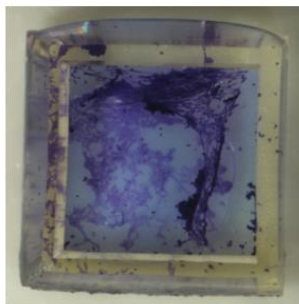
Flat, day 3

Figure 4-19: Microscope images of TPMS scaffolds having been stained with toluidine blue for cell density visualisation. Images are shown at day 1, day 3 and day 7.

It can be noted from Figure 4-20, which shows a gyroid and a Lidinoid scaffold after segmentation, that there are no cells at all inside the Lidinoid scaffold, serving as further proof that the media with cells could not penetrate the pores of the Lidinoid scaffolds. To get some cells inside, centrifugation of the Lidinoid scaffolds was done at 200 x *g* for 5 minutes. This had to be repeated 5 times to achieve liquid permeation.
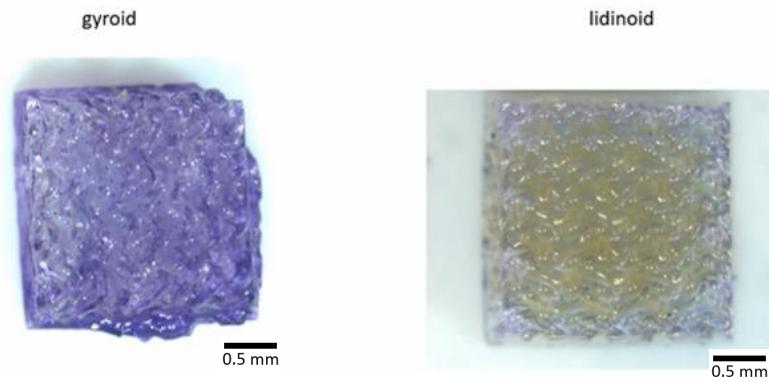
Figure 4-20: Scaffolds stained with Toluidine blue for cells visualisation, segmented to show the cells on the inside.

4.3.3.3   Permeability test:

Having observed the issues in the experiments described above, and aware of the observation regarding the liquid not being able to penetrate the Lidinoid scaffold during the cell culture experiments, a post liquid penetration experiment was carried out to confirm these observations. The results of this experiment can be found on Table 6. It can be noted from this table that while more than 75% of the available volume was filled with water for the Gyroid scaffolds, in the case of the Lidinoid scaffolds, less than 15% of the water managed to penetrate it. It should be noted that for the Gyroid scaffold it has been assumed that 17% of the remaining water was not inside the scaffold but sitting at the walls of the scaffolds and for the Lidinoid scaffold this was 10%. See section 4.2.2.4 for an explanation of this assumption.

Table 6: Scaffold liquid penetration experiments results.

	Gyroid				Lidinoid			
	1	2	3	4	1	2	3	4
Total volume (mm^3)	2	2	2	2	2	2	2	2
Volume scaffold (mm^3)	0.8	0.8	0.8	0.8	0.8	0.8	0.8	0.8
Available volume (mm^3)	1.2	1.2	1.2	1.2	1.2	1.2	1.2	1.2
Density water (mg/mm^3)	1	1	1	1	1	1	1	1
Available mass of water (mg)	1.2	1.2	1.2	1.2	1.2	1.2	1.2	1.2
Scaffold Initial mass (mg)	12.3	11.6	12.4	12.4	12.1	12.3	11.5	12.1
Injected volume of water (µL or mm^3)	10	10	10	10	10	10	10	10
Injected mass of water (mg)	10	10	10	10	10	10	10	10
Scaffold mass after water injection (mg)	13.6	12.8	13.4	13.5	12.2	12.5	11.7	12.4
total water that remained (mg)	1.3	1.2	1	1.1	0.1	0.2	0.2	0.3
total water that remained inside (mg)	1.1	1.0	0.8	0.9	0.1	0.2	0.2	0.3
Percentage of available space that was filled (%)	89.9	83.0	69.2	76.1	7.5	15.0	15.0	22.5
Average percentage filled (%)	**79.5**				**15**			

Percentage of available porosity that was filled with water
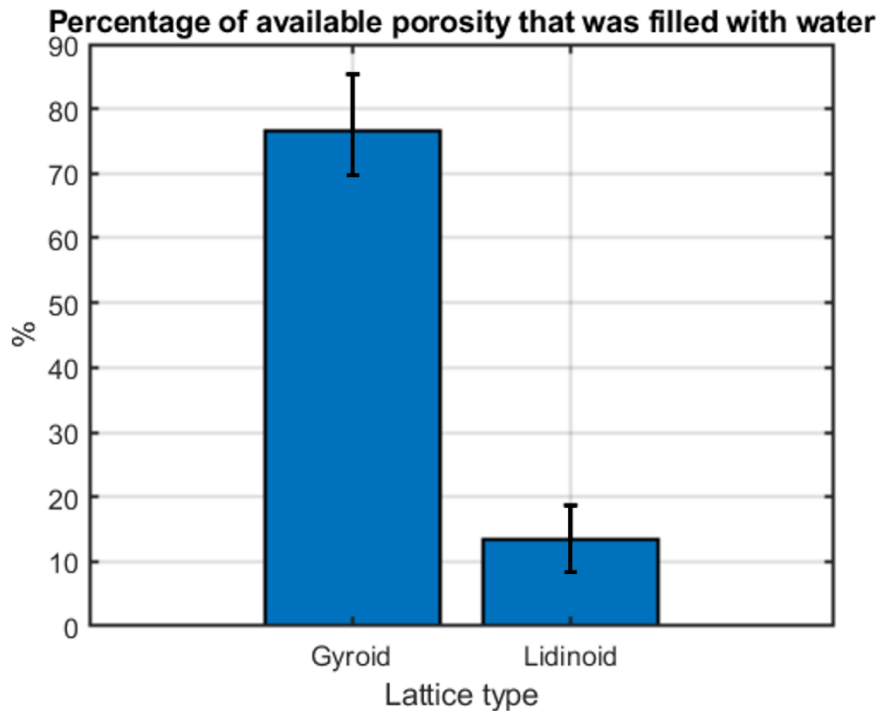
Figure 4-21: Bar plot showing the percentage of available volume in the scaffold that was filled with water in the penetration test. n=4 for both scaffolds and the error bars represent the standard deviation.

4.3.4 Cell culture experiments on SLA scaffolds: Cell proliferation, differentiation, and mineralization within scaffolds

As explained in the methods chapter, cell culture experiments were also carried out using scaffolds manufactured via stereolithography (SLA). The Gyroid scaffold geometry was chosen because it proved very promising in the previous section of this chapter. The effect of Osteogenic Media and BMP-2 on the cell growth was also assessed with the hypothesis that they will both enhance the cell differentiation as supported by literature [[153], [130]], with the objective of observing for the first time how BMP-2 affects cell growth on TPMS scaffolds.

4.3.4.1   Cell attachment test:

With the objective of checking whether cells adhere to the FormLabs dental material printed scaffolds, a cell attachment test was carried out. Cells used were Mesenchymal Stromal cells (hMSCs) at a density of 5000-6000 cells per cm^2. The cells were stained with Toluidine blue which allows for visualisation of the cells as shown in Figure 4-22. The cells had been cultured on the scaffolds for three days.
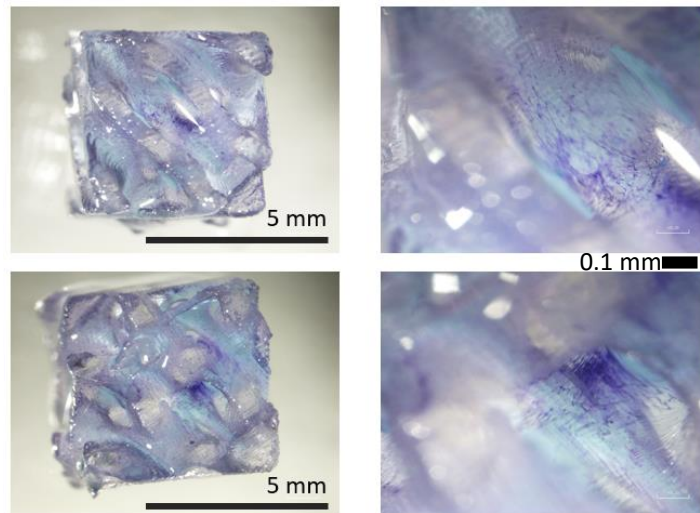
Figure 4-22: Visualisation of hMSC cells on printed scaffolds using Toluidine blue. The cells had been cultured on the scaffolds for three days. The geometry used for these scaffolds was a Gyroid lattice type volume fraction of 40%, with 2 x 2 x 2 unit cells and a bounding volume of 5 x 5 x 5 mm³.

4.3.4.2   Cell proliferation, differentiation and mineralisation:

To get an understanding of how the cells grow with these scaffolds, the surface of the scaffolds was visualized at day 7 and at day 14 as shown in Figure 4-23. As explained in the methodology, by measuring the total amount of DNA in the cells, it is possible to calculate the number of cells by dividing that number by the amount of DNA per cell. Figure 4-24 shows the number of cells for each of the groups at days 1, 7 and 14.

BMP-2 is known to enhance the differentiation rate, but studies show that its effect on cell proliferation is not so straightforward, depending on the concentration and other factors it can positively or negatively affect cell growth [133]. As shown in Figure 4-24 it was found that the difference between the cell growth results for the scaffolds groups was statistically insignificant in all groups. The only changes in cell count that were found to be statistically significant were those with the monolayer groups of standard and BMP-2 media. The change between day 7 and 14 for the standard media was also found to be statistically insignificant, as can be seen from the ANOVA and post-hoc results in Appendix H. See section 6.3 for a discussion of these results.
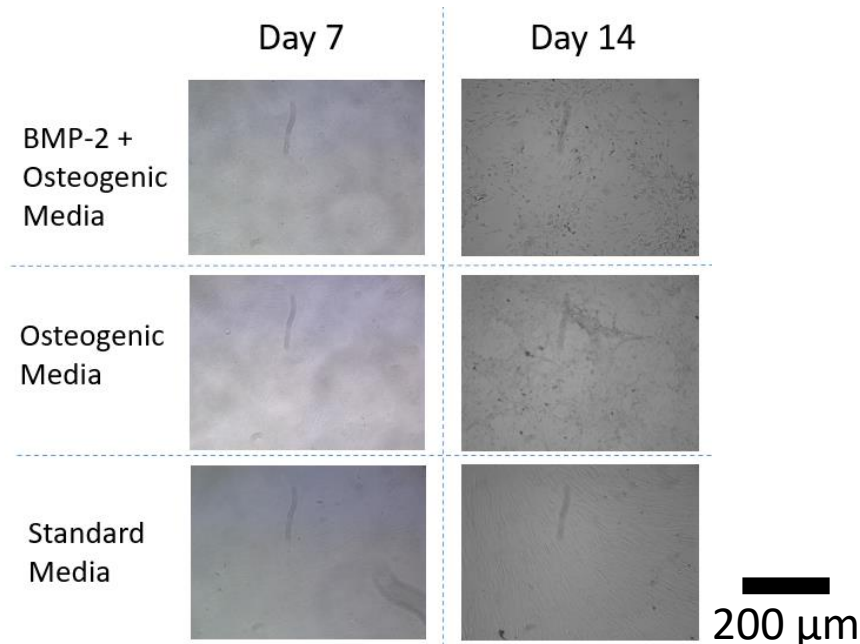
Figure 4-23: Microscope images of cells on scaffolds at day 7 and 14, for three cases: Standard Media (bottom), Osteogenic Media (middle), BMP-2 + Osteogenic Media (top).
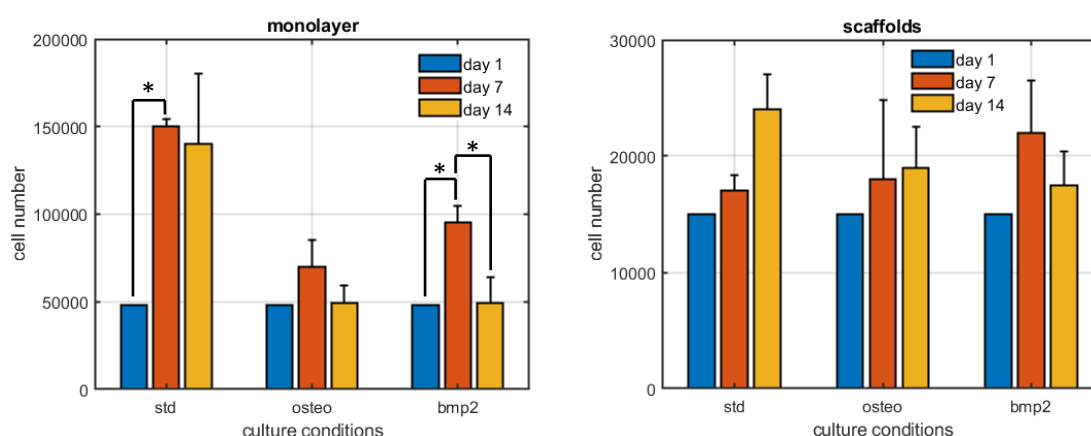
*Figure 4-24: Bar charts showing the quantified number of cells via Quanti PicoGreen, at days 1, 7 and 14, and for the cases of a monolayer (left) and the scaffolds (right). The scaffolds used in this study had a Gyroid geometry with volume fraction of 40%, a unit cell size of 5 mm and 2 x 2 x 2 unit cells. n=3 for all values and the error bars represent the standard deviation. * p < 0.05*

As can be seen in Figure 4-25, the highest ALP content was found for the scaffolds with BMP-2 media followed by the scaffolds with osteogenic media. Strangely, this pattern was not quite the same for the monolayers, there the samples with osteogenic media only, had a lot more ALP content by day 7. This could be due to the time at which the samples were taken, the ALP peak might have been higher for the BMP-2 results as expected but it might have peaked at a different time. The same reasoning applies to all the results presented in these graphs. As explained in section 4.2.3, the ALP content increases as cell differentiation increases until it peaks. The higher amount of ALP secreted by the MSCs with BMP-2 indicates that there was a proportionally higher amount of differentiation taking place. The change in ALP content between days 7 and 14 was not statistically significant in any of the monolayer media groups. See section 6.3 for a discussion of these results.
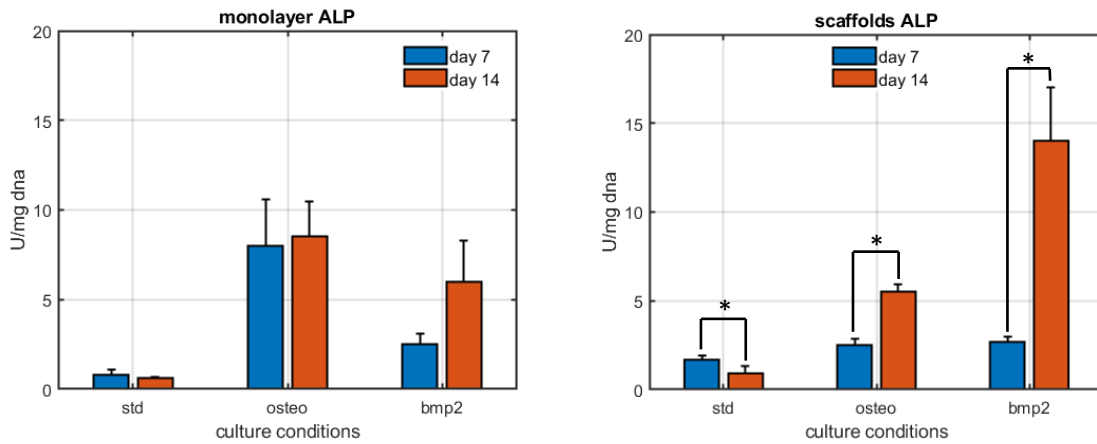
*Figure 4-25: Osteogenic differentiation via ALP quantification. The bar charts show the units of ALP per mg of DNA. As can be observed the results are given for day 7 and 14, for standard, osteogenic or BMP-2 media, and for monolayer or scaffolds groups. n=3 for all values and the error bars represent the standard deviation. * p < 0.05*

Figure 4-26 shows the mineralisation results, it can be observed by looking at the darker red regions that the samples with BMP-2 media calcified far more collagen into minerals. Moreover, it is also evident that the samples with standard media did not lead to much mineral formation at all.
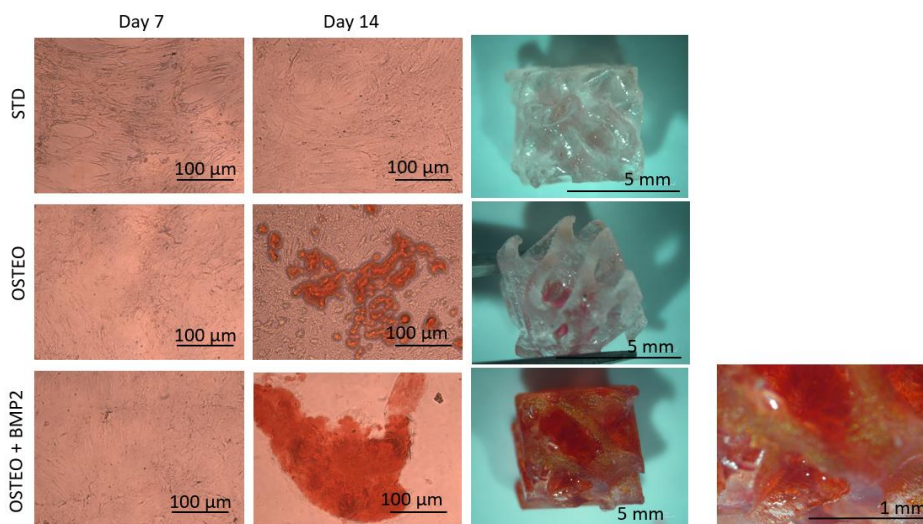
Figure 4-26: Osteogenic mineralisation via Alizarin red for calcium deposition. From top to bottom, the images show results for the use of standard media (top), osteogenic media (middle) and osteogenic +BMP-2 media (bottom). From left to right the images show microscopic images of the stained monolayer surface at day 7 (left), microscopic images of the stained monolayer surface at day 14 (middle) and microscope images of the stained scaffolds at day 14. The image on the far right at the bottom shows a the surface of a stained scaffold at a higher magnification. All the scaffolds were had a TPMS gyroid geometry with a volume fraction of 40% and a unit cell size of 5 mm.

4.4 Summary

For a discussion of the results see chapter 6, the text below simply summarizes the content presented in this chapter.

This chapter started by introducing the previous literature that has focused on Additive Manufacturing of TPMS scaffolds as well as carrying out cell culture experiments with such scaffolds. Next, the objectives of the chapter were outlined, namely developing a strategy for the Additive Manufacturing of TPMS scaffolds for cell growth and finding out whether using BMP-2 as well as TPMS geometry would lead to improved cell proliferation, differentiation and mineralisation.

Next the results from manufacturing scaffolds via PµSLA and SLA were described. For the PµSLA scaffolds, it was found, contrary to what was initially expected, that over the seven days of analysis, the Gyroid scaffold showed higher cell growth potential than the Lidinoid as shown by fluorescence results. A scaffold penetration analysis with water showed however that while about three fourths of the Gyroid scaffold could be filled with water once injected with a syringe, less than one fifth of the Lidinoid scaffold could be penetrated, leading to the conclusion that the reason Lidinoid scaffolds performed worse was the lack of media penetration.

Next, the materials and methods used were described. The latter consisted of manufacturing TPMS scaffolds with projection micro-stereolithography to allow for sub-micrometre pore sizes. The printer used was from Boston Manufacturing Technology (BMF) with a resolution of 5 µm and the base material used was Tricyclo[5.2.1.02,6]decanedimethanol diacrylate (TCDMDA) combined with 0.5wt% 2,2-Dimethoxy-2-phenylacetophenone (DMPA) photoinitiator. The exposure time and intensity level, which are key parameters of the printing process, were tuned to ensure an appropriate curing depth. A custom software was developed to create the TPMS binary printing files.

Cell culture experiments were also described, to compare the modelling results with experimental results. This work consisted of several stages, firstly a cell attachment test was performed to ensure the optimised printer material was suitable for cell growth analysis. This led to the realisation that plasma treating the surfaces of the scaffolds enhanced cell survival as well as permeability, hence, the final scaffolds were all plasma treated. To measure the cell growth at three points over 7 days, Mesenchymal stromal cells (MSCs) were cultured on two types of TPMS scaffolds, as well as on a control scaffold, and the cell growth potential was quantified via the fluorescence level, which gives an indication of the amount of cell activity on a given scaffold. Experiments were then carried out to investigate the effect of combining the promising effects of TPMS geometry with those of BMP-2 growth factor. This was done by printing scaffolds using a Stereolithography (SLA) printer from Formlabs to print scaffolds using their biocompatible dental resin, followed by culturing iMSCs on their surface and quantifying the cell proliferation, differentiation and mineralisation via suitable assays.

Finally, the results of the cell proliferation, cell differentiation and mineralisation experiments with the SLA Gyroid scaffolds were described. For the cell proliferation, it was shown by looking at the results of the Quanti PicoGreen visualisation assay that the only results that were statistically significant were those for the monolayer BMP-2 between days 1,7 and 14 as well as those for the monolayer with standard media between day 1 and 7.

The cell differentiation analysis quantified via units of ALP per mg of DNA showed that between day 7 and day 14 the MSC cells attached to the Gyroid scaffolds with BMP-2 growth factors began to secrete a lot more ALP than for the other groups. This implies as expected that BMP-2 significantly enhances the ability of the MSC cells to differentiate into osteoblasts while attached to Gyroid scaffolds. Finally, the results of the mineralisation were shown by using the Alizarin red assay that shows calcium deposition. As expected, a lot more calcium and thus mineralisation could be observed for the scaffolds that had been supplied with BMP-2 growth factor.

Chapter 5: Optimization of a plate-scaffold assembly

5.1 Introduction

Critical bone fractures are commonly treated with bone autografts or allografts to accelerate bone regeneration [154]. However, as has been explained in chapter 3, there are significant complications with such processes and additively manufactured tissue regeneration scaffolds offer a promising solution [30]. For the fracture to be reconstructed using such a scaffold, a fixation mechanism is needed to provide the necessary stability throughout the healing process [105].

The most common forms of fixation are external fixation, plate fixation and intramedullary nails [72]. Small and moderate axial inter-fragmentary strain (IFS) at the femoral diaphysis has been demonstrated to enhance healing both through Finite Element Modelling and through experiments [74][75][72]. Shear IFS however, has been shown to result in delayed as well as incomplete fracture healing [70][72]. Since intramedullary nails cause mostly a large shear IFS as a consequence of the relative movement between the nail and the bone fragments [76][77], it follows that they are not the preferred fixation method (in some cases it may be the only possible method though). The axial IFS that an external fixator can provide is limited by the large necessary gap between the plate and the bone [68]. Hence, greater stability can be achieved using internal plate fixation devices [155].

Bone resorption at the region directly under rigid fracture fixation plates was detected [79] and is now very well accepted as a fact thanks to further experiments [80]. This phenomenon is often referred to as 'stress shielding' because of a hypothesis that the bone is subject to lower stress due to it being 'shielded' by the more rigid plate. 'stress shielding' is defined in the field as a bone being deprived of functional stimulation by having its physiological stress reduced by a load-sharing implant and thus causing the bone to become less dense in accordance with Wolff's law [156]. For more details on the 'stress shielding' phenomenon please refer to section 2.8. The von mises stress magnitude changes both due to the Young's modulus and the change in geometry. The axial rigidity of a tube (simplified bone geometry used in this study) depends on the material Young's modulus as well as the cross sectional area [72], with a higher value of both resulting in a higher axial rigidity. If the contact conditions between a fracture plate and a bone are ignored and it is assumed they are one multi-material part, the addition of a plate adds cross sectional area as well as a higher Young's modulus to the section of the bone where the plate is attached. This is why studies have shown that the stress shielding can be reduced by modifying the plate cross sectional area [86] or its material [87].

A bone is constantly undergoing remodelling, where osteoblast cells synthesize bone matrix and osteoclast cells dissolve it, and the ratio of these two defines the remodelling rate. This remodelling rate of the bone is proportional to the level of stress in the bone [69] and given that a rigid plate causes the stress levels in the bone to be reduced [157], it follows that the bone resorbs. A lower density causes the bone to weaken at the relevant regions and the risk of re-fracture after plate removal is increased.

Several concepts have been developed to solve this 'stress shielding' problem. Titanium plates have reduced stress shielding somewhat due to their lower modulus of elasticity than stainless steel [83], but this is still not sufficient given that the modulus of elasticity of titanium is about seven times higher than that of cortical bone [85]. Continuing to lower the modulus of elasticity of the whole plate would in fact reduce the 'stress-shielding' further, but it would also cause the IFS at the fracture gap to increase. This would in turn cause the fracture not to heal. The challenge is to minimise the 'stress-shielding' while still providing a low enough IFS at the fracture site. Defining "stress shielding" as well as "low enough IFS" in terms of measurable quantities is a further challenge that is addressed here.

A promising solution to this dilemma is the use of plates with graded stiffness. The stiffness may be varied by use of either the material modulus of elasticity or the thickness (which affects the moment of Inertia of the construct). An approach that modifies the thickness was recently investigated through the use of a Finite Element model [86]. The concept was a plate with a thickness that decreased gradually from the middle towards the longitudinal ends. This solution did in fact minimize both the stress-shielding and the axial IFS, however, it is expected that in the regions of low thickness the connection between the screw and the plate will not be very effective.

The concept of a stiffness graded plate was investigated in a 2D Finite Element analysis both longitudinally as well as transversely [87]. In the longitudinal case the Young's modulus of the fracture fixation plate was 200 GPa at the middle and was gradually decreased towards the ends down to 20 GPa. The same was done in the transverse direction. The study successfully proved that a stiffness graded plate will reduce the 'stress-shielding' both in the case of transverse grading as well as axially grading. Whether the stability of the construct would be sufficient was however not so clear. Moreover, it has been shown that when analysing local stress patterns of these geometries, 3D Finite Element studies should be carried out rather than 2D because one- and two-dimensional models of can only be qualitative [107]. Another study attempted this experimentally via AM but was not successful due to adhesion issues at the interface between different materials relating to unmelted particles [89].

Another exciting concept that has recently been investigated is the use of plates with an auxetic lattice structure [90]. Auxetic structures are especially interesting lattice structures because they provide a negative Poisson's ratio (NPR) which means that in the plane perpendicular to the loading they expand under tension and contract under compression [91]. This property has been shown to be beneficial for several biomedical applications [92]. For use in fracture plates there was first a study that investigated the use of a completely auxetic plate made of polyurethane [93] and showed that auxetic fracture plates lead to more contact points thus reducing the contact pressure. Recently a study was conducted which proved that by having an auxetic geometry on a section of the plate, not only can the stress shielding be reduced but the plate will remain strong enough to avoid failure [90]. The latter study used a Finite Element model as well as experimental results. Auxetic plates are therefore believed to have a beneficial effect on fracture fixation because by causing the plate to compress in all directions upon axial bone compression, it allows it to have a higher contact area with the screws and thus a lower concentration of contact pressure.

The current chapter intends to combine the promising concept of graded material properties with the more recent advances in auxetic materials, to develop a methodology which may be used to yield an optimal additively manufactured fracture fixation plate-scaffold assembly. Although some of the results are relevant for any fracture fixation of a long bone, the chapter focuses particularly on critical fractures to be reconstructed using an additively manufactured tissue regeneration scaffold. Thus, this study makes use of the scaffold optimisation method presented in chapter 3. The aim here is to propose a methodology to minimise the stress shielding seen with normal plates while keeping the construct within desired stability limits and avoiding the fracture of any part.

The chapter begins with the results of an auxetic plate that has no stiffness grading, which is used to determine the strut thickness that will be used at the middle of the plate in the following sections where the plate geometry considered is both auxetic and offering stiffness grading. The strut thickness is expected to influence the stress distribution because it modifies the porosity of the plate and therefore its rigidity. The first of these following sections presents the effect of the end plate strut thickness as well as the scaffold effective elastic modulus on the interfragmentary strain. The next section is structured in the same way as this latter one but the response variable under analysis is the

maximum von mises stress for the bone and the plate. The last results section presents first a structure-property relationship for the objective function, the minimum von mises stress in the bone, in a similar fashion as for the other sections but then this is used together with the constrained space in order to find the optimal end plate strut thickness and scaffold elastic modulus.

5.2   Materials and Methods

5.2.1   Plate-scaffold optimization strategy

The optimisation routine described here makes use of the optimal tissue regeneration scaffold geometry that can be achieved using the methodology described in chapter 3. The fixation plate is then optimised to work in combination with the scaffold. Similar to the work in chapter 3, here a graphical design selection framework was used, but this time there are two optimisation variables rather than one. The graded auxetic plate design was made to be controlled with only two variables, the minimum and maximum strut thickness, as explained in the paragraph below. The objective function to be maximized is the minimum stress experienced by the bone, which is equivalent to minimising the stress shielding. The design variables to be optimised were the end strut thickness of a plate with graded auxetic porosity and the volume fraction of a titanium Lidinoid scaffold. The end strut thickness was chosen as it was observed to have the most significant effect on the maximum and minimum bone stresses out of the investigated variables, while the volume fraction of the scaffold was chosen given that the Lidinoid lattice type was shown to perform best at all volume fractions of a fixed unit cell size (see chapter 3), so the only other variable to vary was the volume fraction. The volume fraction here refers to the fraction of solid material within the enclosed volume of the scaffolds outer dimensions.

As illustrated in Figure 5-1, the first step was to select a scaffold type with optimal TPMS geometry using the methodology described in section 3.2.1 as well as suitable limits, as explained in section 3.2.1. This was followed by defining the limits of the linearly graded auxetic plate as explained in section 5.2.3. After this, as explained thoroughly in section 5.2.4, two finite element models were developed corresponding to the initial and final time points of the healing process. This was followed by applying yield strength and Inter-fragmentary strain constraints as described in sections 5.2.6 and 5.2.7 respectively. Applying these constraints provides the viable solution space 'window' for the plate design. After this, the stress shielding was quantified in section 5.2.8, followed by fitting mathematical surfaces to the data in section 5.2.9 and finally section 5.2.10 explains how an experimental demonstration was carried out.
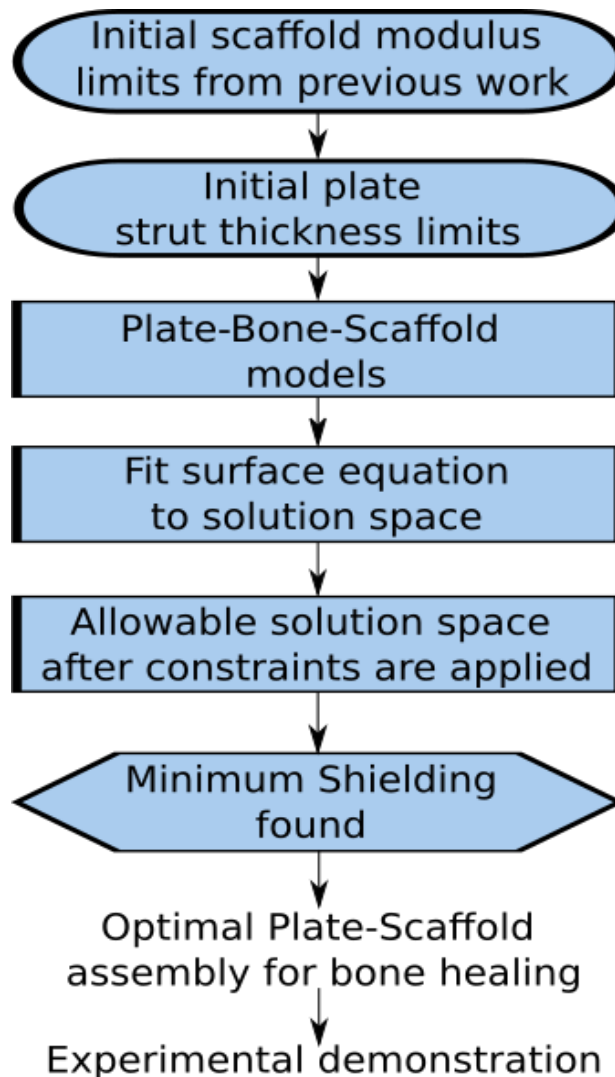
Figure 5-1: Schematic showing the overall optimisation procedure.

5.2.2   Scaffold Stiffness

chapter 3 dealt with presenting a novel scaffold optimisation routine as well as using this routine to find an optimal scaffold with TPMS geometry. The optimisation process involved a cell growth solution space consisting of a range of volume fractions for different TPMS unit cell types. The Lidinoid unit cell type was shown to achieve the highest cell growth rate for a range of volume fractions between 0.2 and 0.9.

Moreover, a recent study that includes in-vivo experiments with sheep bones and a finite element analysis, showed that titanium scaffolds with an effective Young's modulus of 0.84 GPa (compliant) and 2.88 GPa (stiff) yield beneficial healing conditions [158]. More so with the more compliant scaffold. 0.84 GPa for titanium is equivalent to a Lidinoid scaffold with a volume fraction of 22% while 2.88 GPa is equivalent to a titanium Lidinoid scaffold of 27%. As can be seen in section 3.3, this range of Lidinoid scaffolds have a suitable pore size for in vivo cell growth (see chapter 3). Therefore, titanium Lidinoid scaffolds were used and the volume fraction values were varied between the limits shown above.
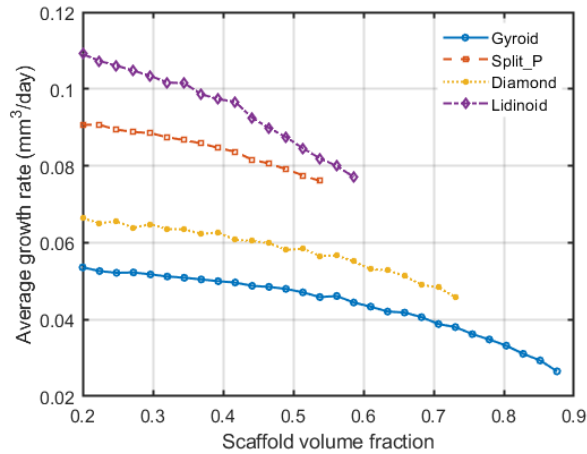
Figure 5-2: Average cell growth rate vs the volume fractions of the different scaffold types.

TPMS scaffold:
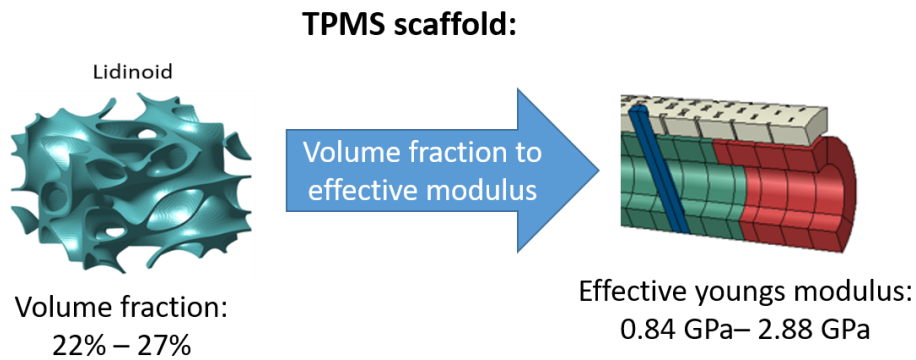
Figure 5-3: Figure illustrating that in the FEM model the scaffold is represented by a solid hollow cylinder of the effective Young´s modulus of the scaffold. The effective Young's modulus was found using the method presented by Maskery et al. [111] the model described in section 3.2.4.
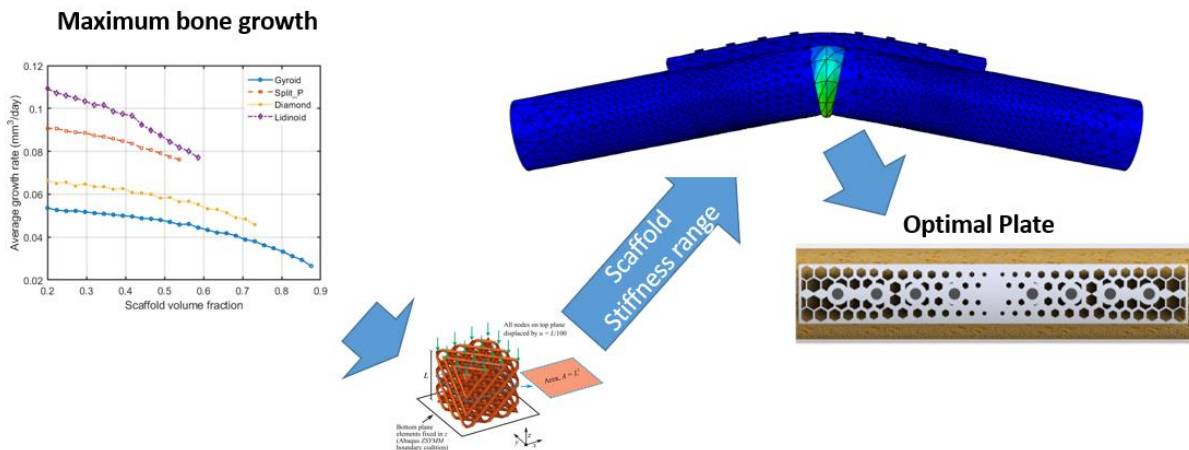
Figure 5-4: Overall process of applying scaffold stiffness range to the Finite Element Analysis as one of the two design variables to be optimised.

5.2.3   Graded auxetic implant design and materials

As shown in *Figure 5-5* the auxetic structure chosen was the re-entrant honeycomb structure with a negative Poisson ratio (NPR) [90]. This geometry consists of a series of struts as can be seen in *Figure 5-5*. The design presented proposes varying the thickness of these struts gradually along the plate length as it is hypothesized that this gradual change in porosity will help minimise stress shielding,

based on the findings of Ganesh et al. [87]. More specifically, the strut thickness at any given column of pores (where a column of pores refers to a series of pores placed along the thickness of the implant) is defined by the linear equation below (equation 3.9), where t_{end} corresponds to the strut thickness at the end of the plate and t_{mid} to the strut thickness at the centre of the plate. t_{end} is the second variable to be optimised along with the scaffold volume fraction. n_{col} is the number of pore columns along the length of the plate and i_{col} refers to any given column as shown in *Figure 5-5*.

The minimum and maximum values for the strut thickness were set to 0.5 mm and 2.1 mm respectively. The lower limit was based on recommendations from the manufacturer of a selective laser melting (SLM) machine from Renishaw and the upper limit was chosen because if the pores between the struts get any smaller than this they would be negligible according to the Finite Element model which showed less than 2% change in the maximum stress when increasing the strut thickness beyond this value. t_{mid} was kept constant throughout the study and its value was selected by comparing several strut thicknesses of non-graded plates as shown in the results chapter. Previous studies have already shown that a stiffer middle section leads to a more adequate stress distribution thus lowering stress shielding [87].

The number of holes, hole spacing, plate thickness and plate width used were those of a nine-hole LCP plate with six inter-locking bicortical screws [159], but only the holes and screws actually used were modelled such as was done in a recent study [158]. Moreover, the length was reduced slightly to account for the filleted ends of the plate. The plate and screw dimensions are shown in Table 1. The material used for the plate was titanium and for the screws stainless steel [158].

$$t = t_{end} + \left(\frac{t_{middle}-t_{end}}{n_{col}}\right) * i\_col \qquad (3.9)$$
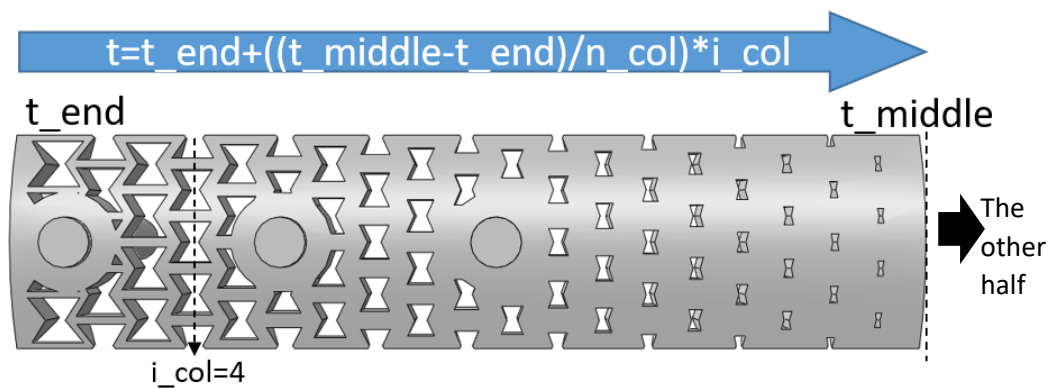
Figure 5-5: Half model of the plate with porous auxetic re-entrant structure as well as screws. The blue arrow and the equation inside it show the relationship through which the strut thickness is varied along the plate.

Table 7: Dimensions of plate, holes and screws

Part	Dimension reference	Dimension value (mm)
Plate	Thickness	4.2
Plate	Width	13.5
Plate	Length	145
Screw/Hole	Diameter	4.5
Screw/Hole	Spacing	17
Screw	Length	26

Part	Material specification	Young's modulus (MPa)
Plate	Isotropic and homogeneous	104000
Screws	Isotropic and homogeneous	200000

There are two models in this study, one corresponding to the time point immediately after fracture fixation and one corresponding to the time point after all healing has occurred but the plate is still fixed with the screws. The models are relatively simplified however and the only difference between these two models is that one has a constant Young's modulus value throughout the whole length of the bone and the other has a lower value for the material in the section where the scaffold is attached. This was done because it is assumed that when a bone has healed it has a constant Youngs modulus along the entire length, whilst before it has healed; it is assumed that the fracture region, where a scaffold is placed, will have a lower Youngs modulus than the bone. Otherwise, both models consist of the same parts: a bone, a plate, and screws. The dimensions of these parts are also the same for both models. The next few sections describe the design of each part in more detail as well as the assembly, meshing, boundary conditions and contacts.

5.2.4   Bone model

The bone chosen for analysis was the human tibia with a fracture at the diaphysis, which represents the most common anatomical site for a segmental bone defect to occur [154]. However, the methodology is intended to work with any long bone and hence the bone was simply modelled as a tube. The dimensions of this simplified tibia model are the same that were used in a similar recent study [105] and are shown in Table 1. As explained previously, the two models used only differ in that one has a section in the middle with the Young's modulus of a previously optimised scaffold and in the other this section has healed. For the main study, the Young's modulus of the bone was chosen to be the same as in a recent similar study focusing on tibial segmental fractures [158]. The scaffold was made of titanium and thus had the same Young's modulus as the plate, the effective Young's modulus of the scaffold however was not fixed but rather a design variable as explained in section 5.2.2. The materials are shown in Table 10. As it can be observed, all materials were assumed to be isotropic, linearly elastic and homogeneous. In reality, cortical bone is transversely isotropic, viscoelastic and it isn't perfectly homogeneous, but these assumptions are common practice when modelling bone within computational models, as explained in section 2.9.
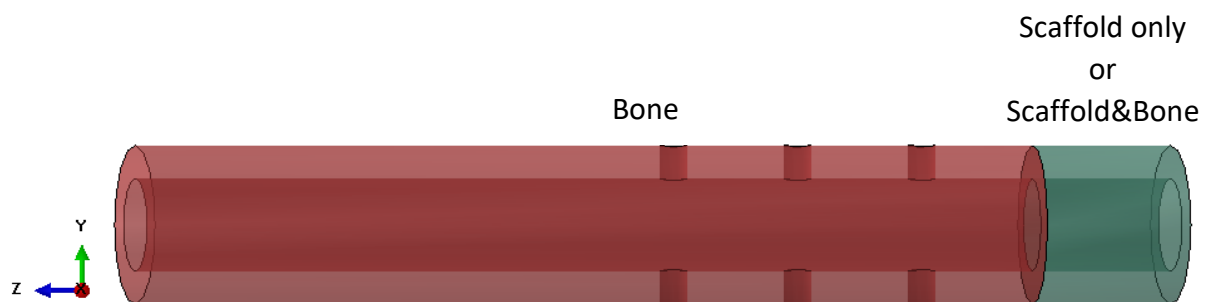
Figure 5-6: Bone and scaffold with transparency and colour coding. The axis on the left serves as a reference for when any of these axes are mentioned throughout the chapter.

Table 9: Dimensions of bone and scaffold

Part	Dimension reference	Dimension value (mm)
Bone	Inner Diameter	15
Bone	Outer Diameter	25
Bone	Length	300
Scaffold and fracture	Inner Diameter	15
Scaffold and fracture	Outer Diameter	25
Scaffold and fracture	Length	40

Table 10: Materials of bone and scaffold

Part	Material specification	Young's modulus (MPa)
Bone average adult	Isotropic and homogeneous	17000
Bone of children with OI	Isotropic and homogeneous	5400
Scaffold	Isotropic and homogeneous	104000

5.2.5   Contacts, Boundary conditions and Mesh

In the Locked Compression Plate being considered, there are usually three main contacts. The contact between the plate and the bone, the contact between the plate and the screws and the contact between the screws and the bone. The screw-plate and screw-bone contacts were modelled as tied, meaning the interface was assumed to be fully bonded. The screw-bone contact has been the subject of much debate but a recent study showed that it is suitable to use a tied contact as changing it affected the construct stiffness by less than 1% [160]. As in the study by Mehboob et al. [105], a gap of 1 mm between the bone and the plate was left. Hence, there was no contact between these parts.

The boundary conditions used were similar to those used by Pobloth et al. [158]. One end of the bone was fixed and the other end was loaded with the maximum axial load used by Mehboob et al. [105], 2100 N, equivalent to three times an average body weight. Moreover, as in the study by Pobloth et al. [158], an anterior-posterior bending moment of 0.025 BWm was used. Here "BW" stands for body weight and the bending moment was applied at the longitudinal end of the bone on the central axis, about the x axis shown on Figure 5-6. To reduce the computation time, a quarter model was used by employing two planes of symmetry. However, for simplicity this was referred to as "half model" throughout the rest of the thesis. To achieve this half model, suitable boundary conditions were required to provide symmetry on the x and z axes. A validation of these half model assumptions was carried out and the results are presented in Figure 5-7 . The validation consisted of ensuring that the stress distribution of the half model along the length of the bone was accurate relative to the full model. The difference between the stress values was found to be lower than 5 % and therefore acceptable.

Full Model:

(view cut)
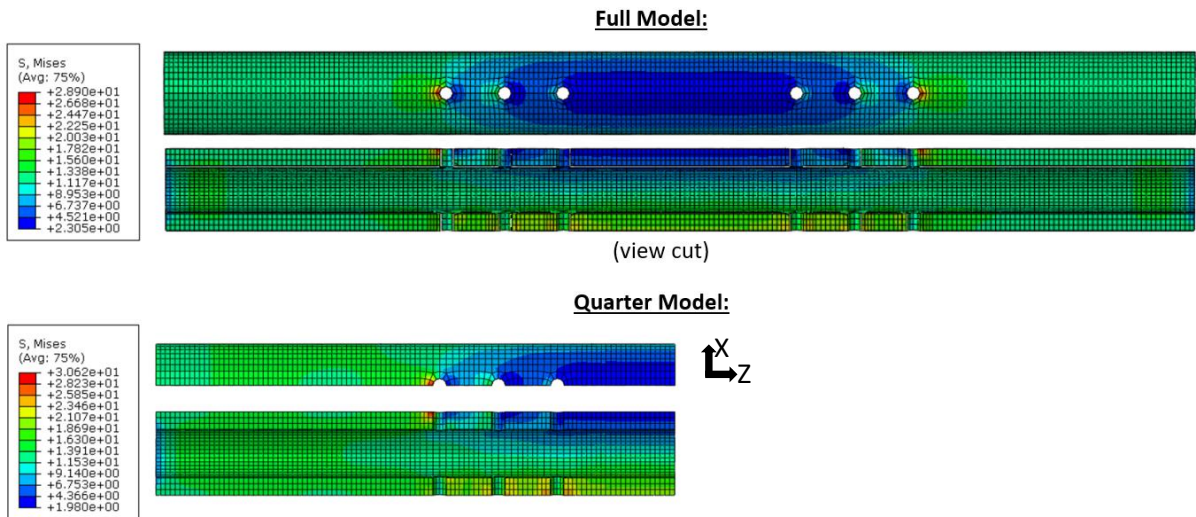
Quarter Model:

Figure 5-7: Validation of the quarter model via a contour plot. Please note that in the rest of the text "half model" refers to what is shown here as the Quarter Model.
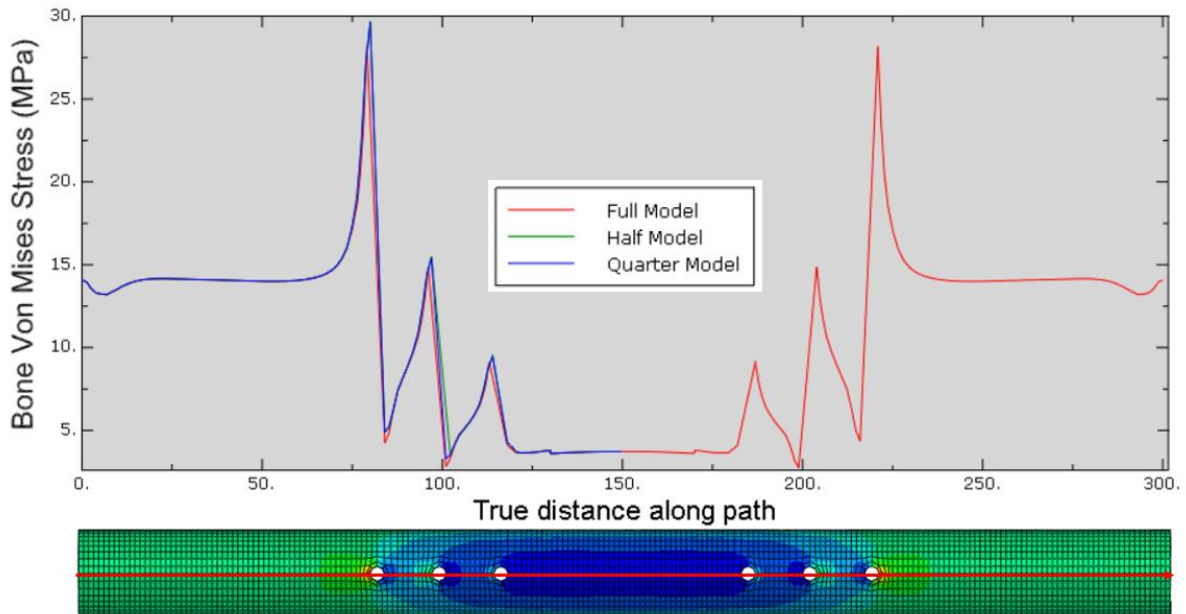
Figure 5-8: Validation of the quarter model via a path along the top axial line of the bone. Please note that in the rest of the text "half model" refers to what is shown here as the quarter model.

A mesh convergence study was carried out to minimise numerical errors associated with the finite element method. This was done by looking at the change in construct stiffness with varying the number of elements. The convergence results are presented in the results chapter.

5.2.6   Von Mises constraint

As used by Arnone et al. [161], the Von Mises criterion can help ensure that a material does not fail under stress. The criterion makes use of a factor of safety (F_s) which should be lower or equal to the yield strength (σ_y) of the material divided by the maximum Von Mises stress (σ_{vm_max}) in the material [161]. In this work the factor of safety has been fixed at a value of 2 [162]. This criterion was applied to all materials: bone, scaffold (titanium), plate (titanium) and screws (stainless steel). Table 11 shows the yield strength values for all these materials as well as the corresponding maximum allowed Von Mises stress value.

$$\sigma_{vm\_max} \leq \frac{\sigma_y}{F_s} \tag{4.0}$$

Table 11: Yield strength and maximum Von Mises stress of different materials

Part	Material	σ_y (Mpa)	σ_{vm_max} (Mpa)
Bone	Cortical bone	59.00 [163]	29.50
Scaffold	Titanium	797.2 [164]	398.6
Plate	Titanium	797.2 [164]	398.6
Screws	Stainless steel	360.0 [165]	180

5.2.7 Inter-fragmentary strain constraint

A plate with a very low stiffness would lead to a minimal fracture risk for the bone and a minimal stress shielding. However, it would cause large Inter-fragmentary strains (IFS) in the defect region and that would cause no healing to take place [83]. This means that there exists a region of IFS outside which no acceptable healing occurs. Much work has been carried out to define this range for typical fractures of lengths lower than 3 mm [83][72]. Claes [83] highlights the importance of IFS for fracture healing as well as how new concepts have been developed to achieve sufficient IFS in order to improve bone healing underneath the fracture fixation plate [83]. He also reviews thoroughly the work that has been done to define a range of IFS which leads to appropriate healing for fractures smaller than 3 mm [83].

When it comes to large critical fractures longer than 2 cm, the situation is very different and there haven't been many studies in that area. Nevertheless, there was a very thorough recent study that determined such an IFS range [158]. It used sheep bones as well as a Finite Element analysis to demonstrate that IFS between 0.23% and 0.6% lead to acceptable endochondral and intra-membranous ossification. Therefore, the solution space was constrained by these minimum and maximum values of IFS.

5.2.8 Stress shielding

The objective function to be maximized in this study was the minimum Von Mises stress in a fractured bone fixed with a plate (σ_{vm_bmax}) when loaded in tension as shown in equation 4.1. This ensures that the minimum stress in the bone is closest to that experienced by a regular unbroken bone. As supported by a previous study of Ganesh et al. [87], the decrease in the stress experienced by a bone directly under the fracture fixation plate is a suitable representation of the amount of stress shielding taking place. Stress shielding is an essential criterion in the design of fracture fixation implants because a shielded bone will lack the necessary stimulus to keep the bone remodelling rate at an appropriate level, where bone remodelling refers to the removal and subsequent formation of bone [166]. This in turn leads to bone resorption and weakening at the shielded regions and hence why a more uniform bone stress distribution is desired. By maximising the minimum von Mises stress, the amount of stress shielding is effectively being minimized and causing a more uniform stress distribution.

$$f(x) = \text{Maximize min} \left(\sigma_{vm\_bmax} \right) \tag{4.1}$$

5.2.9 Data Fitting

Once the results of the modelling were collected, the data was fitted in order to create a set of polynomial equations. Such a mathematical representation compliments the visual approach as it allows for a continuous solution space which in turn can be used to get a more exact optimal solution and expand the solution space beyond the limits considered. The result of the data fitting process is a polynomial equation that describes a mathematical surface. This process was carried out for all the response variables considered and the resulting equations are given in the results section.

5.2.10 Experimental demonstration

The experimental demonstration had two main objectives. Firstly, to demonstrate the potential of the proposed optimisation and secondly to provide complementary proof for the idea that the stress shielding experienced by a bone fixed with a fracture plate is not caused solely by the difference in material properties. With this objective in mind, three cases were considered for comparison; (a) the optimised porous stiffness graded plate, (b) a regular non-graded plate and (c), a bone cylinder with no plate attached. The experiment consisted of subjecting each of these parts to axial compression to simulate the most critical loading of human tibia and measure the strain in the sample at key locations. As predicted by an FE analysis, the axial strain in the bone near the region below the plate with the optimised implant was expected to be significantly closer to the stress seen at this region in the case of a bone cylinder with no plate than without an optimised implant.

The three parts had the same overall dimensions described in 5.2.4, apart from the length of the bone which was reduced to 100 mm for ease of handling (a validation was performed to ensure this would not affect the results significantly). Due to the second objective of this experimental section, it was decided to assume the same Young's modulus for the implant and the bone. Given that the contacts were all 'tied', it was justified to print every assembly as a single part. Further validation of this was carried out.

The parts were printed using Selective Laser Sintering (SLS) from EOS polyamide PA2200, which is based on Nylon 12. The manufacturing platform was an EOS P100 machine. The laser power used was 21W, the scan speed was set at 2500 mm/s, the power bed temperature was 172.5 °C, the powder deposition thickness was 0.1 mm and the powder size varied between 0.05 and 0.01 mm. The parts were both subjected to a compressive test using an Instron 5966 universal testing machine equipped with a 50 kN load cell. Markers were used to measure the strain at 20 regions in the bone. The axial strain distribution was then compared for the different cases.

Figure 5-9: Printed parts showing the black markers at which the strain was calculated. A) is the case with a conventional plate, b) is the case with a stiffness graded auxetic plate and b) shows the case with just a bone.

5.3   Results

5.3.1   Auxetic plate with ungraded stiffness

For choosing the strut thickness at the plate middle section, the whole auxetic plate was initially given a constant strut thickness which was optimised by fixing the Lidinoid TPMS scaffold volume fraction at a value of 22%. Chapter 3 has shown how the equations derived from the work of Maskery et al. [110] correlate the volume fraction of TPMS scaffolds to its effective stiffness. This volume fraction was chosen as it yields a scaffold with 880 MPa effective stiffness which is an optimal scaffold stiffness for maximising bone mineralization according to a previous study that looked at in vivo tissue formation in sheep [158]. The auxetic plate strut thickness was then optimised using the strut thickness limits described in the methodology and 10 equally spaced strut thickness values within the range of these limits. The curves in Figure 5-10 show an overview of how decreasing the strut thickness increases the minimum Von Mises stress in the bone, and therefore decreases the stress shielding under the plate.

The result of this was that the plate with a constant auxetic strut thickness of 1167 µm (or 1.167 mm) was found to be the optimal before applying stiffness grading. Although lower values of the strut thickness clearly show a lower stress shielding in the figure below, in these plates the inter-fragmentary strain was too high in the case of the unhealed bone as shown in appendix E.
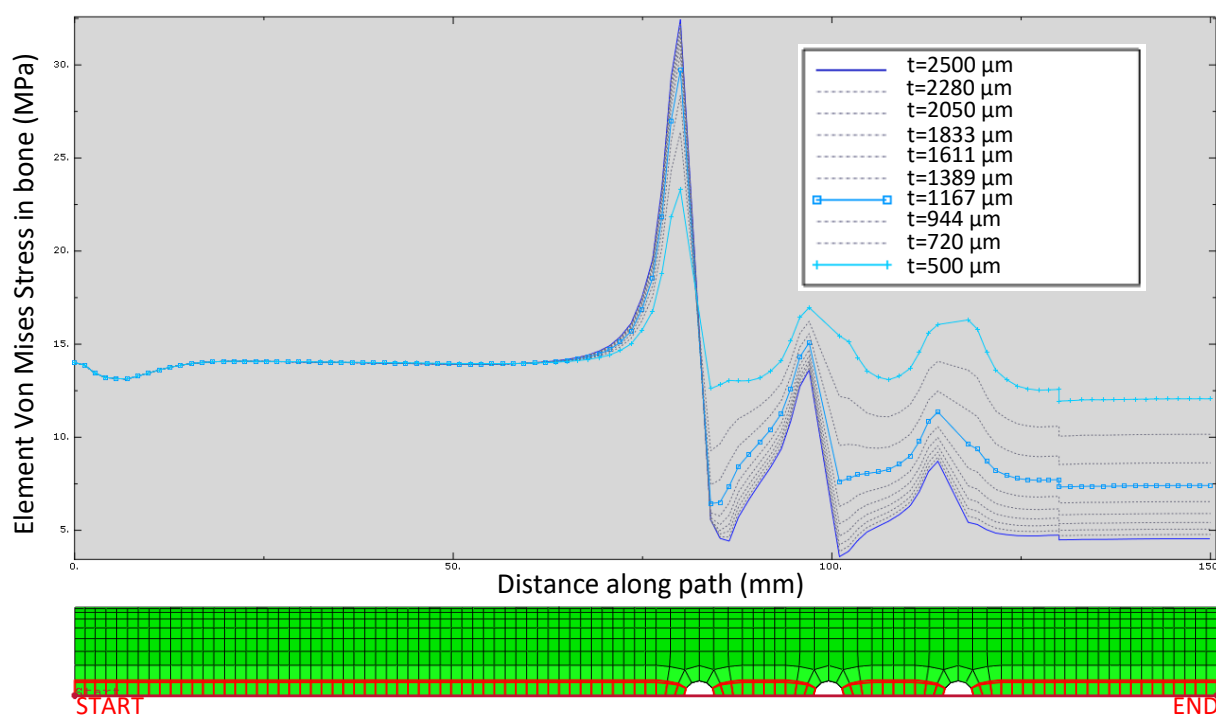
Figure 5-10: Element Von Mises stress in the bone for a plate auxetic strut thickness varying from 2500 µm to 500 µm. The red markings on the mesh below the graph illustrate the path used to compute the element Von Mises stress values. This data is all for the case of when the bone has healed.

As can be seen in Figure 5-10, the maximum Von Mises stress is observed at the outer screw. This phenomenon has been observed before [167] by simulating a plate-bone construct as was done here and comparing various cases with different number of screws as shown in Figure 5-11 and showing that the maximum stress is always observed at the outer screws. As also demonstrated before [167], the biggest contributor to this stress peaks is the contact pressure (CPRESS), as shown in Figure 5-12. Although the frictional shear stresses (CSHEAR) are shown to be relatively low in magnitude, the resultant shear stress component in the plane parallel to the screw axis (S13) is shown to be relatively

high at the outer screws. To further demonstrate these two aspects in this thesis, a similar Finite Element simulation study has been carried out in Appendix I.
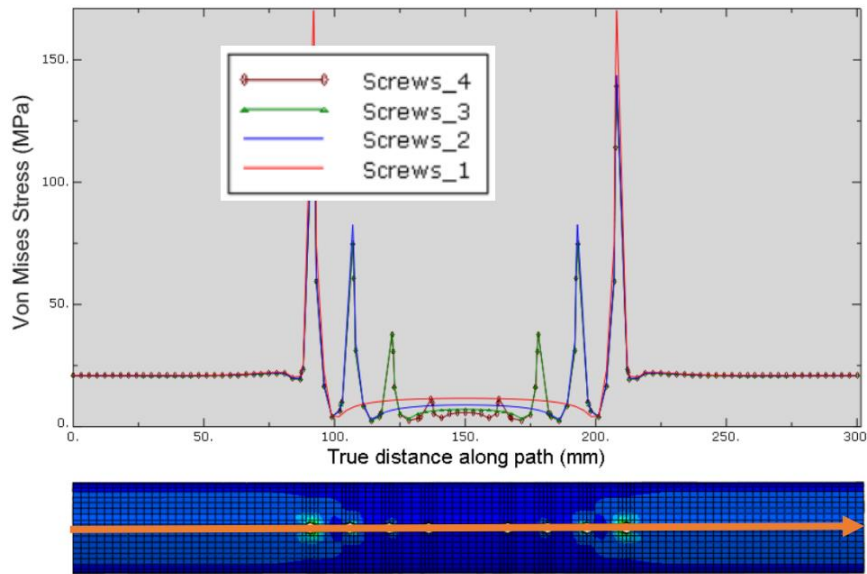
Figure 5-11: The maximum Von Mises stress is always observed at the outer screw regardless of what number of screws is used. Figure taken from [167]. It should be noted that the number of screws shown on the legend refers to the number of screws on either half of the construct. Therefore the total number of screws present is actually twice the number shown.
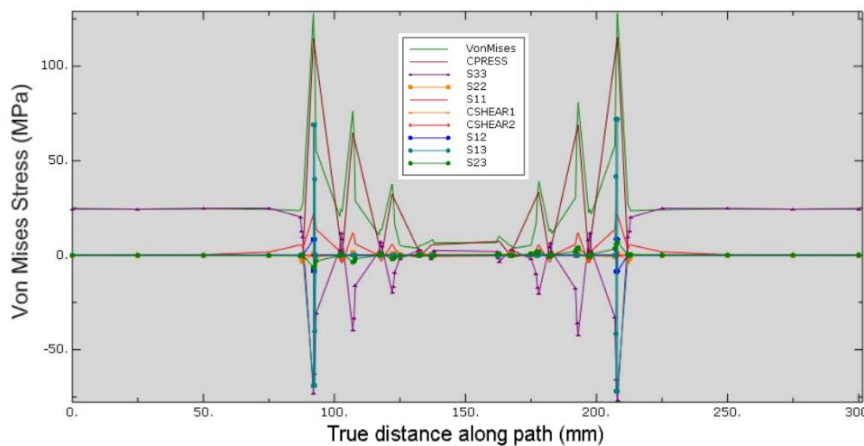
Figure 5-12: The main contributor to the Von Mises stress peak is the contact pressure. Figure taken from [167]. The variables of interest here are CPRESS, CSHEAR and S12. CPRESS refers to the contact pressure, CSHEAR refers to the frictional shear stress and S13 refers to the shear stress component in the plane parallel to the screw axis.

5.3.2   Inter-fragmentary strain constraint

The Inter-fragmentary strain (IFS) only plays a role before healing has completed, most significantly at the very beginning of the healing phase when no bone has grown on the scaffold. The figure below shows the location of the scaffold within the half model assembly. Given that all the considered materials are assumed to be linearly elastic, a higher strain shown in the plate is indicative of a higher stress, which is expected here due to the higher Young's modulus of the plate.

E, E33
(Avg: 75%)
+1.142e-03
−2.373e-05
−1.189e-03
−2.355e-03
−3.520e-03
−4.686e-03
−5.851e-03
−7.016e-03
−8.182e-03
−9.347e-03
−1.051e-02
−1.168e-02
−1.284e-02
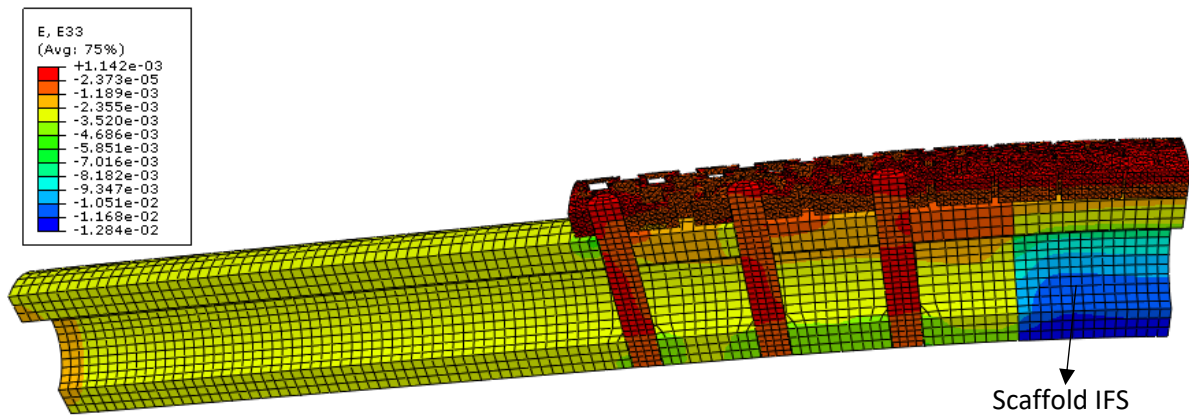
Scaffold IFS

Figure 5-13: Element strain in the axial direction, which for the scaffold results in the interfragmentary strain (IFS). The values for all the elements of the scaffold are averaged to find the average IFS plotted in the figure below.

In Figure 5-14 is the average inter-fragmentary strain seen in the scaffold with all the combinations of end plate strut thickness and scaffold effective Young's modulus. This also shows the predetermined IFS limits as flat surfaces, meaning that only data points that are within these two surfaces represent allowable combinations of the design variables. The resulting constrained solution space, eliminating all the data points outside these bounds, is shown in Figure 5-14b.

It can be observed that the scaffold elastic modulus has a much more significant effect on the average IFS than the end plate strut thickness. Moreover, a higher scaffold elastic modulus leads to a lower average IFS as can be expected.

(a)

(b)
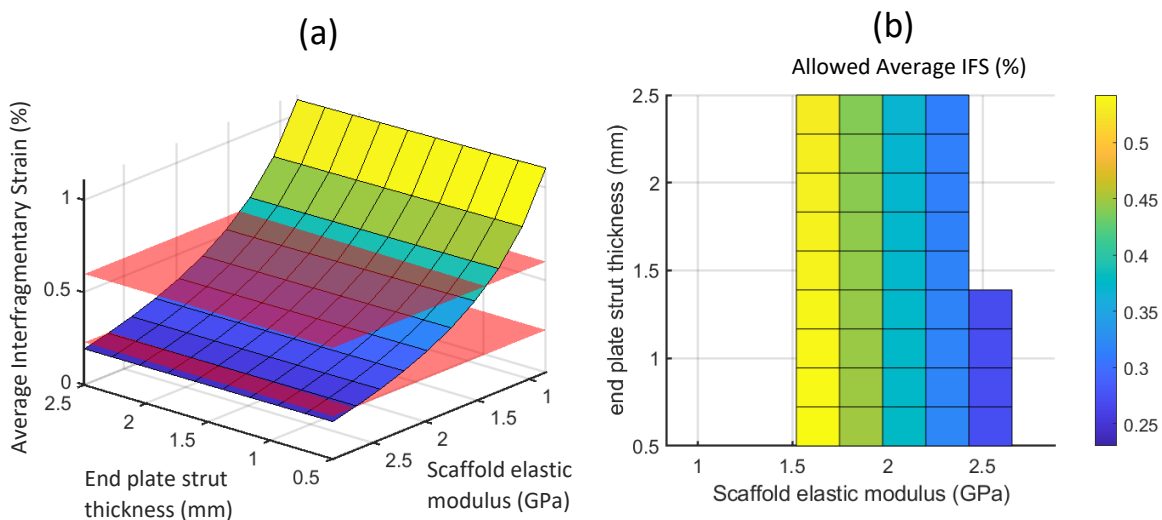
Figure 5-14: Average interfragmentary strain variation with changes in end plate strut thickness and scaffold elastic modulus. (a) surface plot shown in isometric view and (b) surface plot as seen with the z axis coming out of the page.

5.3.3   Von Mises Stress constraint

The following sub-sections focus on the maximum Von Mises stress values of different parts of the bone-plate-scaffold assembly for all the computed combinations of the scaffold elastic modulus and the end plate strut thickness. The Von Mises stress was used as a constraint in order to predict the yielding of the materials and therefore avoid such failure. This is often used in computational modelling of fracture fixation plates as was demonstrated in section 2.9.

5.3.4 Scaffold

In the graph below, it can be observed that the scaffold maximum Von Mises stress increases as the scaffold modulus increases. As the end plate strut thickness increases, with low values of the scaffold modulus, the maximum Von Mises stress in the scaffold also increases, but as the scaffold gets stiffer, the effect of the end plate strut thickness appears to diminish. The maximum scaffold maximum Von Mises stress was so far below the maximum allowed value in all combinations that it was decided not to show the threshold plane here.
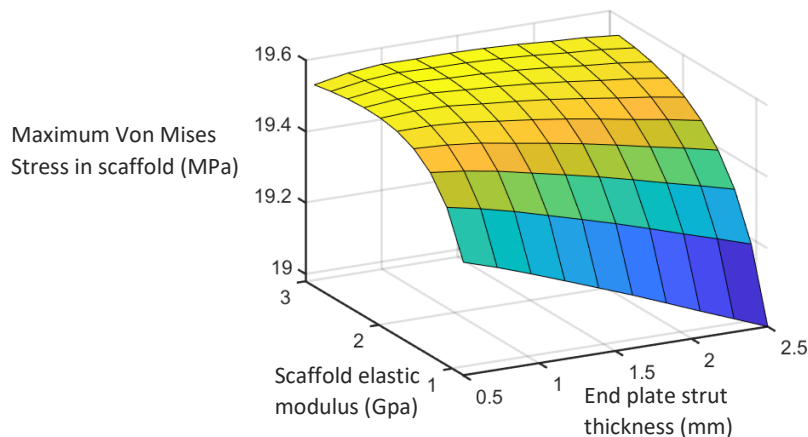
Figure 5-15: Maximum Von Mises stress in the scaffold for all possible combinations of the design variables.

5.3.5 Bone

Figure 5-16 below shows the location of the maximum Von Mises stress seen in the bone. It is found at the screw hole furthest away from the fracture and is caused by the contact pressure between the bone and the screw.
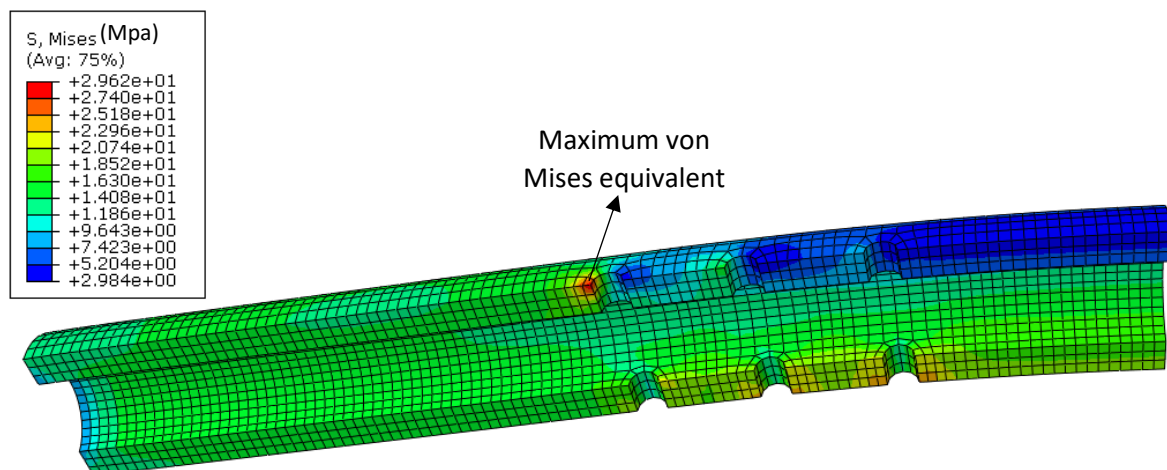
Figure 5-16: Maximum Von Mises stress location in the bone for the 'healed' case of a 1.5 GPa scaffold and an end plate strut thickness of 0.5 mm.

For the case of the bone, the end plate strut thickness has the most significant effect, with an increase in strut thickness causing an increase in the maximum Von Mises stress of the bone overall. However, at around 2 mm strut thickness, the maximum Von Mises stress starts decreasing. The maximum stress in the bone after healing occurs at the region in contact with the screw at the edge of the plate due to the contact pressure which is higher when there is a lower porosity in the edge of the plate.

Therefore, the trend seen here is expected because as the end plate strut thickness increases, the end plate porosity decreases, making the contact pressure higher and thus the observed increase in the maximum Von Mises stress. The maximum Von Mises stress is expected to be higher when the scaffold stiffness is lower, as observed in Figure 5-17a. Figure 5-17b shows the allowable solution space. Note that for every combination the higher value of the maximum Von Mises stress between the two healing scenarios was chosen. Also note that the combinations that did not satisfy the IFS constraint were also dismissed in figure Figure 5-17b.
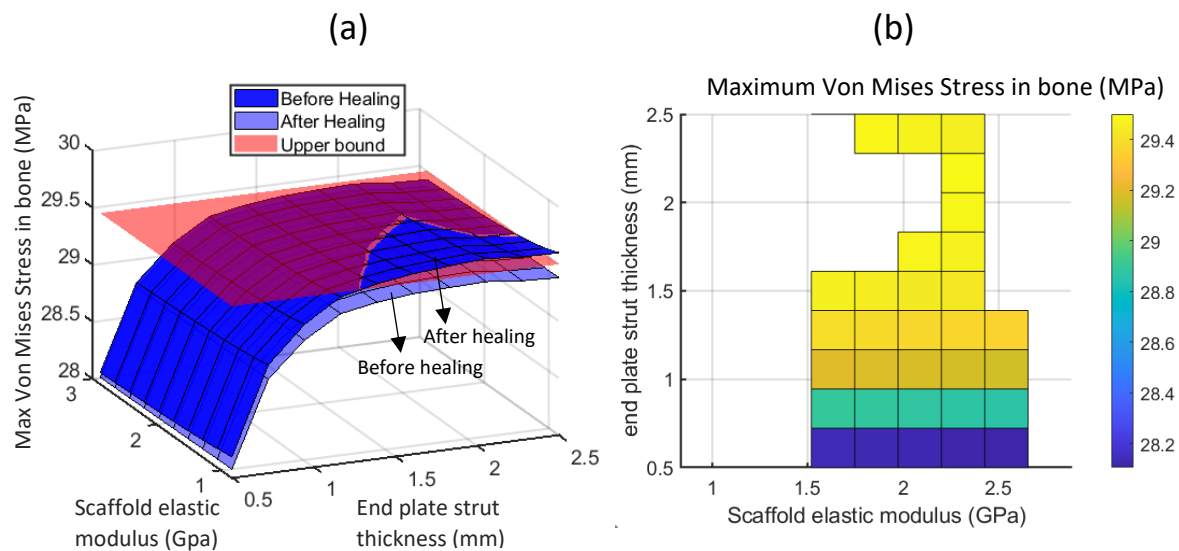
Figure 5-17: (a) Maximum Von Mises stress in the bone for all combinations, showing also the maximum allowable value as a flat surface and (b) a colour plot showing only the combinations that yield a maximum Von Mises stress lower than the threshold value.

5.3.6   Plate

The figure below shows the location of the maximum Von Mises stress found in the plate. Note that this maximum stress is also found at the region close to the screw furthest away from the fracture.
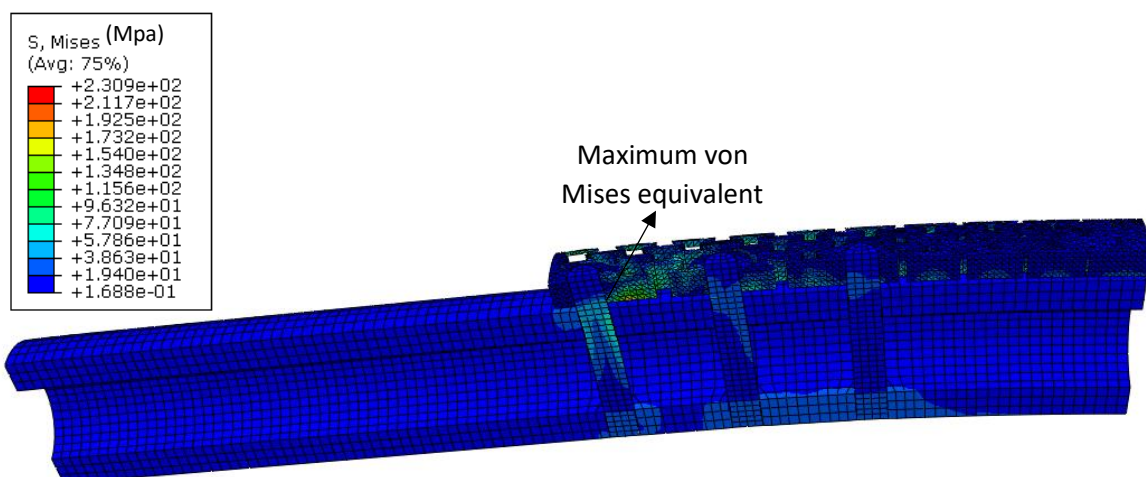
Figure 5-18: Maximum Von Mises stress location in the plate for the healed combination of a 1.5 GPa scaffold and an end plate strut thickness of 0.5 mm.

The graph in Figure 5-19 of the maximum stress in the plate is highly non-linear. When the scaffold stiffness is low and the end plate strut thickness is high, the maximum stress in the plate is higher,

which is reasonable given that this is the case that leads to the highest moment on the plate since there is more weight at the ends of the plate and the least stiffness in the scaffold. Overall, the maximum stress observed in the plate is much higher before healing than after healing. This was expected as a lower effective Young's modulus in the fracture region causes a higher deformation and therefore a higher maximum Von Mises stress. The unconstrained maximum stress slightly exceeds the maximum allowed value but in the constrained solution space that is not the case. Ultimately the only constraints that affect the solution space are the IFS and the maximum Von Mises stress in the bone. It should be noted that this may not be the case with a different bone diameter or fracture geometry.
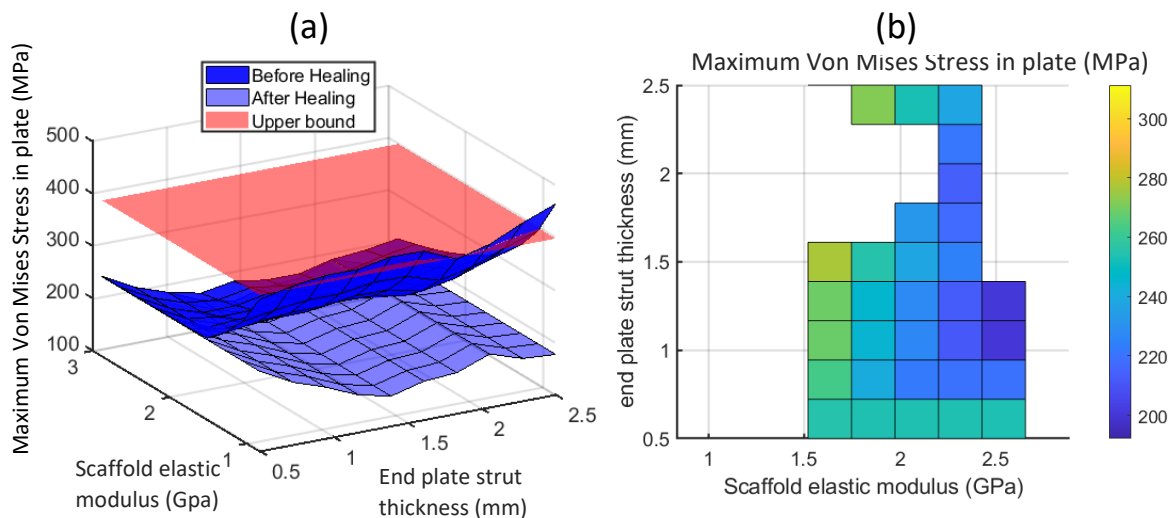
Figure 5-19: (a) Maximum Von Mises stress in the plate for all combinations, showing also the maximum allowable value as a flat surface and (b) a colour plot showing only the combinations that yield a maximum Von Mises stress lower than the threshold value.

5.3.7 Minimizing stress shielding

As can be observed in Figure 5-20, the highest value in the distribution of the minimum Von Mises stress in the bone, having applied the constraints, was found at an end plate strut thickness of 0.5 mm and a scaffold effective modulus of 1.5 GPa which corresponds to a volume fraction of 24% for the titanium Lidinoid scaffold. This therefore corresponds to the combination of design variables that yields the minimum stress shielding. The minimum Von Mises stress in the bone before and after healing was consistent within +/- 2% for most combinations of design variables apart from the region of low-end plate strut thickness and low scaffold elastic modulus, as can be observed from Figure 5-20. In the case before healing, this region of the solution space yields much lower values of minimum Von Mises stress. A discussion of the results is presented in chapter 6.
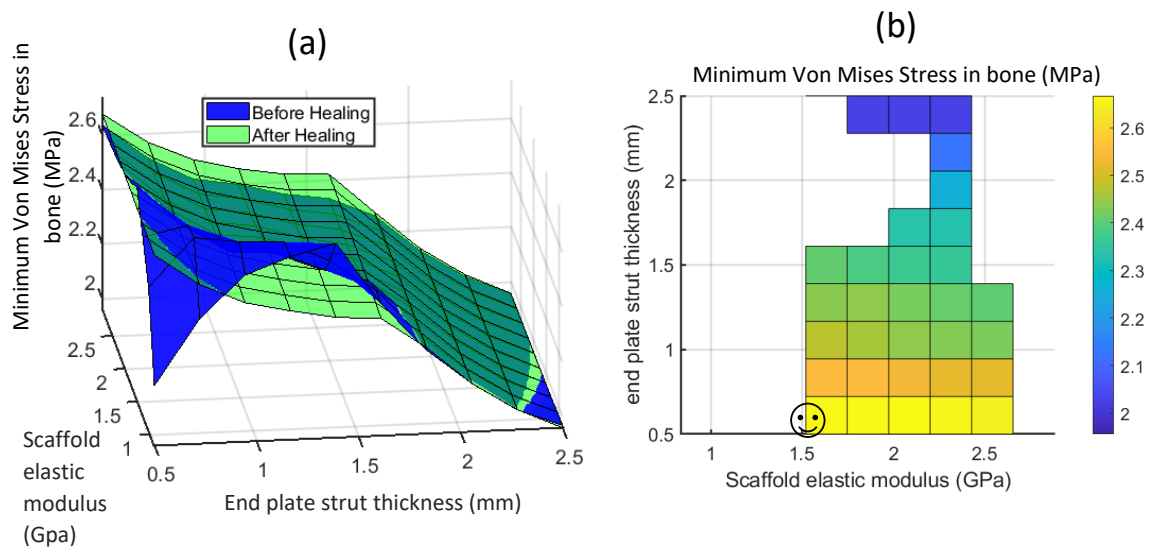
Figure 5-20: (a) Minimum Von Mises stress in the bone for all combinations and (b) a colour plot showing only the combinations that are allowed according to the previously presented constraints.

Figure 5-21 shows the improvement brought about by the optimised plate and scaffold by showing how the minimum absolute stress in the distribution (found on the right side of the figure for all curves) increases with the optimal plate-scaffold combination (the blue line). Moreover, it shows that the maximum stress is also lower for the optimal combination when compared to a standard plate-scaffold combination (purple line).
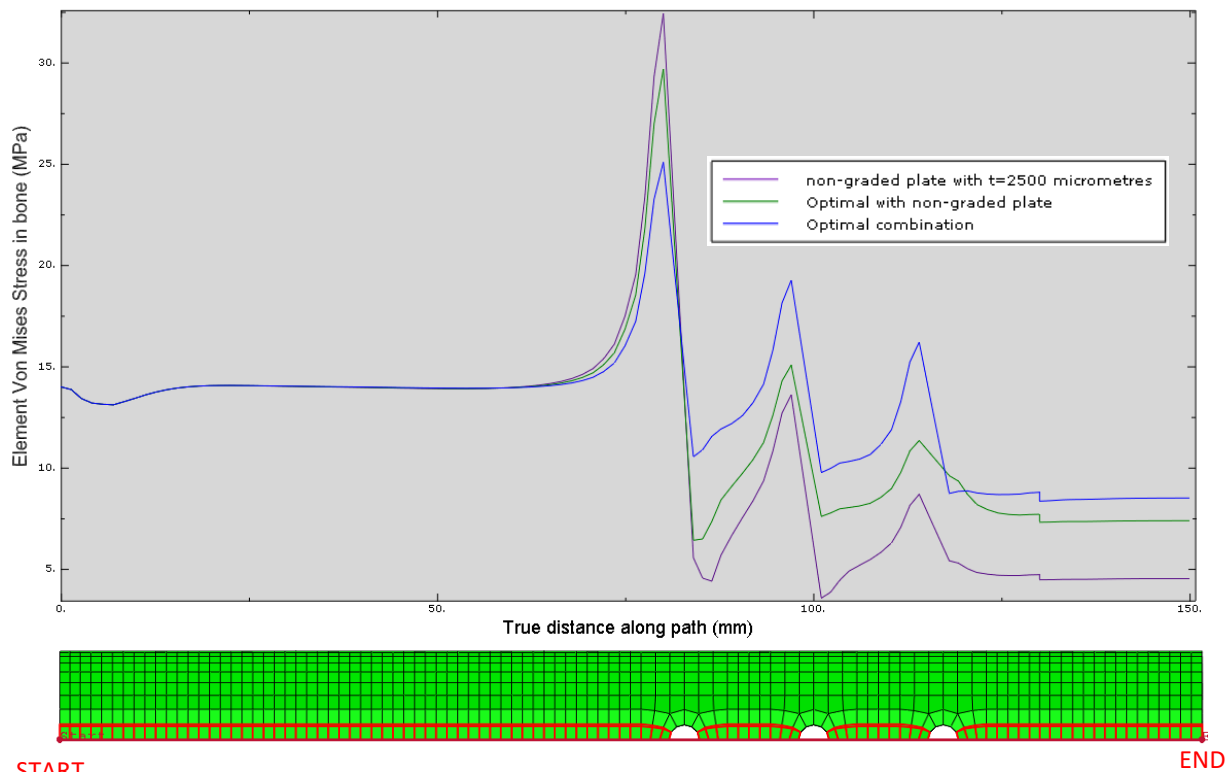
Figure 5-21: Element Von Mises stress in the bone for the optimal combination of auxetic plate strut thickness and scaffold volume fraction being compared to the worst combination of parameters and the optimal non-graded plate. The red markings on the mesh below the graph illustrate the path used to compute the element Von Mises stress values. This data is all for the case of when the bone has healed.

116

5.3.8 Data Fitting

The equations below represent the multivariate polynomial regression equations that result from the third order approximation data fitting process. Since all r squared and adjusted r squared values were above 0.9 and all scatter index values were below 5%, it was deemed that the fits describe the data well enough for this case, even though they may not be generalised to other problems. In the equations below, "d" stands for end plate strut thickness and "E" is the scaffold elastic modulus.

$$\text{IFS}(t, y) = a_1 + a_2 d + a_3 E + a_4 dE + a_5 E^2$$

$$\text{MaxS\_bone\_NotHealed}(d, E) = a_1 + a_2 d + a_3 E + a_4 dE + a_5 E^2 + a_6 d^3 + a_7 d^2 * E + a_8 dE^2$$

$$\text{MaxS\_bone\_Healed}(d, E) = a_1 + a_2 d + a_3 E + a_4 dE + a_5 E^2 + a_6 d^3 + a_7 d^2 * E + a_8 dE^2$$

$$\text{MaxS\_plate\_NotHealed}(d, E) = a_1 + a_2 d + a_3 E + a_4 d^2 + a_5 dE + a_6 E^2$$

$$\text{MaxS\_plate\_Healed}(d, E) = a_1 + a_2 d + a_3 E + a_4 d^2 + a_5 dE + a_6 E^2$$

$$\text{MinS\_bone}(d, E) = a_1 + a_2 d + a_3 E + a_4 d^2 + a_5 dE + a_6 E^2$$

Table 12: Coefficients for the curve fitting equations shown above

Equation:	a1	a2	a3	a4	a5	a6	a7	a8
IFS	0.397	-0.004	-0.261	0.002	0.098			
MaxS_bone_NotHealed	29.516	0.054	-0.040	-0.276	-0.009	0.013	0.151	0.001
MaxS_bone_Healed	29.436	0.042	-0.005	-0.274	0.001	0.001	0.152	0.000
MaxS_ plate_NotHealed	230.961	6.186	-61.436	11.234	-7.797	26.906		
MaxS_plate_Healed	170.382	-15.709	-0.038	19.182	0.028	0.001		
MinS_bone_Healed	2.360	-0.196	0.003	-0.039	-0.014	-0.014		

Figure 5-22 shows the IFS values for the original set of models, as well as a much finer surface based on the fitted polynomial equation. The same type of figure was computed for every one of the equations, see appendix D. It should be noted that this is only shown here for clarification, the equations define a continuous solution space which can effectively be discretized into an infinite number of points. These equations would allow for extending the design method beyond the ranges of auxetic plate strut thickness and scaffold effective Young's modulus examined here.
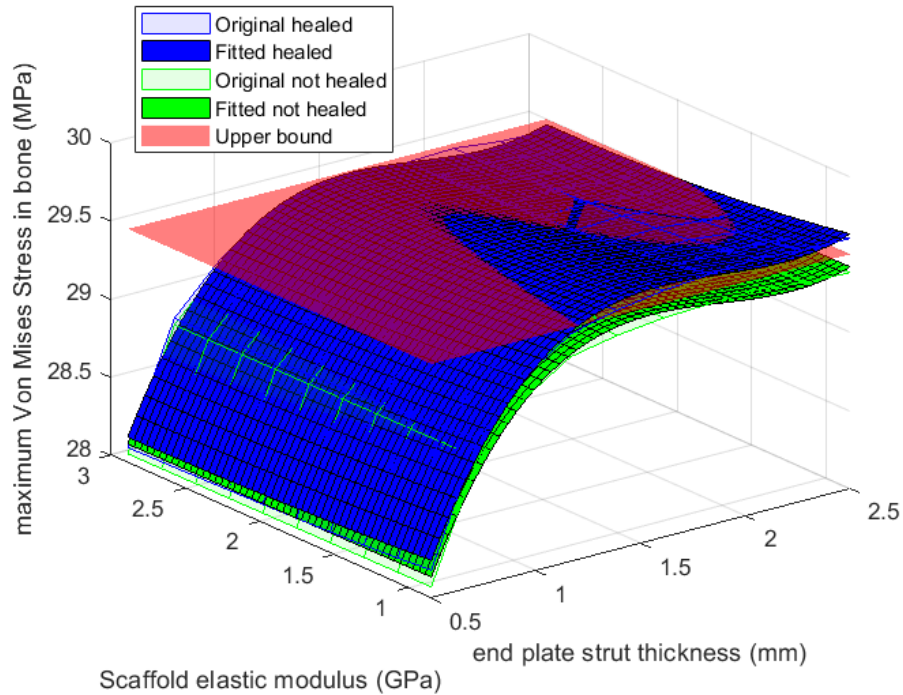
Figure 5-22: Surface fit for the maximum Von Mises stress in the bone for both the healed and not healed cases.

5.3.9   Experimental demonstration

As explained in the methods section, a compression experiment was done with the samples shown in Figure 5-23 to demonstrate the potential of the proposed optimisation and to provide complementary proof for the idea that the stress shielding experienced by a bone fixed with a fracture plate is not caused solely by the difference in material properties.

and as explained in the methods section, the three different cases were subjected to a compression experiment where a camera was used to record the deformation of the black markers drawn on the samples as shown in Figure 5-23. The load was 2100 N, the same as that used on the FEA analysis. The results in Figure 5-25 show how the axial strain distribution when having a graded auxetic plate is closer to that of the bone without plate than the solid plate case. This data collection method is not able to capture the strain accurately, so the mean strain was used at the region of interest which is the longitudinal region next to the plate. This average axial strain in the auxetic case was significantly closer to the bone case than that of the solid case was. The experimental results were compared to the model through the mean axial strain in the solid case and the error was of only 2.13%. Mean axial strain is a good indicator because assuming the material is linearly elastic, strain is proportional to stress and throughout the study the stress has used as the indicator for stress shielding. A figure of the Modelling results for this analysis can be found in Appendix E.

Figure 5-23: Samples used for the compression tests. Sample with a conventional plate (top), sample with an auxetic graded plate (middle), and sample without a plate (bottom).
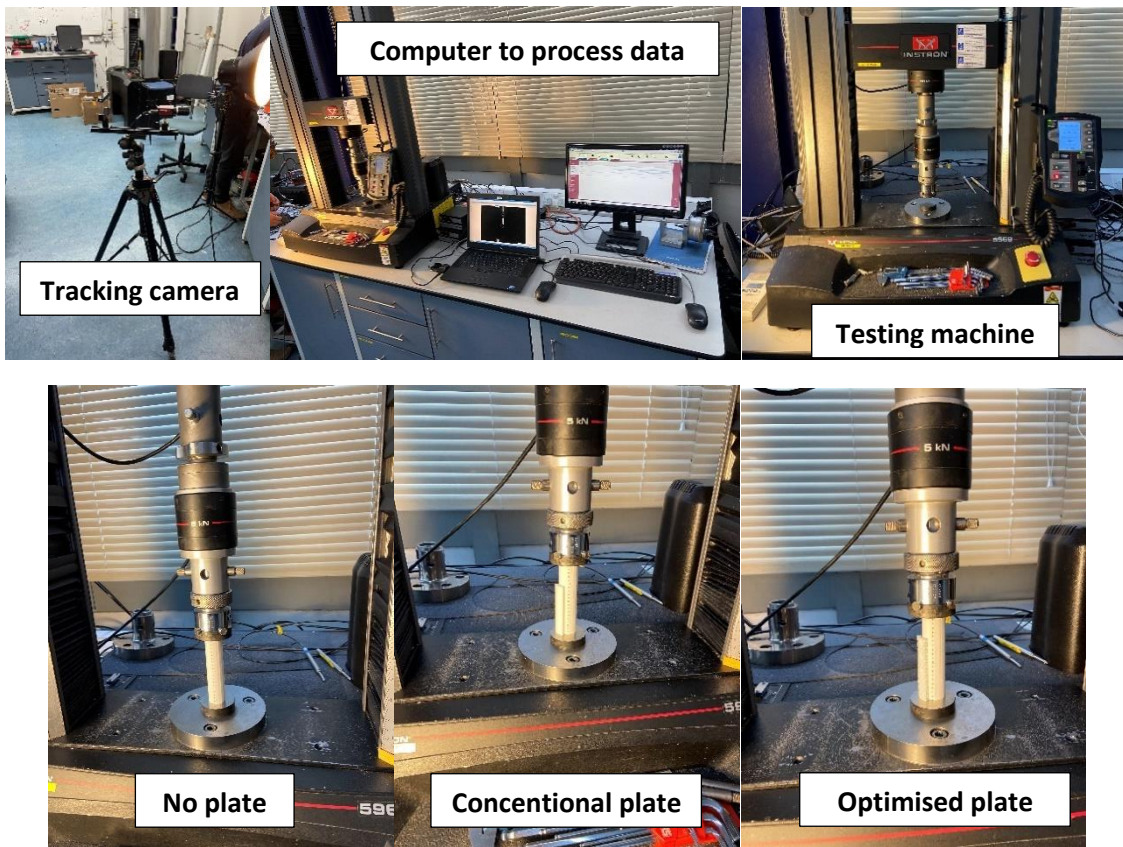
Figure 5-24: Setup for the compression strain tests. The top left image shows the camera used to track the displacement of the markers, the top middle figures show the machine for performing the test as well as the computers to process the data and the bottom images show the three different samples at the start of the compression test.
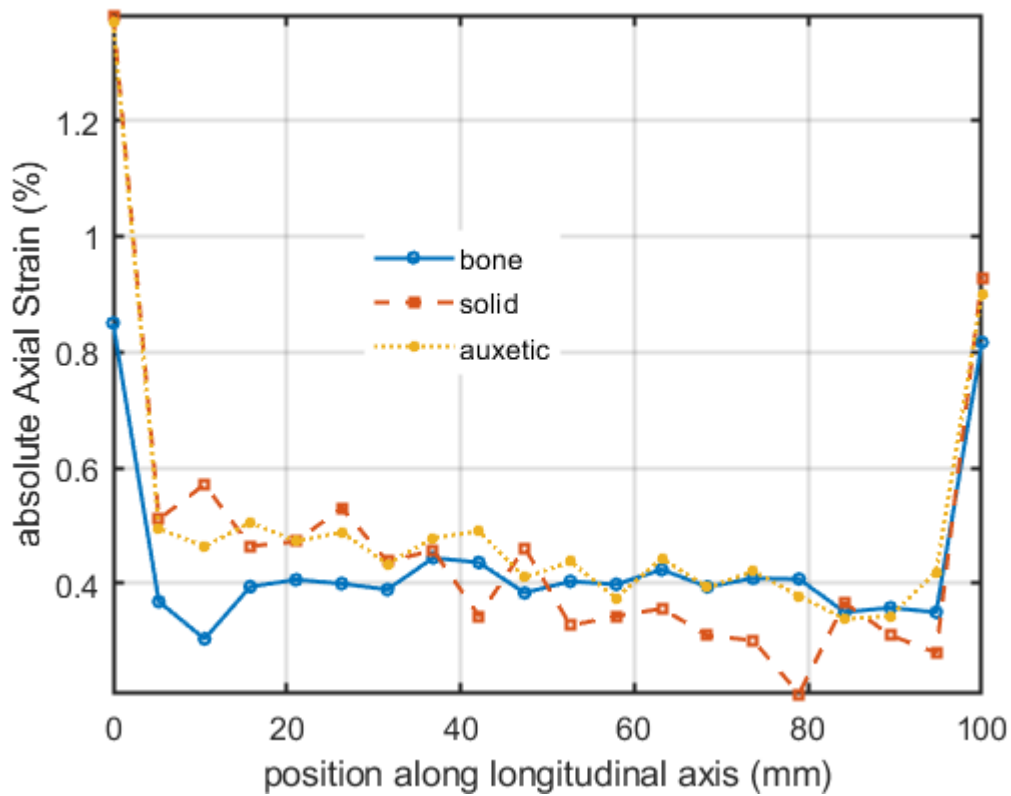
Figure 5-25: Graph of absolute axial strain distribution along the line of markers drawn on the simplified printed bone. This distribution corresponds to 360 seconds after the compression test had begun. n=1 for each value.
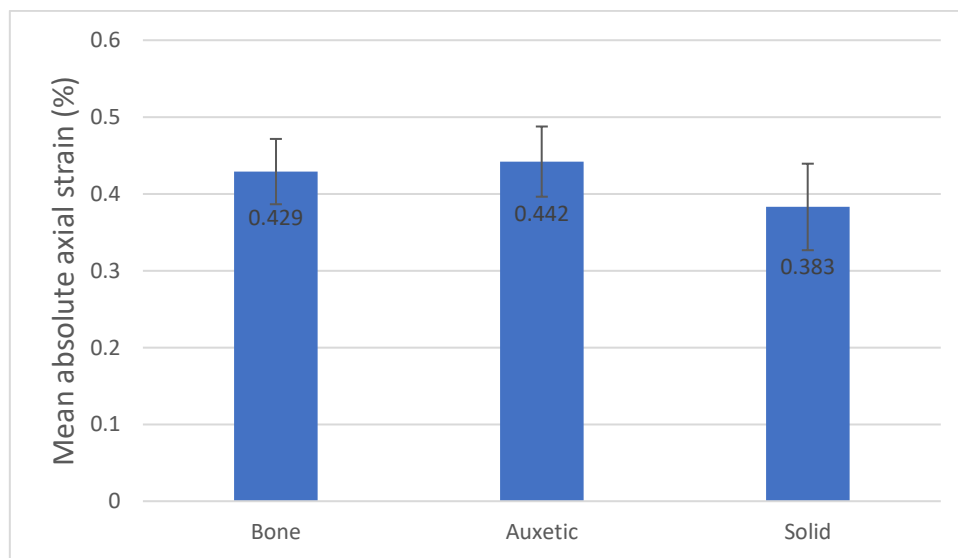
Figure 5-26: Bar plot comparison of average axial strain between bone case, solid case and auxetic case. Error bars were calculated using the standard deviation. n=2100 .

Figure 5-27 shows that the axial strain measured for the auxetic case is significantly lower than that measured for the solid conventional case. Assuming linear elasticity of the material, the axial strain is proportional to the axial stress and therefore this shows that an auxetic plate leads to a lower axial stress as predicted with the FEA simulations.
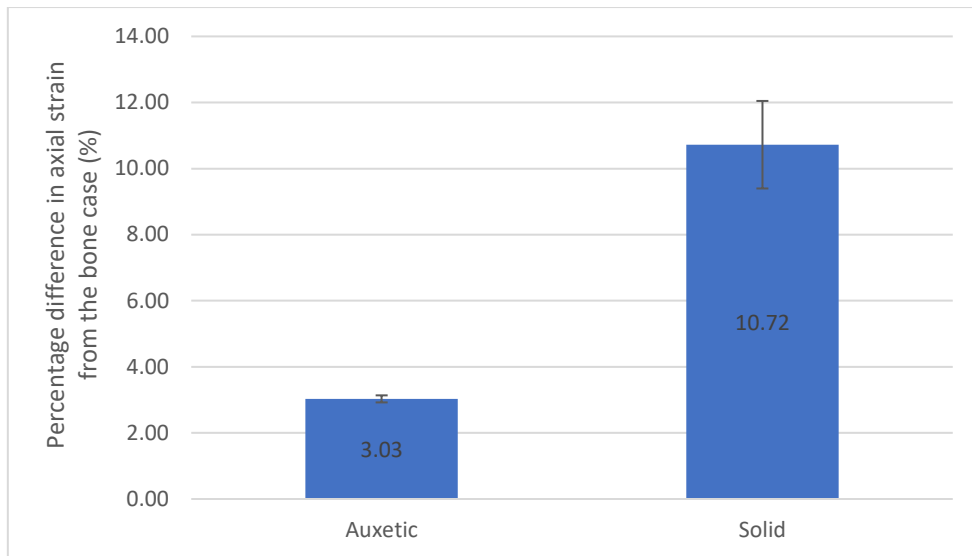
Figure 5-27: Percentage difference from absolute axial strain of auxetic or solid with respect to the axial strain of the bone case. n=2100 and the error bars represent the standard deviation.

The graph below also shows how the solid case is stiffest, followed by the Auxetic case and then the bone case, as expected. The fitted equations to each curve are shown below. The gradients of the curves on the right are the elastic moduli. These are respectively 2067 N/mm², 2349 N/mm² and 2210 N/mm². As can be noted from the bar chart in Figure 5-29, the difference between the stiffness of the auxetic case and the bone case is half that between the solid case and the bone case.

$$\sigma_{bone} = 2067 * \varepsilon_{bone} - 0.2357$$

$$\sigma_{solid} = 2349 * \varepsilon_{solid} - 0.09685$$

$$\sigma_{auxetic} = 2210 * \varepsilon_{auxetic} - 0.1428$$
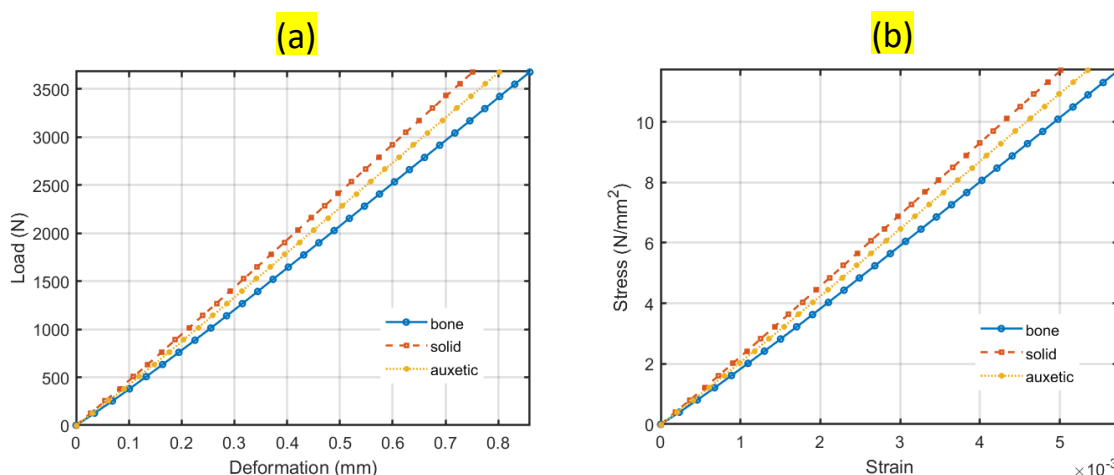
Figure 5-28: (a) graph of the load-displacement throughout the time points. (b) graph with load converted to stress and deformation to strain. The surface area used was the cross-sectional area of the printed bone and the length used was 150 mm. Notice that there were actually 360 time points but for better readability markers were placed in this graph 10 points apart. n=1 for all values.
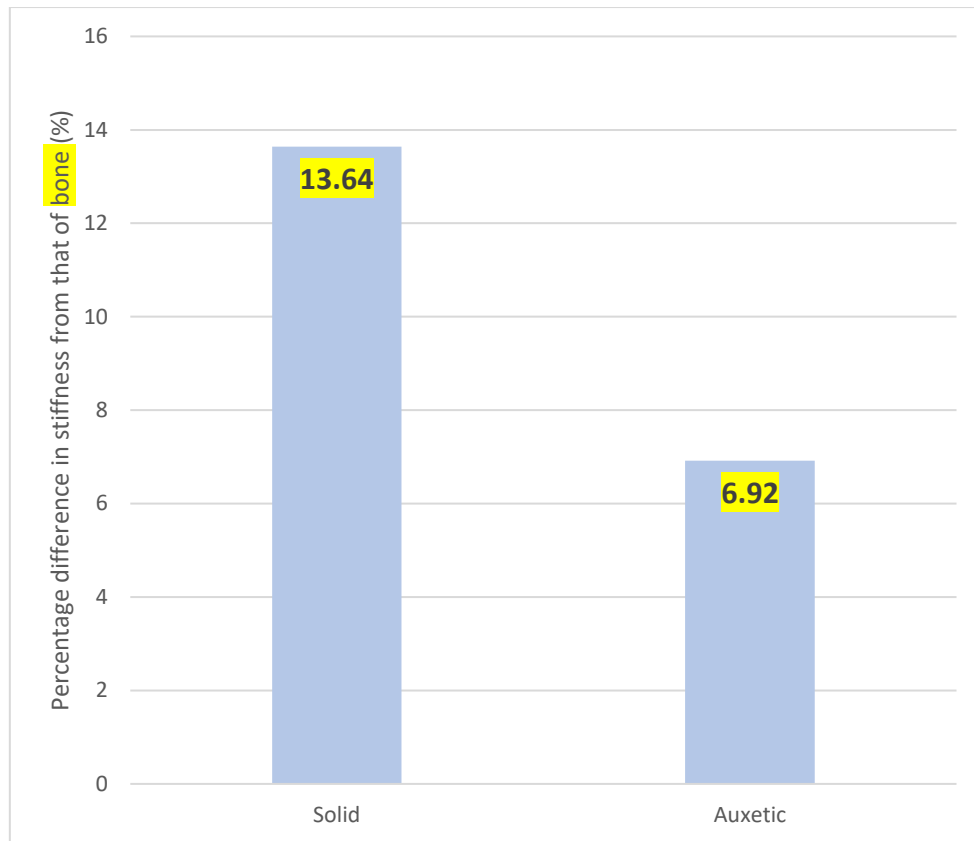
Figure 5-29: Percentage difference from the stiffness for solid or auxetic case to that of the bone case. Notice that the stiffness was measured using the above equations.

A test increasing the load until there was significant plastic deformation or failure of the part was also carried out. The purpose of this was twofold: 1) to show that a conventional plate causes an earlier failure of the assembly and 2) that the plastically deformed shape of an assembly with the auxetic graded optimised plate is closer to that without a plate. It can be seen in Figure 5-30 that the solid case supported the highest compressive load before beginning to plastically deform, followed by the auxetic case and then the bone. Then during plastic deformation, it can be seen that the compressive load decreases more rapidly for the solid case, and this is because the screw at the end failed. This behaviour was as expected given that the maximum stress of the construct is seen at the screw-bone interface of the outer screw. Figure 5-31 illustrates the difference in the deformation of the different samples, it shows quite clearly that the deformed shape of the optimised sample is much closer to the deformed shape of the sample without a plate than that with a conventional plate. The constructs can be observed to have undergone a degree of buckling, which is defined as the sudden change in shape of a structural component under load [168]. The Finite Element models do not illustrate any buckling because buckling is a non-linear dynamic phenomenon and the models presented are linear and static. For a discussion of the results see chapter 6.
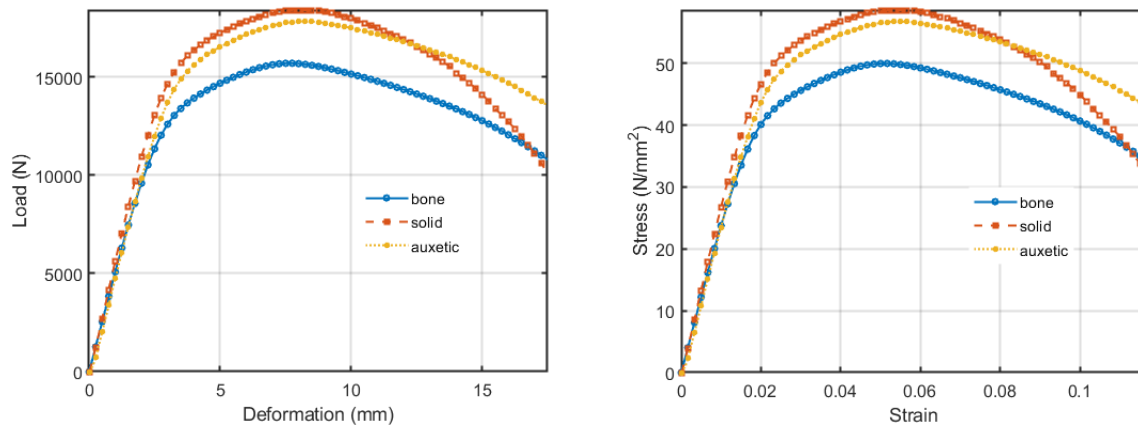
Figure 5-30: On the left is a graph of the load-displacement throughout the time points of the second test going into plastic deformation. On the right is a graph with load converted to stress and deformation to strain. The surface area used was the cross-sectional area of the printed bone and the length used was 150 mm. Notice that there were actually 2100 time points but for better readability markers were placed in this graph 30 points apart.
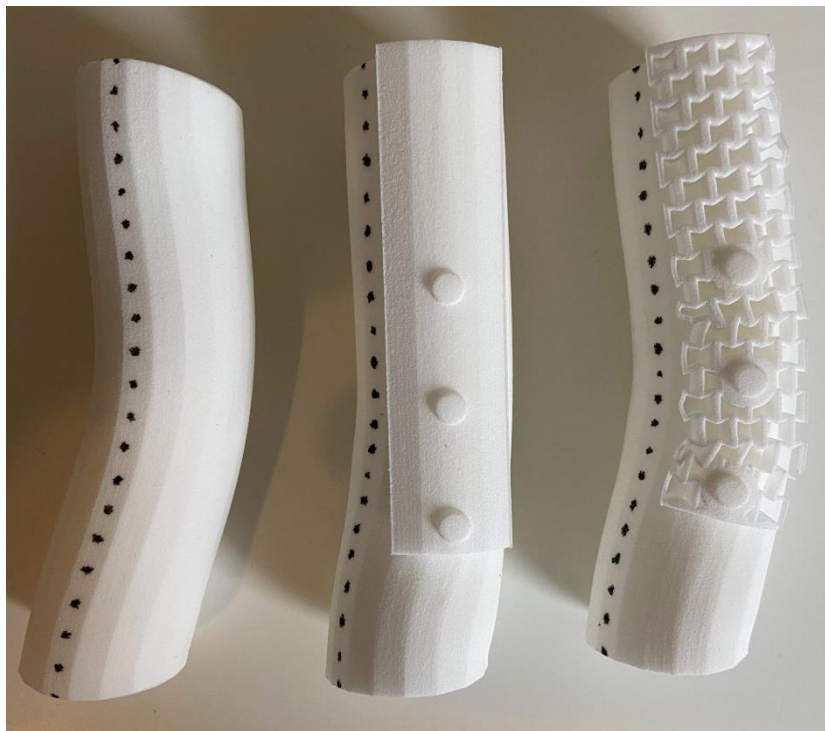
Figure 5-31: Deformed samples for the bone case (left), solid case (middle) and auxetic case (left)

5.4   Summary

For a discussion of the results see chapter 6, the text below simply summarizes the content presented in this chapter.

In this chapter, the problem of stress shielding with fracture fixation plates is first introduced, as well as the solutions that have been explored so far. It is then explained how the aim of the chapter is to combine the potential found in auxetic fracture plates with that of a graded stiffness plate; while also coupling this with 'tuning' the optimal TPMS scaffold type, based on the techniques developed in chapter 3.

Afterwards the materials and methods used were described. This section looked at expanding

The work presented in chapter 3 to include an optimal design for a fracture fixation plate, given that for long bone fractures these are needed to provide stability. To do this a Finite Element Model was developed for analysis of a fractured bone fixed with an auxetic graded plate, having also a scaffold at the fracture site to enhance healing. A python script was written to enable chosen input parameters to easily be tuned to carry out parametric investigations. The method to find the optimal design of the plate and the scaffold was similar to that developed for the scaffold design, but now the objective was to minimise the stress shielding while satisfying strength constraints for every part as well as a constraint for the allowable range of interfragmentary strain (IFS) at the fracture gap. The method, again, was developed in such a way that a medical designer can obtain a clear picture of how the possible combinations of design variables affect the performance metrics.

Next, the Von Mises stress distribution along the length of the bone in the case of a non-graded auxetic plate was described. This enabled the determination of a suitable strut thickness to be used at the middle of the plate, while the end plate strut thickness was set to be one of the design variables of the optimisation, as explained in the methods chapter. After this, the interfragmentary strain (IFS) constraint results were described using 3D contour plots of the element stress distribution as well as 2D contour plots of the parametric correlation of the design variables with the IFS.

Similar to the above, 2D contour plots were also used to visualize and describe the correlation between the design variables and the maximum von Mises Stress in the various parts. In this case however, limits were applied to the solution space to ensure the maximum Von Mises stress would be below a specified upper bound. Finally, the minimal Von Mises stress in the bone was plotted against the design variable, for the remaining possible combinations after having applied the constraints. The minimum of this plot was then found, leading me to the optimal combination of design variables: end plate strut thickness of 0.5 mm and scaffold modulus of 1.5 GPa.

Polynomial surface equations were fitted in order to propose more general relationships and extend the methodology beyond the specified bounds. Lastly, an experimental demonstration was performed to support the computational results, in which three different samples were subjected to compression testing. The sample with an auxetic graded plate led to stiffness and average longitudinal 'bone' strain values much closer to that of a 'bone' without a plate as well as a much more similar deformation shape.

Chapter 6: Discussion and conclusions

6.1   Outline

In this chapter the results presented in chapters 3 to 5 were discussed. Firstly, the results of chapter 3 which dealt with the cell growth model, were discussed by comparing these with previous work as well as by considering the meaning of these results. Next the results of the cell culture experiments were discussed with an emphasis on the objectives laid out for that part of the thesis, which relate to the manufacturing of scaffolds via stereolithography techniques and the quantification of cell growth results using TPMS scaffold geometries. Lastly there is a discussion of the plate-scaffold design selection results, which has a particular focus on the stress shielding problem and how the work carried out helps address this via a novel auxetic stiffness graded plate design.

6.2   Cell growth model

In chapter 4 a novel graphical design selection framework was proposed that can select the optimal scaffold type and volume fraction for a bone regeneration scaffold. The routine currently operates in a 2-variable solution space (the variables being scaffold type and volume fraction), which is sufficient to demonstrate this methodology. The design selection routine is especially useful for medical designers not versed in computational optimisation methods because it enables the designer to visualise the entire solution space graphically and thus understand the scaffold selection criteria clearly and their impact on the responses. The optimal design selection procedure showed that out of the six initially available scaffold types, the Lidinoid scaffold with a volume fraction of 0.49 performed best with a cell growth rate that was 110% higher than that of the worst performing scaffold which satisfied the constraints.

By accounting for the minimum pore size limit of the scaffolds, the proposed routine ensures that blood capillaries can grow throughout the porous network. As described in section 3.2.3, the proposed method to find the minimum pore size effectively calculates intersecting spheres throughout the entire porous network. The method presented here was adopted from that used by Kerschnitzki et al. [118] to measure the position of minerals within a porous network. Calculating the maximum pore size limit based on the diffusion of oxygen and nutrients from capillaries was also essential, as it ensured that the entire porous network could be filled with cells, thus allowing for a fair comparison between different TPMS scaffold types. This step includes the assumption that a capillary follows the medial path (or 'skeleton') shown in Figure 3-3. There are two potential issues with this assumption. First, it excludes the possibility of more than one capillary passing through a given pore [115] and second, the capillaries might not always follow the medial path. The first issue does not invalidate the results of this study because two capillaries would facilitate greater oxygen delivery. The second issue is more of a concern because if the capillary is too far from a scaffold wall, then the cells attached to that wall will not receive sufficient oxygen and die.

As explained in section 3.2.4, mechanical stimulation of the scaffold and surrounding tissue also affects the bone growth outcome [72], if there is too much strain, there will not be any growth, while small amounts of strain can be beneficial. The results of this study highlight the need for stiffness constraints, in the case of the Lidinoid cell type, these constraints reduced the allowable range of volume fractions by about 74%.

A micro-scale level set model was used to simulate the pre-osteoblast cell growth in TPMS scaffolds. The level set model has been validated with simpler geometries previously [37]. As explained in section 3.2.5, the implementation used here was different to that used in the original study [37], and although the method presented has been successfully validated (see Appendix A), It is recommended that anyone interested in implementing this model also looks at the original implementation [37]. The

difference between the implementation of Guyot et al. [37] and that presented in this thesis is that they use a Finite Element Method and here a Finite Difference Method. It was found that the average cell growth rate reduced consistently as the volume fraction was increased. The Lidinoid scaffold type not only yielded the maximum cell growth for its optimal volume fraction but also for the entire range of volume fractions. A recent study [169] presents a useful tool for understanding the interaction between bone and a bio-resorbable scaffold based on a viscoporoelastic model. While some numerical investigation is also undertaken, the study does not propose a method to optimise the design parameters, as is done here. However, the objective of their study was different, hence why an optimisation is not presented.

Although the stiffness and the pore size were the only constraints used here, other constraints can be easily added. An example would be the allowable shear stress caused by the surrounding fluid, which could be incorporated using the relationship between shear stress and cell growth discussed by Guyot et al. [37]. Another example would be looking at multi-material scaffolds, where the growth of capillaries could become a constraint. Such an approach could benefit from the work of Bednarczyk and Lekszycki [170] who proposed a novel model for the growth of capillaries and nutrient supply. Another example is that of biodegradable scaffolds, where the scaffold degradation rate is chosen to complement the cell growth rate, as suggested by Sanz Herrera et al. [171].

The methodology presented here could also be adapted to use different design variables and growth models. Giorgio et al. [169] discuss various interesting bio-inspired cellular scaffold geometries and they also reflect on the importance of considering the effects of the geometry at the micro-scale as well as the macro-scale. It could then be useful to use this methodology in order to optimise the micro- and macro-scale geometry using a multi-scale model with one design variable for each scale.

The optimal Lidinoid TPMS geometry of this study outperforms both the 2D scaffolds in the study of Rumpler et al. [172] as well as those in the study of Guyot et al. [37]. The maximum average cell growth rate achieved with this optimal scaffold was about 140% greater than that achieved by the 2D triangle scaffold in the study of Rumpler et al. [172]. When comparing the cell growth results shown here with those of Guyot et al. [37], where non-optimised 3D geometries are used, the maximum average cell growth rate achieved by the optimal Lidinoid scaffold of this study is about 90% higher than that achieved by the hexagon scaffold type of their study.

6.3   Cell culture

In this chapter it is shown that although there may be biocompatible materials for stereolithography, and the technique offers extensive design freedom, it is limited by the large spot size and layer height when it comes to manufacturing TPMS scaffolds of a suitable pore size. A recent study printed TPMS structures using the FormLabs stereolithography printer [141], and it is possible to see from their images that even at a pore size of about 4 mm (ten times as large as what was deemed the maximum allowed pore size in chapter 3 [114]), TPMS curves are no longer smooth.

Micro-stereolithography on the other hand, has shown to be a promising manufacturing technique that can achieve even smaller pore sizes than required for bone regeneration scaffolds while still allowing for a reasonable overall size of scaffold. The scaffolds manufactured with the BMF non-biocompatible material best demonstrated this with scaffolds almost twice as large as those printed with the biocompatible material, with dimensions of 2 x 2 x 3.5 mm. At the same time these scaffolds were printed with pore sizes of 300 μm and 150 μm. Bone scaffolds of such dimensions can already find suitable applications, such as in hip replacement acetabular cup reconstruction [173], where for the reconstruction grafts an average of 2.5 mm diameter has been used [173]. Moreover, as discussed in chapter 3, for suitable bone regeneration performance, the pore size of a scaffold should not be

smaller than 100 μm [114] or larger than 400 μm [117]. The printing area-resolution advantage of using PμSLA has been shown before in the literature [65] and therefore the analysis done in this study in this regard confirms this result.

As can be noted from the two-way ANOVA analysis found in Appendix H, only the differences between the Lidinoid and other geometries as well as the differences between Day 1 and other days, were statistically significant. In the results normalized by surface area, the Lidinoid is shown to have a lower fluorescence than the other geometries, and while it can be noted that the fluorescence increases with time for the Gyroid and Square scaffolds, for the Lidinoid the fluorescence drops after day 3. It was confirmed via a permeability test that while the media with cells managed to permeate the gyroid and square scaffolds relatively well, for the Lidinoid scaffold this was not the case, it is estimated less than 15% of the media with cells penetrated the Lidinoid scaffold pores, while this figure was over 75% for the Gyroid scaffold. This can be attributed to the pore size of the Lidinoid scaffolds being about 30% smaller than those of the Gyroid scaffolds. At day 7 the few cells that penetrated the scaffold appear to have died and the Lidinoid scaffold no longer showed any significant fluorescence. These results are nevertheless useful because they allow future studies to learn from these results and focus on the issue of permeability at an early stage when dealing with scaffolds of sub-millimetre pore sizes.

A previous study addressed the importance of scaffold permeability in bone regeneration scaffolds [174]. It has been shown before that a higher porosity significantly increases the scaffold permeability [175], by comparing polycaprolactone scaffolds of about 53% porosity with polycaprolactone scaffolds of 70% porosity and showing that the permeability was 5.8 times higher for the scaffolds with 70% porosity [175]. These scaffolds were manufactured via casting, sterilized with 70% ethanol for 24 h followed by sterile water for 24 h [175]. The intrinsic permeability of scaffolds manufactured via μSLA using Accura resin was measured in relation to varying pore size values [175]. It was found that at pore sizes below 0.6 mm the permeability was about 75% lower than that of scaffolds with a pore size of 1.5 mm [175]. Therefore, the findings presented here regarding the limited permeability of scaffolds with microscale pore sizes are in accordance with previous findings in the literature. The permeability is however also dependent on the material, so it is nevertheless useful that this study presents for the first time that for scaffolds manufactured with plasma treated TCDMDA material, the permeability is an important limitation to consider at pore sizes below 500 μm.

Regarding the hypothesis that TCDMDA could be used to 3D Print biocompatible scaffolds via PμSLA, this has indeed been demonstrated here. It was shown via SEM images that by combining TCDMDA with 0.5wt% DMPA photoinitiator, at a UV intensity level of 80 and an exposure time of 5 seconds, well defined Gyroid and Lidinoid scaffold geometries could be printed via PμSLA. Moreover, it was shown that hMSCs attached to TCDMDA disks manufactured via PμSLA, showing that such scaffolds are biocompatible. In order to improve the cell adhesion properties of the scaffolds, an oxygen plasma treatment was used and it was further demonstrated that as expected, oxygen plasma treatment enables TCDMDA scaffolds manufactured via PμSLA to have improved cell adhesion properties.

3D Printing of TCDMDA parts had been previously achieved via inkjet printing of cuboid arrays [10]. However, inkjet technology is not as suitable for printing scaffolds of the required resolution and printing area, as explained in [65] and illustrated in Figure 6-1. As shown, PμSLA is well suited for manufacturing scaffolds with the necessary balance between printing area and printing resolution, therefore demonstrating for the first time that biocompatible TCDMDA scaffolds can be manufactured via PμSLA is a useful finding of this thesis. Oxygen plasma treatment has been used before to enhance the cell adhesion of tissue regeneration scaffolds [147]. It was shown with lactide-TMC scaffolds made via a salt leaching technique that plasma treatment enhanced seeding efficiency, cell growth,

osteogenic differentiation and minerilization for rat bone marrow stromal cells (rBMSC) [147]. Although plasma treatment is known to enhance the cell viability of tissue engineering scaffolds, this had not previously been shown in relation to TCDMDA scaffolds, which makes this another useful finding of this thesis.
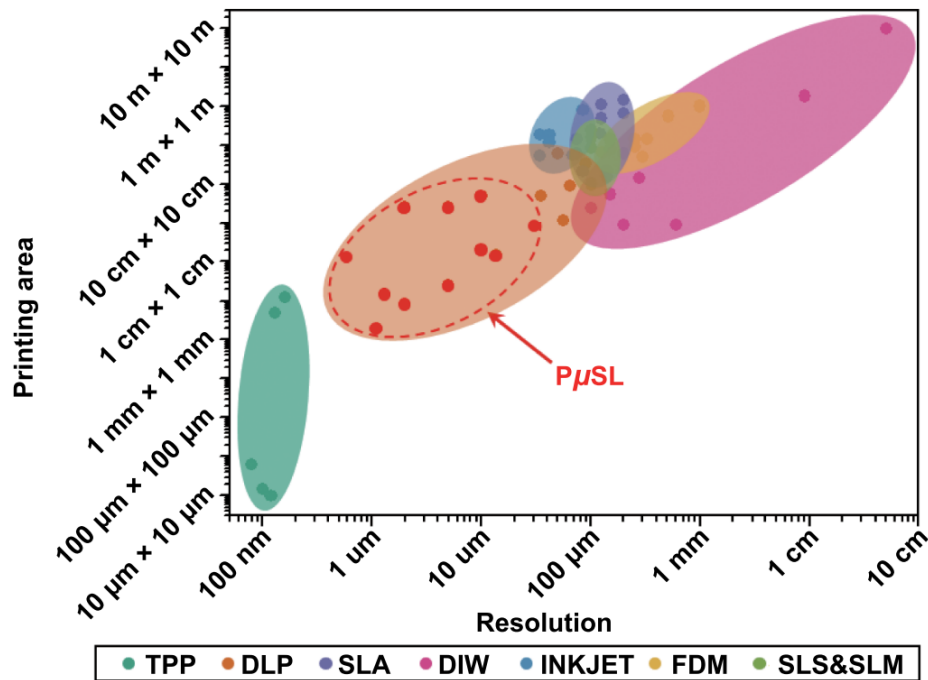
Figure 6-1: Printing area vs resolution for various additive manufacturing technologies. Image taken from [65].

Regarding the SLA experiments, it was demonstrated that as hypothesized, the scaffolds manufactured via stereolithography using the FormLabs dental resin were biocompatible, allowed for cell growth, cell differentiation and cell mineralisation. The biocompatibility was shown in section 4.3.4.1 where hMSCs were shown to attach to the surface of gyroid scaffolds. The ability of the scaffolds to enable cell growth was shown in section 4.3.4.2 where the number of cells attached to the scaffolds was shown to increase from day 1 to day 7 for two of the monolayer groups. Cell differentiation was shown in section 4.3.4.2 where a degree of ALP was secreted by cells attached to both monolayer and scaffold samples tested. Cell mineralisation was also shown in Figure 4-26 using Alizarin red to show the amount of calcium deposition.

A recent study looked at the growth of 3T3 cells on 3D printed samples of the same material under analysis (Dental LT (FormLabs, UK)) here and they found no significant cell growth with this material [176]. Instead, they found significant and promising cell growth when using Dental SG (FormLabs, UK) [176]. The reason given for the poor performance of Dental LT (FormLabs, UK) in this study was the inability to autoclave the material [176]. No other study was found that uses Dental LT (Formlabs, UK) material to manufacture scaffolds for tissue engineering. The reason why as opposed to the latter study, in this thesis a degree of cell growth was found may be because the sterilisation method used was 70% IPA for 1h followed by drying and soaking in serum for 5 days and not autoclaving. This thesis demonstrates for the first time that scaffolds manufactured via stereolithography using Dental LT (Formlabs, UK) and sterilised as explained in section 4.2.3.4 promote the adhesion, proliferation, differentiation and mineralisation of hMSCs.

The hypothesis that TPMS scaffolds lead to a higher cell growth could not be demonstrated here because the change in cell number for the scaffolds was not statistically significant in any group,

therefore it was not possible to compare the cell growth between scaffolds and monolayer. The results as shown would indicate that cells actually grow faster in the monolayer groups. In future studies however, a conventional scaffold should be used for a more appropriate comparison. Given that the only data shown to have statistical significance for the ALP results were the changes between subsequent days for the scaffold samples, it is not possible to say what the effect of geometry on cell differentiation could be based on these results. Since the calcium deposition results were not quantified, it is not possible to tell from the data presented whether the scaffolds promoted higher cell mineralisation than the monolayer samples. The visualised scaffolds, including that shown in Figure 4-26 did show that cell mineralisation was observed in abundance throughout the scaffolds surface. As expected, BMP-2 was shown to enhance cell differentiation and mineralisation on the scaffolds.

It has been shown previously that geometry can influence cell growth, cell differentiation and mineralization [19][22]. It has been demonstrated via visualisation and quantification of the genetic material in cells and the visualisation of collagen fibres that the growth rate of MC3T3-E1 cells is proportional to the curvature profile if it is positive [22]. It has also been shown that mineralization occurs on calcium phosphate cavities but not on planar surfaces of this material [177]. Furthermore it was shown that the amount of mineralization can be controlled by the curvature radius of the calcium phosphate cavity, with a smaller radius leading to higher mineralization [177]. It was recently shown that the cell viability of osteoblasts on Gyroid and Diamond scaffolds made of Ti-4Al-4V via selective laser melting (SLM) was higher than that of tissue culture plastic, and a similar amount of ALP secretion was observed in both Gyroid and Diamond scaffolds [178]. Although the results shown here regarding the effect of geometry are overall inconclusive, based on the literature reviewed this thesis represents the first time that TPMS geometries have been investigated via SLA for promoting cell growth, cell differentiation and mineralization. The method described here for the first time may therefore be useful to future studies that wish to build upon it to investigate the use of TPMS scaffolds.

When it comes to cell differentiation, as measured with the ALP content, the results of this thesis can be compared to those of the study by Davis et al. [134] where BMP-2 was also used but with non TPMS scaffold geometries [134]. In this study, poly(lactide-co-glycolide) (PLG) disk scaffolds were manufactured via a double emulsion technique with a pore size of 250-425 µm, a diameter of 8.5 mm and a thickness of 1.5 mm. They do not provide any more parameters that would allow me to compute the surface area with more accuracy, but by assuming they have half the surface area per unit volume than the scaffolds presented here of equivalent pore sizes, it can be deduced that the surface area of their scaffolds was 3.54 cm^2. The surface area of the SLA scaffolds (2.26 cm^2) was therefore about 50% lower. Furthermore, the BMP-2 amount used here was 40% of the smallest amount they used. The scaffolds presented here also had much larger pore sizes which as has been shown in chapter 3, should lead to a lower amount of differentiation. When normalising the ALP units by the surface area as well as the BMP-2 concentration used, it was found that the scaffolds presented here generated 0.66 ALP units mgDNA^{-1} cm^{-2} (ng/mL)BMP2^{-1} while those in the study of Davis et al. [134] generated 0.45 ALP units mgDNA^{-1} cm^{-2} (ng/mL)BMP2^{-1}, or 47% less. A more thorough analysis is needed to draw any conclusions however, since the studies compared had different conditions and no statistical analysis has been carried out.

6.4   Plate-scaffold Optimisation

The proposed plate-scaffold design selection methodology is a novel routine that can simultaneously select an optimal plate and scaffold geometry for fracture healing. The routine is presented in a 2-variable solution space, one design variable for each implant, which is enough to ensure an optimal fracture healing outcome. This methodology is particularly convenient because it enables designers

to not only find the optimal plate-scaffold geometry combination but also to get an idea of the relationship between input and response variables for the entire solution space under analysis. Similar to the routine focusing only on the scaffold geometry, this methodology can be extended to include other constraints. The results of this analysis showed that the optimal plate-scaffold geometry combination was found at a plate strut thickness of 0.5 mm and a volume fraction of 24% (unit cell size of 1 mm). Moreover, it was shown that the combination of optimal implants with the graded auxetic plate clearly leads to a lower stress shielding than non-optimal implants or than optimal implants with the ungraded auxetic plate.

By tuning the middle strut thickness value prior to carrying out the rest of the design selection, it is then possible to limit the number of design variables to two as desired for the graphical optimal design selection process. It can be clearly observed that as the strut thickness of the plate is decreased in equally spaced steps, the stress shielding decreases in steps of increasing size. The stress peak at the end screw-bone interface follows a similar pattern where it decreases with reduction of the strut thickness. However, it was found that when the strut thickness was lower than 1.167 mm, the Inter-fragmentary strain (IFS) surpassed the limit of 0.6%.

The study takes into account IFS limits because this is typically used as an indicator of how much bone regeneration can be expected at the fracture site [83][158]. The range of IFS that produces a suitable fracture healing outcome has been experimentally found in an in-vivo animal study [158]. As is also found in the results of chapter 6, the animal study found the highest compressive IFS values to be at the scaffold-callus region opposite the plate. In the study, the IFS values at the fracture region were correlated with mineralized bone in the same region for a sheep bone under the same loading conditions [158]. If a designer was only interested in the fracture healing outcome, the inter-fragmentary strain could be used as the objective function to be maximised, but in this thesis the focus was on minimising stress shielding in the bone in order to avoid re-fracture of the bone as is often seen by surgeons [179]. By using a multi-objective optimisation algorithm [180] it would be possible to minimise both the inter-fragmentary strain and the stress shielding simultaneously.

The Von Mises stress criterion is widely used in engineering to avoid failure of a given part. It is a failure criterion used to predict the onset of yielding based on deviatoric energy. A safety factor is often used in an attempt to reduce the risk that the part would fail in the real world, and this is also implemented in this thesis.

The Von Mises stress results for the scaffold show that as the end plate strut thickness decreases the maximum Von Mises stress seen in the scaffold increases. This is a reasonable observation given that a lower plate strut thickness leads to a more compliant assembly which in turn leads to higher strains at the fracture site. Increasing the scaffold elastic modulus is shown to increase the maximum scaffold Von Mises stress, which can be deduced from the assumption that stiffer materials carry more of the stress in an assembly. This assumption comes from considering Hooke's law of elasticity which states that the Young's modulus of a linear isotropic elastic material is equal to the stress divided by the strain it experiences. The analogous analysis for the bone shows that that the highest maximum Von Mises stresses in the bone are experienced with a higher strut thickness and a lower scaffold elastic modulus. Some of the stress that is not going onto the scaffold goes into the bone as the scaffold effective modulus is reduced, and a higher end plate strut thickness leads to a higher contact pressure which is where the maximum Von Mises stress is found. The latter reasoning applies to the plate as well. Overall, it can be noted that the bone and plate are at the highest risk of fracturing and this risk can be reduced by having a lower end plate strut thickness and a higher scaffold elastic modulus.

Using the minimum Von Mises stress in the bone as the representative variable for stress shielding has been proposed previously by Ganesh et al. [87]. Although this study uses different geometry and conditions than their study, it can be observed that the stress distribution along the length of the bone region under the plate is very similar to that in this analysis; this is shown in Figure 5-18. Moreover, in their study [87] they also found that a stiffness graded plate with a more compliant region at the end of the plate reduced the stress shielding. However, the relationship presented in this thesis between the end plate strut thickness, scaffold elastic modulus and minimum Von Mises stress in the bone; has never been presented before. This relationship shows that as the end plate strut thickness is increased, the bone is increasingly shielded when the fracture has healed. It also shows that when the fracture has healed, the change in elastic modulus has very little influence on the stress shielding. Before the fracture heals, the bone appears to be most shielded at the region of lowest end plate strut thickness and lowest scaffold elastic modulus. This is because as the scaffold effective modulus is lowered, the stress is redistributed, and when the end plate strut thickness is too low there is no longer a significant contact force, meaning the stress will mostly go through the plate.

The experimental demonstration was shown to be in agreement with the finite element modeling given that the mean axial strain measured only differed by 2.13% from that computed by the model. The difference in mean absolute axial strain from that of the 'only bone' sample was found to be only 3.03% for the auxetic case and 10.72% for the solid case. Mean axial strain is a good indicator because assuming the material is linearly elastic, the stress is proportional to the strain, and the stress has been used throughout this study as an indicator of stress shielding. This further supports the hypothesis that the graded auxetic plate design leads to lower stress shielding, as was also concluded by [90]. Comparing the axial stiffness of the three cases under analysis showed that the difference between the axial stiffness of the auxetic case and the bone case is half that between the solid case and the bone case. This is as expected given the more flexible auxetic plate. Moreover, it was shown that during plastic deformation of the samples, a screw of the 'solid' case fractured causing a sharp drop in the load-deformation curve. This shows that the local stress at the bone-screw interface is higher for the 'solid' case, as was previously shown with the modelling. Finally, observing the deformation shape of the different samples shows that the 'auxetic' sample was much closer to the 'bone' sample than the 'solid' was, which again demonstrates that the 'auxetic' case yields a behaviour much closer to that of having just a bone.

The project has successfully achieved the aim of the study with the development of a novel experimentally supported computational framework for the selection of an implant design that satisfies specified constraints and minimises a given objective. Due to the user-friendly graphical frameworks used, it can also be concluded that the method developed may be easily adopted by medical designers. Novel structure-property relationships have been proposed to aid in the understanding of fracture healing implant performance.

Chapter 7: Future work

7.1 Future work

7.1.1 Cell growth model

A future study could focus on extending the methodology to include also the scaffold unit cell size in order to generalise the method further. This could involve visualising the results with a 3rd dimension such as is done in chapter 5. It would also be useful to fit mathematical equations to the model data to get relationships that can be extended beyond the chosen limits, such as is also done in chapter 6 of this thesis. Including other lattice types in the analyses would also be interesting and given the material flexibility of the current approach, this would not require much effort. A future study in this area could also include some of the suggested constraints such as the allowable shear stress generated by the fluid flow at the scaffold walls or the difference between scaffold degradation rate and cell growth rate.

7.1.2 Cell culture

Future work regarding the AM of TPMS scaffolds should focus on exploiting the potential of PµSLA by developing suitable biocompatible and biodegradable material resins with appropriate mechanical properties. An example of a material that has all these properties and could therefore be adjusted for PµSLA is that recently developed by Weems et al. [181] for SLA scaffolds. Furthermore, the design freedom provided by PµSLA should be taken advantage of by investigating the manufacturing of patient-specific implants. Regarding the use of BMP-2, it is recommend that future work looks to include the combined effects of TPMS geometry and BMP-2 in a model using a methodology such as that presented in chapters 3 and 5. This would enable optimal concentrations of BMP-2 to be determined in combination with optimal design parameters for the TPMS scaffold. Finally future work carried out with PµSLA scaffolds should always run a permeability study prior to cell culture experiments, to ensure a fair comparison between the cases under analysis.

7.1.3 Plate-scaffold Optimisation

Future work could focus on exploring 3D auxetic graded fracture healing plate geometries as these have been shown previously to provide more promising mechanical properties than 2D auxetic geometries [91]. Moreover, different geometry grading relationships could be investigated, such as quadratic or logarithmic to find out whether they may enhance the fracture healing performance. Future studies could also look to find out how an auxetic graded geometry compares to other graded geometries, and such an investigation could make use of the proposed overall strategy. Further computational work could extend this methodology to be patient-specific by considering a CT scanned bone geometry and using initial plate geometries already in the market, for which the traditional design parameters have already been optimised. A subsequent experimental study could then take the concept which has been demonstrated here closer to being applied by medical practitioners.

7.1.4 Overall

Future work could look to further integrate the curvature-dependent cell growth model with the plate-scaffold mechanical performance model, which would involve the computational challenge of iteratively solving a finite element model for a centimetre-scale scaffold of sub millimetre pore sizes.

References:

[1] E. F. Lehder, I. A. Ashcroft, R. D. Wildman, L. A. Ruiz-Cantu, and I. Maskery, "A multiscale optimisation method for bone growth scaffolds based on triply periodic minimal surfaces," *Biomech. Model. Mechanobiol.*, no. 0123456789, 2021, doi: 10.1007/s10237-021-01496-8.

[2] E. H. Schemitsch, "Size Matters: Defining Critical in Bone Defect Size!," *J. Orthop. Trauma*, vol. 31, no. 10, pp. S20–S22, 2017, doi: 10.1097/BOT.0000000000000978.

[3] W. Tao and M. C. Leu, "Design of lattice structure for additive manufacturing," *Int. Symp. Flex. Autom. ISFA 2016*, no. August, pp. 325–332, 2016, doi: 10.1109/ISFA.2016.7790182.

[4] H. N. G. Wadley, N. A. Fleck, and A. G. Evans, "Fabrication and structural performance of periodic cellular metal sandwich structures," *Compos. Sci. Technol.*, vol. 63, no. 16, pp. 2331–2343, 2003, doi: 10.1016/S0266-3538(03)00266-5.

[5] P. F. Egan, V. C. Gonella, M. Engensperger, S. J. Ferguson, and K. Shea, "Computationally designed lattices with tuned properties for tissue engineering using 3D printing," 2017, doi: 10.1371/journal.pone.0182902.

[6] S. Vijayavenkataraman, L. Zhang, S. Zhang, J. Ying, H. Fuh, and W. F. Lu, "Triply Periodic Minimal Surfaces Sheet Scaffolds for Tissue Engineering Applications: An Optimization Approach toward Biomimetic Scaffold Design," *ACS Appl. Bio Mater.*, 2018, doi: 10.1021/acsabm.8b00052.

[7] G. L. Koons, M. Diba, and A. G. Mikos, "Materials design for bone-tissue engineering," *Nat. Rev. Mater.*, pp. 1–20, 2020, doi: 10.1038/s41578-020-0204-2.

[8] S. B. G. Blanquer *et al.*, "Surface curvature in triply-periodic minimal surface architectures as a distinct design parameter in preparing advanced tissue engineering scaffolds," *Biofabrication*, vol. 9, no. 2, 2017, doi: 10.1088/1758-5090/aa6553.

[9] B. T. O. Donnell, C. J. Ives, O. A. Mohiuddin, and B. A. Bunnell, "Beyond the Present Constraints That Prevent a Wide Spread of Tissue Engineering and Regenerative Medicine Approaches," vol. 7, no. May, pp. 1–12, 2019, doi: 10.3389/fbioe.2019.00095.

[10] Y. He *et al.*, "Inkjet based 3D Printing of bespoke medical devices that resist bacterial biofilm formation," 2020, doi: 10.1101/2020.06.30.180596.

[11] J. Manuel, G. Aznar, C. Valero, • Carlos Borau, and N. Garijo, "Computational mechano-chemo-biology: a tool for the design of tissue scaffolds", doi: 10.1007/s40898-016-0002-1.

[12] G. Zimmermann and A. Moghaddam, "Allograft bone matrix versus synthetic bone graft substitutes," *Injury*, vol. 42, pp. S16–S21, 2011, doi: 10.1016/j.injury.2011.06.199.

[13] W. Wang and K. W. K. Yeung, "Bone grafts and biomaterials substitutes for bone defect repair: A review," *Bioact. Mater.*, vol. 2, no. 4, pp. 224–247, Dec. 2017, doi: 10.1016/J.BIOACTMAT.2017.05.007.

[14] H. Ma, C. Feng, J. Chang, and C. Wu, "3D-printed bioceramic scaffolds: From bone tissue engineering to tumor therapy," *Acta Biomater.*, vol. 79, pp. 37–59, 2018, doi: 10.1016/j.actbio.2018.08.026.

[15] S. H. Jariwala, G. S. Lewis, Z. J. Bushman, J. H. Adair, and H. J. Donahue, "3D Printing of Personalized Artificial Bone Scaffolds," *3D Print.*, vol. 2, no. 2, 2015, doi: 10.1089/3dp.2015.0001.

[16] T. D. Ngo, A. Kashani, G. Imbalzano, K. T. Q. Nguyen, and D. Hui, "Additive manufacturing (3D printing): A review of materials, methods, applications and challenges," *Compos. Part B Eng.*,

vol. 143, pp. 172–196, Jun. 2018, doi: 10.1016/j.compositesb.2018.02.012.

[17] S. M. Giannitelli, D. Accoto, M. Trombetta, and A. Rainer, "Current trends in the design of scaffolds for computer-aided tissue engineering," *Acta Biomater.*, vol. 10, no. 2, pp. 580–594, 2014, doi: 10.1016/j.actbio.2013.10.024.

[18] Z. Zhang, B. Wang, D. Hui, J. Qiu, and S. Wang, "3D bioprinting of soft materials-based regenerative vascular structures and tissues," *Compos. Part B Eng.*, vol. 123, pp. 279–291, 2017, doi: 10.1016/j.compositesb.2017.05.011.

[19] A. A. Zadpoor, "Bone tissue regeneration: the role of scaffold geometry," no. November, 2014, doi: 10.1039/C4BM00291A.

[20] B. Chen, B. Ji, and H. Gao, "Modeling Active Mechanosensing in Cell-Matrix Interactions," 2015, doi: 10.1146/annurev-biophys-051013-023102.

[21] X. Chen *et al.*, "Scaffold structural microenvironmental cues to guide tissue regeneration in bone tissue applications," *Nanomaterials*, vol. 8, no. 11, pp. 1–15, 2018, doi: 10.3390/nano8110960.

[22] C. M. Bidan, K. P. Kommareddy, M. Rumpler, P. Kollmannsberger, P. Fratzl, and J. W. C. Dunlop, "Geometry as a Factor for Tissue Growth: Towards Shape Optimization of Tissue Engineering Scaffolds," *Adv. Healthc. Mater.*, 2013, doi: 10.1002/adhm.201200159.

[23] M. Rumpler, A. Woesz, J. W. C. Dunlop, J. T. Van Dongen, and P. Fratzl, "The effect of geometry on three-dimensional tissue growth," *J. R. Soc. Interface*, 2008, doi: 10.1098/rsif.2008.0064.

[24] E. Gamsjäger, C. M. Bidan, F. D. Fischer, P. Fratzl, and J. W. C. Dunlop, "Modelling the role of surface stress on the kinetics of tissue growth in confined geometries," *Acta Biomater.*, vol. 9, pp. 5531–5543, 2013, doi: 10.1016/j.actbio.2012.10.020.

[25] V. Hosseini *et al.*, "Fiber-Assisted Molding (FAM) of surfaces with tunable curvature to guide cell alignment and complex tissue architecture," *Small*, vol. 10, no. 23, pp. 4851–4857, 2014, doi: 10.1002/smll.201400263.

[26] C. M. Bidan, K. P. Kommareddy, M. Rumpler, P. Kollmannsberger, and Y. Bréchet, "How Linear Tension Converts to Curvature: Geometric Control of Bone Tissue Growth," *PLoS One*, vol. 7, no. 5, p. 36336, 2012, doi: 10.1371/journal.pone.0036336.

[27] C. M. Bidan, K. P. Kommareddy, M. Rumpler, P. Kollmannsberger, and Y. Bréchet, "How Linear Tension Converts to Curvature: Geometric Control of Bone Tissue Growth," *PLoS One*, vol. 7, no. 5, p. 36336, 2012, doi: 10.1371/journal.pone.0036336.

[28] C. M. Bidan, K. P. Kommareddy, M. Rumpler, P. Kollmannsberger, P. Fratzl, and J. W. C. Dunlop, "Geometry as a Factor for Tissue Growth: Towards Shape Optimization of Tissue Engineering Scaffolds," *Adv. Healthc. Mater.*, vol. 2, no. 1, pp. 186–194, 2013, doi: 10.1002/adhm.201200159.

[29] D. A. Garzó N-Alvarado, M. A. Velasco, and C. A. Narvá Ez-Tovar, "Modeling porous scaffold microstructure by a reaction-diffusion system and its degradation by hydrolysis," *Comput. Biol. Med.*, vol. 42, pp. 147–155, 2012, doi: 10.1016/j.compbiomed.2011.11.002.

[30] J. Van Der Stok *et al.*, "Selective laser melting-produced porous titanium scaffolds regenerate bone in critical size cortical bone defects," *J. Orthop. Res.*, vol. 31, no. 5, pp. 792–799, 2013, doi: 10.1002/jor.22293.

[31] M. Werner *et al.*, "Surface Curvature Differentially Regulates Stem Cell Migration and Differentiation via Altered Attachment Morphology and Nuclear Deformation", doi:

10.1002/advs.201600347.

[32]   A. J. Steward and D. J. Kelly, "Mechanical regulation of mesenchymal stem cell differentiation," *J. Anat.*, vol. 227, no. 6, pp. 717–731, 2015, doi: 10.1111/joa.12243.

[33]   N. Huebsch *et al.*, "Harnessing traction-mediated manipulation of the cell/matrix interface to control stem-cell fate," *Nat. Mater.*, vol. 9, no. 6, pp. 518–526, 2010, doi: 10.1038/nmat2732.

[34]   M. Olausson, N. Esfahani, J. Östlin, and C. Hägglin, "Native-born versus foreign-born patients' perception of communication and care in Swedish dental service," *Swed. Dent. J.*, vol. 40, no. 1, pp. 91–100, 2016.

[35]   N. Riaz, S. L. Wolden, D. Y. Gelblum, and J. Eric, "Degradation-mediated cellular traction directs stem cell fate in covalently," vol. 118, no. 24, pp. 6072–6078, 2016, doi: 10.1002/cncr.27633.Percutaneous.

[36]   A. M. DiMarino, A. I. Caplan, and T. L. Bonfield, "Mesenchymal stem cells in tissue repair," *Front. Immunol.*, vol. 4, no. JUL, pp. 1–9, 2013, doi: 10.3389/fimmu.2013.00201.

[37]   Y. Guyot *et al.*, "A computational model for cell/ECM growth on 3D surfaces using the level set method: a bone tissue engineering case study," *Biomech Model Mechanobiol*, vol. 13, pp. 1361–1371, 2014, doi: 10.1007/s10237-014-0577-5.

[38]   P. N. Tawakoli, A. Al-Ahmad, W. Hoth-Hannig, M. Hannig, and C. Hannig, "Comparison of different live/dead stainings for detection and quantification of adherent microorganisms in the initial oral biofilm", doi: 10.1007/s00784-012-0792-3.

[39]   Y. Guyot, F. P. Luyten, J. Schrooten, I. Papantoniou, and L. Geris, "A three-dimensional computational fluid dynamics model of shear stress distribution during neotissue growth in a perfusion bioreactor," *Biotechnol. Bioeng.*, vol. 112, no. 12, pp. 2591–2600, 2015, doi: 10.1002/bit.25672.

[40]   S. J. Mousavi and M. H. Doweidar, "Role of Mechanical Cues in Cell Differentiation and Proliferation: A 3D Numerical Model," 2015, doi: 10.1371/journal.pone.0124529.

[41]   J. A. Sanz-Herrera, J. M. Garci´a, G. Garci´a-Aznar, and M. Doblaré, "A mathematical approach to bone tissue engineering", doi: 10.1098/rsta.2009.0055.

[42]   S. C. Kapfer, S. T. Hyde, K. Mecke, C. H. Arns, and G. E. Schröder-Turk, "Minimal surface scaffold designs for tissue engineering," *Biomaterials*, vol. 32, no. 29, pp. 6875–6882, 2011, doi: 10.1016/j.biomaterials.2011.06.012.

[43]   M. Mehrian *et al.*, "Maximizing neotissue growth kinetics in a perfusion bioreactor: An in silico strategy using model reduction and Bayesian optimization," *Biotechnol. Bioeng.*, vol. 115, no. 3, pp. 617–629, 2018, doi: 10.1002/bit.26500.

[44]   D. Eglin *et al.*, "Surface curvature in triply-periodic minimal surface architectures as a distinct design parameter in preparing advanced tissue engineering scaffolds," *Biofabrication*, vol. 9, no. 2, p. 025001, 2017, doi: 10.1088/1758-5090/aa6553.

[45]   H. Puga, V. H. Carneiro, P. Correira, V. Vieira, J. Barbosa, and J. Meireles, "Mechanical behavior of honeycomb lattices manufactured by investment casting for scaffolding applications," *Proc. Inst. Mech. Eng. Part L J. Mater. Des. Appl.*, vol. 231, no. 1–2, pp. 73–81, 2017, doi: 10.1177/1464420716665414.

[46]   H. S. and J. B. J. Weise, "Semi solid processing of complex shaped foamable material," *Cell. Met. Met. Foam. Technol.*, 2014.

[47]   A. A. Al-Tamimi, C. Quental, J. Folgado, C. Peach, and P. Bartolo, "Stress analysis in a bone fracture fixed with topology-optimised plates," *Biomech. Model. Mechanobiol.*, vol. 19, no. 2, pp. 693–699, 2020, doi: 10.1007/s10237-019-01240-3.

[48]   M. Gibson, I. and Ashby, "The mechanics of three-dimensional cellular materials," vol. 59, pp. 43–59, 1982.

[49]   N. A. Chartrain, C. B. Williams, and A. R. Whittington, "A review on fabricating tissue scaffolds using vat photopolymerization," *Acta Biomater.*, vol. 74, pp. 90–111, 2018, doi: 10.1016/j.actbio.2018.05.010.

[50]   D. H. Leatrese, K. Byung-Soo, and J. M. David, "Open pore biodegradable matrices formed with gas foaming," *J. Biomed. Mater. Res.*, vol. 42, no. 3, pp. 396–402, 1998, [Online]. Available: http://dx.doi.org/10.1002/(SICI)1097-4636(19981205)42:3%3C396::AID-JBM7%3E3.0.CO;2-E

[51]   D. Puppi, F. Chiellini, A. M. Piras, and E. Chiellini, "Polymeric materials for bone and cartilage repair," *Prog. Polym. Sci.*, vol. 35, no. 4, pp. 403–440, 2010, doi: 10.1016/j.progpolymsci.2010.01.006.

[52]   A. G. Mikos and J. S. Temenoff, "Formation of highly porous biodegradable scaffolds for tissue engineering," 2000. Accessed: Jun. 04, 2019. [Online]. Available: http://www.ejb.org/content/vol3/issue2/full/5

[53]   S. Samavedi, S. A. Guelcher, A. S. Goldstein, and A. R. Whittington, "Response of bone marrow stromal cells to graded co-electrospun scaffolds and its implications for engineering the ligament-bone interface," *Biomaterials*, vol. 33, no. 31, pp. 7727–7735, Nov. 2012, doi: 10.1016/j.biomaterials.2012.07.008.

[54]   A. Prasad, M. R. Sankar, and V. Katiyar, "State of Art on Solvent Casting Particulate Leaching Method for Orthopedic ScaffoldsFabrication," *Mater. Today Proc.*, vol. 4, no. 2, pp. 898–907, 2017, doi: 10.1016/j.matpr.2017.01.101.

[55]   T. GILBERT, T. SELLARO, and S. BADYLAK, "Decellularization of tissues and organs," *Biomaterials*, Mar. 2006, doi: 10.1016/j.biomaterials.2006.02.014.

[56]   I. Gibson, D. Rosen, B. Stucker, and M. Khorasani, *Additive Manufacturing Technologies*. 2021. doi: 10.1007/978-3-030-56127-7.

[57]   R. Hague, I. Campbell, and P. Dickens, "Implications on design of rapid manufacturing," *Proc. Inst. Mech. Eng. Part C J. Mech. Eng. Sci.*, 2003, doi: 10.1243/095440603762554587.

[58]   D. Chen, S. Heyer, S. Ibbotson, K. Salonitis, J. G. Steingrímsson, and S. Thiede, "Direct digital manufacturing: Definition, evolution, and sustainability implications," *J. Clean. Prod.*, 2015, doi: 10.1016/j.jclepro.2015.05.009.

[59]   T. D. Ngo, A. Kashani, G. Imbalzano, K. T. Q. Nguyen, and D. Hui, "Additive manufacturing (3D printing): A review of materials , methods , applications and challenges," *Compos. Part B*, vol. 143, no. February, pp. 172–196, 2018, doi: 10.1016/j.compositesb.2018.02.012.

[60]   M. Tilton, G. S. Lewis, H. Bok Wee, A. Armstrong, M. W. Hast, and G. Manogharan, "Additive manufacturing of fracture fixation implants: Design, material characterization, biomechanical modeling and experimentation," *Addit. Manuf.*, vol. 33, no. February, p. 101137, 2020, doi: 10.1016/j.addma.2020.101137.

[61]   A. Bertsch and P. Renaud, *Chapter 1.2 - Microstereolithography*. Elsevier Inc., 2016. doi: 10.1016/B978-0-323-35321-2/00002-9.

[62]   S. F. S. Shirazi *et al.*, "A review on powder-based additive manufacturing for tissue engineering:

Selective laser sintering and inkjet 3D printing," *Sci. Technol. Adv. Mater.*, vol. 16, no. 3, pp. 1–20, 2015, doi: 10.1088/1468-6996/16/3/033502.

[63] S. V. Murphy and A. Atala, "3D bioprinting of tissues and organs," *Nature Biotechnology*, vol. 32, no. 8. Nature Publishing Group, pp. 773–785, 2014. doi: 10.1038/nbt.2958.

[64] D. L. Cohen, W. Lo, A. Tsavaris, D. Peng, H. Lipson, and L. J. Bonassar, "Increased Mixing Improves Hydrogel Homogeneity and Quality of Three-Dimensional Printed Constructs," *Tissue Eng. Part C Methods*, vol. 17, no. 2, pp. 239–248, 2010, doi: 10.1089/ten.tec.2010.0093.

[65] Q. Ge *et al.*, "Projection micro stereolithography based 3D printing and its applications," *Int. J. Extrem. Manuf.*, vol. 2, no. 2, 2020, doi: 10.1088/2631-7990/ab8d9a.

[66] M. J. Männel, C. Fischer, and J. Thiele, "A Non-Cytotoxic Resin for Micro-Stereolithography for Cell Cultures of HUVECs," 2020.

[67] D. J. Yoo, "Advanced projection image generation algorithm for fabrication of a tissue scaffold using volumetric distance field," *Int. J. Precis. Eng. Manuf.*, vol. 15, no. 10, pp. 2117–2126, 2014, doi: 10.1007/s12541-014-0571-y.

[68] H. M. Frost, "The biology of fracture healing. An overview for clinicians. Part I.," *Clin. Orthop. Relat. Res.*, 1989, doi: 10.1016/j.injury.2011.03.031.

[69] L. E. Claes and C. A. Heigele, "Magnitudes of local stress and strain along bony surfaces predict the course and type of fracture healing," *J. Biomech.*, vol. 32, pp. 255–266, 1999, [Online]. Available: https://ac.els-cdn.com/S0021929098001535/1-s2.0-S0021929098001535-main.pdf?_tid=85ca999d-da62-4138-ab87-6d4222285334&acdnat=1524034109_003922b15df74f8e3cc29255306ed9e9

[70] P. Augat, J. Burger, S. Schorlemmer, T. Henke, M. Peraus, and L. Claes, "Shear movement at the fracture site delays healing in a diaphyseal fracture model," *J. Orthop. Res.*, vol. 21, no. 6, pp. 1011–1017, 2003, doi: 10.1016/S0736-0266(03)00098-6.

[71] L. Claes, R. Blakytny, Melanie Göckelmann, M. Schoen, A. Ignatius, and B. Willie, "Early dynamization by reduced fixation stiffness does not improve fracture healing in a rat femoral osteotomy model," *J. Orthop. Res.*, vol. 27, no. 1, pp. 22–27, 2009, doi: 10.1002/jor.20712.

[72] M. Steiner, L. Claes, A. Ignatius, U. Simon, and T. Wehner, "Numerical Simulation of Callus Healing for Optimization of Fracture Fixation Stiffness," *PLoS One*, vol. 9, no. 7, 2014, doi: 10.1371/journal.pone.0101370.

[73] DePuy Synthes, "LCP Locking Compression Plate Surgical Technique," 2004, [Online]. Available: http://synthes.vo.llnwd.net/o16/LLNWMB8/INT Mobile/Synthes International/Product Support Material/legacy_Synthes_PDF/DSEM-TRM-0115-0278-3_LR.pdf

[74] H. T. Aro and E. Y. Chao, "Bone-healing patterns affected by loading, fracture fragment stability, fracture type, and fracture site compression.," *Clinical orthopaedics and related research*, vol. 293, no. 293. pp. 8–17, 1993. doi: 10.1097/00003086-199308000-00003.

[75] L. E. E. Claes, H. J. Wilke, P. Augat, S. Rübenacker, and K. J. J. Margevicius, "Effect of dynamization on gap healing of diaphyseal fractures under external fixation," *Clin. Biomech.*, vol. 10, no. 5, pp. 227–234, 1995, doi: 10.1016/0268-0033(95)99799-8.

[76] T. Wehner, R. Penzkofer, P. Augat, L. Claes, and U. Simon, "Improvement of the shear fixation stability of intramedullary nailing," *Clin. Biomech.*, vol. 26, no. 2, pp. 147–151, 2011, doi: 10.1016/j.clinbiomech.2010.09.009.

[77] G. A. Ateshian and V. C. Mow, "Basic Orthopaedic Biomechanics and Mechano-Biology,"

Friction, lubrication, and wear of articular cartilage and diarthrodial joints. pp. 447–494, 2005. doi: 9780781739337.

[78] E. A. Lewallen *et al.*, "Biological strategies for improved osseointegration and osteoinduction of porous metal orthopedic implants," *Tissue Eng. - Part B Rev.*, vol. 21, no. 2, pp. 218–230, 2015, doi: 10.1089/ten.teb.2014.0333.

[79] H. K. Uhthoff and F. L. Dubuc, "Bone structure changes in the dog under rigid internal fixation.," *Clin. Orthop. Relat. Res.*, 1971, doi: 10.1097/00003086-197111000-00026.

[80] A. Tonino, C. Davidson, P. Klopper, and L. Linclau, "Protection from stress in bone and its effects.," *J Bone Jt. Surg Br*, vol. 58-B, no. 1, pp. 107–113, 1976, [Online]. Available: http://www.bjj.boneandjoint.org.uk/content/58-B/1/107.short

[81] H. Weinans, R. Huiskes, and H. J. Grootenboer, "Effects of material properties of femoral hip components on bone remodeling," *J. Orthop. Res.*, vol. 10, no. 6, pp. 845–853, 1992, doi: 10.1002/jor.1100100614.

[82] S. J. Ferguson, U. P. Wyss, and D. R. Pichora, "Finite element stress analysis of a hybrid fracture fixation plate," *Med. Eng. Phys.*, vol. 18, no. 3, pp. 241–250, 1996, doi: 10.1016/1350-4533(95)00041-0.

[83] L. Claes, "Biomechanical principles and mechanobiologic aspects of flexible and locked plating," *J. Orthop. Trauma*, vol. 25, no. 2 SUPPL., pp. 4–7, 2011, doi: 10.1097/BOT.0b013e318207093e.

[84] P. Cronier, G. Pietu, C. Dujardin, N. Bigorre, F. Ducellier, and R. Gerard, "The concept of locking plates," *Orthop. Traumatol. Surg. Res.*, vol. 96, no. 4 SUPPL., 2010, doi: 10.1016/j.otsr.2010.03.008.

[85] R. Wauthle *et al.*, "Revival of pure titanium for dynamically loaded porous implants using additive manufacturing," *Mater. Sci. Eng. C*, vol. 54, pp. 94–100, 2015, doi: 10.1016/j.msec.2015.05.001.

[86] J. FICE and N. CHANDRASHEKAR, "TAPERED FRACTURE FIXATION PLATE REDUCES BONE STRESS SHIELDING: A COMPUTATIONAL STUDY," *J. Mech. Med. Biol.*, vol. 12, no. 04, p. 1250072, Sep. 2012, doi: 10.1142/S021951941200506X.

[87] V. K. Ganesh, K. Ramakrishna, and D. N. Ghista, "Biomechanics of bone-fracture fixation by stiffness-graded plates in comparison with stainless-steel plates," *Biomed. Eng. Online*, vol. 4, pp. 1–15, 2005, doi: 10.1186/1475-925X-4-46.

[88] B. R. Simon *et al.*, "Evaluation of one-, two-, and three-dimensional finite element and experimental models of internal fixation plates," *J. Biomech.*, vol. 10, no. 2, pp. 79–86, 1977.

[89] D. D. Lima *et al.*, "Laser additive processing of a functionally graded internal fracture fixation plate," *Mater. Des.*, vol. 130, no. March, pp. 8–15, 2017, doi: 10.1016/j.matdes.2017.05.034.

[90] S. Vijayavenkataraman, A. Gopinath, and W. F. Lu, "A new design of 3D-printed orthopedic bone plates with auxetic structures to mitigate stress shielding and improve intra-operative bending," *Bio-Design Manuf.*, vol. 3, no. 2, pp. 98–108, 2020, doi: 10.1007/s42242-020-00066-8.

[91] H. M. A. Kolken and A. A. Zadpoor, "Auxetic mechanical metamaterials," *RSC Adv.*, vol. 7, no. 9, pp. 5111–5129, 2017, doi: 10.1039/c6ra27333e.

[92] H. M. A. Kolken, S. Janbaz, S. M. A. Leeflang, K. Lietaert, H. H. Weinans, and A. A. Zadpoor, "Rationally designed meta-implants: A combination of auxetic and conventional meta-biomaterials," *Mater. Horizons*, vol. 5, no. 1, pp. 28–35, 2018, doi: 10.1039/c7mh00699c.

[93] S. Mehmood, M. N. Ali, U. Ansari, M. Mir, and M. A. Khan, "Auxetic polymeric bone plate as internal fixator for long bone fractures : Design , fabrication and structural analysis," vol. 23, pp. 819–833, 2015, doi: 10.3233/THC-151021.

[94] J. Williams, *Ao Principles of Fracture*, vol. 2. 2017. doi: 10.1017/CBO9781107415324.004.

[95] R. Huiskes and E. Y. S. Chao, "A SURVEY OF FINITE ELEMENT ANALYSIS IN ORTHOPEDIC BIOMECHANICS: THE FIRST DECADE," vol. 16, no. 6, pp. 385–409, 1983, [Online]. Available: http://www.jbiomech.com/article/0021-9290(83)90072-6/pdf

[96] J. Arnone, "Z. Computer-Aided Engineering Approach for Parametric Investigation of Locked Plating Systems Design," *J. Med. Device.*, vol. 7, no. June 2013, p. 21001, 2013, doi: 10.1115/1.4024644.

[97] S. Samiezadeh, P. Tavakkoli, and Z. Fawaz, "On optimization of a composite bone plate using the selective stress shielding approach," vol. 42, pp. 138–153, 2015, doi: 10.1016/j.jmbbm.2014.11.015.

[98] N. D. Chakladar, L. T. Harper, and A. J. Parsons, "Optimisation of composite bone plates for ulnar transverse fractures," *J. Mech. Behav. Biomed. Mater.*, vol. 57, pp. 334–346, 2016, doi: 10.1016/j.jmbbm.2016.01.029.

[99] A. Synek, Y. Chevalier, S. F. Baumbach, and D. H. Pahr, "The influence of bone density and anisotropy in finite element models of distal radius fracture osteosynthesis: Evaluations and comparison to experiments," *J. Biomech.*, vol. 48, pp. 4116–4123, 2015, doi: 10.1016/j.jbiomech.2015.10.012.

[100] R. Moreno, O. Smedby, and M. Borga, "On the Efficiency of the Mean Intercept Length Tensor," *SSBA Symp.*, 2011.

[101] P. Varga, L. Grünwald, J. A. Inzana, and M. Windolf, "Fatigue failure of plated osteoporotic proximal humerus fractures is predicted by the strain around the proximal screws," *J. Mech. Behav. Biomed. Mater.*, vol. 75, no. March, pp. 68–74, 2017, doi: 10.1016/j.jmbbm.2017.07.004.

[102] P. Varga, J. A. Inzana, B. Gueorguiev, N. P. Südkamp, and M. Windolf, "Validated computational framework for efficient systematic evaluation of osteoporotic fracture fixation in the proximal humerus," *Med. Eng. Phys.*, vol. 57, pp. 29–39, 2018, doi: 10.1016/j.medengphy.2018.04.011.

[103] D. Dragomir-daescu, J. O. Den Buijs, S. Mceligot, Y. Dai, and C. Rachel, "NIH Public Access," vol. 39, no. 2, 2013, doi: 10.1007/s10439-010-0196-y.Robust.

[104] S. Cowin and J. Telega, "Bone Mechanics Handbook, 2nd Edition. -," *Appl. Mech. Rev.*, 2003, doi: 10.1115/1.1579463.

[105] H. Mehboob and S. H. Chang, "Effect of structural stiffness of composite bone plate-scaffold assembly on tibial fracture with large fracture gap," *Compos. Struct.*, vol. 124, pp. 327–336, 2015, doi: 10.1016/j.compstruct.2015.01.011.

[106] A.-M. Pobloth *et al.*, "Mechanobiologically optimized 3D titanium-mesh scaffolds enhance bone regeneration in critical segmental defects in sheep," 2018. Accessed: Apr. 29, 2019. [Online]. Available: http://stm.sciencemag.org/

[107] D. T. Simon, B. R., "EVALUATION OF ONE-. TWO-, AND THREE-DIMENSIONAL FINITE ELEMENT AND EXPERIMENTAL MODELS OF INTERNAL FIXATION PLATES*," 1977, [Online]. Available: https://ac.els-cdn.com/0021929077900719/1-s2.0-0021929077900719-main.pdf?_tid=35aaf206-cc8a-11e7-a0fc-

00000aab0f27&acdnat=1511028143_c9d9f6424e665b6c6bf0e349fa348034

[108] E. Gamsjäger, C. M. Bidan, F. D. Fischer, P. Fratzl, and J. W. C. Dunlop, "Modelling the role of surface stress on the kinetics of tissue growth in confined geometries," *Acta Biomater.*, vol. 9, pp. 5531–5543, 2013, doi: 10.1016/j.actbio.2012.10.020.

[109] A. Diez-escudero, H. Harlin, P. Isaksson, and C. Persson, "Porous polylactic acid scaffolds for bone regeneration : A study of additively manufactured triply periodic minimal surfaces and their osteogenic potential," 2020, doi: 10.1177/2041731420956541.

[110] I. Maskery *et al.*, "Insights into the mechanical properties of several triply periodic minimal surface lattice structures made by polymer additive manufacturing," *Polymer (Guildf).*, vol. 152, pp. 62–71, 2018, doi: 10.1016/j.polymer.2017.11.049.

[111] I. Maskery, A. O. Aremu, L. Parry, R. D. Wildman, C. J. Tuck, and I. A. Ashcroft, "Effective design and simulation of surface-based lattice structures featuring volume fraction and cell type grading," *Mater. Des.*, vol. 155, pp. 220–232, Oct. 2018, doi: 10.1016/j.matdes.2018.05.058.

[112] I. Maskery *et al.*, "Insights into the mechanical properties of several triply periodic minimal surface lattice structures made by polymer additive manufacturing," *Polymer (Guildf).*, vol. 152, pp. 62–71, 2018, doi: 10.1016/j.polymer.2017.11.049.

[113] S. F. Hulbert, F. A. Young, J. Klawitter, and C. D. Talbert, "Potential of Ceramic Materials as Permanently Implantable Skeletal Prostheses," *J. Biomed. Mater. Res.*, vol. 4, pp. 433–456, 1970.

[114] I. Bružauskaitė, D. Bironaitė, E. Bagdonas, and E. Bernotienė, "Scaffolds and cells for tissue regeneration: different scaffold pore sizes—different cell effects," *Cytotechnology*, vol. 68, no. 3, pp. 355–369, 2016, doi: 10.1007/s10616-015-9895-4.

[115] K. S. Lim, M. Baptista, S. Moon, and T. B. F. Woodfield, "Microchannels in Development , Survival , and Vascularisation of Tissue Analogues for Regenerative Medicine," *Trends Biotechnol.*, vol. 37, no. 11, pp. 1189–1201, 2019, doi: 10.1016/j.tibtech.2019.04.004.

[116] P. Carmeliet and R. K. Jain, "Angiogenesis in cancer and other diseases," *Insight Rev. Artic.*, pp. 249–257, 2000.

[117] J. Rouwkema *et al.*, "Supply of Nutrients to Cells in Engineered Tissues Supply of Nutrients to Cells in Engineered," *Biotechnol. Genet. Eng. Rev.*, vol. 8725, 2013, doi: 10.5661/bger-26-163.

[118] M. Kerschnitzki *et al.*, "Architecture of the osteocyte network correlates with bone material quality," *J. Bone Miner. Res.*, vol. 28, no. 8, pp. 1837–1845, 2013, doi: 10.1002/jbmr.1927.

[119] C. R. Maurer, R. Qi, and V. Raghavan, "A linear time algorithm for computing exact Euclidean distance transforms of binary images in arbitrary dimensions," *IEEE Trans. Pattern Anal. Mach. Intell.*, vol. 25, no. 2, pp. 265–270, 2003, doi: 10.1109/TPAMI.2003.1177156.

[120] G. N. Duda, E. Schneider, and E. Y. S. Chao, "Internal forces and moments in the femur during walking," *J. Biomech.*, vol. 30, no. 9, pp. 933–941, 1997, doi: 10.1016/S0021-9290(97)00057-2.

[121] "Medmovie.com." https://medmovie.com/topic/ml_0022/ml_0022_femur_fracture/

[122] D. Wu, P. Isaksson, S. J. Ferguson, and C. Persson, "Young's modulus of trabecular bone at the tissue level: A review," *Acta Biomater.*, vol. 78, pp. 1–12, 2018, doi: 10.1016/j.actbio.2018.08.001.

[123] N. Reznikov *et al.*, "Individual response variations in scaffold-guided bone regeneration are determined by independent strain- and injury-induced mechanisms," *Biomaterials*, vol. 194,

pp. 183–194, 2019, doi: 10.1016/j.biomaterials.2018.11.026.

[124] Y. Yang, G. Wang, H. Liang, C. Gao, S. Peng, and L. Shen, "Additive manufacturing of bone scaffolds," vol. 0, pp. 1–25, 2019.

[125] P. Tack, J. Victor, P. Gemmel, and L. Annemans, "3D-printing techniques in a medical setting: a systematic literature review," *Biomed. Eng. Online*, vol. 15, no. 1, p. 115, 2016, doi: 10.1186/s12938-016-0236-4.

[126] Z. Cai, Z. Liu, X. Hu, H. Kuang, and J. Zhai, "The effect of porosity on the mechanical properties of 3D-printed triply periodic minimal surface (TPMS) bioscaffold," *Bio-Design Manuf.*, vol. 2, no. 4, pp. 242–255, 2019, doi: 10.1007/s42242-019-00054-7.

[127] Z. Dong and X. Zhao, "Application of TPMS structure in bone regeneration," *Eng. Regen.*, vol. 2, no. August, pp. 154–162, 2021, doi: 10.1016/j.engreg.2021.09.004.

[128] S. Ma *et al.*, "Manufacturability, Mechanical Properties, Mass-Transport Properties and Biocompatibility of Triply Periodic Minimal Surface (TPMS) Porous Scaffolds Fabricated by Selective Laser Melting," *Mater. Des.*, vol. 195, 2020, doi: 10.1016/j.matdes.2020.109034.

[129] S. Wang, Z. Shi, L. Liu, X. Zhou, L. Zhu, and Y. Hao, "The design of Ti6Al4V Primitive surface structure with symmetrical gradient of pore size in biomimetic bone scaffold," *Mater. Des.*, vol. 193, p. 108830, 2020, doi: 10.1016/j.matdes.2020.108830.

[130] I. Nishimura *et al.*, "Effect of osteogenic differentiation medium on proliferation and differentiation of human mesenchymal stem cells in three-dimensional culture with radial flow bioreactor," *Regen. Ther.*, vol. 2, pp. 24–31, 2015, doi: 10.1016/j.reth.2015.09.001.

[131] L. Meinel *et al.*, "Bone tissue engineering using human mesenchymal stem cells: Effects of scaffold material and medium flow," *Ann. Biomed. Eng.*, vol. 32, no. 1, pp. 112–122, 2004, doi: 10.1023/B:ABME.0000007796.48329.b4.

[132] S. D. Boden, J. Kang, H. Sandhu, and J. G. Heller, "Use of Recombinant Human Bone Morphogenetic Protein-2 to Achieve Posterolateral Lumbar Spine Fusion in Humans A Prospective , Randomized Clinical Pilot Trial 2002 Volvo Award in Clinical Studies," vol. 27, no. 23, pp. 2662–2673, 2002.

[133] H. Lysdahl, A. Baatrup, C. B. Foldager, and C. Bünger, "Preconditioning human mesenchymal stem cells with a low concentration of BMP2 stimulates proliferation and osteogenic differentiation in vitro," *Biores. Open Access*, vol. 3, no. 6, pp. 278–285, 2014, doi: 10.1089/biores.2014.0044.

[134] H. E. Davis *et al.*, "Osteogenic Response to BMP-2 of hMSCs Grown on Apatite-Coated Scaffolds", doi: 10.1002/bit.23227.

[135] A. J. Engler, S. Sen, H. Lee Sweeney, and D. E. Discher, "Matrix Elasticity Directs Stem Cell Lineage Specification", doi: 10.1016/j.cell.2006.06.044.

[136] S. M. Giannitelli, D. Accoto, M. Trombetta, and A. Rainer, "Current trends in the design of scaffolds for computer-aided tissue engineering," 2014, doi: 10.1016/j.actbio.2013.10.024.

[137] K. A. Kilian, B. Bugarija, B. T. Lahn, and M. Mrksich, "Geometric cues for directing the differentiation of mesenchymal stem cells", doi: 10.1073/pnas.0903269107.

[138] "Boston Micro Fabrication (BMF)." https://bmf3d.com/

[139] "Formlabs SLA printer." https://formlabs.com/store/form-2/

[140] "Formlabs dental clear material." https://dental-media.formlabs.com/datasheets/Dental_LT_Clear_Technical.pdf

[141] C. Zhang *et al.*, "Mechanical characteristics and deformation mechanism of functionally graded triply periodic minimal surface structures fabricated using stereolithography," *Int. J. Mech. Sci.*, vol. 208, no. July, p. 106679, 2021, doi: 10.1016/j.ijmecsci.2021.106679.

[142] L. Germain, C. A. Fuentes, A. W. van Vuure, A. des Rieux, and C. Dupont-Gillain, "3D-printed biodegradable gyroid scaffolds for tissue engineering applications," *Mater. Des.*, vol. 151, pp. 113–122, Aug. 2018, doi: 10.1016/j.matdes.2018.04.037.

[143] S. N. Khaderi, V. S. Deshpande, and N. A. Fleck, "The stiffness and strength of the gyroid lattice," *Int. J. Solids Struct.*, vol. 51, no. 23–24, pp. 3866–3877, 2014, doi: 10.1016/j.ijsolstr.2014.06.024.

[144] et al. Mori, T., Kiyono, T., Imabayashi, H., Takeda, Y., Tsuchiya, K., Miyoshi, S., "Combination of hTERT and Bmi-1 , E6, or E7 Induces Prolongation of the Life Span of Bone Marrow Stromal Cells from an Elderly Donor without Affecting Their Neurogenic Potential," *Mol. Cell Biol.*, vol. 25, no. 5183–5195, 2005, doi: 10.1128/mcb.25.12.5183-5195.2005.

[145] et al. Balducci, L., Blasi, A., Saldarelli, M., Soleti, A., Pessina, A., Bonomi, A., "Immortalization of Human Adipose-Derived Stromal Cells: Production of Cell Lines with High Growth Rate, Mesenchymal Marker Expression and Capability to Secrete High Levels of Angiogenic Factors.," *Stem Cell Res. Ther.*, vol. 5, no. 63, 2014, doi: 10.1186/scrt452.

[146] et al. Burroughs, L., Amer, M. H., Vassey, M., Koch, B., Figueredo, G. P., Mukonoweshuro, B., "Discovery of Synergistic Material-Topography Combinations to Achieve Immunomodulatory Osteoinductive Biomaterials Using a Novel In Vitro Screening Method: The ChemoTopoChip.," *Biomaterials*, vol. 271, no. 120740, 2021, doi: 10.1016/j.biomaterials.2021.120740.

[147] S. Yamada, M. A. Yassin, T. Weigel, T. Schmitz, J. Hansmann, and K. Mustafa, "Surface activation with oxygen plasma promotes osteogenesis with enhanced extracellular matrix formation in three-dimensional microporous scaffolds," *J. Biomed. Mater. Res. - Part A*, vol. 109, no. 9, pp. 1560–1574, 2021, doi: 10.1002/jbm.a.37151.

[148] T V. N. Ratna Kumari and B. R. Ahmed Mujib, "Toluidine Blue with a Synergistic Effect in Morphological Assessment of Oral Cytosmears." 2018.

[149] C. Bäumer, E. Fisch, H. Wedler, F. Reinecke, and C. Korfhage, "Exploring DNA quality of single cells for genome analysis with simultaneous whole-genome amplification," *Sci. Rep.*, vol. 8, no. 1, pp. 2–11, 2018, doi: 10.1038/s41598-018-25895-7.

[150] D. Koley and A. J. Bard, "Triton X-100 concentration effects on membrane permeability of a single HeLa cell by scanning electrochemical microscopy (SECM)," *Proc. Natl. Acad. Sci. U. S. A.*, vol. 107, no. 39, pp. 16783–16787, 2010, doi: 10.1073/pnas.1011614107.

[151] Y. C. Kwon and M. C. Jewett, "High-throughput preparation methods of crude extract for robust cell-free protein synthesis," *Sci. Rep.*, vol. 5, pp. 1–8, 2015, doi: 10.1038/srep08663.

[152] A. K. Nguyen and R. J. Narayan, "Two-photon polymerization for biological applications," *Mater. Today*, vol. 20, no. 6, pp. 314–322, 2017, doi: 10.1016/j.mattod.2017.06.004.

[153] F. O. Ribeiro, M. José Gómez-Benito, J. Folgado, P. R. Fernandes, and J. Manuel García-Aznar, "In silico Mechano-Chemical Model of Bone Healing for the Regeneration of Critical Defects: The Effect of BMP-2," 2015, doi: 10.1371/journal.pone.0127722.

[154] J. C. Reichert *et al.*, "Custom-made composite scaffolds for segmental defect repair in long

bones," *Int. Orthop.*, vol. 35, no. 8, pp. 1229–1236, 2011, doi: 10.1007/s00264-010-1146-x.

[155] H. K. Uhthoff, P. Poitras, and D. S. Backman, "Internal plate fixation of fractures: short history and recent developments," *J Orthop Sci*, vol. 11, pp. 118–126, 2006, doi: 10.1007/s00776-005-0984-7.

[156] M. Niinomi and M. Nakai, "Titanium-based biomaterials for preventing stress shielding between implant devices and bone," *Int. J. Biomater.*, vol. 2011, 2011, doi: 10.1155/2011/836587.

[157] V. Ganesh, K. Ramakrishna, and D. N. Ghista, "Biomechanics of bone-fracture fixation by stiffness-graded plates in comparison with stainless-steel plates," 2005, doi: 10.1186/1475-925X-4-46.

[158] A. M. Pobloth *et al.*, "Mechanobiologically optimized 3D titanium-mesh scaffolds enhance bone regeneration in critical segmental defects in sheep," *Sci. Transl. Med.*, vol. 10, no. 423, 2018, doi: 10.1126/scitranslmed.aam8828.

[159] Synthes GmbH, "Large Fragment Locking Compression Plate (LCP) - Technique Guide," no. 432, 2003.

[160] A. R. MacLeod, P. Pankaj, and A. H. R. W. Simpson, "Does screw-bone interface modelling matter in finite element analyses?," *J. Biomech.*, vol. 45, no. 9, pp. 1712–1716, 2012, doi: 10.1016/j.jbiomech.2012.04.008.

[161] J. C. Arnone, A. Sherif El-Gizawy, B. D. Crist, G. J. Della Rocca, and C. V. Ward, "Computer-Aided Engineering Approach for Parametric Investigation of Locked Plating Systems Design," *J. Med. Device.*, vol. 7, no. 2, p. 021001, 2013, doi: 10.1115/1.4024644.

[162] V. Shim, J. Böhme, P. Vaitl, S. Klima, C. Josten, and I. Anderson, "Finite element analysis of acetabular fractures-development and validation with a synthetic pelvis," *J. Biomech.*, vol. 43, no. 8, pp. 1635–1639, 2010, doi: 10.1016/j.jbiomech.2010.01.017.

[163] C. Albert, J. Jameson, S. Tarima, P. Smith, and G. Harris, "Macroscopic anisotropic bone material properties in children with severe osteogenesis imperfecta," *J. Biomech.*, 2017, doi: 10.1016/j.jbiomech.2017.09.003.

[164] C. N. Elias, D. J. Fernandes, F. M. De Souza, E. D. S. Monteiro, and R. S. De Biasi, "Mechanical and clinical properties of titanium and titanium-based alloys (Ti G2, Ti G4 cold worked nanostructured and Ti G5) for biomedical applications," *J. Mater. Res. Technol.*, vol. 8, no. 1, pp. 1060–1069, 2019, doi: 10.1016/j.jmrt.2018.07.016.

[165] A. Saboori, A. Aversa, G. Marchese, S. Biamino, M. Lombardi, and P. Fino, "Microstructure and mechanical properties of AISI 316L produced by directed energy deposition-based additive manufacturing: A review," *Appl. Sci.*, vol. 10, no. 9, 2020, doi: 10.3390/app10093310.

[166] J. E. Compston, S. Vedi, S. Kaptoge, and E. Seeman, "Bone Remodeling Rate and Remodeling Balance Are Not Co-Regulated in Adulthood: Implications for the Use of Activation Frequency as an Index of Remodeling Rate," vol. 22, no. 7, 2007, doi: 10.1359/JBMR.070407.

[167] E. Lehder, "Optimisation of a stiffness-graded fracture fixation plate," Delft University of Technology, 2018. [Online]. Available: https://repository.tudelft.nl/islandora/object/uuid%3A4ea1a40a-82df-4dc3-a322-fc6551935b8b

[168] J. A. Elishakoff, E., Li, Y., Starnes Jr, J.H. and Cheney, "Non-classical problems in the theory of elastic stability," *Appl. Mech. Rev.*, vol. 54(5), pp. B86–B86, 2001.

[169] et al. Giorgio, Ivan, "In-depth gaze at the astonishing mechanical behavior of bone: A review for designing bio-inspired hierarchical metamaterials," *Math. Mech. Solids*, vol. 26.7, no. 1074–1103, 2021.

[170] E. Bednarczyk and T. Lekszycki, "A novel mathematical model for growth of capillaries and nutrient supply with application to prediction of osteophyte onset," 2016, doi: 10.1007/s00033-016-0687-2.

[171] L. Zhang *et al.*, "Investigation of mechanism of bone regeneration in a porous biodegradable calcium phosphate (CaP) scaffold by a combination of a multi-scale agent-based model and experimental optimization/validation," *Nanoscale*, vol. 8, p. 14877, 2016, doi: 10.1039/c6nr01637e.

[172] M. Rumpler, A. Woesz, J. W. C. Dunlop, J. T. Van Dongen, and P. Fratzl, "The effect of geometry on three-dimensional tissue growth," *J. R. Soc. Interface*, 2008, doi: 10.1098/rsif.2008.0064.

[173] S. B. T. Bolder, B. W. Schreurs, N. Verdonschot, J. M. J. Van Unen, J. W. M. Gardeniers, and T. J. J. H. Slooff, "Particle size of bone graft and method of impaction affect initial stability of cemented cups: Human cadaveric and synthetic pelvic specimen studies," *Acta Orthop. Scand.*, vol. 74, no. 6, pp. 652–657, 2003, doi: 10.1080/00016470310018144.

[174] A. G. Mitsak, J. M. Kemppainen, M. T. Harris, and S. J. Hollister, "Effect of polycaprolactone scaffold permeability on bone regeneration in vivo," *Tissue Eng. - Part A*, vol. 17, no. 13–14, pp. 1831–1839, 2011, doi: 10.1089/ten.tea.2010.0560.

[175] N. Abbasi, S. Hamlet, R. M. Love, and N. T. Nguyen, "Porous scaffolds for bone regeneration," *J. Sci. Adv. Mater. Devices*, vol. 5, no. 1, pp. 1–9, 2020, doi: 10.1016/j.jsamd.2020.01.007.

[176] K. Piironen, M. Haapala, V. Talman, P. Järvinen, and T. Sikanen, "Cell adhesion and proliferation on common 3D printing materials used in stereolithography of microfluidic devices," *Lab Chip*, vol. 20, no. 13, pp. 2372–2382, 2020, doi: 10.1039/d0lc00114g.

[177] M. Bianchi *et al.*, "Substrate geometry directs the in vitro mineralization of calcium phosphate ceramics," *Acta Biomater.*, vol. 10, no. 2, pp. 661–669, 2014, doi: 10.1016/j.actbio.2013.10.026.

[178] F. Liu, Q. Ran, M. Zhao, T. Zhang, D. Z. Zhang, and Z. Su, "Additively Manufactured Continuous Cell-Size Mechanical Properties and Biological Responses In Vitro," *Materials (Basel).*, vol. 13, no. 2589, 2020.

[179] S. Tsai *et al.*, "Risk factors for refracture after plate removal for midshaft clavicle fracture after bone union," pp. 1–8, 2019.

[180] A. Azapagic and R. Clift, "Life cycle assessment and multiobjective optimisation," *J. Clean. Prod.*, vol. 7, no. 2, pp. 135–143, 1999, doi: 10.1016/s0959-6526(98)00051-1.

[181] A. C. Weems, M. C. Arno, W. Yu, R. T. R. Huckstepp, and A. P. Dove, "scaffolds for soft tissue repair," no. 2021, pp. 1–14.

[182] T. Adachi, Y. Osako, M. Tanaka, M. Hojo, and S. J. Hollister, "Framework for optimal design of porous scaffold microstructure by computational simulation of bone regeneration," *Biomaterials*, vol. 27, pp. 3964–3972, 2006, doi: 10.1016/j.biomaterials.2006.02.039.

[183] J.-L. Milan, J. A. Planell, and D. Lacroix, "Simulation of bone tissue formation within a porous scaffold under dynamic compression," *Biomech Model Mechanobiol*, vol. 9, pp. 583–596, 2010, doi: 10.1007/s10237-010-0199-5.

[184] J. A. Sanz-Herrera, J. M. Garcia-Aznar, and · M Doblare, "A mathematical model for bone tissue

regeneration inside a specific type of scaffold," *Biomech Model Mechanobiol*, vol. 7, pp. 355–366, 2008, doi: 10.1007/s10237-007-0089-7.

[185] A. R. Patrachari, J. T. Podichetty, and S. V Madihally, "Application of computational fluid dynamics in tissue engineering," *J. Biosci. Bioeng.*, vol. 114, pp. 123–132, 2012, doi: 10.1016/j.jbiosc.2012.03.010.

[186] C. Jungreuthmayer, M. J. Jaasma, A. A. Al-Munajjed, J. Zanghellini, D. J. Kelly, and F. J. O'brien, "Deformation simulation of cells seeded on a collagen-GAG scaffold in a flow perfusion bioreactor using a sequential 3D CFD-elastostatics model," *Med. Eng. Phys.*, vol. 31, pp. 420–427, 2009, doi: 10.1016/j.medengphy.2008.11.003.

[187] A. L. Olivares, L. Marsal, J. A. Planell, and D. Lacroix, "Finite element study of scaffold architecture design and culture conditions for tissue engineering," *Biomaterials*, vol. 30, pp. 6142–6149, 2009, doi: 10.1016/j.biomaterials.2009.07.041.

[188] R. J. Mccoy, C. Jungreuthmayer, and F. J. O'brien, "ARTICLE Influence of Flow Rate and Scaffold Pore Size on Cell Behavior During Mechanical Stimulation in a Flow Perfusion Bioreactor," *Biotechnol. Bioeng*, vol. 109, pp. 1583–1594, 2012, doi: 10.1002/bit.24424.

[189] F. Zhao, T. J. Vaughan, · Laoise, and M. Mcnamara, "Quantification of fluid shear stress in bone tissue engineering scaffolds with spherical and cubical pore architectures," *Biomech Model Mechanobiol*, vol. 15, pp. 561–577, 2016, doi: 10.1007/s10237-015-0710-0.

[190] T. J. Vaughan, C. A. Mullen, · S W Verbruggen, and · L M Mcnamara, "Bone cell mechanosensation of fluid flow stimulation: a fluid-structure interaction model characterising the role integrin attachments and primary cilia," *Biomech. Model. Mechanobiol.*, vol. 14, pp. 703–718, 2015, doi: 10.1007/s10237-014-0631-3.

[191] T. Rüberg and J. Manuel Garcí Aznar, "Numerical simulation of solid deformation driven by creeping flow using an immersed finite element method," *Model. Simul. Eng. Sci*, vol. 3, p. 9, 2016, doi: 10.1186/s40323-016-0061-0.

[192] R. H. Skes, W. D. Van Driel, P. J. Prendergast, and K. Søballe, "A biomechanical regulatory model for periprosthetic fibrous-tissue differentiation," 1997. Accessed: May 06, 2019. [Online]. Available: https://link.springer.com/content/pdf/10.1023/A:1018520914512.pdf

[193] D. P. Byrne, D. Lacroix, J. A. Planell, D. J. Kelly, and P. J. Prendergast, "Simulation of tissue differentiation in a scaffold as a function of porosity, Young's modulus and dissolution rate: Application of mechanobiological models in tissue engineering," *Biomaterials*, vol. 28, pp. 5544–5554, 2007, doi: 10.1016/j.biomaterials.2007.09.003.

[194] Y. Guyot, · I Papantoniou, F. P. Luyten, and · L Geris, "Coupling curvature-dependent and shear stress-stimulated neotissue growth in dynamic bioreactor cultures: a 3D computational model of a complete scaffold," *Biomech Model Mechanobiol*, vol. 15, pp. 169–180, 2016, doi: 10.1007/s10237-015-0753-2.

[195] M. M. Nava, M. T. Raimondi, R. Pietrabissa, M. M. Nava, · M T Raimondi, and · R Pietrabissa, "A multiphysics 3D model of tissue growth under interstitial perfusion in a tissue-engineering bioreactor," *Biomech Model Mechanobiol*, vol. 12, pp. 1169–1179, 2013, doi: 10.1007/s10237-013-0473-4.

[196] J. A. Sanz-Herrera, J. M. García-Aznar, and M. Doblaré, "Micro-macro numerical modelling of bone regeneration in tissue engineering," 2008, doi: 10.1016/j.cma.2008.02.010.

[197] S. Soliman *et al.*, "Multiscale three-dimensional scaffolds for soft tissue engineering via multimodal electrospinning," *Acta Biomater.*, vol. 6, pp. 1227–1237, 2009, doi:

10.1016/j.actbio.2009.10.051.

[198]   S. Jamaleddin Mousavi, M. Doblaré, M. Hamdy Doweidar -, M. J. Gómez-Benito, and al -, "Mechano-sensing and cell migration: a 3D model approach," 2011, doi: 10.1088/1478-3975/8/6/066008.

[199]   C. Borau, W. J. Polacheck, R. D. Kamm, and J. M. García-Aznar, "Probabilistic Voxel-Fe model for single cell motility in 3D", doi: 10.1186/2196-050X-1-2.

[200]   P. Moreo, J. Manuel García-Aznar, and M. Doblaré, "Modeling mechanosensing and its effect on the migration and proliferation of adherent cells," 2007, doi: 10.1016/j.actbio.2007.10.014.

[201]   C. Borau, R. D. Kamm, and J. M. García-Aznar, "A TIME-DEPENDENT PHENOMENOLOGICAL MODEL FOR CELL MECHANO-SENSING", doi: 10.1007/s10237-013-0508-x.

[202]   Y. Y. Biton and S. A. Safran, "The cellular response to curvature-induced stress Related content," 2009, doi: 10.1088/1478-3975/6/4/046010.

[203]   T. Ozdemir, L.-C. Xu, C. Siedlecki, and J. L. Brown, "Substrate curvature sensing through Myosin IIa upregulates early osteogenesis," *This J. is c R. Soc. Chem.*, vol. 5, p. 1407, 2013, doi: 10.1039/c3ib40068a.

[204]   J. A. Sanz-Herrera, P. Moreo, J. M. García-Aznar, and M. Doblaré, "On the effect of substrate curvature on cell mechanics," 2009, doi: 10.1016/j.biomaterials.2009.08.053.

[205]   C. M. Bidan, K. P. Kommareddy, M. Rumpler, P. Kollmannsberger, and Y. Bréchet, "How Linear Tension Converts to Curvature: Geometric Control of Bone Tissue Growth," *PLoS One*, vol. 7, no. 5, p. 36336, 2012, doi: 10.1371/journal.pone.0036336.

[206]   E. C. Holden, J. Collis, B. S. Brook, and R. D. ODea, "A multiphase multiscale model for nutrient limited tissue growth," *ANZIAM J.*, vol. 59, no. 4, pp. 499–532, 2018, doi: 10.1017/S1446181118000044.

[207]   V. S. Cheong, P. Fromme, A. Mumith, M. J. Coathup, and G. W. Blunn, "Novel adaptive finite element algorithms to predict bone ingrowth in additive manufactured porous implants," *J. Mech. Behav. Biomed. Mater.*, vol. 87, pp. 230–239, Nov. 2018, doi: 10.1016/j.jmbbm.2018.07.019.

[208]   A. Boccaccio, A. E. Uva, M. Fiorentino, L. Lamberti, and G. Monno, "A Mechanobiology-based Algorithm to Optimize the Microstructure Geometry of Bone Tissue Scaffolds," *Int. J. Biol. Sci*, vol. 12, no. 1, pp. 1–17, 2016, doi: 10.7150/ijbs.13158.

[209]   V. B. Shim, J. Böshme, P. Vaitl, C. Josten, and I. A. Anderson, "An Efficient and Accurate Prediction of the Stability of Percutaneous Fixation of Acetabular Fractures With Finite Element Simulation," *J. Biomech. Eng.*, vol. 133, no. 9, p. 094501, 2011, doi: 10.1115/1.4004821.

[210]   M. Ni, D. W. C. Wong, J. Mei, W. Niu, and M. Zhang, "Biomechanical comparison of locking plate and crossing metallic and absorbable screws fixations for intra-articular calcaneal fractures," *Sci. China Life Sci.*, vol. 59, no. 9, pp. 958–964, 2016, doi: 10.1007/s11427-016-0010-9.

[211]   H. Y. K. Cheng, C. L. Lin, Y. H. Lin, and A. C. Y. Chen, "Biomechanical evaluation of the modified double-plating fixation for the distal radius fracture," *Clin. Biomech.*, vol. 22, no. 5, pp. 510–517, 2007, doi: 10.1016/j.clinbiomech.2006.12.010.

[212]   J.-J. Zhou, M. Zhao, D. Liu, H.-Y. Liu, and C.-F. Du, "Biomechanical Property of a Newly Designed Assembly Locking Compression Plate: Three-Dimensional Finite Element Analysis," *J. Healthc. Eng.*, vol. 2017, pp. 1–10, 2017, doi: 10.1155/2017/8590251.

[213] C. Lee, C. Hsu, and P. Huang, "Biomechanical study of different fi xation techniques for the treatment of sacroiliac joint injuries using fi nite element analyses and biomechanical tests," *Comput. Biol. Med.*, vol. 87, no. 43, pp. 250–257, 2017, doi: 10.1016/j.compbiomed.2017.06.007.

[214] C.-L. Lin, Y.-H. Lin, and A. C.-Y. Chen, "Buttressing angle of the double-plating fixation of a distal radius fracture: a finite element study," *Med. Biol. Eng. Comput.*, vol. 44, no. 8, pp. 665–673, 2006, doi: 10.1007/s11517-006-0082-9.

[215] J.-K. Oh *et al.*, "Effect of fracture gap on stability of compression plate fixation: A finite element study," *J. Orthop. Res.*, no. April, p. n/a-n/a, 2009, doi: 10.1002/jor.20990.

[216] C. Salas, D. Mercer, T. A. DeCoster, and M. M. Reda Taha, "Experimental and probabilistic analysis of distal femoral periprosthetic fracture: A comparison of locking plate and intramedullary nail fixation. Part B: Probabilistic investigation," *Comput. Methods Biomech. Biomed. Engin.*, vol. 14, no. 2, pp. 175–182, 2011, doi: 10.1080/10255842.2010.539207.

[217] S. Chen, M. Chiang, C. Hung, S. Lin, and H. Chang, "Finite element comparison of retrograde intramedullary nailing and locking plate fi xation with / without an intramedullary allograft for distal femur fracture following total knee arthroplasty," *Knee*, vol. 21, no. 1, pp. 224–231, 2014, doi: 10.1016/j.knee.2013.03.006.

[218] G. Sztrinkai *et al.*, "Further development of our finite element pelvic model to compare fixation methods for pelvic fractures," *Eklem Hast. ve Cerrahisi*, vol. 25, no. 1, pp. 8–14, 2014, doi: 10.5606/ehc.2014.03.

[219] A. Shirurkar, A. Tamboli, and P. N. Jagtap, "Mechanical Behavior of ZM21 Magnesium Alloy Locking Plates – An Experimental and Finite Element Study," *Mater. Today Proc.*, vol. 4, no. 6, pp. 6728–6736, 2017, doi: 10.1016/j.matpr.2017.06.448.

[220] S. Shah, S. Y. R. Kim, A. Dubov, E. H. Schemitsch, H. Bougherara, and R. Zdero, "The biomechanics of plate fixation of periprosthetic femoral fractures near the tip of a total hip implant: Cables, screws, or both?," *Proc. Inst. Mech. Eng. Part H J. Eng. Med.*, vol. 225, no. 9, pp. 845–856, 2011, doi: 10.1177/0954411911413060.

[221] A. Dubov, S. Y. R. Kim, S. Shah, E. H. Schemitsch, R. Zdero, and H. Bougherara, "The biomechanics of plate repair of periprosthetic femur fractures near the tip of a total hip implant: The effect of cable-screw position," *Proc. Inst. Mech. Eng. Part H J. Eng. Med.*, vol. 225, no. 9, pp. 857–865, 2011, doi: 10.1177/0954411911410642.

[222] N. D. Chakladar, L. T. Harper, and A. J. Parsons, "Optimisation of composite bone plates for ulnar transverse fractures," 2016, doi: 10.1016/j.jmbbm.2016.01.029.

[223] S. Sezek, B. Aksakal, M. Gürger, M. Malkoc, and Y. Say, "Biomechanical comparison of straight and helical compression plates for fixation of transverse and oblique bone fractures: Modeling and experiments," *Biomed. Mater. Eng.*, vol. 27, pp. 197–209, 2016, doi: 10.3233/BME-161576.

Appendices

Appendix A: Cell growth model validation and calibration

To validate the level set cell growth model used here, the triangular scaffold from the original cell growth study by Guyot et al [37] was used. The geometry was acquired from the authors of that work. The implementation described in section 3.2.5 was used to compute the cell growth on the surface of the triangular scaffold and the results were then compared with those provided by Guyot et al. [37]. The results are shown in Figure 0-2, where it can be seen that the prediction of cell growth for the triangular scaffold closely matches that of the original work.

There are some differences in the curves, and it is hypothesised that these are because the original study used a tetrahedral mesh while here a hexagonal mesh is used. To ensure the result is correct however, a mesh convergence study was performed, and the cell growth rate was found to converge below a threshold of 1% at around 106 elements. For the purpose of this study, presenting a novel overall methodology to optimise bone regeneration scaffolds, this validation was deemed acceptable.
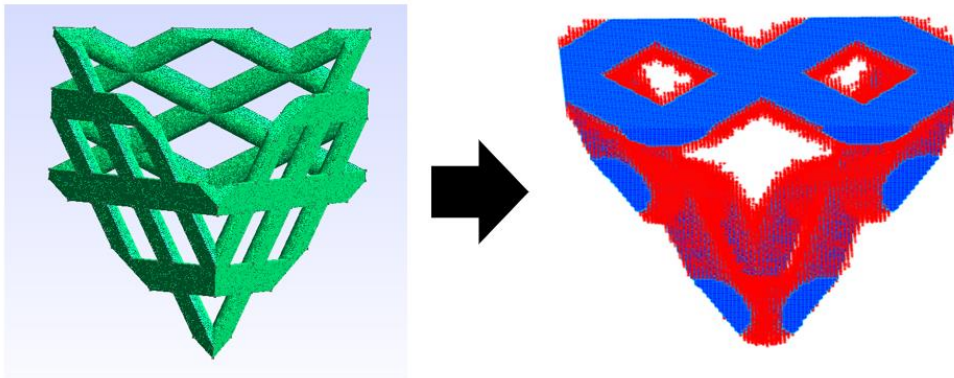

Figure 0-1: Tetrahedral mesh from Guyot et al. [37] (left) and voxelized mesh used in this study as well as darker voxels showing cell growth after five days (right).
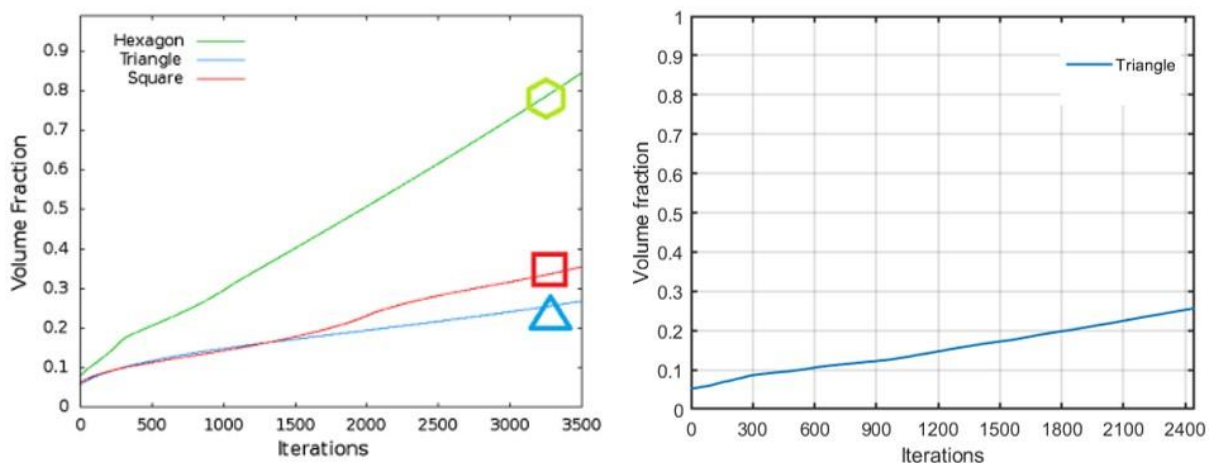

Figure 0-2: Model results from Guyot et al. [37] (left) and those computed in this study (right). In both graphs the number of iterations is equivalent to 16.3 days. Note that 'Volume fraction' in these figures refers to the cell growth as a fraction of the total volume enclosing the scaffold.
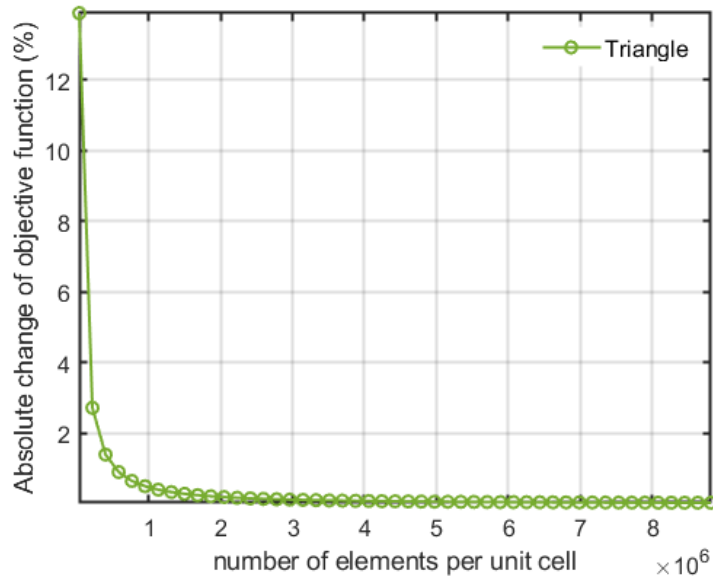
Figure 0-3: Mesh convergence for the triangular geometry. The objective function was the average growth rate and the y-axis on the plot represents the absolute change of this objective function in percentage. The x-axis shows the number of elements per scaffold unit cell.

Appendix B: Validation of bone-plate-scaffold half model

Full Model:

(view cut)

Quarter Model:
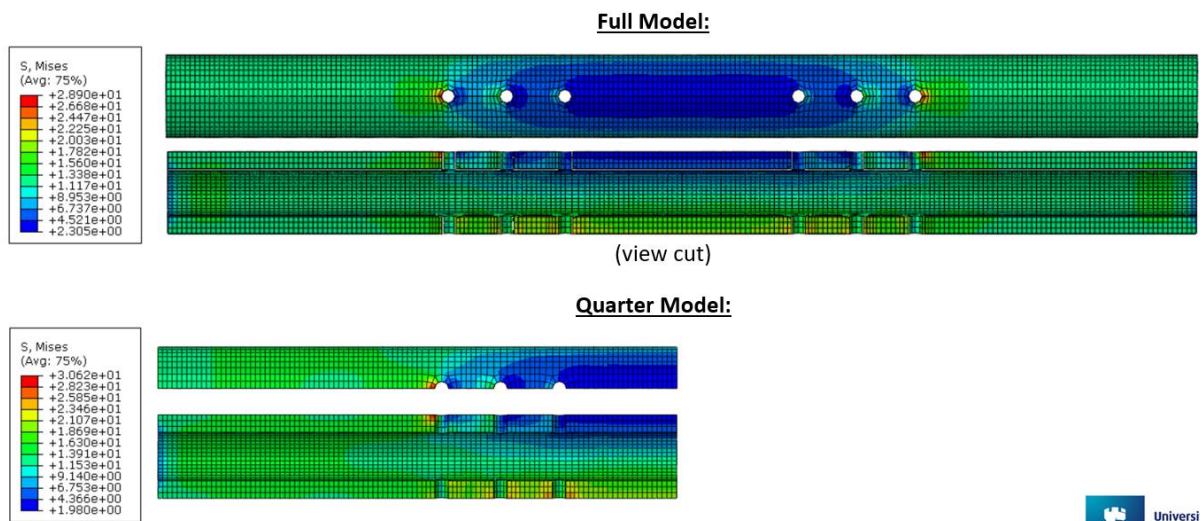
Figure 0-4: Validation of the half model via a contour plot.
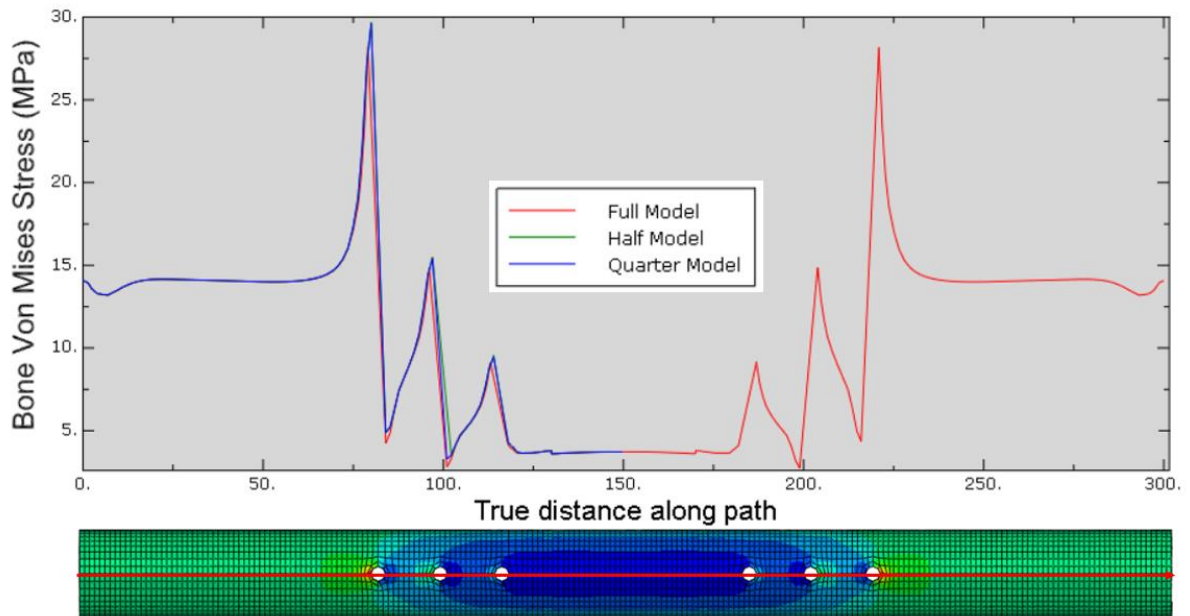
Figure 0-5: Validation of the half model via a path along the top axial line of the bone.

Appendix C: Mesh convergence for the bone-plate-scaffold Finite Element model
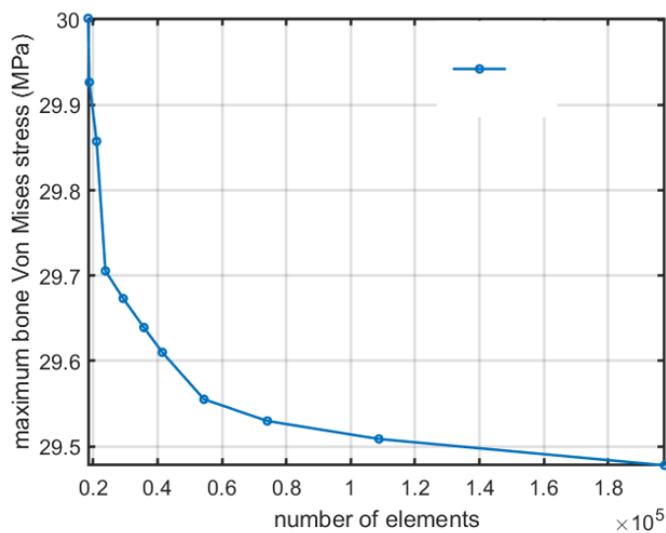
The variation percentage change at 41470 elements is 0.5%. Hence this number of elements was used.

Figure 0-6: Mesh convergence plot

Appendix D: Additional data fitting plots for bone-plate-scaffold modeling results

Figure 0-7: Mathematical fitted surface for the average interfragmentary strain as a function of end plate strut thickness and scaffold elastic modulus. Note that the other fitted surfaces can be found in the appendix.

Figure 0-8: Surface fit for the maximum Von Mises stress in the plate for both the healed and not healed cases.

Appendix E: Bone-plate-scaffold Finite Element result predictions
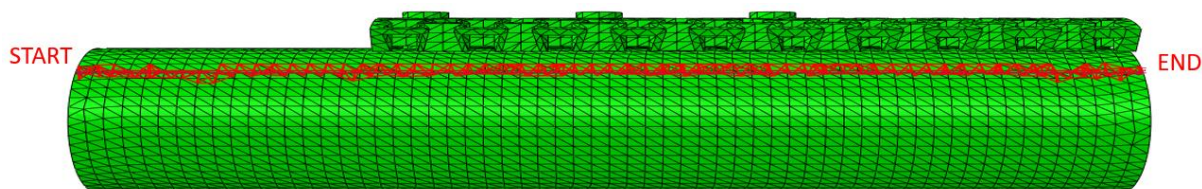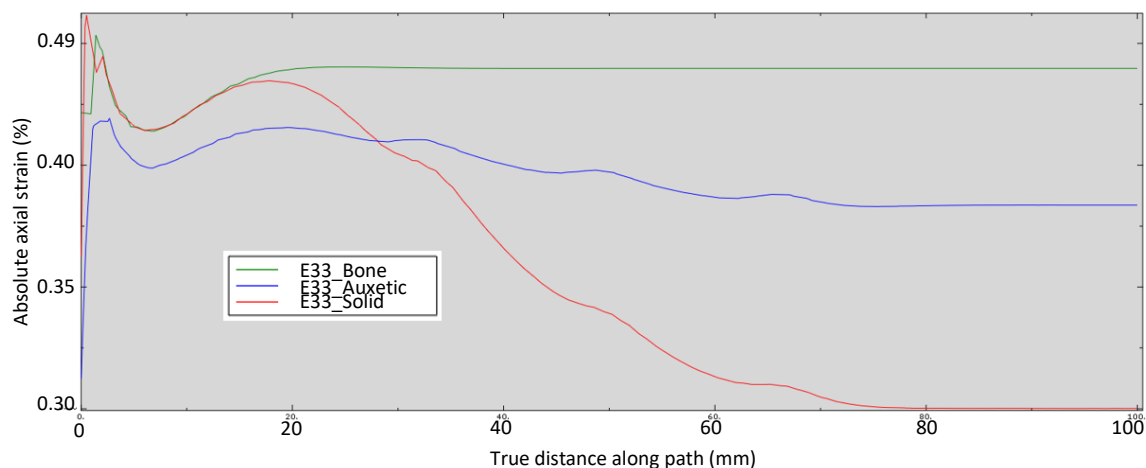
Figure 0-9: Graph showing the predicted strain distribution along the path to be measured experimentally.

Appendix F: Scaffold performance modelling articles

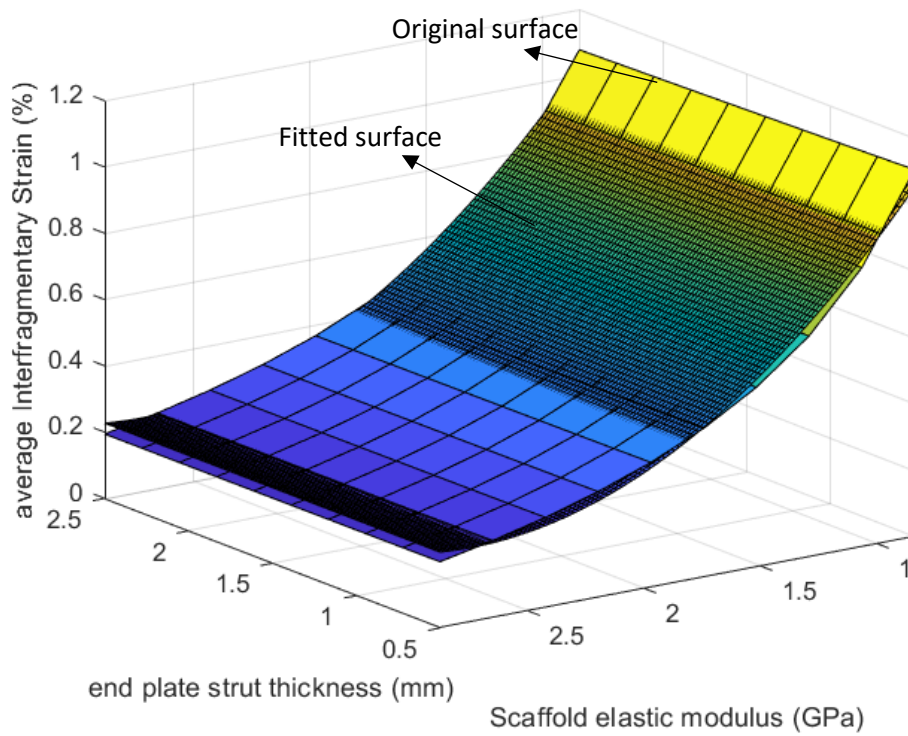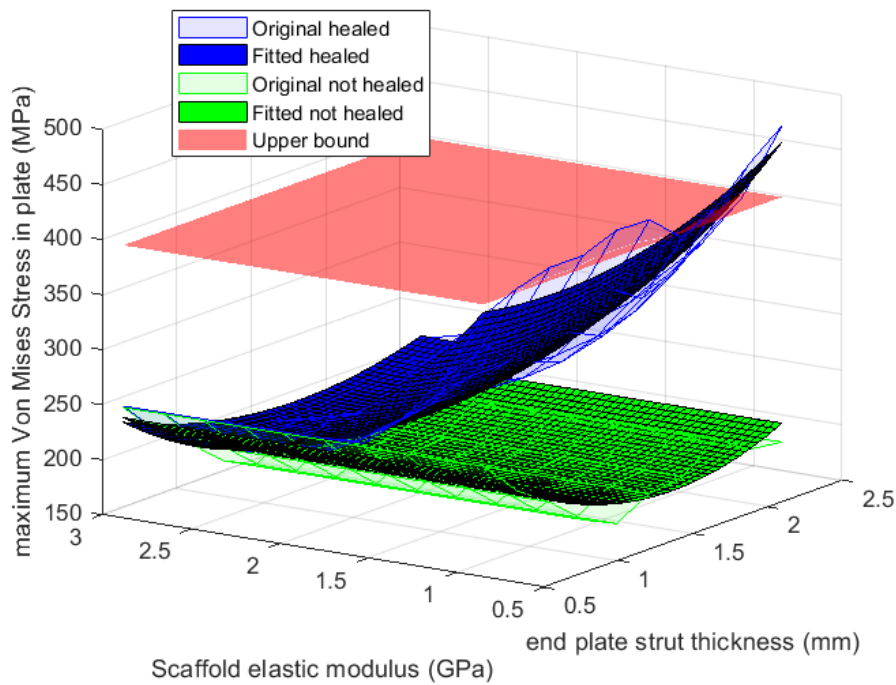On the table below, "S" stands for solid mechanics, "B" stands for biochemistry, "F" stands for fluid mechanics, "P" stands for pore scale, "T" stands for tissue scale and "C" stands for cell scale.

#	General				Physics	Scale	Ref
	Source	Title	Author1	Year			
1	Aznar2016	Framework for optimal design of porous scaffold microstructure by computational simulation of bone regeneration	Adachi T	2006	S	P	[182]
2	Aznar2016	Simulation of bone tissue formation within a porous scaffold under dynamic compression	Jean-Louis Milan	2010	S	T,P	[183]
3	Aznar2016	A mathematical model for bone tissue regeneration inside a specific type of scaffold	J. A. Sanz-Herrera	2007	S	T,P	[184]
4	Aznar2016	A mathematical approach to bone tissue engineering	J. A. SANZ-HERRERA	2009	S	T,P	[41]
5	Aznar2016	Application of computational fluid dynamics in tissue engineering	Anirudh R. Patrachari	2012	F	T	[185]

6	Aznar2016	Deformation simulation of cells seeded on a collagen-GAG scaffold in a flow perfusion bioreactor using a sequential 3D CFD-elastostatics model	C. Jungreuthmayer	2008	F	T,P,C	[186]
7	Aznar2016	Finite element study of scaffold architecture design and culture conditions for tissue engineering	Andy L. Olivares	2009	F	T,P	[187]
8	Aznar2016	Influence of flow rate and scaffold pore size on cell behaviour during mechanical stimulation in a flow perfusion bioreactor.	R.J. McCoy	2012	S,F	T,P	[188]
9	Aznar2016	Quantification of fluid shear stress in bone tissue engineering scaffolds with spherical and cubical pore architectures	Feihu Zhao	2016	S,F	T,P	[189]
10	Aznar2016	Bone cell mechano-sensation of fluid flow stimulation: a fluid-structure interaction model characterising the role integrin attachments and primary cilia	T. J. Vaughan	2015	S,F	C	[190]
11	Aznar2016	Numerical simulation of solid deformation driven by creeping flow using an immersed finite element method	Thomas Rüberg	2016	S,F	C	[191]
12	Aznar2016	A biomechanical regulatory model for periprosthetic fibrous-tissue differentiation	R. HUISKES	1997	S,F	T,P	[192]
13	Aznar2016	Prediction of the optimal mechanical properties for a scaffold used in osteochondral defect repair	Kelly DJ	2006	S,F	T,P	
14	Aznar2016	Simulation of tissue differentiation in a scaffold as a function of porosity, Young's modulus and dissolution rate: application of mechanobiological	Byrne DP	2007	S,F	T,P	[193]

15	Aznar201 6	Coupling curvature-dependent and shear stress-stimulated neotissue growth in dynamic bioreactor cultures: a 3D computational model of a complete scaffold	Guyot Y	2016	S,F	P	[194]
		models in tissue engineering					
16	Aznar201 6	A multiphysics 3D model of tissue growth under interstitial perfusion in a tissue- engineering bioreactor	Nava MM	2013	F,B	P	[195]
17	Aznar201 6	In silico mechano-chemical model of bone healing for the regeneration of critical defects: the effect of BMP-2	Ribeiro FO	2015	B	T	[153]
18	Aznar201 6	Micro–macro numerical modelling of bone regeneration in tissue engineering	J.A. Sanz-Herrera	2007	S	T,P	[196]
19	Aznar201 6	Multiscale three-dimensional scaffolds for soft tissue engineering via multimodal electrospinning	Soliman S	2010	S	P	[197]
20	Aznar201 6	Mechano-sensing and cell migration: a 3D model approach	C Borau	2011	S	C	[198]
21	Aznar201 6	Probabilistic Voxel-Fe model for single cell motility in 3D	Carlos Borau	2014	S,F,B	C	[199]
22	Aznar201 6	Modelling mechanosensing and its effect on the migration and proliferation of adherent cells	Pedro Moreo	2007	S	C	[200]
23	Aznar201 6	A time-dependent phenomenological model for cell mechano-sensing	Carlos Borau	2014	S	C	[201]
24	Aznar201 6	The cellular response to curvature- induced stress	Y Biton	2009	S	C	[202]
25	Aznar201 6	Substrate curvature sensing through Myosin IIa upregulates early osteogenesis	Tugba Ozdemir	2013	S,B	C	[203]

26	Aznar2016	On the effect of substrate curvature on cell mechanics	José´ A. Sanz-Herrera	2009	S,B	C	[204]
27	Aznar2016	How linear tension converts to curvature: geometric control of bone tissue growth	Bidan CM	2012			[205]
28	Thesis review	A multiphase multiscale model for nutrient limited tissue growth	Reuben O'Dea	2018	S,F	T,P	[206]
29	Thesis review	Novel adaptive finite element algorithms to predict bone ingrowth in additive manufactured porous implants	Vee San Cheong	2018	S	P	[207]
30	Thesis review	Computationally designed lattices with tuned properties for tissue engineering using 3D printing	Paul F. Egan	2017	S	T,P	[5]
31	Thesis review	A Mechanobiology-based Algorithm to Optimize the Microstructure Geometry of Bone Tissue Scaffolds	Antonio Boccaccio	2016	S,F	T,P	[208]
32	Thesis review	Investigation of mechanism of bone regeneration in a porous biodegradable calcium phosphate (CaP) scaffold by a combination of a multi-scale agent-based model and experimental optimization/validation	Le Zhang	2016	B	T,P,C	[171]

Appendix G: Table of Fracture Fixation plate modelling articles reviewed

Study name	Journal	Authors	Study year
An Efficient and Accurate Prediction of the Stability of Percutaneous Fixation of Acetabular Fractures with Finite Element Simulation	Journal of Biomechanical Engineering	Shim et al.	2011
Biomechanical comparison of locking plate and crossing metallic and absorbable screws fixations for intra-articular calcaneal fractures	Science China Life Sciences	Ni et al.	2016
Biomechanical evaluation of the modified double-plating fixation for the distal radius fracture	Clinical Biomechanics	Cheng et al.	2007

Biomechanical Property of a Newly Designed Assembly Locking Compression Plate: Three-Dimensional Finite Element Analysis	Journal of Healthcare Engineering	Zhou et al.	2017
Biomechanical study of different fixation techniques for the treatment of sacroiliac joint injuries using finite element analyses and biomechanical tests	Computers in Biology and Medicine	Lee et al.	2017
Buttressing angle of the double-plating fixation of a distal radius fracture: a finite element study	Medical and Biological Engineering and Computing	Lin et al.	2006
Effect of Fracture Gap on Stability of Compression Plate Fixation: A Finite Element Study	Journal of Orthopaedic research	Oh et al.	2009
EVALUATION OF ONE-. TWO-, AND THREE-DIMENSIONAL FINITE ELEMENT AND EXPERIMENTAL MODELS OF INTERNAL FIXATION PLATES	Journal of Biomechanics	Simon et al.	1977
Experimental and probabilistic analysis of distal femoral periprosthetic fracture: a comparison of locking plate and intramedullary nail fixation. Part B: probabilistic investigation	Computer Methods in Biomechanics and Biomedical Engineering	Salas et al.	2011
Fatigue failure of plated osteoporotic proximal humerus fractures is predicted by the strain around the proximal screws	Journal of the Mechanical Behaviour of Biomedical Materials	Varga et al.	2017
Finite element comparison of retrograde intramedullary nailing and locking plate fixation with/without an intramedullary allograft for distal femur fracture following total knee arthroplasty	The knee	Chen et al.	2014
Further development of a finite element pelvic model to compare fixation methods for pelvic fractures	Eklem Hastaliklari ve Cerrahisi	Sztrinkai et al.	2014
Mechanical Behaviour of ZM21 Magnesium Alloy Locking Plates – An Experimental and Finite Element Study	Materials Today: Proceedings	Shirurkar et al.	2017
On optimization of a composite bone plate using the selective stress shielding approach	Journal of the mechanical behaviour of biomedical materials	Samiezadeh et al.	2015
The biomechanics of plate fixation of periprosthetic femoral fractures near the tip	Journal of Engineering in Medicine	Shah et al.	2011

of a total hip implant: cables, screws, or both?			
The biomechanics of plate repair of periprosthetic femur fractures near the tip of a total hip implant: the effect of cable-screw position	Journal of Engineering in Medicine	Dubov et al.	2011
The influence of bone density and anisotropy in finite element models of distal radius fracture osteosynthesis: Evaluations and comparison to experiments	Journal of Biomechanics	Synek et al.	2015
Validated computational framework for efficient systematic evaluation of osteoporotic fracture fixation in the proximal humerus	Medical Engineering and Physics	Varga et al.	2018
Computer-Aided Engineering Approach for Parametric Investigation of Locked Plating Systems Design	Journal of Medical Devices	Arnone et al.	2013
Optimisation of composite bone plates for ulnar transverse fractures	Journal of the mechanical behaviour of biomedical materials	Chakladar et al.	2016
Biomechanical comparison of straight and helical compression plates for fixation of transverse and oblique bone fractures: Modelling and experiments	Bio-Medical Materials and Engineering	Sezek et al.	2016

Appendix H: t-test and ANOVA tables

Table 13: One-way ANOVA p-values comparing for successive days in the ALP quantification experiment. The significance level was chosen to be 5%. The differences that the analysis finds statistically significant are highlighted in green.

|		Var 1	Var 2	p-value
Monolayer	**Standard media**	Day 7	Day 14	0.3349
	Osteo media	Day 7	Day 14	0.8050
	BMP2 media	Day 7	Day 14	0.0633
Scaffolds	**Standard media**	Day 7	Day 14	0.0363
	Osteo media	Day 7	Day 14	0.0006
	BMP2 media	Day 7	Day 14	0.0029

Table 14: One-way ANOVA p-values comparing for successive days in the cell count quantification experiment. The significance level was chosen to be 5%. The differences that the analysis finds statistically significant are highlighted in green.

		Var 1	Var 2	p-value
Monolayer	Standard media	Day 1	Day 7	0.0046
		Day 7	Day 14	0.8600
	Osteo media	Day 1	Day 7	0.0880
		Day 7	Day 14	0.1100
	BMP2 media	Day 1	Day 7	0.0045
		Day 7	Day 14	0.0047
Scaffolds	Standard media	Day 1	Day 7	0.4416
		Day 7	Day 14	0.0113
	Osteo media	Day 1	Day 7	0.6500
		Day 7	Day 14	0.9800
	BMP2 media	Day 1	Day 7	0.0738
		Day 7	Day 14	0.2570

Cell count - Monolayer

Source				Prob>F
Day (7 or 14)	1.49668e+10	2	7.4834e+09	30.3554	0
Media type	1.67597e+10	2	8.37985e+09	33.9917	0
Interaction	9.44868e+09	4	2.36217e+09	9.5818	0.00025
Error	4.43748e+09	18	2.46526e+08		
Total	4.56127e+10	26			

Days comparison

Media type comparison
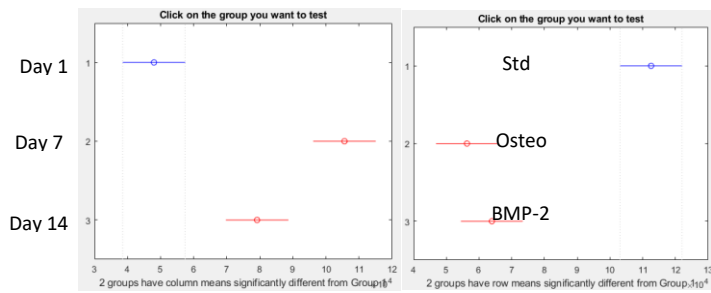
Cell count - Scaffolds

ANOVA Table

Source	SS	df	MS	F	Prob>F
Day (7 or 14)	1.41656e+08	2	7.08278e+07	6.79101	0.00635
Media type	8.97197e+06	2	4.48598e+06	0.43012	0.65694
Interaction	1.1047e+08	4	2.76176e+07	2.64799	0.06732
Error	1.87734e+08	18	1.04296e+07		
Total	4.48831e+08	26			

Days comparison

Media type comparison
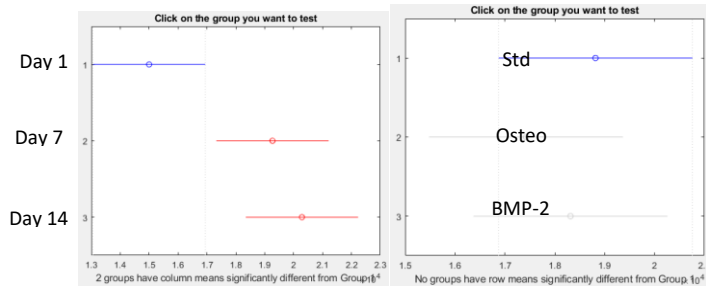
ALP - Monolayer

ANOVA Table

Source	SS	df	MS	F	Prob>F
Day (7 or 14)	7.22	1	7.22	2.6239	0.13123
Media type	171.21	2	85.605	31.1102	0.00002
Interaction	11.59	2	5.795	2.106	0.16446
Error	33.02	12	2.7517		
Total	223.04	17			

Days comparison

Media type comparison
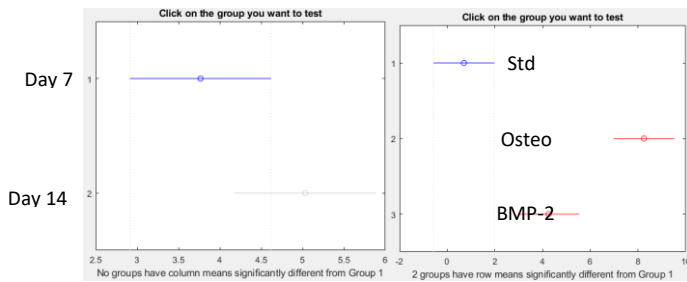
ALP - Scaffolds

ANOVA Table

| Source	SS	df	MS	F	Prob>F
Day (7 or 14)	7.22	1	7.22	2.6239	0.13123
Media type	171.21	2	85.605	31.1102	0.00002
Interaction	11.59	2	5.795	2.106	0.16446
Error	33.02	12	2.7517		
Total	223.04	17			

Days comparison

Media type comparison
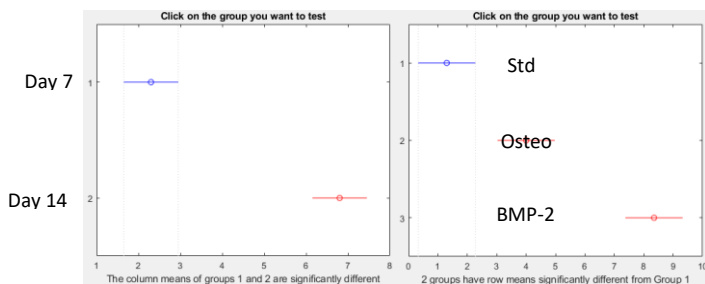
Figure 0-10: SLA experiments Two-way Anova tables as well as multiple comparison test using Tukey's honest significant difference criterion.

159

ANOVA Table

Source	SS	df	MS	F	Prob>F
Geometry	2.05981e+08	2	1.02991e+08	31.3517	0
Day	7.43527e+07	2	3.71764e+07	11.317	0.00066
Interaction	4.7288e+07	4	1.1822e+07	3.5988	0.02524
Error	5.91303e+07	18	3.28502e+06		
Total	3.86752e+08	26			
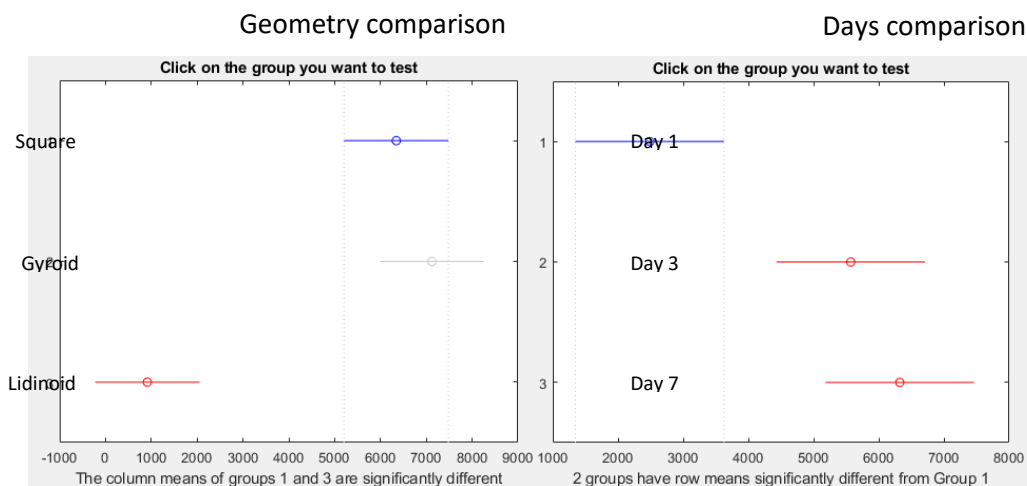
Geometry comparison

Days comparison

Figure 0-11: μSLA experiments Two-way Anova tables as well as multiple comparison test using Tukey's honest significant difference criterion.

Appendix I: The maximum stress is observed at the outer screw and is caused by the contact pressure

The maximum Von Mises stress is always at the end screw:

a) Three screws at either side:
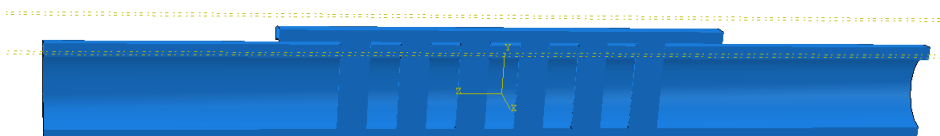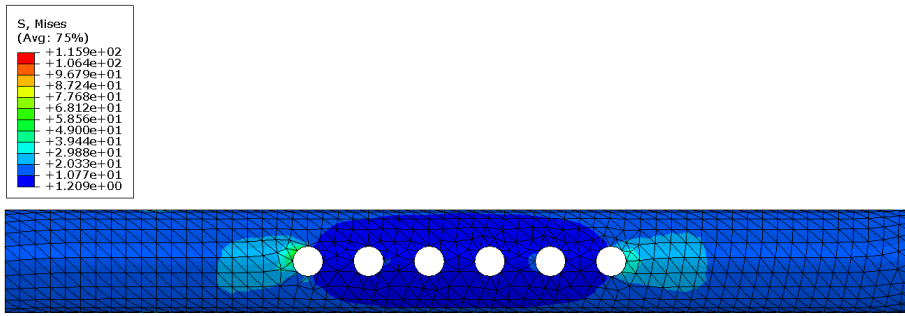
Figure 0-12: Bone-plate construct showing that the maximum Von Mises stress is a the outer screws for a case with three screws at either side.
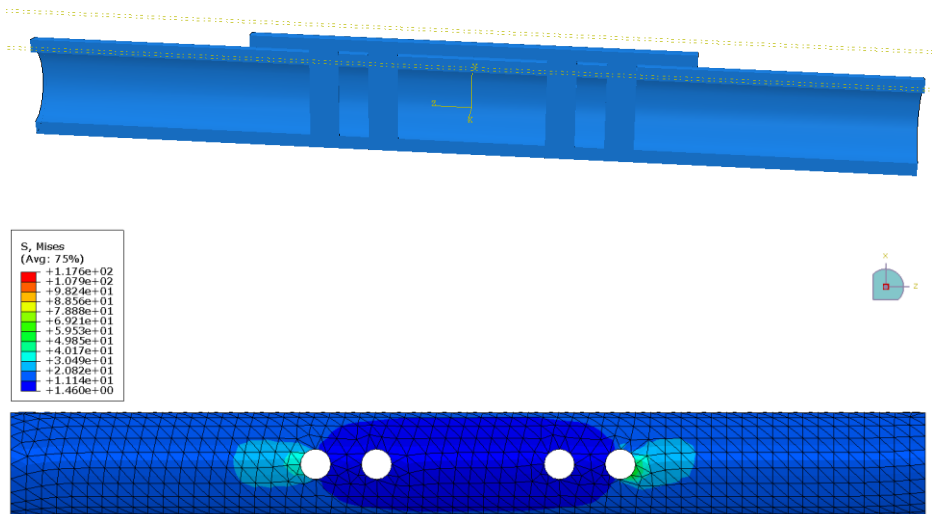
b) Two screws at either side:

Figure 0-13: Bone-plate construct showing that the maximum Von Mises stress is a the outer screws for a case with two screws at either side.
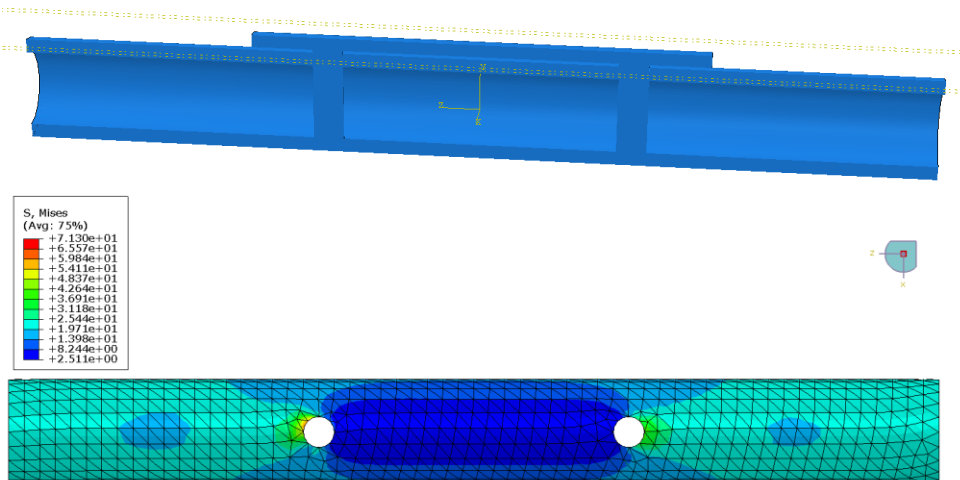
c) One screw at either side:

Figure 0-14: Bone-plate construct showing that the maximum Von Mises stress is a the outer screws for a case with one screw at either side.

Plot along path comparing the three above cases:
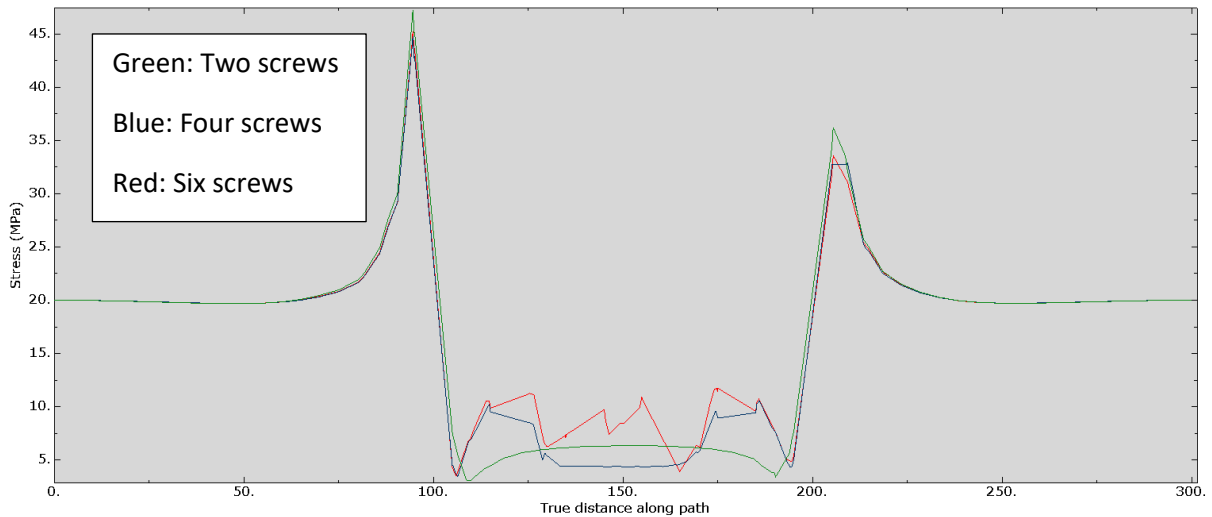
Figure 0-15: Stress plot showing the maximum stress peaks at the outer screws. It is worth noting that the plot is not symmetric due to a lack of mesh convergence which was not necessary for the intended use of this appendix. No
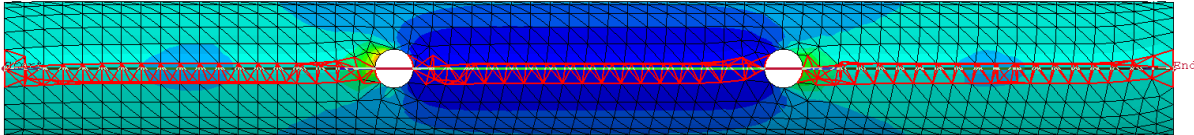
Path:

Figure 0-16: Path that was used for the above plot.

The maximum Von Mises stress is highest at the end screws because of the contact pressure:

The assembly below consists of a bone tied to screws and a plate. The loading applied were two axial loads of 20 N each as shown.
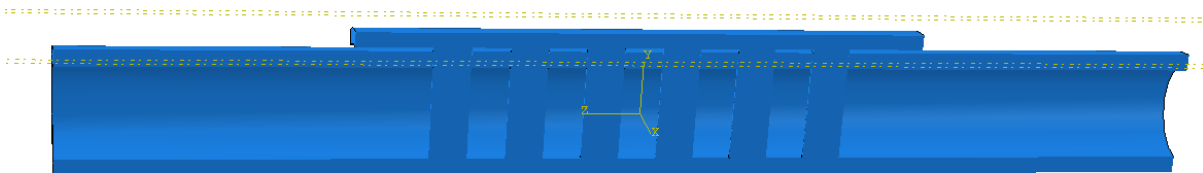

Figure 0-17: Bone-plate construct showing the assembly for the case with three screws at either side.

It can be seen below that the Von Mises stress in the bone is highest at the two outer screws.
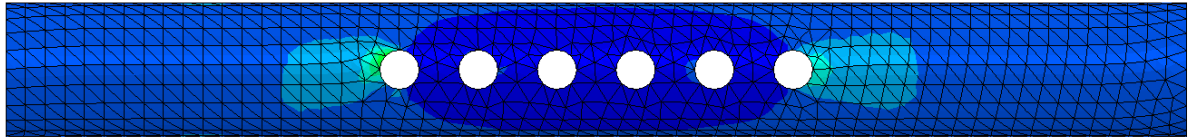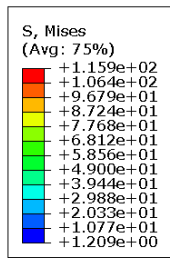
162

Figure 0-18: Bone showing that the maximum Von Mises stress is a the outer screws for a case with three screws at either side.

Below the Von Mises stress is plotted together with the contact pressure and frictional shear stresses.
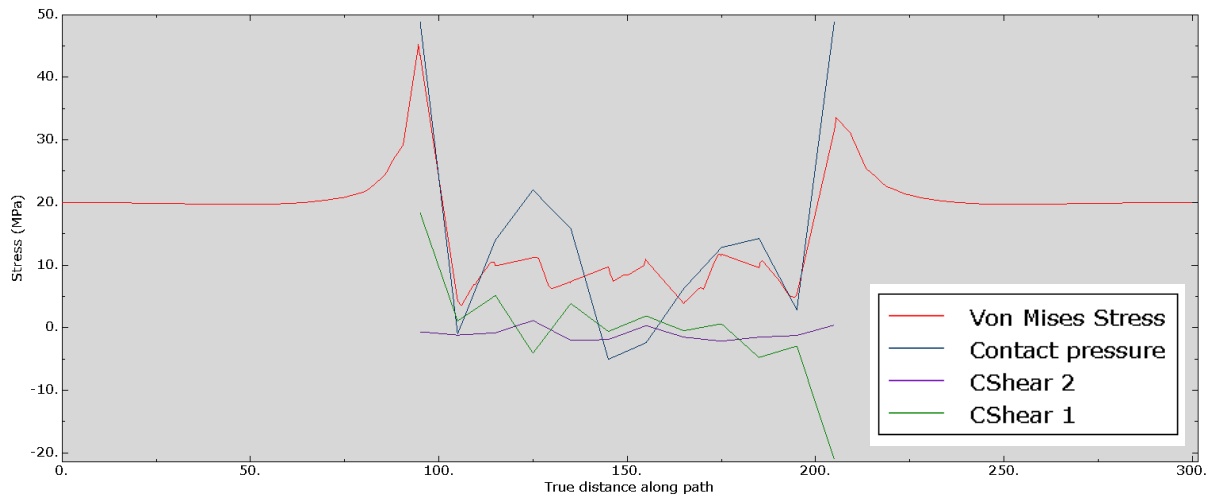

Figure 0-19: Bone showing that the maximum Von Mises stress is a the outer screws for a case with three screws at either side.

Table 15: Definitions of the different stress components as given in ABAQUS.

Name	Description (* indicates complex)
COPEN	Contact opening at surface nodes
CPRESS	Contact pressure at surface nodes
CSHEAR1	Frictional shear stress at surface nodes
CSHEAR2	Frictional shear stress at surface nodes
CSLIP1	Relative tangent at surface nodes
CSLIP2	Relative tangent at surface nodes
E	Strain components at integration points
RF	Reaction force at nodes
S	Stress components at integration points
U	Spatial displacement at nodes